Inaugural-Dissertation

zur Erlangung der Doktorwürde
der
Fakultät für Physik
der
Universität Bielefeld

vorgelegt von
Diplom-Chemiker Andreas Biebricher
aus Göttingen

04.05.2006

Development and Investigation of Probes for High-Resolution Colocalization Microscopy

Gutachter: Prof. Dr. Markus Sauer
Prof. Dr. Günter Reiss

Hiermit erkläre ich an Eides statt, dass ich die vorliegende Arbeit selbstständig und ohne unerlaubte Hilfsmittel durchgeführt habe.

Bielefeld, 04.05.2006

_____

Andreas Biebricher

Summary

A thorough understanding of biological processes and their control in living systems requires the ability to follow the fate and the interaction of different single biomolecules within a living cell. Whereas single molecule fluorescence spectroscopy (SMFS) is a powerful tool to image a single dye molecule with high signal-to-background ratio, it possesses the limitation that no resolution below 200 nm is possible with conventional set-ups due to the wavelike nature of light. Among other techniques, spectrally-resolved fluorescence lifetime imaging microscopy (SFLIM) has been developed to circumvent this problem. This allows for high accuracy localization of two fluorophores with a distance of less than 50 nm. The aim of the presented work was to advance and expand the performance of this imaging technique in order to facilitate the realization of the task stated above.

One problem of improved imaging techniques is that they allow only the determination of the relative motion between two dyes, neglecting that also the absolute motion with respect to the cell compartments conceals important information. A device capable of solving this problem would be a so-called Cellular Positioning System (CPS) that provides a set of at least three differently fluorescing spots on a solid substrate. Once it is possible to control their relative distance with nanometer accuracy, they can be taken as coordinate system for any labeled biomolecule within a fixed cell. A second obstacle is the search for suitable dyes which have distinct spectral and lifetime characteristics, but can be excited with the same laser and are not subject to photobleaching. Semiconductor nanocrystals (NCs) have already proved their superiority compared to common dyes when imaging living systems containing many dye particles. However, they show complicated photophysics on the single particle scale, and a potential use for the tasks stated above requires a detailed understanding and control of their photophysics.

In the first part of this work, gold-surfaces patterned by electron-beam-lithography were tested concerning application as substrates for a CPS system. Electron-beam-lithography enabled the creation of amino-groups on the surface with nanometer accuracy. These groups could be employed for covalent coupling of different substrates by standard techniques. The patterned gold surfaces were provided from the collaborating group of

Prof. Dr. Armin Gölzhäuser (University of Bielefeld). As test patterns, usually circular structures of 1.5 µm diameter were used. To prevent strong quenching of the dye fluorescence by the nearby gold surface, proteins labeled with fluorophores where used as scaffold system. Protein layers placed the dyes at different distances from the surface and furthermore allowed for a creation of 3D buildings blocks by consecutive crosslinking of proteins on modified structures. Suitable proteins consisted either of streptavidin labeled with the biotinylated dye Cy5, or commercially available IgG antibodies coupled with the dyes Alexa633 or Alexa680.

Successful immobilization of each protein layer could be verified by atomic force microscopy, which revealed an average height increase of ~ 2 nm per layer. For the fluorescence, a strong increase of intensity was observed for each additional layer and best results were obtained for three immobilized layers giving a signal-to-background ratio of four on 1.5 µm circles. A similar immobilization scheme was repeated on line structures with a width of 1000-50 nm. It was found that on the smallest structures fluorescence was still strong enough for perceptibility.

In a second set of experiments, the linker tetraethylene-pentaamine (TEPA) was coupled to irradiated areas to both enhance the coupling efficiency of proteins to the surface and to increase the distance from the dyes to the surface. Best results were obtained for a subsequent modification with two layers TEPA and additionally two labeled protein layers which were found to increase the S/B ratio to at least 30. By using dye labels with different emission wavelengths for the protein layers, the stronger fluorescence of the upper layer due to weaker quenching from the gold surface could be proved. These results showed that the used gold surfaces in combination with the developed modification technique have a high potential for the construction of a CPS substrate.

In the second part of the work, photophysical fluctuations of three different, commercially available NC samples with maximum emission wavelengths at 605, 655 and 705 nm (denoted QD605/655/705, respectively) were investigated with the aid of SFLIM. The signature of spectral fluctuations of NC emission was resolved by splitting the photoluminescence (PL) with a dichroic mirror onto two different single-photon detectors while simultaneously detecting the PL lifetime using time correlated single photon counting. Altogether, the set-up facilitated resolution of spectral, lifetime and intensity fluctuations down to a timescale of 1 ms with high accuracy. By correlation of the measured parameters for a number of single NCs for all three samples, it was shown for the

first time, that spectral diffusion (SD) of single NCs is intrinsically correlated to fluctuations of the PL lifetime, i.e. a spectral red shift is accompanied by an increased lifetime. Independent of quenching states, the intensity measured from single NCs was found to be anticorrelated with SD, i.e. a spectral red shift leads to a decrease in maximum emission intensity. By constructing scatter plots of PL lifetime versus emission intensity in which the spectral signature is color encoded for a single NC, a characteristic photophysical fingerprint for each of the imaged NCs was determined. In particular, this novel depiction method revealed a notable "wedge"-like shape in the plots for all NCs investigated which is defined by a distinct lower and upper bound. It could be demonstrated that lower and upper bound represents photophysical regimes where the interrelation between PL lifetime and intensity is dominated by either non-radiative or radiative rate constant, k_{nr} and k_r, respectively. Since it could be shown that fluctuations of k_{nr} and k_r are independent of each other, the existence of a novel non-radiative rate constant k_{nr}^{int} could be revealed, which is an intrinsic property of the NC. This could be used to estimate the average PL quantum yield for single NCs which was found in a range between 80-85% for most of the investigated NCs. Furthermore, k_r could be calculated for a single NC, and a clear correlation of k_r with shifts of the band edge energy E was found for most of the photophysical regimes. This proved for the first time that in colloidal NCs also k_r is subject to fluctuations which are associated to SD by means of the quantum-confined Stark-effect (QCSE). This finding is in agreement with theoretical calculations in the literature. In addition, it could be demonstrated that states where the described correlation is not valid can be ascribed to a so far unreported emissive state with fundamentally different properties of the NC. Finally, the novel depiction method was successfully applied to demonstrate that the addition of antiblinking reagents such as mercaptoethylamine accelerates the observed fluctuations between different photophysical states.

A modified SFLIM set-up in which the dichroic mirror was exchanged by a 50/50 non-polarizing beamsplitter was used to study multiexciton emission especially for QD655. By monitoring the coincidence ratio R_C under variable excitation intensity a significant biexciton (BX) emission was verified in accordance with a recent publication. A novel analysis method was developed which enabled the highly specific extraction of spectrally non-separable BX photons exploiting pulsed excitation. With this method, the BX lifetime could be determined with high accuracy even for single NCs and it was demonstrated that even for the same sample of QD655 the BX lifetimes may vary significantly from NC to

NC. By measuring R_C under constant excitation power it was demonstrated for the first time that it is also subject to fluctuations which cannot be attributed to background contribution. Instead, the data strongly indicate that quenching, i.e. a reduction of the exciton PL quantum yield ϕ_X, results in an increase of the relative BX quantum yield. This in the literature yet unprecedented finding could be explained using a simple model system, in which it is assumed that the additional quenching pathway affects both exciton and BX emission in the same way.

Finally, the slightly blue-shifted triexciton (TX) emission could be separated from exciton with the aid of a dichroic mirror in the detection path. BX emission and the relative triexciton quantum yield could be determined by the spectral signature. Investigations of the fluctuations of TX emission confirmed the assumption made for BX emission that the relative TX quantum yield also increases with decreasing ϕ_X. By investigation of the TX decay which could be derived by cross-talk correction it could be furthermore demonstrated that quenching of exciton emission also leads to a slight decrease of the TX lifetime.

Altogether, both the versatility and accuracy of SFLIM for the investigation of NC photophysics could be demonstrated. The obtained results have a high potential impact on the development of NC samples with optimized photophysical properties on the single particle level.

Table of Contents

1 Introduction

Fluorescence microscopy is one of the most popular and important techniques for biological imaging both *in vitro* and *in vivo* [1]. Studying biological processes with the aid of fluorescent labels offers many favorable properties: Nowadays specific fluorescence labeling is feasible for almost any probe, detection is highly specific with suitable excitation and emission filters, time resolution is possible down below the ms-time scale, and it is non-invasive. On the other hand, fluorescence spectroscopy displays the intrinsic limitation, that its imaging resolution is restricted by the wavelength of fluorescence, so that structures below 200 nm cannot be resolved. In cellular dimensions, where all specific binding and recognition interactions occur on distance scales well below 100 nm, this is a serious disadvantage. Whereas recent years have seen the development of detection and processing methods to allow for relative distance measurements below 100 nm, so far none addressed positioning of binding partners, e.g. active proteins on DNA, with respect to the cell compartments. Since all binding processes take place in specific compartments of the cell and cell organization is central for an understanding of molecular biology, an absolute positioning method of the active units is required. Therefore, part of this work is dedicated to the development of fluorescently patterned surfaces which allow for an absolute positioning of labels within an immobilized cell, a Cellular Positioning System (CPS) in analogy to the Global Positioning System (GPS).

Furthermore, in fluorescence microscopy, the choice of suitable dyes for imaging is of the outmost concern to attain the desired accuracy. A great improvement in this regard has been made by the introduction of semiconductor nanocrystals (NCs) some ten years ago which in contrast to organic dyes are not subject to photobleaching [2]. However, so far the photophysical properties of NCs concerning fluctuations and sensitivity on the single particle level are not yet fully understood. Hence, the second part of the presented work focused on the investigation of photophysical fluctuations of NCs on the single particle level, especially highlighting spectral and lifetime properties.

Improvements of optical devices and development of sophisticated imaging techniques especially in the last decade have pushed fluorescence microscopy to the ultimate level. Thus, Single Molecule Fluorescence Spectroscopy (SMFS), detection and tracking of single dye molecules both *in vitro* and *in vivo* is now firmly established [3-8]. The employment of

SMFS for biological imaging is not only important because it facilitates investigation of samples with fewer labels, it allows in fact a much more truthful insight into the functioning of biological systems. This is because SMFS enables the depiction of heterogeneities of an ensemble and of a single molecule. This is explained by means of a simple example: If one thinks e.g. of a set of enzymes within a cell which catalyze a certain reaction it is obviously a large difference whether all process the reaction at the same speed or whether some enzymes are much more efficient than others (static heterogeneity). Likewise, for a single enzyme it is important information to know whether catalysis is performed always at the same rate or e.g. stops and sudden accelerations occur (dynamic heterogeneity). Whereas it is possible to distinguish between the demonstrated cases with the aid of SMFS, the information about the heterogeneity is lost in an ensemble method due to averaging. Research of recent years has demonstrated that this heterogeneity is crucial for an understanding of cell organisation, since e.g. many enzyme reactions [9-13] and gene expression [14-17] have been found to occur in a stochastic manner, whereas diffusion is a central process in the organization of cell membranes [18,19].

Despite all the advantages which common SMFS techniques offer and the high sensitivity available, common SMFS displays one intrinsic limitation. It is well known that due to the wavelike nature of light, no structures can be resolved in the microscope that are much smaller than the wavelength of the light. A mathematical description is given by the so-called Rayleigh criterion, which states that even a point-like emitter shows an imaging function (point-spread function, PSF) whose radius from the intensity maximum to the first minimum is given by $r \approx 0.61\frac{\lambda}{NA}$. Since for biological imaging most often wavelengths in the visible range (e.g.: $\lambda \approx 500$ nm) are used and the best microscope objectives have a numerical aperture of NA = 1.5, this means that no objects or distances < 200 nm can be resolved. This is in contrast to the diameter of typical proteins below 10 nm and size of typical biomolecular machines such as trancription factories in the range of tens of nanometers [20-24]. Although fluorescence resonance energy transfer (FRET) [25-27] or photoinduced electron transfer (PET) [28-31] have been exploited extensively to study binding and conformational changes of DNA and protein-molecules, these methods are only sensitive for distances below 10 nm (in the case of PET < 1 nm).

In this respect, a number of different imaging techniques have been developed which tried to close the remaining distance gap from 10-200 nm for fluorescence microscopy. Technical demanding microscope set-ups have been used to reduce the spatial dimensions

of either excitation or emission path. Among these are near-field scanning optical microscopy [32,33], which uses a tiny aperture before the imaging object, and 4Pi- [34,35], and standing wave fluorescence microscopy [36-38] where interference effects from several laser beams are exploited. Probably the most spectacular advances have been achieved by stimulated emission depletion microscopy [39-41], which can also be used in combination with a 4Pi set-up [42] and demonstrated resolution down to 16 nm corresponding to about 1/50 of the responsible wavelength [43]. Very recently, this technique was employed to elucidate the fate of synaptic vesicles after release of transmitter in neurons by achieving a resolution better than 70 nm (Fig. 1.1) [44].

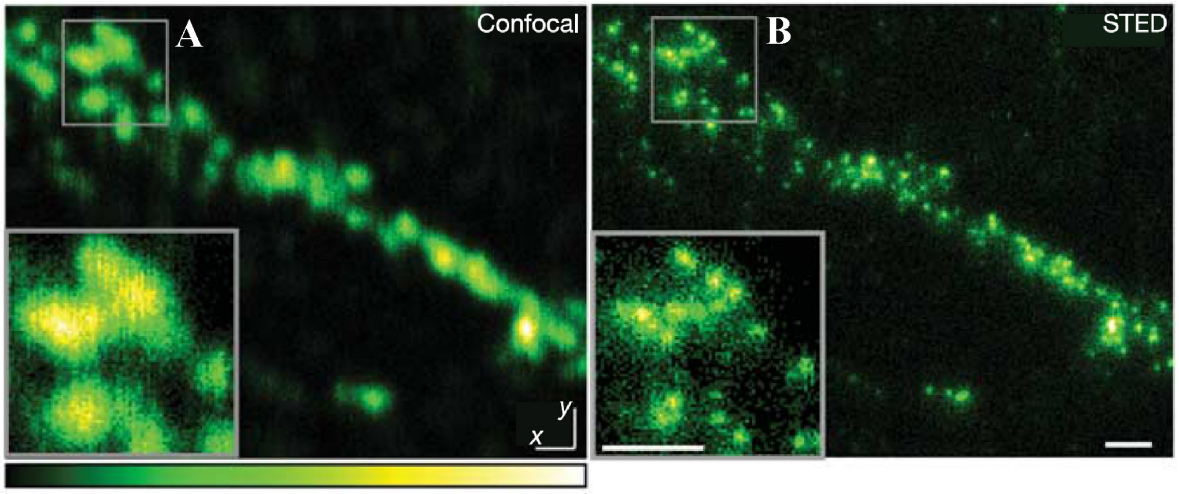

Figure 1.1: *Fluorescence scan image of synaptic vesicles in hippocamal neurons* ***(A)*** *in the confocal* ***(B)*** *and in the STED mode. Whereas in the confocal image the PSF of about 200 nm does not allow for a separation of single vesicle images (inset in* ***A****), this is possible in the STED mode because of a PSF of below 70 nm diameter (inset in* ***B****). Scalebars in the right image are 500 nm. From* [44].

A much simpler approach has been used to track single dye labels under wide-field illumination in the total internal reflection (TIR) mode also resolving diffusion with nanometer precison and accuracy. This procedure benefits from the homogeneous intensity distribution of the PSF which facilitates localization of the center of the dye with high accuracy, i.e. for bright dyes down below 5 nm [45]. Hence, with this technique the detailed courses and increments of motion of individual motor proteins could be elucidated [45,46]. With the aid of subsequent photobleaching events, it has also been extended for distance measurements down to 10 nm between two individual fluorophores [47,48]. A similar technique has been proposed for high-resolution colocalization of individual semiconductor nanocrystals (NCs). Since these show frequent lapses of photoluminescence ("blinking"), no irreversible photodestruction of the particles is required for colocalization measurements

[49]. The drawback of these methods is that only the 2D projection of the distance can be measured since the z-axis is inaccessible in the wide-field image.

Although these methods are comparatively easy to implement, they also display the further disadvantage that their only specific information is the brightness of the employed dyes. This leads to problems when encountering autofluorescence in cells since an inhomogeneous background results in distortion of the PSF. Quite early after the first successful visualization of single fluorophores it has been realized that any specific dye characteristic can enable colocalization below the optical resolution [50]. Whereas the most straightforward realization is the application of dyes with different spectra, as is the case for multicolor confocal scanning microscopy, serious problems arise when the dyes have to be excited with different laser wavelengths [51,52]. This is because a certain amount of chromatic aberration cannot be prevented even for the best optical components and reduces the attainable accuracy. A solution for this problem was presented by Lacoste *et al.* with the application of luminescent particles (labeled beads or NCs) which can be excited with the same laser but at the same time allow for spectral separation of the emission wavelength [53,54]. Therefore, the PSF of each of the nanoparticles can be recorded on a different detector with the aid of a dichroic beamsplitter, a separate localization of the particles center is possible and allows for distance measurements below 50 nm. However, both of the employed samples proved to be problematic: Due to their large size (diameter ≈ 40 nm) beads cannot be used for labeling of small biomolecules and do not strictly represent the required “point-like sources”. On the other hand, NCs often display blinking yielding patched PSF images which reduce localization precision.

In the present work, samples were investigated with the aid of spectrally-resolved fluorescence lifetime imaging microscopy (SFLIM) [55,56]. This method differs from the above described set-ups in that two specific characteristics of the same dye can be obtained simultaneously, both spectral and lifetime information [57,58]. Spectral separation is facilitated by a dichroic beamsplitter separating the light on two detectors, while lifetime resolution is achieved by excitation with a pulsed laser in combination with a TCSPC card for single photon detection. Moreover, it is possible to extract a third characteristics from the obtained data, the coincidence ratio. In the case of an assembly of identical proteins e.g. within a multi-enzyme complex, this information can be used to count the number of assembled proteins [59,60].

The suitability of SFLIM for high resolution colocalization has been demonstrated recently by using two dyes with different lifetime and spectral characteristics [58]. Despite their

spectral difference, both dyes used, i.e. Bodipy 630/650 with a lifetime ≈ 4 ns and maximum emission wavelength ≈ 660 nm compared to Cy5.5 (≈ 2 ns/700 nm) could be excited with the same laser at 635 nm. In this case, PSF separation was accomplished by correlating both the spectral as well as the lifetime distribution within the recorded intensity function. Since both dyes were attached at different ends of double stranded DNA of different lengths, the results of the colocalization could be compared to the expected values and were found to yield good agreement [58].

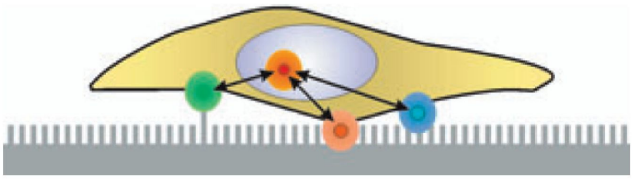

Figure 1.2: *Schematics of a Cellular Positioning System (CPS). The cell is fixed on the surface which is labeled at three defined "fixed spots" with different fluorescence markers at different heights. Thus, an absolute localization of any labeled biomolecule within the cell with respect to the "fixed spots" is possible. From* [58].

So far, high resolution colocalization has only be used in terms of determining the relative distance and its variations between two or more compartments within the cells. However, for a thorough understanding, not only knowledge about the relative distance change between the particles, but also the absolute motion of the assembly is of interest. This could be accomplished with the aid of an absolute, fluorescent coordinate system in analogy to the Global Positioning System (GPS) for earth-bound localization, i.e. a Cellular Positioning System (CPS) [8,58]. Such a scheme requires the 3D positioning of at least three differently labeled "fixed spots" on the surface, which constitute the coordinate system (Fig. 1.2). Hence the absolute position of any fluorophore within a fixed cell near the coordinate system could be determined, and the 3D organization within the cell could be revealed.

Of course, in addition to a high resolution imaging method several demands have to be met for a successful realization of the CPS scheme: For an arrangement of "fixed spots", a technique has to be developed which allows for a fabrication of very small spots (diameter << wavelength) that can be positioned on the surface with nanometer accuracy. The fluorescence signal from the spots has to be bright, stable, and specific since it is used as a positioning standard. To facilitate 3D imaging, a method has to be found for building structures of well-defined heights on the surface. Finally, each of the fabricated spots must be addressed separately, since it is required that each bears a different label.

With regard to the use for CPS, a crucial demand is the requirement of both positioning and patterning of a surface with nanometer accuracy. In the presented work, gold surfaces

modified with an organic layer were used as substrate since they can be patterned by electron-beam lithography which in principle allows structuring down to the nm-scale with high accuracy [61,62]. The use of gold as surface for fluorescent probes has the disadvantage that strong quenching of the dyes occurs [63]. Therefore, a modification scheme was developed which enables a controlled modification of the surface with fluorescently labeled proteins. The protein labels used are efficient spacers to reduce the quenching effect of the gold and to facilitate immobilization of further protein layers. Additionally, an organic linker was used to enhance the protein binding efficiency to the gold and to further increase the distance from the gold surface to the dyes [64]. By controlled growing of several layers of organic linker and subsequent layers of protein, it could be demonstrated that via this method high signal to background ratios can be obtained even for structures smaller than 100 nm.

Apart from the prospect of a CPS scheme, the presented method of high resolution colocalization with SFLIM still displays several drawbacks with respect to the use of organic fluorophores: There are comparatively few dyes available which can be excited with the same laser while showing significant different emission spectra. Even then, due to the broadness of the emission spectra, a significant crosstalk between the two detectors cannot be prevented. The necessity of different fluorescence lifetimes restrains the choices of possible dyes further and finally, colocalization requires high photon statistics corresponding to sufficient photostability. Especially the latter is of importance since for correct assignment of dye distances in 3D space a scanning through the whole cell volume is required. In the case of e.g. a volume of 10x10x5 μm^3 which is scanned with a resolution of 50x50x200 nm^3 and 3 ms integration time, an illumination time of 50 min is needed. However, photobleaching is known to be an intrinsic property of organic dyes and hence inevitable [65].

On the other hand, NCs [2] constitute near ideal features as potential labels for high precision colocalization: They are commercially available throughout the visible spectrum with high photoluminescence quantum yields and can be excited anywhere below their emission wavelength with very high extinction coefficients (Fig. 1.3). At the same time, the emission spectrum is narrower than that of typical dyes, and it is also known, that the PL lifetime shifts with the emission wavelength [66,67]. This means that not only crosstalk between the dyes but also autofluorescence may be prevented, when excitation occurs far from the detection wavelength, thus increasing the resolution capabilities. Probably their most important characteristic is, that in most cases no photobleaching can be observed,

even after hours of imaging [68]. Although blinking has been mentioned to constitute serious problems [69-71]. However, blinking might be circumvented by using efficient anti-blinking agents [72].

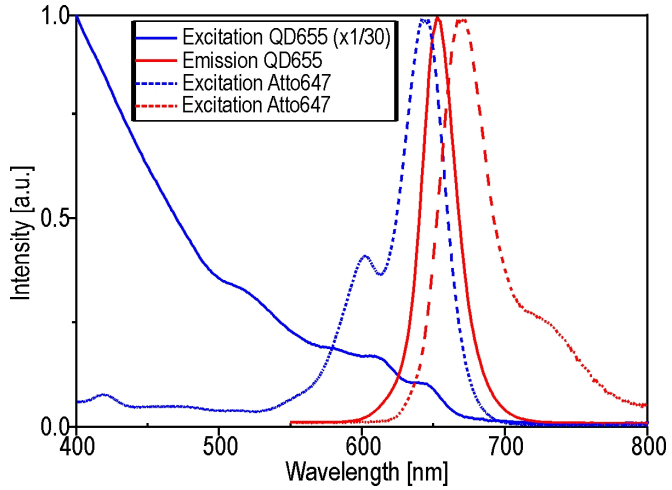

Figure 1.3: *Comparison of absorption (blue) and excitation (red) spectra of the organic dye Atto647 (dashed line) with spectra of a commercially available NC sample QD655 (full line) Note that the absorption spectrum of QD655 is reduced by a factor of about 1/30 to allow for a comparison.*

Because of these favorable features, NCs are already widely used as highly sensitive labels for biological imaging [73-75]. A large number of different functionalization procedures are available, so that they can be linked to any specific marker as is the case for organic dyes. Despite their large size (10-15 nm diameter) they can be coupled to smaller biomolecules, which still retain their biological activity, even though the diffusion is somewhat slower compared to labeling with organic dyes [18]. Nevertheless, apart from tracking of single NCs where simply the PL intensity is recorded [18], the spectral and lifetime properties have never been fully exploited on the SM level.

The reason for these findings lies in the fact, that the PL emission from NCs is fundamentally different from the fluorescence observed for organic dyes. Organic dye molecules are intrinsically homogeneous and have a well-defined number of atoms and bonds. If transitions into a different state occur, i.e. e.g. isomerization or bleaching, these are well defined, i.e. seldom intermediate levels are observed. The main regimes of fluorescence are therefore fairly well understood: compared to the ensemble level, single dye molecules exhibit only a slightly broadened spectral and lifetime contribution immobilized on surfaces [56-58]. Spontaneous spectral shifts can occur, but seldom and mostly in a binary manner, i.e. transition between two distinct energy levels [76-78]. The same finding holds for the fluorescence lifetime which is usually well described by a monoexponential decay and fluctuations occur stepwise [56,79]. Blinking is known to be due to intersystem crossing from the singlet into the triplet state [80,81] and can be influenced by addition or removal of special reagents [82-84]. The relative distribution of on- (fluorescence) and off- (no fluorescence) levels is described by an exponential distribution and can be analyzed using an autocorrelation function [85,86]. The bleaching is

characterized by a sudden jump from the on- to a background level. Concerning the coincidence characteristics, single dye molecules display ideal single photon emitters, i.e. transition into any excited state can result in only one emitted photon until relaxation back into the ground state has occurred [76,81,87].

In contrast, NCs consist of several hundred to thousands of different atoms, which are grown statistically, and slight changes of shape and size do not result in a dramatic change of the stability. Hence, a batch of NCs displays always an intrinsic heterogeneity concerning both size and shape, which manifest itself in differences of photophysical properties. The same characteristics are observed on the single NC scale: Changes of the emission wavelength are denoted as "spectral diffusion", since seldom jumps are observed and no distinct levels can be defined [88-90]. Likewise, the lifetime measured even on the single NC scale is in most cases found to be non-exponential and is best described by a stretched exponential model [91,92]. Correlated with fluctuations of the lifetime, also variation of the emission intensity occur, but again no levels can be differentiated. Whereas also for NCs there exists an on/off-intermittency in a binary manner, this is observed on all time scales without a significant correlation, i.e. the duration of the off-level can last from mikroseconds to hours [69-71,93]. Depending on the type of the investigated NC, in some cases nearly perfect antibunching characteristics are found [94-97], whereas in other cases excitation into states were detected which allowed for the emission of more than one photon per excitation cycle [98-101]. In conclusion, although there exist models describing certain aspects of the fluctuations, a consistent scenario which accounts for all observed variations is still lacking.

Before a thorough understanding of the possible fluctuations can be achieved, a detection method has to be found which allows for a simultaneous recording of all relevant parameters both with high sensitivity and time resolution. In this respect, SFLIM constitutes one of the most suited tools for detailed analysis of NC photophysics: Thus, a confocal set-up equipped with avalanche photodiodes (APDs) for detection provides the highest detection sensitivity possible, i.e. several percent of all emitted photons from the luminescent particle can be detected. A dichroic beamsplitter in the detection path splits the light between two or more APDs and facilitates determination of spectral shifts with unprecedented time resolution. Using a time-correlated single photon counting (TCSPC) card in combination with a pulsed laser, in most cases hundred photons are sufficient to yield the average PL lifetime for the corresponding time range with the aid of a maximum likelihood estimator (MLE) algorithm [102-105]. Finally, it has already been demonstrated

that pulsed excitation is also beneficial for the determination of antibunching characteristics [8,106].

Once the corresponding photophysical information from a single NC has been recorded, a method for disentangling different emission regimes has to be found, i.e. identification of spectral diffusion, different intensity levels and lifetime fluctuations has to be accomplished. Potential correlations between the detected parameters have to be unraveled which might give hints to fundamental aspects of photophysical regimes. Finally, a depiction method is required which allows for a quick "deciphering" of different emission regimes and can be used for characterization of NC emission. Different samples of NCs can then be compared and investigated for significant differences of their photophysical properties. Likewise, the influence of environmental changes on photophysical properties of the same NCs should be analyzed with respect to systematic influences. These might then be used for a controlled modification of properties.

Such studies are not only of interest for the employment of NCs as probes for high resolution colocalization. NCs are furthermore of high interest as model systems, e.g. often referred to as "artificial atoms" [107,108]. Therefore, an accurate detection of the relevant photophysical parameters might yield quantitative information about the underlying photophysics. In view of the large preparation and manipulation options, a method which allows for a characterization, classification and assessment of prepared batches is desirable for an efficient optimization of chemical synthesis.

The aim of the present work was to improve and extend the existing scheme for high resolution colocalization *in vivo* using SFLIM. Two different strategies were pursued: The first focused on establishing of patterned gold surfaces as potential coordinate system for a CPS. In the second, detailed photophysical studies of NC photophysics were carried out in order to evaluate their employment as efficient labels for high resolution colocalization.

In a second set of experiments, a SFLIM set-up was used to determine and quantify photophysical fluctuations measured from three commercially available NC samples with a time resolution down to 1 ms. By calibration and test measurements it could be verified, that in this fashion, photoluminescence intensity, lifetime and spectral fluctuations can be determined with high accuracy. By correlation of the observables an interrelation between spectral diffusion and lifetime fluctuations caused by changes of the radiative rate was uncovered. This novel connection was exploited to calculate radiative rate fluctuations and photoluminescence quantum yields of single NCs. In addition, a novel subpopulation of quenched emission could be uncovered indicating NC transition into a fundamentally

different state. The obtained data was furthermore used to construct density plots containing all three observables which are characteristic for a certain type of NC and can also be used for NC assessment. Finally, with the aid of the developed depiction method it could be shown that anti-blinking agents lead to a significant acceleration of photophysical fluctuations.

The set-up was also employed in a modified form to investigate the antibunching characteristics of the NC samples. In particular, it was demonstrated that the NC sample of type QD655 display significant biexciton emission. A novel analytical method was presented which allows for the unequivocal extraction of photons stemming from biexciton emission. This was used to calculate the biexciton decays for single NCs which was shown to vary significantly from NC to NC. For a given NC, it was also found for the first time that the relative biexciton quantum yield compared to the exciton is not constant but shows a strong increase for quenched states. This finding could be confirmed by spectrally resolved investigation of triexciton emission, which can also be used to extract the lifetime information of triexction emission.

2 Theory

2.1 Principles of fluorescence

Basics

Different from atoms, which show unsaturated valences and therefore have permitted, low lying transitions between 1.7 and 3 eV corresponding to wavelengths in the visible range, in organic molecules with stable bonds, the low energy has to be accomplished by electron delocalization. Therefore, all organic fluorophores consist of an aromatic system, often in combination with several conjugated double bonds, which leads to more or less strong transitions of ππ* with extinction coefficients $\varepsilon > 10^5$/(mol*cm). Examples of well known chromophoric systems suitable for high sensitive detection and imaging on the single molecule (SM) level and their corresponding spectra are shown in Fig. 2.1.

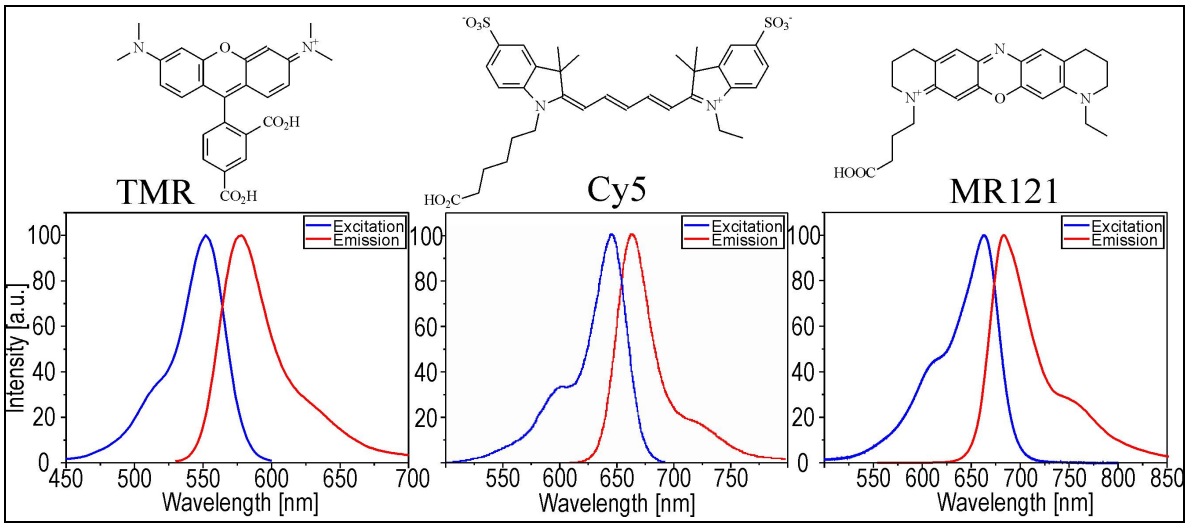

Figure 2.1: *The dyes tetramethylrhodamine (TMR), Cy5 and MR121 together with the corresponding spectra. Note the symmetric appearance of excitation (blue) and emission (red) spectra.*

In terms of the classical concept, the absorption of light with the energy $E = h\nu_{ex}$ (with Plancks constant h and frequency ν_{ex}), i.e. an electro-magnetic wave, implies induction of an oscillating electrical field, or rather, the change of oscillation direction in the molecule. Translated into the concept of Bohr's atom, this means that the electron (since it is the only moving charge) has to change its orbit around the nucleus from one stable (non-radiating) energy state to a different state at higher energy to create a transition dipole moment $\vec{\mu}$.

These two concepts can be combined by quantum mechanics considering the wave-particle dualism for both the electron states and the photon to calculate the transition dipole moment as overlap between the initial and end electron wavefunctions, Ψ_{S0} and Ψ_{S1}, integrated over the system volume element V: $\vec{\mu} = -e\int \Psi_{S1}^{*}\vec{r}\Psi_{S0}dV$, where $\vec{r}$ is the space operator. The indices S_0 and S_1 denote the ground and the first excited state, respectively, which are singlet terms, since all electron spins are paired. Theoretically, each state is defined by a sharp energy level $E(S_0)$ and $E(S_1)$ and accordingly there would be only one transition energy $\Delta E = h\nu = E(S_1) - E(S_0)$ and absorption frequency. However, since these chromphores are multi-atomic systems, whose energy levels are broadened by different vibronic and rotational couplings of the bound atoms, a frequency or wavelength spectrum exists, over which significant absorption of radiation can occur.

On the macroscopic scale, this is considered by integrating the molar extinction coefficient ε over the frequency spectrum to obtain the integral absorption coefficient $A = \int \varepsilon(\nu)d\nu$, which is a measure for the tendency of a chromophore to absorb light. This can be connected with the theoretical fraction of electrons that participate in this particular transition, the oscillator strength f which is given by $f = (4m_e c\varepsilon_0 / e^2)A$ (electron mass m_e, speed of light c and vacuum permittivity ε_0) and is near unity for strong transitions. Finally, the oscillator strength gives access to $\vec{\mu}$ via the average squared transition dipole moment $|\vec{\mu}|^2$: $f = (8\pi^2/3)(m_e\nu / he^2)|\vec{\mu}|^2$.

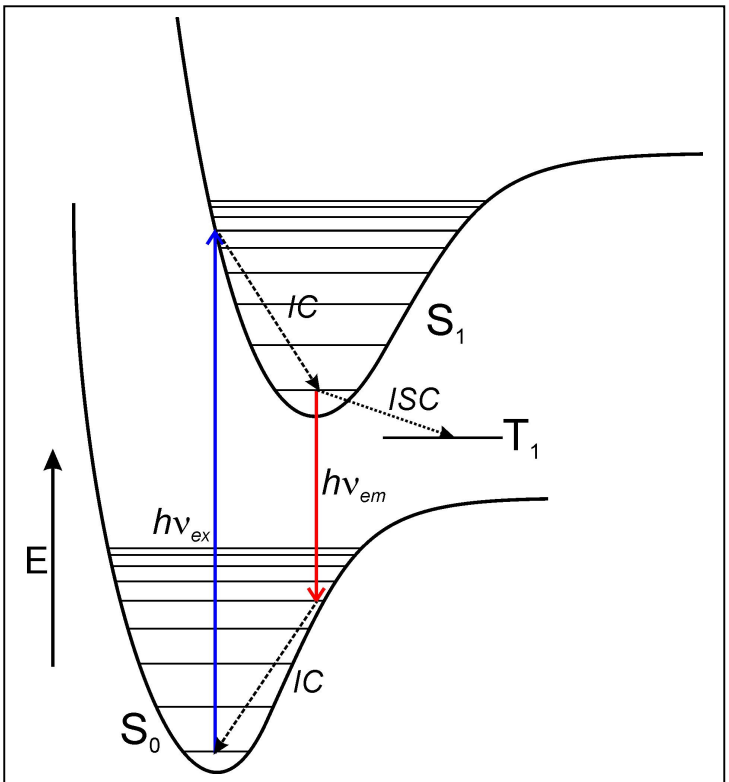

Figure 2.2: *Schematics of process of photon absorption (blue) from S_0-S_1, rapid vibrational relaxation by IC, and photon emission (red). Alternatively, from the ground state of S_1 also a transitio into the triplet state T_1 (only ground state shown) by intersystem crossing is possible, leading to a dark state.*

These concepts can now be used to qualitatively understand absorption and emission spectra,

together with the schematic energy diagram depicted in Fig. 2.2. First, it has to be considered that an electron is much lighter than the nucleus, and accordingly faster, which means that during electron transition from the ground into the excited state virtually no movement of the nuclei occurs (Franck-Condon-Principle). Furthermore, the overlap integral strongly depends on the distribution probability of the wave function and is in the vibronic ground state at its maximum in the middle, but at higher levels at the border of the potential well. Together with the fact, that the first excited state S_1 has a shifted potential curve, since one electron is in an antibonding orbital, it follows that excitation will occur vertical from the vibronic ground state level of S_0 into an vibrationally excited state of S_1. Vibronic thermalization is due to the lower energy differences (≈ 0.1 eV) of the states much faster ($\tau < 10^{-10}$ s) than electronic relaxation (10^{-7}-10^{-9} s), and rapid internal conversion (IC) of the excited level to the vibronic ground state takes place, before electronic relaxation can set in. For the latter, it is obvious that most probably a photon is emitted for the vertical transition into an excited vibrational state of S_0, which relaxes into the ground state by IC. Altogether, it can be rationalized, that the emitted light shows a red shift compared to the excitation wavelength which is known as Stokes shift. Further considerations lead to the conclusion that due to the similarities of the potential wells for S_0 and S_1, absorption and emission will display antithetic characteristics. Hence, the blue shifted absorption tail for most dyes (Fig. 2.1) is reflected by a similar red shifted emission feature.

Of course, this consideration is only a simplification of the underlying photophysics; two further processes shall be mentioned here briefly: First, it has to be considered that also states S_2, S_3, etc., i.e. higher excited states exist which exhibit increasing energetic overlap . Although the transition of S_1-S_2 or even higher is possible, e.g. by subsequent absorption of photons, the increasing density of states leads to a rapid vibronic relaxation back into S_1, so that the spectrum does not change with higher excitation intensity. Alternatively, a populated S_N-state can react upon collision with oxygen (O_2) and destroy the chromophoric system, which stops the fluorescence emission (bleaching). A different relaxation pathway into the triplet state T_1 by intersystem crossing (ISC) leads to an interruption of fluorescence, which resumes after a certain delay. In the triplet state, the excited electron has the same spin orientation as the remaining electron in the ground state which leads to a slight stabilization, therefore T_1 is always lower in energy than S_1. Because of the conservation law of spin orientation, the ISC is a forbidden process, necessitates spin-orbit coupling and can be accelerated in the presence of heavy atoms. Likewise the relaxation of

T_1 back into S_0 is very slow since in this process a second spin-flip is required (10^{-3}-100 s, phosphorescence).

So far the kinetics of the different processes have not been discussed, although they are of great importance. Principally, the processes like excitation, and vibronic relaxation by IC are very fast and can be neglected in comparison to the radiative transition from S_1-S_0, which in turn is much faster than the S_1-T_1 conversion. It should be noted that the rapid internal thermalization has the consequence, that the emission spectrum does not depend on the excitation wavelength (Kasha's rule) which is important, since the dye emission is than solely dependent on its surroundings. If the decay process is described from a kinetic point of view and *N* states with an excited electron are observed, the probability for the decay of the fraction *dN/N* of electron in the time range *dt* into the S_0 level by emission of a photon can be described as: $\frac{dN}{N} = -(k_r + k_{nr})dt$. Here, k_r and k_{nr} are constants of proportionality describing the relative probability of radiative decay, i.e. under emission of a photon, and non-radiative decay, respectively. Since they are given in units of 1/s they are denoted radiative and non-radiative rate constant, respectively. The non-radiative rate constant not only includes triplet conversion but is summed over the probabilities of all other, much more complicated processes where S_1-S_0 transition does not lead to emission of a photon. From the above equation it is obvious, that the time course of the transition S_1-S_0 is described by a monoexponential decay: $N = N_0 e^{-(t/\tau)}$, where $\tau = \frac{1}{(k_r + k_{nr})}$ is denoted as lifetime, since after a time lapse τ after excitation, a fraction of $N/N_0 = 1/e \approx 0.37$ of the excited molecules has decayed back to the ground state. For organic fluorophores, τ is generally in the range of a few ns, i.e. much faster than ISC or phosphorescence (typically 100 ns-100 µs), but slow compared to rotational and vibrational relaxation processes ($\tau <$ 10^{-12} s).

Since k_r and k_{nr} are measures for the transition probability, they can be used for the calculation of another, important parameter, the fluorescence quantum yield ϕ. This is given by $\phi = \frac{k_r}{(k_r + k_{nr})}$ and yields the fraction of states, where absorption of a photon results in emission of a photon. ϕ is typically > 0.5 for efficient dyes. The radiative rate constant is

also important from a microscopic view, since it is connected to both the oscillator strength and the transition dipole moment $k_r = (\frac{8\pi^2 e^2}{m_e c}) \frac{|\vec{\mu}|^2}{\nu^2} f$.

Interactions with other fluorophores

As it has been stated that an excited fluorophore constitutes an oscillating dipole, it is obvious that in principle it might interact with any charge or dipole which might lead to exchange of energies or particles. However, in many cases the interaction is too weak to lead to considerable alteration of the fluorescence. Several stronger interactions which are widely used for investigations of biological systems will be discussed here.

Redox properties, Photoinduced Electron Transfer (PET)

In terms of molecular orbitals, the S_0 and S_1-level of a dye A are referred to as HOMO and LUMO, i.e. highest occupied and lowest unoccupied molecular orbital, respectively. In the excited state A*, one has two SOMOs (singly occupied molecular orbitals), which become important if the lower orbital (the former HOMO) is at comparatively low energy. In these cases, contact with a different molecule D having a completely filled HOMO at an energy level above the lower SOMO can result in electron transfer from its HOMO to the SOMO of the dye. Hence, an anionic dye radical $A^{\bullet -}$ together with a cationic donor radical $D^{\bullet +}$ are formed and a complete loss of fluorescence is observed since the electron in S_1 cannot relax back into the completely filled S_0-state.

$$A + h\nu \rightarrow A^*; \quad A^* + D \rightarrow A^{\bullet -} + D^{\bullet +}$$

This photoinduced electron transfer (PET) is highly sensitive to the distance of the donor molecule and the dye, i.e. because of electron tunneling it requires near contact (< 1 nm) and fluorescence resumes as soon as the contact is broken. Because of a comparatively high electron affinity, the dye MR121 has proved to be a valuable quenching indicator [30,109], since it can be both quenched by the nucleobase guanosine as well as by the amino acid tryptophan. Therefore, the distance dependent quenching of MR121 has already been used in numerous studies to either investigate specific sequence recognition of DNA hairpins [110,111] or for the evaluation of protein folding kinetics [112-114].

Fluorescence Resonance Energy Transfer (FRET)

Whereas the PET mechanism involves transfer of a particle (electron) which is induced by photon absorption, the direct transfer of the photon energy from the excited dye to an

acceptor molecule is more common. This becomes important in the specific case when two dyes are close together and one of the dyes is in its photo-activated state. The rationale behind an interaction is that each dye is a potential dielectric oscillator, hence there is a regime upon which the two dyes form a system of coupled oscillators. Under certain conditions, fluorescence resonance energy transfer (FRET) of one excited dye to the other can occur, even if the distance is much larger than the van-der Waals radius. The quantitative description is derived from an expression of two oscillating dipoles with averaged relative orientation which show a spectral distribution over a range of frequencies and was first carried out by Förster [115]. The essence of these calculations are the finding that the energy transfer efficiency ϕ_E (defined as the "quantum yield" of the coupled system, i.e. excitation of one dye and emission from the other dye) for two dyes with a quantum yield of unity scales with the power of six of the inter-dye distance R: $\phi_E \propto \left(\frac{{R_0}^6}{{R_0}^6 + R^6} \right)$. In this term, R_0 denotes the "Förster radius" which depends most notably on the relative orientations of the dyes (of course, two dipoles at 90° relative orientation can experience no coupling) and on the "spectral overlap", i.e. the relative overlap of the absorption spectrum of one dye (the acceptor A) with the emission spectrum of the other dye (donor D).

$$D + h\nu \rightarrow D^*; \quad D^* + A \rightarrow D + A^*; \quad A^* \rightarrow A + h\nu$$

It has to be pointed out here that the energy transfer is not accomplished via emission and absorption of photons, but via the field energy, i.e. virtual photons. As is obvious from the dependence on the spectral overlap, the energy transfer can be reversible for two identical dyes, but is unidirectional if one dye (the donor) absorbs light at much shorter wavelengths and emits in the spectral range of absorption from the other dye. The energy transfer in this case can by observed by two different parameters: Due to the use of a dye with higher absorption, also the emission wavelength will be much higher than expected if the excited dye would emit. Furthermore, since the transfer rate is also a depopulation process of S_1 without emission from the excited dye, the residual fluorescence of the latter (if the emission is spectrally separable) will show a much shorter lifetime. On the other hand, the excitation process of the acceptor dye is then not only limited by internal thermalization, but by the lifetime of the donor dye and the resulting lifetime is a convolution with the latter. It is also important to realize that the quantum yield of the acceptor is not important for the occurrence of FRET, thus a nearby molecule which absorbs in the range of the

donor emission, but shows no fluorescence might likewise act as an efficient FRET acceptor.

Typically, the Förster radius has a value of around 5 nm for the most common dye-constructs (e.g. TMR-Cy5, compare Fig. 2.1) and because of the strong dependency on the distance FRET has been used extensively for distance measurements and to monitor distance changes in biological systems [25,80]. Furthermore, FRET constructs consisting of five different dyes have been recently used to build "photonic wires" which allow for directional energy "conduction" of up to 14 nm [116,117].

2.2 Gold surfaces

In recent decades gold has found wide applications as substrate for different chemical and biological substances. Gold surfaces show a number of advantages compared to other substrates for immobilization: They can be prepared by various techniques ranging from vapor deposition to decomposition of instabile precursors. Whereas the surfaces are chemically inert, highly specific and stable modification can be achieved with primary thiol groups. The further advantage of this modification is also that many, especially long-chained thiols are known to undergo spontaneous formation of self-assembled monolayers (SAMs) on the gold surfaces [118]. In a SAM, the adsorbing molecules show ordered condensation in a sense of a two-dimensional crystal, i.e. adsorbance is controlled by thermodynamics and regular surface structures are formed. Because of their well-defined structure, high surface density, and stability they have become an important field in surface science.

Furthermore, nanoparticles of gold in the diameter range from 1-500 nm are easily prepared and are also widely used [119]. Their potential applications vary from labels for Transmission Electron Microscopy (TEM) [120,121] via colorimetric detection sensors for DNA [122-125] up to substrates for nanoparticle building blocks [126,127].

Interaction of metals with fluorophores

Basic work on the influence of a conducting surface on nearby fluorophores stems from the end of the sixties and seventies, where in pioneering experimental and theoretical efforts much of the present knowledge has been acquired [128-131]. Thus, it was found that fluorophores which were kept by Langmuir-Bodgett-layers at a well-defined distance from

a metal surface, displayed a fluorescence lifetime oscillating with the surface distance in a distance range from 10-600 nm. However, when the distance decreased below 10 nm a dramatic decrease together with strong quenching of the fluorescence was observed (see Fig 2.3). Subsequently, a number of different theoretical approaches appeared to derive a sufficient explanation for the experimental results, most of which were found to give acceptable results within a certain range. Finally, Chance, Prock, and Silbey developed a consistent model in a series of papers which to date still gives the most complete and accurate description of the interaction [63,132-139].

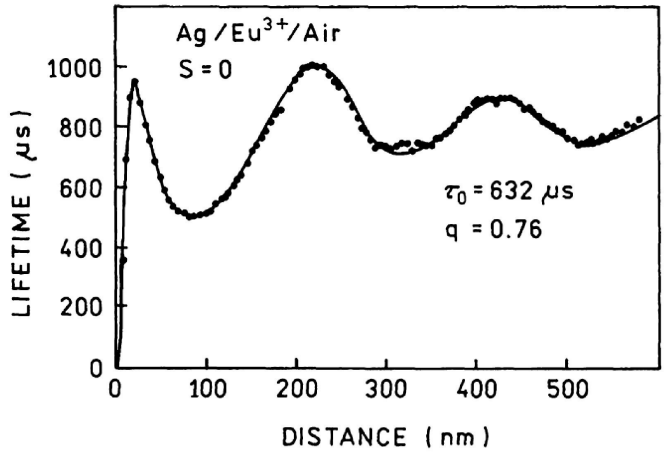

Figure 2.3: *Lifetime of a Eu^{3+}-complex measured in dependence of the distance to a silver surface (Ag). For distances beyond 100 nm the lifetime shows an oscillating behavior due to either negative or positive interference of the light field with its mirror image. Below 20 nm, the lifetime decreases drastically because of influence of "lossy surface waves" which induce strong quenching.From* [136].

In the model, the excited fluorophore is described as an oscillating dipole and its interaction with the metal consists both of far and near field interaction. According to the model, in the range of large distances > 10 nm the dominating factor arises from the interaction of the fluorophore with its own electromagnetic field which is reflected from the surface. Hence, either positive interference with the "image" field can occur which leads to an increased radiative rate and shortened lifetime, whereas for negative interference the lifetime increases. On the other hand, this interaction is only of minor importance for the near field interaction, which is dominated by additional non-radiative energy transfer from the fluorophore to the metal resulting in a strong quenching of fluorescence. Generally, this interaction is denominated "lossy surface waves" and can be described in short as non-resonant excitation of electrons which subsequently loose their energy by scattering processes in the lattice. The mathematical treatment is similar to the description of interaction with an induced dipole and therefore is analogous to the FRET calculation, where the dye is the donor and the metal the (non-radiative) acceptor.

Recently, the distance dependence of the quenching was determined using semiconductor nanocrystals linked to gold nanoparticles of 1.4 nm diameter via a double stranded DNA

[140]. By measuring the relative quenching of the PL from the nanoparticles for various DNA lengths, it was possible to confirm the FRET-like dependence. In a similar approach, gold nanoparticles have also been used for construction of molecular beacons [141,142]. In these experiments, a dye is linked to gold via an single stranded DNA which forms a loop ("hairpin") (Fig. 2.4A). Since in the hairpin structure nanoparticle and dye are in close contact, the dye is efficiently quenched. However, upon addition of a specific binding sequence which matches with the sequence of the DNA hairpin loop, binding occurs and the hairpin structure is disrupted. The increased distance of the dye from the surface due to the relative stiffness of double stranded DNA, results then in a decreased quenching, and together with the specific binding sequence, a strong increase of fluorescence is observed (Fig 2.4B/C).

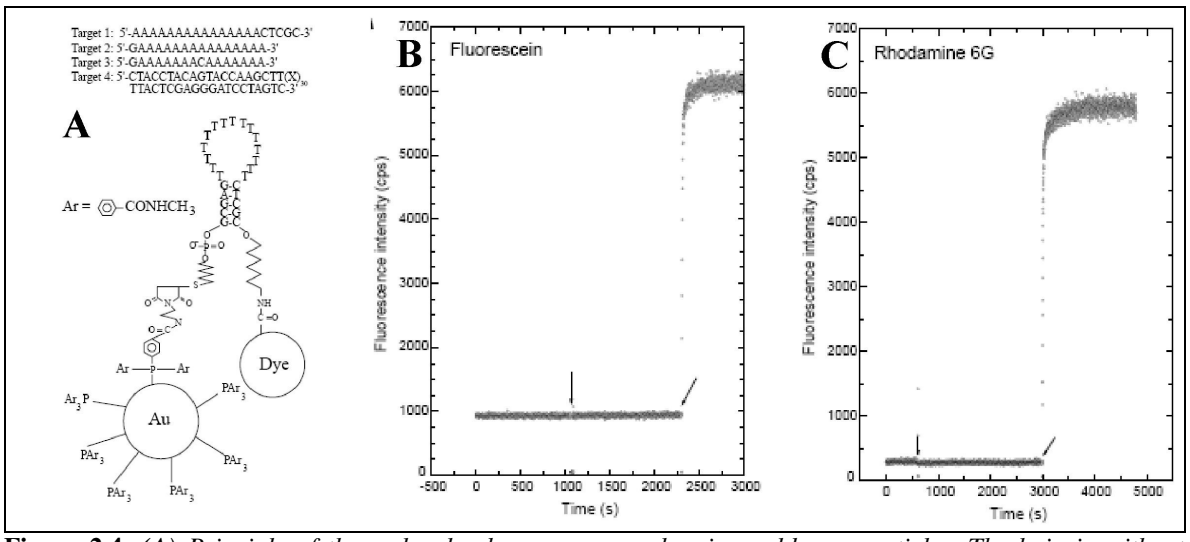

Figure 2.4: ***(A)*** *Principle of the molecular beacon approach using gold nanoparticles. The hairpin without specific sequence is closed and leads to dye-quenching by the gold.* ***(B)/(C)*** *Two resulting curves of a molecular beacon with a gold nanopartcle. The fluourescence intensit is measured in a spectrometer. After addition of the specific sequence (indicated by second arrows), the intensity increases rapidly due to opening of the hairpin.From* [141].

Nevertheless, since quenching most often occurs on a surface and not with a point-like object, it is obvious that the distance dependence because of dimensional reasons will be different from the FRET dependence. Accordingly, a cubic dependence of fluorescence lifetime and intensity on the distance to the metal is predicted for this quenching regime, i.e. $\tau \propto R^3$. In some cases it has been argued, that not the whole electron volume in the metal contributes significantly to quenching, but that only the surface electrons are efficiently deexcited by collisions. Then, a dependency of the quenching on the fourth power to the metal distance is expected ($\tau \propto R^4$) [143-145].

Numerous studies of fluorescence on or near gold surfaces have been accomplished [146-150], although only a few of them examined the distance dependence of the quenching efficiency. However, in most cases for distances below 15 nm an agreement with the cubic dependence model has been found [151-153] (although in some cases a lifetime decrease with the fourth power has been observed) [154,155]. The situation is greatly complicated since several publications in recent years reported about a significant fluorescence enhancement of fluorescence intensity especially on rough metal surfaces [156-160]. These findings are far from being understood, but it is commonly believed that the effect denominated surface enhanced fluorescence (SEF) is similar to the surface-enhanced Raman spectroscopy (SERS) which is well established [161]. In both cases it is assumed, that induced field oscillations on a rough surface can create so called "hot spots" where the incoming field is enhanced by orders of magnitude. This enhanced field increases the radiative fluorescence rate, so that the quantum yield increases whereas the lifetime decreases. However, so far this technique has not been established as system for controlled fluorescence enhancement, and no reports about results on the SM level exist so far.

2.3 Semiconductor nanocrystals

2.3.1 **Basics** [162,163]

The characteristics of a semiconductor is that different from metals there exists a significant energy gap E_G (typically in the eV range) between the fully occupied valence and the empty conduction band. This difference can be explained by the fact, that the attracting potential of the metal nuclei is not completely screened by the inner shell electrons. This has the consequence that a moving electron interacts with a weak periodic potential leading to a significant probability of reflection at the potential barrier. Due to the wavelike nature, the electron-gas in the semiconductor can be supposed to exist as a superposition of standing waves. The reflection results in negative interference for distinct energy levels. Hence, no electrons can be found in these states (band gaps). Classical semiconductor materials are based on the electronic structure of 4^{th} row elements (IV) in the periodic table, thus they have an element combination yielding the same valence electron number as in IV, i.e. semiconductors from an element combination III-V, II-VI or I-VII are frequently found.

Generally, the calculation of the detailed wave functions of the electrons for a given material is very time consuming. For this reason several simplifications are made: The momentum of an electron can be described as $p = \hbar k$, where k is the wave vector. Although it has to be considered that the periodic potential results in a different behavior than found for a freely moving particle, one can calculate its kinetic energy as $E(k) = \frac{\hbar^2 k^2}{2m^*(k)}$, where the function $m^*(k)$ is denoted as "effective mass". This often allows for correct interpretation since the electron is often found near the potential well, where changes of the effective mass are very small, i.e. the well can be described by a parabolic potential. This effective mass can be described in some relevant cases as a constant instead of a function, namely near the maxima and minima of the periodic potential. Within this model, e.g. exertion of a force can then simply be described as $F = m^* a$, even though the effective mass might be considerably "distorted" from normal behavior, e.g. it can be negative for a given potential.

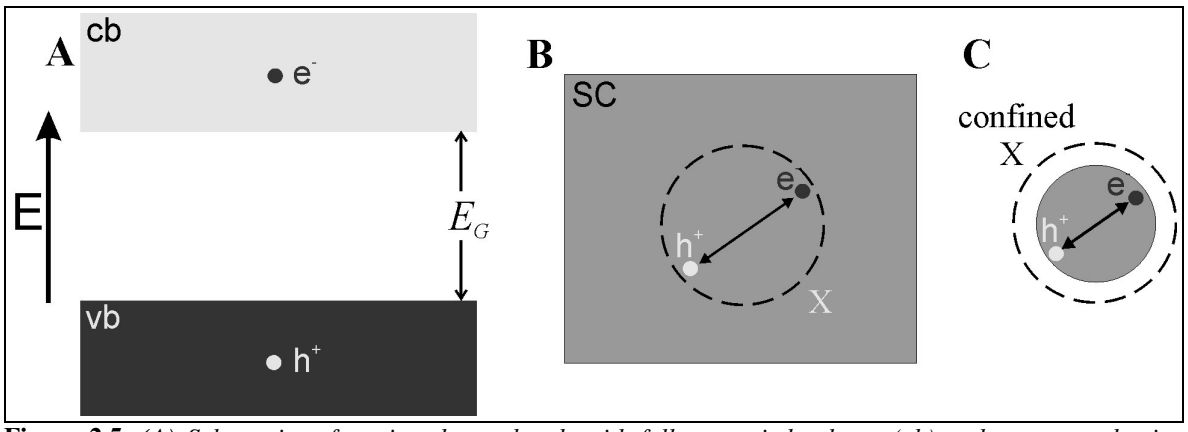

Figure 2.5: ***(A)*** *Schematics of semiconductor bands with fully occupied valence (vb) and empty conduction band (cb) separated by the band gap energy E_G. Excitation of an electron e^- into cb leaves a hole h^+ in vb.* ***(B)*** *In the semiconductor (SC) an exciton (X) might be formed as e-h-pair for which a radius a (dashed circle) can be defined.* ***(C)*** *If the semiconductor is smaller than the X radius (dashed circle), the e-h-pair is confined, resulting in a nanocrystal.*

Although due to the band gap most of the outer shell electrons are in the valence band, even at room temperature there is a certain fraction which is excited into the conduction band and responsible for the conductive properties of semiconductors. Each electron (e) in the conduction band leads to a reduced screening of the nuclear charge in the valence band. Therefore theoretically, the missing electron is described by a new particle, the "hole" (h) (Fig. 2.5A). Both charges, electrons and holes, may occupy many free (unoccupied) energy levels and are responsible for the electric conduction as charge "carriers". Since they are "embedded" in the semiconductor matrix, i.e. no free particles, their effective mass is

usually smaller than that of a free electron. In most cases, the effective mass of the hole is several times larger than that of the matrix electron. Although, electrons and holes are generally moving free within the bands, due to their opposite charge they can also interact with each other to form an electron-hole(e-h)-pair ("exciton", X). The exciton is a quasi-particle with a paired spin (= Boson) and can be regarded similar to a hydrogen-atom or a positronium as a state where electron and hole orbit around their center-of-mass (Fig. 2.5B). Thus, the e-h-binding energy E_B is given for the nth state by $E_B = \frac{\mu^* e^4}{2(4\pi\varepsilon_0\varepsilon\hbar)^2}\frac{1}{n^2}$, where μ^* denotes the reduced mass of the electrons and holes effective mass and ε the electric permittivity of the semiconductor. Note that since the reduced mass is much smaller and the permittivity is higher than for the hydrogen atom (H), E_B is much smaller than 13.6 eV, generally below 100 meV. Likewise, the exciton radius a_X in the ground state which is the average distance between e and h is much larger than the Bohr radius of hydrogen H (a_H 0.5x10^{-10} m), but in the range of several nm: $a_X = \frac{\varepsilon}{\mu^*/m_e} a_H$ (see table 2.1).

Material (rows)	E_G [eV]	μ^*/m_e	ε	E_B [meV]	a_X [nm]
GaAs (III-V)	1.424	0.056	13.2	4.4	12.5
InP (III-V)	1.34	0.070	12.6	6.0	9.5
ZnS (II-VI)	3.91	0.28	8.9	49	1.7
CdS (II-VI)	2.51	0.16	9.4	24.7	3.1
CdSe (II-VI)	1.75	0.088	10.2	11.6	6.1
CdTe (II-VI)	1.475	0.083	10.2	10.9	6.5
CuCl (I-VII)	3.395	0.39	7.9	85.1	1.1

Table 2.1: *Exciton data for some typical semiconductors. From* [162].

The absolute exciton energy is then given as $E_X = E_G - E_B$, i.e. only marginally below the band gap energy because of $E_G >> E_B$. As can be deduced from the specifications for the different elements, mass and energy increase, thus permittivity and radius decrease for lighter elements (such as S to Te) and with the row difference (I-VII versus III-V). This can be rationalized by both a lower polarizability and a higher polarity, by which the carrier screening is significantly reduced.

In the beginning of the eighties, it was realized that significant deviations from bulk properties occur, when the semiconductor crystal size is reduced in one or more dimensions

to the diameter of the exciton radius (Fig. 2.5C) [164-168]. Because of the large size of the exciton radius, i.e. much larger than that of the unit cell of the crystal, this can easily be achieved.

The influence of the small size can be understood, if it is considered that both electron and hole can at least in theory only exist within the semiconductor material, hence its interface constitutes (in vacuum) an infinite potential. The Schrödinger equation states that each particle within such boundaries ("particle in the box") has energy states of $E_C = \frac{h^2}{8\mu^* a^2}\frac{1}{n^2}$, if a is the distance between the boundaries. Whereas for sizes $a >> a_X$ this is of minor importance for the energy levels of the e-h-pair, since it is their average distance due to the Coulomb interaction, in the case when a gets near or falls below this value, both carriers and the exciton energy are "forced" to a higher energy level. For these reasons, this regime is called confinement and as can be deduced from the energy levels, it is possible to control the exciton energy by the size reduction.

Principally, confinement is possible in all three dimensions, hence there exist structures called "quantum wells" (1D confinement), "quantum wires" (2D) and "quantum dots" (3D). Although all three types of confinement play in important role in present research, the present work will focus mainly on quantum dots, which for simplicity are here called "nanocrystals" (NCs).

2.3.2 Preparation of colloidal NCs

Growing of small clusters can be achieved by different methods and on different materials, however, one of the most important types of clusters are colloidal NCs, which are prepared freely dispersed in solution and can be used for labeling of surfaces and biomolecules. The crucial step for fabrication of such small particles is a controlled growing procedure, which leads to crystals of similar composition, similar structure and nearly equal size (monodisperse particles). Since each fabrication procedure underlies statistical variations, which lead to a certain distribution of the mentioned criteria it is furthermore important to allow for a sensitive separation method to select a range of desired species.

The growing starts from an atomic precursor of both materials involved, i.e. labile substances that yield the atoms by simple means at high concentration. The decisive factor behind this procedure is that the atoms are produced under supersaturation conditions, at much higher concentrations than necessary for a start of the nucleation (spontaneous

formation of atom clusters). Under these conditions, a very large amount of clusters (nuclei) is formed directly after the start of the reaction which displays a high nucleation rate as long as supersaturation persists. As soon as clusters have been formed, there are two competing reactions in the supersaturated solution, growth of initially formed clusters and formation of new nuclei. Since the latter will lead to increasing heterodispersity (nuclei formed later result in smaller nanoparticles), the nucleation process has to be interrupted instantaneously, e.g. by sudden change of temperature. Once a sufficient amount of nuclei has been produced further growth can continue under milder conditions, where no new nucleation occurs. Thereby, it has to be considered that the nucleation is not irreversible, i.e. with a certain probability an integrated atom might dissolve from the surface back into the solution. This can advantageously be used for "Ostwald ripening", in which after depletion of free atom concentration smaller crystals due to their higher surface energy slowly dissolve into the solution whereas growth of larger crystals continues. The extent of this process can be carefully controlled by the temperature and leads to a further sharpening of size distributions. These reactions can only be carried out in a solvent which is inert to any interference with the formation and growth process, e.g. side-reactions with the reagents, but which at the same time stabilizes formed clusters and crystals since precipitation of the latter is detrimental for the reaction. This is accomplished using a stable solvent with strong complexing properties, so that the surface of the clusters is always "protected" by solvent molecules.

For the most widely used material, CdSe, which was also used in this work, these precursor substances generally consist of Dimethylcadmium (Me_2Cd) and Tri-n-octylphosphineselenide ($(C_8H_{17})_3PSe$), both of which rapidly disintegrate into non-reactive organic compounds and Cd and Se atoms upon heating to 250-300°C [169]. Before the reaction starts the solvent (Tri-n-octylphosphineoxid, TOPO) is heated to about 300°C, then a mixture of the precursor materials is quickly added under stirring. If the heating has been interrupted directly before the reaction, the addition of precursor leads to a rapid cooling of the reaction mixture (< 200°C) which prevents further nucleation. Growth continues for several hours under slow heating at around 250°C. Exact time and temperature depend strongly on the desired particle size. Reactions can be easily followed by the absorption spectra of aliquots of the mixture. Purification is achieved by various precipitation techniques, which include addition of solvent and centrifugation to remove side products in the supernatant after which the NCs are redispersed. A more sophisticated procedure is the size-selective precipitation where under careful conditions only the largest NCs in the

solution are precipitated and removed from the rest to yield highly monodisperse NCs, with a size distribution < 5% of root mean square in the diameter.

This method can be used to yield CdSe NCs with a diameter range from 1.2-11.5 nm, corresponding to a PL emission range of 400-700 nm. NCs synthesized by this method have a wurtzite like crystal structure and are more or less spherical, although the hexagonal crystal leads to a slide elongated grow in one direction. Note, that the heterodispersity does not only refer to the size, but there are also slight differences in shape, and lattice mismatches or stacking faults can occur.

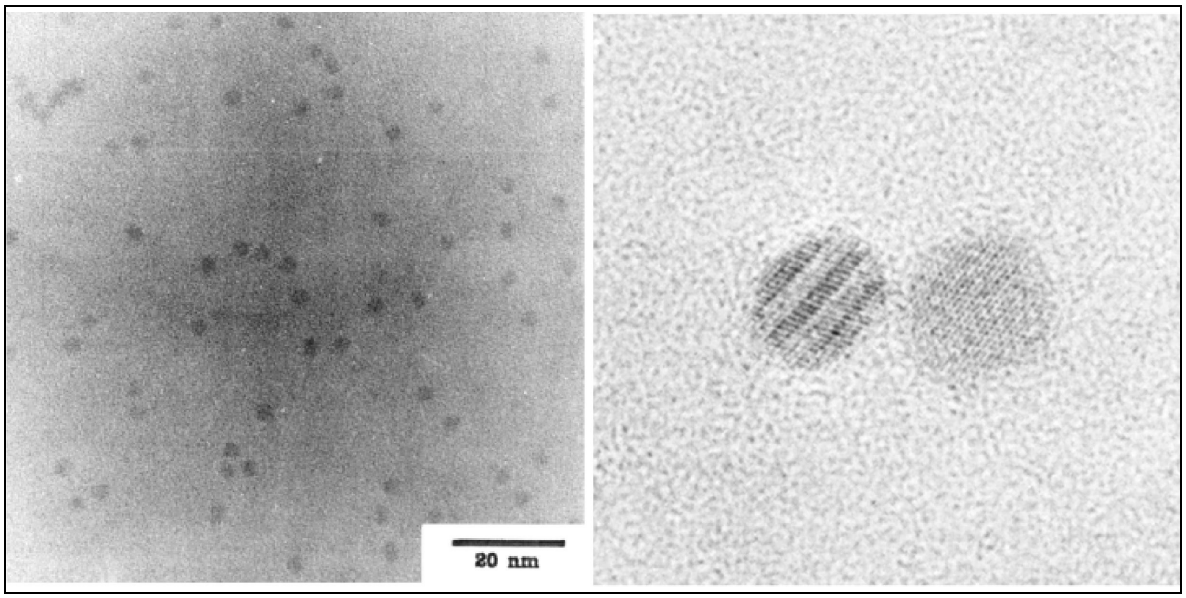

Figure 2.6: ***(A)*** *TEM image of CdSe nanocrystals after preparation and size-selective precipitation. Note the homogeneity of the size.* ***(B)*** *Enlarged picture of two NCs of CdSe from the sample in* ***(A)****. Even single atoms can be distinguished and several stacking faults in the NC to the right are visible as stripes. From* [169].

Although NCs prepared in this manner have also been used for the study of photophysics, they display only low PL quantum yield (< 10% in solution). This is because the NC and thus created e-h-pairs are not isolated, but in strong contact with the environment which leads to increased non-radiative relaxation via "traps". Therefore, nowadays the preparation of the NC "core" is usually followed by a coating with an insulator material ("shell") to yield stabilized core-shell NC with high quantum yield [170,171]. As best material for this purpose, ZnS has been found which can be grown onto the NCs in an analogous manner to the NC preparation, by adding precursors (Dimethylzinc Me_2Zn and Hexamethyldisilathiane $(Me_3Si)_2S$) to a heated NC solution in TOPO. Since ZnS has a much higher bandgap energy (see Table 2.1) than CdSe, interactions of the carriers with the environment is greatly reduced, leading to much higher quantum yields in solution (> 50% possible) if a certain layer thickness (about 1.3 monolayers) is fabricated.

Even when these preparations are accomplished, one problem remains: The greatest importance of fluorophores lies in the field of bioscience, which requires solubility in aqueous solutions, whereas NCs described by the above methods are strongly hydrophobic. A number of different approaches have been used to overcome this hurdle. Thiols with charged residues, e.g. thioglycolic acid, are the simplest approach to facilitate solubility in water. However, they have the major drawback that the coating is not very stable [172,173]. Different materials include silanes [174,175], peptides [176-179] and ambiphilic polymers [74,180-182], which already facilitated use of NCs for biological imaging under in vivo conditions [18,73,75,183-186]. The latter modification has even been used to prepare large scale batches of NCs which are commercially available with a wide range of surface modifications and are stable over months.

Further improvements aim for growing new types of shells around the dots for better protection, a so-called multi-shell protection [187]. This approach is based on the finding that ZnS displays a considerable lattice mismatch (> 10%) compared to CdSe which should lead to strain on the core and growth of elongated shells. The new method allows for a gradual core-shell transition, in that the composition can be described by the formula CdSe/CdS/$Zn_{0.5}Cd_{0.5}S$/ZnS, which reduces the strain considerably since the mismatch of CdSe/CdS is less < 5% [187]. This leads to almost perfectly spherical NCs and has been shown to improve the optical properties significantly and result in > 75% PL quantum yield measured for the ensemble.

2.3.3 General photophysical properties

It has already been stated that the confinement leads to an increase of the band gap energy compared to that of the bulk material. Obviously, however, confinement does occur on a steady level. Therefore, two different confinement regimes can be defined, either weak or strong, where weak means that the confinement energy is significantly lower than the exciton binding energy and vice versa. This somewhat arbitrary differentiation results from the need of mathematical solutions of the problem, which necessitates that the two influences are split into a main and a secondary part. The latter can then be described as perturbation of the former and the resulting Schrödinger equation can be solved. In the present case, only implications of the strong confinement regime will be mentioned, meaning that the energy shift arising from the confinement is much stronger and the coulombic exciton binding term can be treated as mathematical correction. (Strictly

speaking, the term exciton is not quite correct for a confined system because of the weak coulomb interaction and electron and hole levels have to be considered separately). The interesting implication in the strong confinement regime is that in theory the exciton should in contrast to the bulk semiconductor exhibit discrete spectra as is the case for a particle in the box. For this reason, systems with confined excitons have raised great interest from a theoretical point of view as model for an ideal atomic system. Since their energy levels can be manipulated at will by changing the size they are also sometimes referred to as "artificial atoms" [107,108].

Problematic in the case of a confined exciton is that the system of the confined e-h-pair is much more complicated than the simple model system invokes. First, the system cannot be described by the particle in a box, for which the simple equation given above holds, but constitutes rather a particle (more accurately two, e and h) in a sphere which necessitates description by additional orbital quantum numbers. Then, both particles are not freely moving but "embedded" in the semiconductor which distorts the energy levels by its hexagonal crystal field. Among other implications, this results e.g. in the finding that there is not one, but rather three hole levels, which are commonly divided in so-called light (the highest and therefore most important level), heavy and split of hole. Furthermore, the strong spin-orbit coupling of the heavy atoms has to be considered, i.e. the spin also plays an important role. Finally, it has already been mentioned that the effective mass is not constant in real semiconductors, which necessitates a suitable parameterization of the latter. For all these reasons, detailed understanding of NC processes still heavily relies on experimental results, and different mathematical models have to be used to describe interactions in different regimes. In the following, the basic known steps concerning the general photophysics of NCs will be outlined briefly.

The most principle interaction of light with matter is given by its absorption. If one refers to the absorption spectrum of an NC, it has to be understood that in difference to any normal system the NC is not excited from its ground state to an excited state, but that rather the photon absorption leads to the creation of a new particle, the confined e-h-pair. In this sense, the lowest transition band which can be observed is from "zero energy" to the ground state level of the exciton, and its energy can be calculated by subtraction of the highest hole from the lowest electron energy state. If all major interactions mentioned above are considered (e.g. in the multiband effective mass approximation), it is possible to calculate both energy and hole levels with high accuracy and thereby derive both the optical transitions as well as the corresponding oscillator strength. Since these values are derived

from the time-independent Schrödinger-equations, the line widths furthermore are supposed to be infinitely small.

Fig. 2.7A shows exemplary absorption spectra of CdSe NC samples of different sizes with narrow size distribution (≈ 5%) [169]. The findings can be summarized a follows: All spectra show more or less structured bands, starting from an absorption on-set at a maximum wavelength. This on-set shifts to higher energy with decreasing size, at the same time the absorption bands become more distinct, and the distance from band to band increases. Furthermore, the absorption increases distinct from the on-set to lower wavelengths.

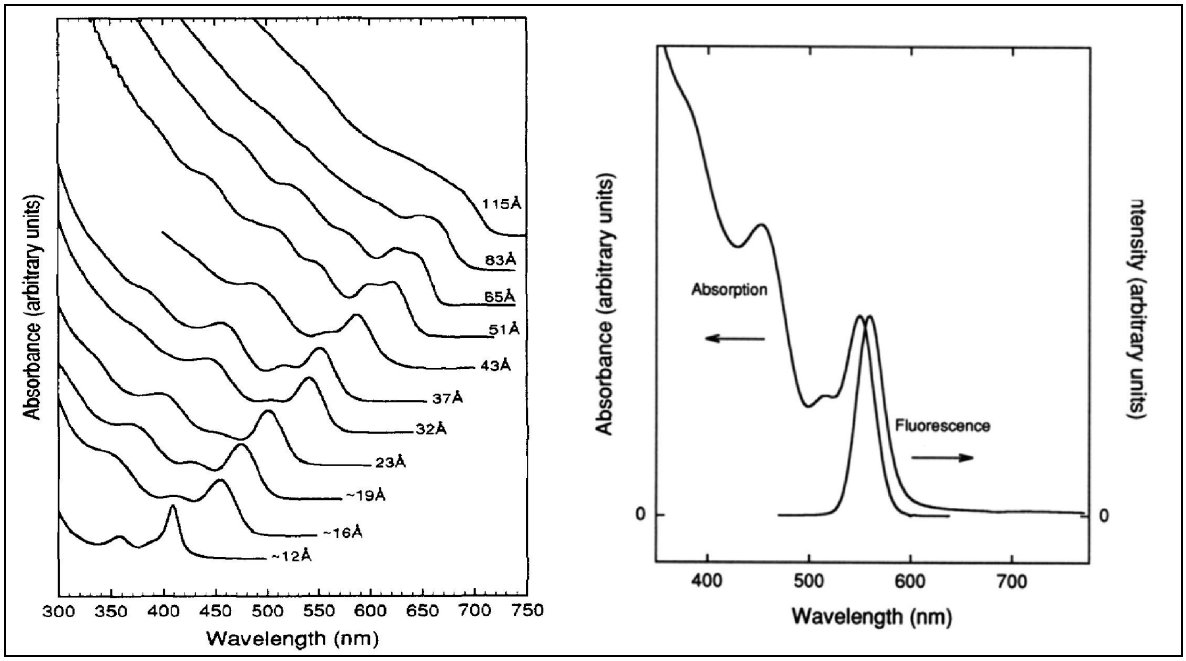

Figure 2.7: ***(A)*** *Absorption spectra of CdSe NCs prepared without shell for different sizes (diameters given in Angstrom). It is obvious that the spectra are more homogeneous, i.e. without distinct bands, for larger size. For 11.5 nm diameter, the absorption is already quite similar to the bulk material (not shown here).* ***(B)*** *Absorption (right) and emission curve (left) for a NC sample of size 3.7 nm). Note that the absorption feature with the highest wavelength (= ground state of X) is almost identical to the emission curve, however blue shifted. From* [169].

On the basis of the stated principles of e-h-pair confinement, it is now possible to explain the observed features: Absorption stems from photoinduced creation of discrete e-h-pair combinations, hence the absorption would be rather expected to consist of narrow bands instead of a broad band distribution. This can be explained by the slight heterodispersities of the samples which results in an inhomogeneous line width broadening. The overlap of the broadened bands with different absorption cross sections leads then to the absorption shape. The on-set represents the e-h-pair with the lowest creation energy which because of increasing confinement rises with increasing size. For the same reason, also the energy

separation is larger for smaller samples, i.e. even broadened bands become more distinct. This is especially prominent at the absorption on-set, the so called 1S state, whereas the second band is referred to as 1P [188,189]. A further rationalization for these characteristics can be found in the correspondence principle which states that for no confinement the separation of different bands should be infinitely small, so that larger NCs almost display a unstructured absorption which is very similar to the bulk spectrum. Finally, the steady increase of absorption to higher energies reflects the fact that as is the case in the hydrogen-atom the density of states increases for higher energies to a quasi-continuum.

If the discussed absorption features are compared to the resulting PL spectra, as is shown exemplary for an NC in Fig. 2.7B, it seems surprising that the broad excitation result only in a very narrow emission band. This is the more astonishing, since excitation at any wavelength below the absorption on-set creates the same spectrum. In order to understand these findings, it is necessary to discuss the elementary steps between photon absorption and photon emission and the dependencies on the internal NC structure.

Up to now, the NC has only been referred to in terms of a quasi-atomic system, neglecting that it consists of up to many thousand atoms. Although unlike in organic fluorophores, molecular distortions do not directly lead to energy level changes which causes the broadness of fluorescence spectra, interaction of e-h-pairs with lattice vibrations is nevertheless very important in NCs. Lattice vibrations within solids are described by the phonon-concept, which accounts for the fact, that oscillations can only occur in discrete quanta, which are called phonons. In this simple model, a solid at a certain temperature can be thought of containing a certain concentration of phonon gas which increases if the temperature is elevated (note that similar to photons, phonons constitute bosons, i.e. there is no restriction of particle number conservation). Likewise, the Ohmic resistance in metals can be understood as scattering of the moving carriers (electrons) with phonons, i.e. elastic energy transfer. Since the concept is much to complicated to be discussed here in detail, it shall only be outlined, that in semiconductor NCs with a hexagonal crystal structure, two types of phonons can be distinguished, a so called acoustic and an optical branch. These can furthermore be divided in two transversal and one longitudinal mode, so that there are four types of phonons, transversal and longitudinal acoustic (TA and LA), as well as optical (TO and LO) phonons [162]. The term "optic" points towards the fact, that lattice vibrations of optical phonons in solids of two atom types with different polarities lead to variation of the electric dipolar field, which means that they can interact with light. Therefore, optical

phonons show the strongest interaction with excited carriers whereas acoustic phonons can only interact in an indirect manner.

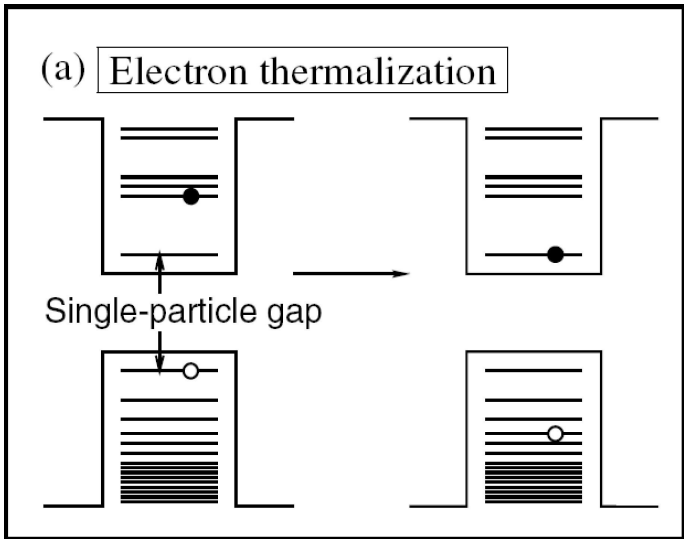

Figure 2.8: *Schematic energy diagram for both electron (upper, black circle) and hole (lower, white circle) states. Because of the large h-mass, the spacing between the energy levels is smaller than for e. Note the large spacing between first and second state, which in small dots cannot be spanned by single phonons. Due to the efficient Auger transfer from e to h, i.e. e is deexcited and h excited, the PBN is circumvented. From* [209].

The kinetics in an NC after the absorption of a photon to produce an e-h-pair above the lowest energy level occur in two different domains: First, due to coupling with acoustic phonons the phase coherence of the exciton wave function with the absorbed photon is lost, a process described as dephasing [190]. Afterwards, optical phonon mediate relaxation of electron and hole to their respective ground states occurs. This is highly efficient since the energy level spacing for states are generally very small < 10 meV so that band transitions can occur via one-phonon processes (which have similar energy ranges). On the other hand, once thermalization to the ground state has occurred, the remaining energy gap to span the e-h-spacing > 1 eV would require multiple phonon relaxation, accordingly a highly improbable process. Altogether, a photon circle for the creation of an e-h-pair takes place in four steps, absorption to a higher energy states, dephasing and thermalization to the ground state (usually within several ps) and slow radiative decay (> 10 ns).

However, investigations in recent years have demonstrated that these are by no means the only possible pathways for excited state relaxation in NCs. Thus, calculations at the beginnings of the nineties predicted a scenario in which for strongly confined excitons, the relaxation to the ground state should be exceedingly hindered [191,192]. This can be rationalized by the finding that for very small NCs the level spacing of the first transitions (energy difference from 1S to 1P state) is comparatively high, i.e. in the range > 100 meV visible by the distinct bands in the absorption spectra. Simplified, this would have predicted the occurrence of multiple phonon processes for successful relaxation into the ground state, a highly unlikely process as has been mentioned. In contrast to the prediction which has

been dubbed "phonon-bottleneck" (PBN) relaxation processes in very small NCs have been found to be very efficient, in the subpicosecond range [193-195]. The discrepancy between theory and experiment has been found to be due to a different, but in NC photophysics especially important relaxation pathway, the Auger effect [188,195-198]. In semiconductor physics, all processes involving energy redistribution between two or more carriers are generally referred to as Auger- or Auger-type interactions. For the case of the PBN, this means that the phonon-assisted relaxation from the 1P to the 1S state is not possible whereas the hole has already thermalized to its ground state. The hole relaxation is not hindered since its effective mass as stated above is much higher than that of the electron and the spacing of the hole energy levels is much smaller than for the electron, and phonon mediated relaxation possible. In a process called Auger-like thermalization, the electron relaxes back into the 1S ground state while the released energy is transferred to the hole, which in turn quickly relaxes back into its own ground state (Fig. 2.8).

A further NC characteristics which has led to a year long debate about internal photophysics [199] can be deduced from the comparison of absorption and the resulting emission spectrum depicted in Fig. 2.7. At the absorption on-set the 1S like feature is well discernible even if overlapping with higher excited states due to inhomogeneous broadening and it shows a similar shape as the emission spectrum. However, from what was stated above about absorption and emission, it would have been expected that both spectra show complete overlap. In contrast, the emission spectrum displays a distinct (pseudo-Stokes) red-shift, for which in NCs there is no ready explanation. This is accompanied by an inexplicably long lifetime for the radiative e-h-recombination from the ground state at low temperature (≈ 1 µs at 10 K) compared to the bulk state recombination (≈ 1ns). Whereas previously this had been attributed to the surface localized carriers [200,201], careful analysis of the fine-splitting of the 1S state by electron-hole-exchange revealed that the lowest energy state represents a coupled spin of $J = \pm 2$ [199,202]. Since this means that for this state e-h-pair recombination is spin-forbidden (after recombination the spin is $J = 0$), it is not optically active and cannot be seen in the absorbance spectrum. In contrast, a photon can only be emitted from the state $J = \pm 1$, which is located significantly above the lowest state (≈ 10 meV). Since this transition is only possible by phonon assistance, it is a ready explanation for the slow recombination, since for the conditions applied (10 K) the phonon "concentration" is very low [203,204]. Alternatively, by application of an external magnetic field at the right angle to the NC axis, an admixture of

the spin-allowed in the spin-forbidden state can be induced, which shortens the exciton lifetime considerably [199].

Single NC spectroscopy

The implementation of SM spectroscopy for the investigation of NC photophysics has brought a wealth of new information about their interaction with the environment. Although many of the PL characteristics are still not fully understood, these investigations have opened many new fields of applications.

2.3.4 Blinking

Arguably one of the most intriguing photophysical features on the SM level is the random intermittency of PL from NCs in a binary manner [69,205,206]. Thus, the NC PL might switch back and forth between strong ("on") and negligible ("off") intensity for all types of dots that have been investigated, i.e. independent of size temperature and coating. However, one of the most striking features is the self-similar behavior of the blinking events (Fig. 2.9I) [70,71,93].

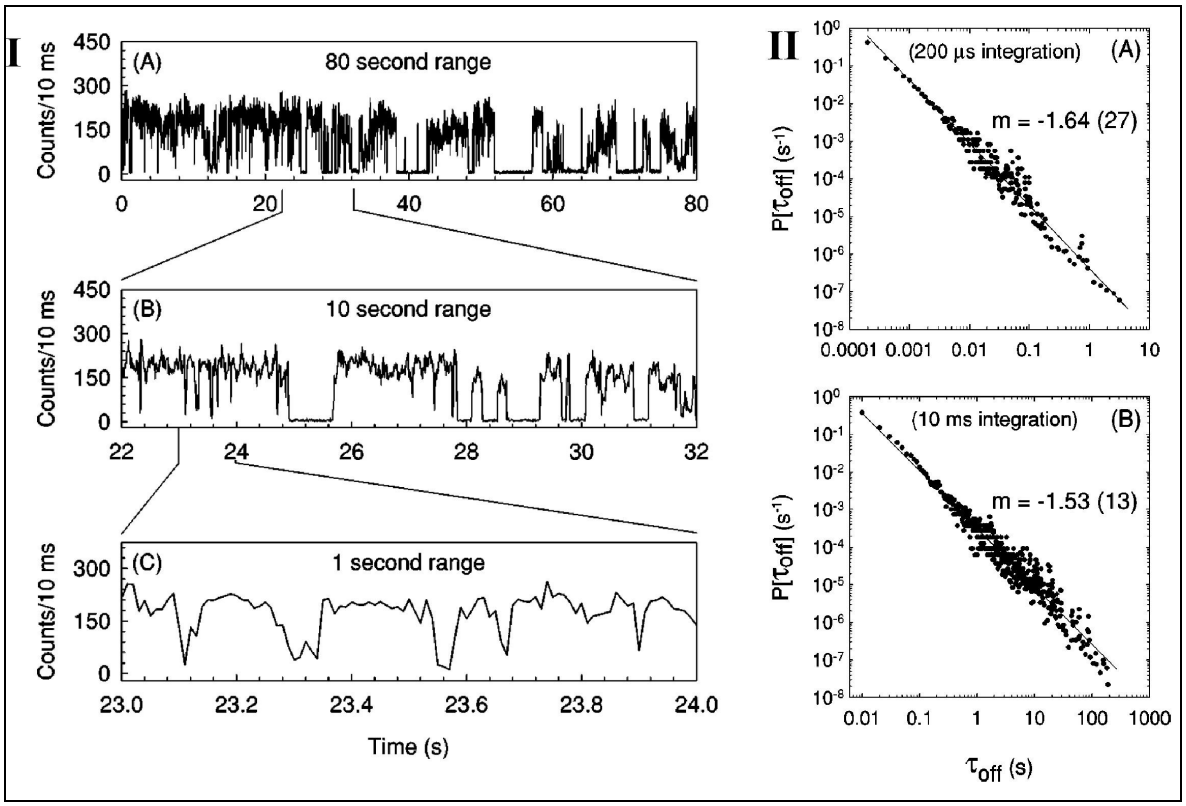

Figure 2.9: ***(I)*** *Demonstration of self-similarity of NC blinking, i.e. the kinetics looks similar on different time scales.* ***(II)*** *Power law behavior of the off-time probability versus the off-time duration. For every single NC the log-log-plot monitors a linear function with similar negative slope m. From* [70].

That is, the on/off-characteristics does not change on different time-scales. This results in a so called power-law distribution of both on- and off-times. which means that any “off”-time duration τ_{off} is connected to its own probability of occurrence $P(\tau_{off})$ by $P(\tau_{off}) \propto \frac{1}{\tau_{off}^{1+\alpha}}$. The same relation holds also for the "on"-state. Therefore, in a log-log-plot of P versus the time, always a linear function is observed with a negative slope of $-m = (1+\alpha)) \approx 1.5-1.6$ for the "off"-state and about 1.5-2.0 for the "on"-state versus time distribution (Fig. 2.9II). This is furthermore astonishing, since the yielded slope seems to be nearly independent of the surrounding conditions, e.g. of size, employed laser power and atmospheric conditions and hold over a wide range of observed times (at least five decades of time [70,206,207].

A number of different model systems have been used in order to explain the observed characteristics [208]. Most commonly, it is assumed that trapping of a charge occurs, probably an electron (because of its lighter mass) induced by photon absorption. Here, trapping means that the electron is emitted into the surrounding of the NC, leaving a charged NC behind. Although the charged NC is still subject to photoexcitation, i.e. the absorption cross section should not have changed dramatically, excitation leads to a three carrier system, i.e. an e-h-pair together with a "lone" carrier. Then, similar to the PBN scenario described above, carriers in NCs are known to display highly effective Auger-interactions [209]. In the discussed case of a three-carrier system this means, that the energy from recombination of the e-h-pair will not be released in the form of a photon. Instead, the "lone" carrier is excited into the quasi-continuum of the NC high-energy states, from where rapid thermalization back into the ground state occurs. After a certain time, the electron is apparently released back into the NC, possibly via a thermal, neutralizing the charge and resulting in an emitting NC (Fig. 2.10).

Such a model, especially the ejection of an electron, is supported by a number of findings. Hence, the on-state has been found to depend linearly on the excitation intensity [206], i.e. the on-time shortens with increasing excitation intensity, whereas the off-time is not affected. This was consistent with experiments using an electrostatic force microscope demonstrating that photoionization could be induced in NCs immobilized on a surface, leaving them positively charged, when they were exposed to light [210,211]. The photoionization probability was found to depend linearly on the power. Furthermore, PL measurements of NCs on gold surfaces have shown no blinking but rather reversible transitions to a weakly emitting state, which was found to stem most probably from a charged exciton [212]. Most notably, the transition times between charged and neutral NCs

also displayed a power-law behavior. The fact that in this case the charge did not lead to complete PL quenching could be accounted for by a significantly increased radiative rate induced by the gold surface. Hence radiative emission could compete successfully with the Auger-induced quenching by the charge. Finally, it has been recently found, that small thiol-containing organic molecules could effectively prevent blinking [72]. This argues for positively charged NCs since thiols are known to be efficient reducing agents and can neutralize the NC [213].

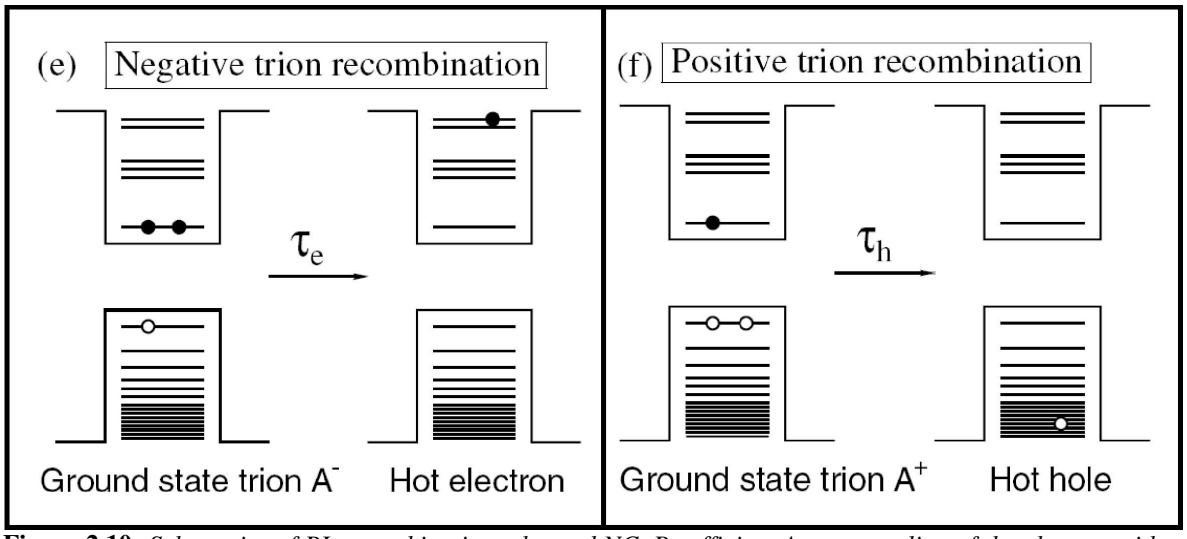

Figure 2.10: *Schematics of PL quenching in a charged NC. By efficient Auger-coupling of the charges, either in a negatively (left) or –as is probable for blinking- positively charged NC (right), the energy released for e-h-recombination is transmitted to the free carrier, i.e. the excessive e (left) or h (right). From* [209].

However, whereas these points seems to have been clarified, no model system so far could account satisfactorily for the power law distribution of both off- and on-time distribution. This is because e.g., an ordinary three-state model, in which there are NCs, excited NCs and the trap states would imply only an exponential dependence of the probability on the state duration. Hence, certain conditions have to be presumed, such as an exponential distribution of trap states [214,215], or the existence of an exponential distribution of recombination rates caused by tunneling [216]. Alternatively, it has been assumed, that an energy resonance condition between trap state and charge particle has to be present before the carrier may tunnel back to the NC [71].

The understanding of the blinking mechanism is not only important from a photophysical point of view, it is also the most serious problem encountered when dealing with single NCs. This means that in principal it might stay in the non-emitting state for minutes to hours and is thus of similar significance as bleaching. On the other hand, a thorough

understanding of the mechanism might facilitate controlled modification or even prevention of blinking.

Blinking can also be related to the phenomenon of the "dark particle" fraction, which has been deduced from correlated AFM and scanning fluorescence imaging [217]. There, it was shown that only a fraction of the NCs visible in the AFM exhibited fluorescence during the time of the measurement. This finding is supported from measurements of NC samples in solution with fluorescence correlation spectroscopy [179,218,219]. This method allows both for the determination of the number of NCs diffusing through the focus within a time span and the measurement of their diffusion time. Comparison with the calculated concentration using the extinction coefficient showed a significant discrepancy which could either be caused by particles in an off-state or aggregation.

2.3.5 Spectral fluctuations and dipole moment

Analysis of PL emission spectra has raised special interest as a potential test for atomic-like features of the NCs. This implies that the obtained line width should reflect the limit of the Heisenberg uncertainty principle to be limited only by the PL decay time. As has already been stated, the main obstacle for the analysis of such characteristics is the heterodispersity of each prepared NC batch which is also the reason for the continuous absorption spectra whereas line spectra would be expected. At the beginning of the nineties several ensemble techniques have been developed such as photoluminescence excitation [220-222] or fluorescence line narrowing [88,199,221], which are suitable for selection of only a specific size range of dots. These methods allowed for a narrowing of the absorption features This enabled comparison with calculations possible and helped to elucidate the influence of the fine-splitting. However, the apparent line widths which were obtained (> 2meV) were significantly larger than what was expected from a quasi-atomic system (≈10μeV) [199,223,224].

On the other hand, measurements of PL from single NCs is difficult to accomplish because of the high sensitivity especially at low temperature. Thus, cryogenic tempertures at or below 10 K are usually employed to prevent any external broadening. Despite these measures, even on the single NC level, often line widths significantly above 1 meV have been found [225,226]. These had been attributed to lifetime shortening due to trap states, absorption bleaching, or even for the low temperatures employed the influence of acoustic phonons [227].

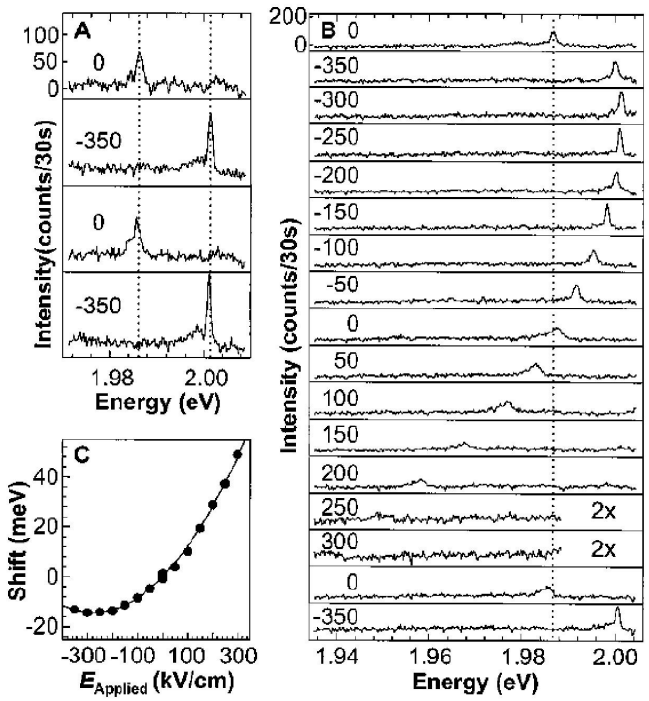

Figure 2.11: *Demonstration of the QCSE for single NCs.* ***(A)*** *Spectra taken from a single NC between two electrodes either without (first and third) or with the application of an exteral field (two and four, -350 kV/cm), which leads to a significant blue shift.* ***(B)*** *Spectra from the same NC under various fields, showing a correlated spectral shift with the field.* ***(C)*** *Distribution of the shif versus the field which reveals both a linear and a quadratic dependency of the shift on the field. Accordingly, one obtains a parabola shifted to negative values. From* [89].

Nevertheless, it was found that under certain conditions line widths around 0.1 meV are accessible and were even supposed to rather constitute an upper value [88]. Moreover, in a number of papers the main intrinsic obstacle to reveal "true" emission lines from single NCs was found to consist of changes of the emission band edge energy over time, denoted "spectral diffusion" (SD) [228,229]. Thus, when taking consecutive NC spectra of 1 min duration, the spectrum was observed to shift at will from frame to frame or split spectra were observed within one frame with the shift being much larger than the average line width within one frame. Furthermore, it was found that also the obtained line widths vary from NC to NC and increases with the spectrum integration time. From this data it could be concluded that even spectra without obvious spectral jumps exhibited line widths considerably affected by SD. In investigations of the dependency of the measured line width, which was taken to be an indicator of the amount of SD, it was found that the former increased when either integration time, temperature, or excitation intensity was increased [229]. In fact, the influence of SD was measured to be so large that other sources which had been suggested before such as dephasing were suggested to be negligible for the line width broadening [90,229]. However, recent measurements stated that line widths are too large to be explained solely by SD and favor contribution of LO phonons [230,231].

Together with findings from ensemble data that showed a decrease of band edge luminescence and increased coupling with LO phonons [88], the observed spectral shifts were assigned to a Stark effect, i.e. the distortion of energy levels ΔE by means of an

electric field F: $\Delta E = -\vec{p} * \vec{F} - \frac{\alpha}{2} * \vec{F}^2$. Ultimately, this assumption could be verified by measuring spectra from single NCs between µm-sized electrodes which allowed for a controlled change of the electric field [89]. Under these conditions, it could be established that the emission band was reversibly shifted by up to ≈ 60 meV, if a strong field was applied to the NC (Fig. 2.11). Moreover, it was demonstrated that the observed NCs displayed both a linear and a quadratic term, i.e. a permanent dipole moment p as well as a strong polarizability α. The quadratic Stark effect is most notable at strong fields and always leads to a red shift (the shifted exciton has a lower energy), whereas the linear effect can - depending on relative orientations of *F* and *p* - also induce a shift to lower wavelengths. Effectively, what is observed in the case of NCs, is not assigned to an ordinary Stark effect measured for excitons in bulk materia. Here, the strength of the field will induce a breakdown of the exciton binding and a significant quenching of the recombination. In contrast, in confined systems the e-h-pair is, due to the limited space of the system even for strong fields in contact and radiative recombination is not disrupted. Commonly, the effect of a strong electrical field on a confined semiconductor is therefore described as quantum confined Stark effect (QCSE) [232,233].

One of the astonishing findings of the QCSE experiments were that comparatively low fields < 1000 kV/cm^2 are sufficient to induce such large shifts. From the data presented in the literature, average values of both dipole moment and the polarizability were calculated as p ≈ 88.3 Debye and $\alpha > 2\text{x}10^5$ Å^3, which are found to be very large compared to "ordinary" molecules such as water (p < 2 Debye) or anthracene ($\alpha \approx 25$ Å^3) [89].

In case that no external electric field is applied, spectral diffusion is commonly related to varying charges near the NC. These are generally assumed to be distributed very narrow, most probably directly on the surface which is supported from simple field strength estimations. Hence, fields that are required to account for the observed shifts (≈ 100 kV/cm) can be induced by an electron at the distance of about 10 nm from the center. Whereas there is little dispute about these assumptions, there exist several possibilities, as to where these charges stem from and how many are participating in the field induction [230,231,234]. Significant stimulation has come from experiments which demonstrate a connection between the observed spectral diffusion and the blinking [235]. These conclusions were based on the fact that under low temperature conditions many off-states were accompanied by a distinct spectral shift, whereas shifts observed during on-times were rather seldom. Further aspects suggest an intrinsic connection between blinking and SD:

both show a dependency of the excitation intensity, the illumination can induce charging of the NCs, and both models are based on charge fluctuations.
Though several aspects are still unsolved, the occurrence of SD is generally explained by photoinduction of a carrier loss from the NC core to the near surroundings. The charged NC is then efficiently quenched and results in an off-state until recapture of the charge occurs. In many cases, recapture of the charge neutralizes the dot without changing the field, however, sometimes this process might lead to a reorganization of charges in the NC surroundings. Therefore, it is assumed that surface states exist, i.e. shallow potential wells which can lead to localization of surface charges. Emission and recapturing of a charge might then lead to a different charge distribution in these wells, creating a different field. This theory is supported by the temperature dependence on the line width, i.e. an increased temperature might cause more rapid movement of the charges between these wells, so that SD is accelerated. The surface localization of charges would also be in accordance with results showing that capping of the NCs results in a reduced average shift for SD. Hence, on the surface charges would be screened more efficiently by a ZnS layer than on the uncoated NC and the net field is reduced.

Despite these agreements concerning the mechanism, several aspects are vividly discussed. Hence, it has been mentioned that the Stark data indicate existence of a strong permanent dipole moment which causes the linear Stark effect. The existence of a dipole moment has been postulated as early as 1992, stimulated by pseudopotential calculations [236]. In the following, this dipole moment has been connected to the exciton fine splitting which results in the "dark exciton" effect. Since forbidden and allowed states have different transition dipole moments, it was concluded that CdSe NCs should exhibit a "dark axis", i.e. a single axis from which no emission occurs [237,238]. This is compared to a "bright axis" for most organic dye molecules which leads to a dipole moment in 1D space. In contrast, the "dark axis" predicts existence of a 2D moment, i.e. a dipole which is doubly degenerated in space. In fact, the existence of a 2D, or near perfect 2D dipole moment has been confirmed in many publications and has also been extensively used for determination of the 3D localization of immobilized NCs in space [238-242]. However, there exists still dispute about the size of this dipole moment, especially in view of the magnitude deduced from the Stark effect results since is has been claimed that the postulated effect would be much smaller and out-ruled by external influences [90]. Although there has been support from calculations based on the lack of inversion symmetry in hexagonal crystals [237] and a

possible induced strain of piezo-electric effects caused by lattice mismatch [243], there has been increasing evidence about external sources for the large dipole moment. Primarily, this was postulated due to PL measurement which implied a coupling between the forbidden states, induced by internal electric fields [244,245]. Dipole moments were shown to be similar to the Stark results (≈ 50 Debye), but it was demonstrated that also materials with crystal inversion symmetry exhibit dipole moments of similar strength indicating an influence of other sources [246]. These assumptions have partly been supported by results from the Stark-shift experiments: Thus, in several instances it was found that the permanent dipole showed significant jumps from a large to an almost negligible linear Stark contribution [89]. This gives strong evidence that the dipole moment is at least in part driven by external sources which might lead to considerable "internal fields" compared to external fields which cause the Stark shifts.

2.3.6 Lifetime measurements and PL quantum yield

Whereas pump-probe spectroscopy and fast relaxation kinetics have been used extensively to investigate relaxation, Auger- and trap-state kinetics [247-249], detailed investigations of the PL decay have remained sparse. One of the reasons is that in early years with non overcoated samples, multiexponential decays with a very broad range of lifetimes were measured which prevented further analysis [250-253]. However, upon coating with a protection shell lifetimes were found to increase considerably in accordance with a decrease of the non-radiatives rate to yield higher PL quantum yields [170,218]. On the other hand, in several instances such as extensive shell growth prolonged lifetimes > 100 ns are observed with decreasing quantum yield which have been explained by emission from surface states or traps [67].

With the preparation and coating procedures being a standard technique, nowadays most lifetimes are found to be well described by monoexponential decays, although detailed analysis of the underlying lifetime distributions have remained sparse [218,241,254]. Because of the strong PL, monoexponential decays and stability in a variety of different solvents, NCs have even been used as test model systems for the influence of the refractive index on the radiative decay [254]. Typical lifetime values found for core-shell CdSe or CdTe NCs are in the range of 10-30 ns [66,67,241,254]. Quite well established is the fact that the lifetime increases with increasing wavelength attributed to a decreasing overlap with increasing size which results in a reduced oscillator strength of the transition [66,67].

On the single NC level, it has been demonstrated that lifetimes may also fluctuate extensively correlated with the PL intensity [91,92]. Thus, unlike in blinking events, where two levels with strong and negligible PL are observed (on- and off-state, respectively), some NCs show an undetermined range of intermediate levels. These intermediate states are connected by a variation of the non-radiative lifetimes, i.e. a decreased lifetime (= increased non-radiative rate) is accompanied by a reduced intensity level. Furthermore, lifetimes within these fluctuations could be described satisfactorily with a monoexponential model if only states with the same intensity level were considered which gave a good prove of intrinsically monoexponential decay characteristics (Fig. 2.12). Although the exact nature of these trap states which lead to increased non-radiative relaxation is not known, they have been implicated to consist of charges near the NC core. Thus, they should display only weak quenching, i.e. not complete quenching as for a charged NC (blinking) neither strong electric field as is the case if the charge is on the NC surface [216,255,256].

In many publications it is assumed that in accordance with a quasi atomic NC picture the PL quantum yield is near unity, if quenching states are not present [92,207,219,254]. Explicitly, since quenching is assumed to show a variety of different states and lead to multiexponential decays, the observation of strong monoexponential characteristics is taken as indicator of very high quantum yields. Hence, in many cases the reduced ensemble value below unity is frequently accounted for by the presence of dark NCs.

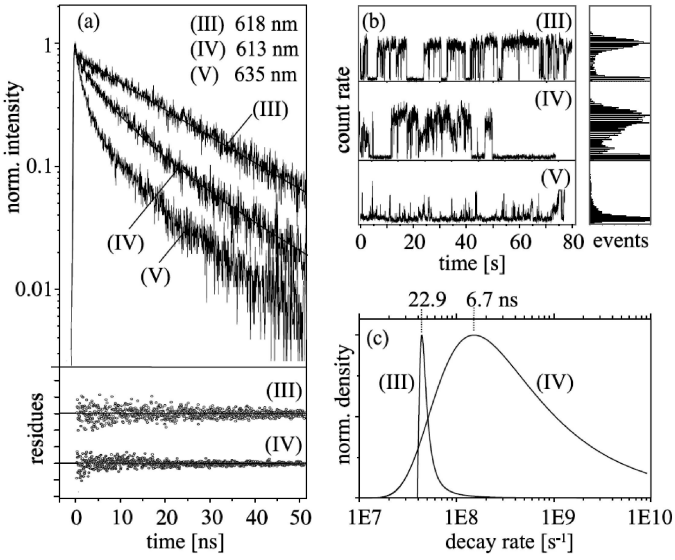

Figure 2.12: *Depiction of the correlation between lifetime and intensity fluctuations for a single NC.* ***(a)*** *PL decay curves of the three single NCs shown in the transients in* ***(b)****. To the right of the transient are the distribution histograms of various intensity levels. Obviously the NC (III) has the narrowest distribution and also displays the lifetime with strong monoexponential characteristics. This is also obvious from the narrow lifetime distribution in the fits in* ***(c)****. From* [91].

Brokmann et al conducted several experiments to determine the quantum yield for single NCs immobilized on a surface [241]. This was done by measuring the absolute dipole orientation of the NC on the surface and determining the change of the lifetime upon change of the refraction index. Since this yields a different

radiative rate constant, the absolute quantum yield could be calculated from the lifetime change and the dipole orientation. For all NCs, a quantum yield > 95% was found and taken as clear sign of atomic-like emission properties [241].

2.3.7 Multiexcitonic emission

Because to the many atoms that form an NC, the valence band contains hundreds to thousands of electrons. Explicitly, this means that it is possible to create many more than one e-h-pair, which can in contrast to organic dyes coexist within the shell since they constitute bosons. Hence, under high power excitation, i.e. the probability of photon absorption is higher than that of photon emission, one can create states with more than one exciton within the NC, so called multiexcitons (MX) [163]. The nature of these multiexcitonic states is still more complicated than in monoexcitons (X), since the interaction of more carriers has to be considered. In the weak confinement regime, there exist simple model systems, e.g. the coupling of two excitons (which are similar to hydrogen atoms) can be described in terms of a weak chemical bond (biexciton (BX) = dihydrogen molecule). The description in strongly confined systems is much more difficult since both attractive (exchange terms) and repulsive forces (charge terms) have to be considered [257]. A further complication arises in cases of triexcitons (TX) and excitons of higher multiplicity, since before recombination each carrier relaxes in its ground state. However, this can for both hole and electron only be occupied by two carriers which means, that in a TX different carriers may be on different energy levels.

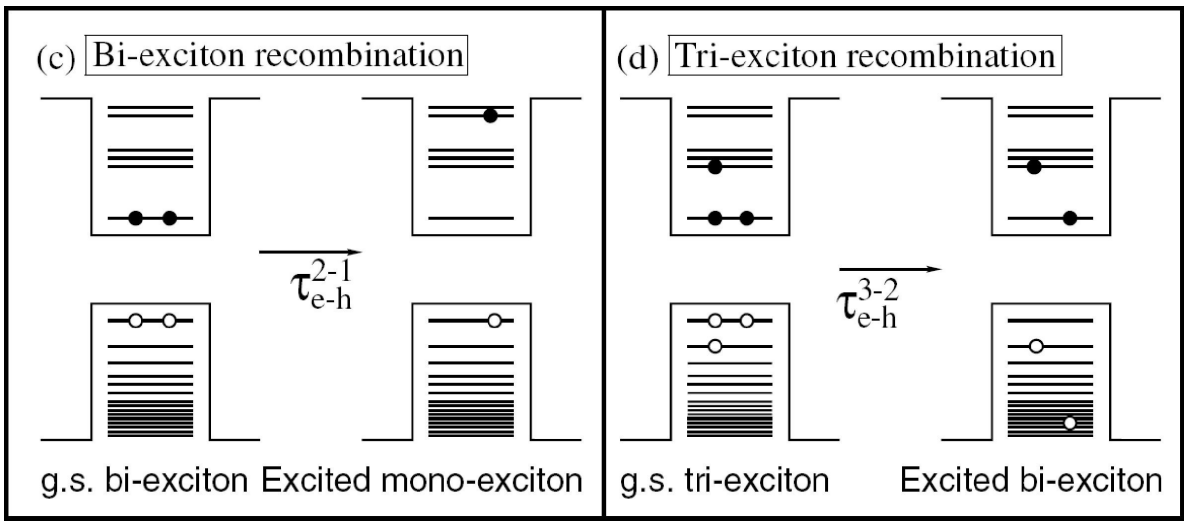

Figure 2.13: ***(c)*** *Schematic energy diagram of electron and hole levels for the ground state of BX (left). Upon recombination of the first e-h-pair, the energy is transmitted to the electron via an Auger process, i.e. non-radiative recombination (right).* ***(d)*** *Energy diagram of TX. Note especially the single electron and hole, respectively, in the first excited states, since the ground state is already completely filled. From* [209].

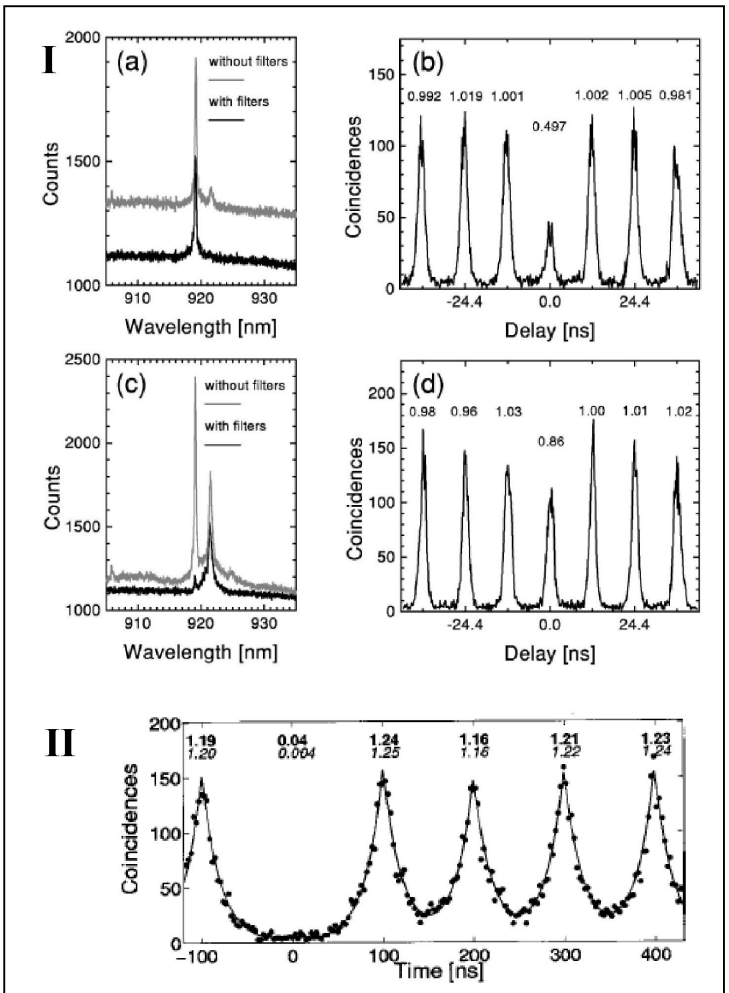

Figure 2.14: ***(I)*** *Significant BX emission measured from epitaxially grown NCs. In (a), the spectrum of a single NC is shown with and without filtering of the BX emission line (small peak at higher wavelength). In the corresponding interphoton histogram(b), significant antibunching is observed for filtering, i.e. the probability of photon detection for the same pulse (peak at zero delay) is low. In (c) and (d) the same is shown for strong BX emission and specific filering of only BX emission. Strong bunching characteristics can be observed. From* [101]. ***(II)*** *Interpohoton histogram foir a single colloidal NC which shows nearly perfect antibunching characteristics. From* [96].

Generally, it is found that the interaction in a BX results in a slight energy decrease, whereas tri- and higher excitons are shifted to higher energies. Since the excitons within a NC are coupling but independent particle, the recombination occurs independently as well, e.g. TX decays into BX into X into a neutral NC. A TX has a slightly increased interaction energy which means that its energy in the ground state E_{TX} is larger than that of three X$\Rightarrow$ $E_{TX} > 3xE_X$. Accordingly, upon TX decay a blueshift with respect to X-decay should be observed, compared to a slight red-shift for BX decay.

So far, different interactions have been neglected, since for recombination of one e-h-pair in MX, the other carriers cannot be supposed to be unaffected. Hence, the importance of Auger processes has already been mentioned either for thermalization into the ground state (missing "phonon bottle-neck") as well as for strong quenching of charged NCs ("blinking"). This means that radiative decay of MX for e-h-recombination competes with energy transfer of released energy on one or several carriers. These are excited into higher energy states, from which rapid thermalization back into the ground state occurs, resulting in efficient quenching of MX decay (Fig. 2.13).

Multiexcitonic emission or a lack of it has been of considerable interest in recent years concerning quantum cryptography. One main interest for the use of single NCs is as

sources for single photon generation or single photon sources (SPS) [94,96,258-260]. This is because SPS require efficient photon emission on demand, i.e. high photostability which organic dyes do not possess, and high PL quantum yield.

Under high excitation conditions, multiexcitonic emission is well known for epitaxially grown NCs [98-101,259,261], where it has already been used for generation of correlated or entangled photon pairs [262,263]. Since multiexciton excitation requires the absorption of a photon for an already excited NC, the relative multiexciton emission can be controlled by the power. Hence, under low power excitation, only emission from the X state can be obtained. Otherwise, spectral separation of the X emission from the other peaks has to be accomplished in order to use epitaxially grown NCs as SPS, which results in a loss of photons and is of disadvantage for the use as SPS.

On the other hand, it has been well established that most colloidal NCs display negligible multiphoton emission, which was proved to be due to highly efficient Auger quenching of MX emission [94,95,264]. For this type of NCs it was shown that the quenching efficiency increases with the inverse cube of the NC size, thus was found to display a dependency expected for an Auger-type of relaxation. Otherwise, quite recently it has been demonstrated that for comparatively large NCs (diameter > 5 nm, emission 655 nm) significant BX and even TX can be observed when imaging under high excitation conditions [265-267]. Apart from the large size of the NCs, it has also been suggested that Auger efficiency decreases considerably with size increase in only one dimension, i.e. for NCs with prolonged axis [268]. Therefore, it is of interest to tune the shape of the NCs or nanorods to decrease the Auger efficiency still further, since even for the NCs investigated, BX emission was strongly quenched to MX emission [267].

2.4 High-resolution colocalization beyond the Rayleigh criterion

Despite the progress in recent years concerning the sensitivity of SM detection, the spatial resolution which may be acquired with conventional fluorescence microscopy is intrinsically limited by the wave-like nature of light. Thus, it is long known that every aperture causes Fraunhofer diffraction in the far-field, limiting the optical resolution of an optical system. Since the relative size of the aperture of an imaging lens system is limited by the refractive index n, i.e. the numerical aperture NA cannot exceed n, it follows that

also the resolution has an upper limit, given by the Rayleigh criterion: $0.61 * \frac{\lambda}{NA}$. This means that a point like fluorophore in a system with NA = 1.45 and λ = 600 nm will show an apparent diameter of around 250 nm in the fluorescence image called Airy disk (or "point spread function" PSF). Hence two fluorophores at a distance below the PSF cannot be separated anymore.

Since the main interest of high sensitivity fluorescence imaging lies in the investigation of biological systems, this is a pitfall because relevant biomolecules have a typical diameter around or below 10 nm and the investigation of their interactions requires a resolution of at least several tens of nanometers. Therefore, recent years have seen the development of several new techniques, which circumvent this limitation, from which the most important are presented briefly:

Near-field Optical Scanning Microscopy (NSOM) [269-271]

This technique is the most intuitive approach, since it uses a very small aperture around or below 100 nm diameter directly in front of the dyes to reduce the excitation volume. As aperture usually a small metal tip with a hole of the respective size is used into which a laser fiber is fabricated for excitation.

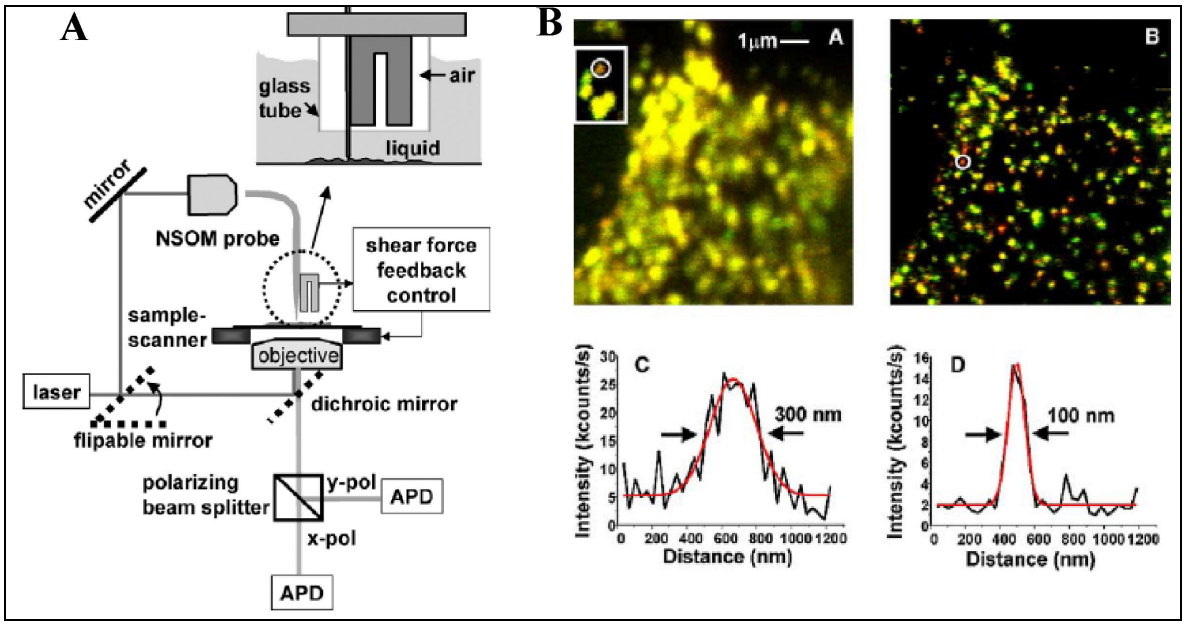

Figure 2.15: ***(A)*** *Schematic set-up of an NSOM microscope: The moving tip measures the contact force to the surface and facilitates aproximation of the aperture to the sample. The laser is coupled into the aperture and the fluorescence light cllected by the objective. From there the light is directed onto to APDs separated by a polarizing beamsplitter. Be switching the mirror before the laser, the light can alternatively be coupled directly into the objective, giving a standard confocal set-up.* ***(B)*** *The same labeled part of a cell membrane imaged in the confocal A or in the NSOM mode B. With NSOM the resolution is increased three-fold. From* [272].

To ensure that no diffraction of the excitation light occurs, the tip has to be held in a position very near to the surface (5-10 nm distance from the dyes) which necessitates adjustment in z-direction as well. The resulting fluorescence is collected with a high-numerical objective and detected with a confocal set-up. To accomplish the surface localization with nm-precision, usually a shear-force technique is employed in which surface dampening of the vibrating tip is monitored. Although this method provides additionally topographic information about the investigated surface, it is only suited for imaging of membranes due to its invasive nature.

Stimulated Emission Depletion (STED) [40,43,273]

The concept of the STED-technology is based on the fact that the S_1-level from which fluorescence occurs can be depleted by stimulated emission. Briefly, on a scanning confocal microscope, a pulsed excitation laser excites all dyes in the diffraction limited area, while a second laser directly afterwards with an "inverse", e.g. dough-nut shaped focus depletes those excited molecules which are not directly in the focus. With this technique, PSF-narrowing down to below 50 nm in one dimension has been achieved. However, a number of specific conditions has to be met, in order to obtain such results:

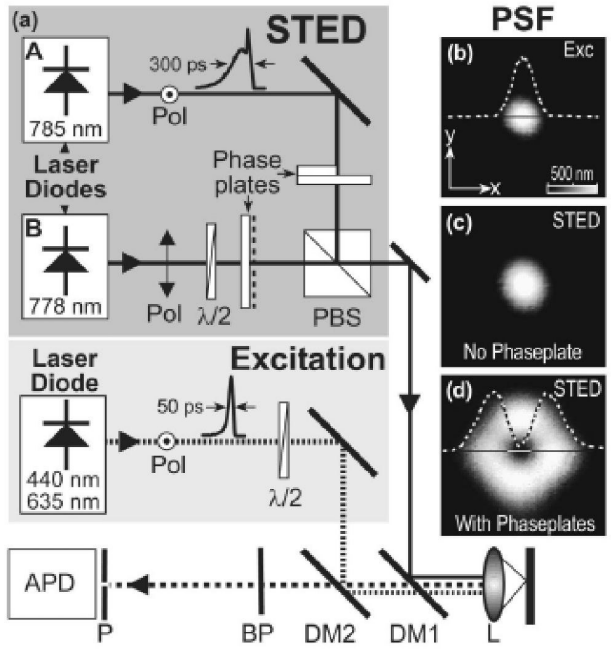

Figure 2.16: *Principle of STED excitation. In* ***(a)*** *the set-up is shown with the excitation laser (light gray) whose intensity profile is depicted in* ***(b)*** *and the detection set-up for photon detection (APD). For the STED pulse (dark gray) two pulses from the same laser are superimposed either without* ***(c)*** *or with* ***(d)*** *a phaseplate. The latter leads to a doughnut shaped focus, with efficiently deexcites all dyes out of the focus center. From* [43].

Although in principle no upper limit for the resolution is given, very high pulse intensities (> 1 GW/cm^2 at the maximum) are required for the STED laser to achieve sufficient depopulation of S_1 near the center of the spot. The high intensity is necessary since depletion has to be effected into a highly red shifted S_0-level, to ensure that no reexcitation by the laser occurs, e.g. for an excitation laser at

558 nm a depletion laser at 766 nm was used. The dye selection is also critical, since few dyes show sufficient response to the depletion, that are at the same time photostable enough or in a suitable wavelength range for the available laser sources. Thus, so far only one group worldwide has been able to establish this system for use in biological imaging.

Colocalization using Total Internal Reflexion (TIR)

Recently, a number of papers appeared that used TIR excitation and CCD detection of suitable dyes for high resolution colocalization of two nearby dyes. Their approach benefits from the high S/B ratios which can be obtained with high-sensitivity, low-noise CCD cameras, so that localization of the dyes center is possible with high accuracy (below two nm) [47,48]. Colocalization can be achieved, if one of the dyes bleaches significantly before the other, so that from the shape of the superimposed PSFs of both dyes and the remaining dye, both positions can be determined using a Gaussian fit for each PSF. The systems were tested using double-stranded DNA constructs below its persistence length (≈ 50 nm) with two identical dyes at each end as a "molecular ruler". The average end-to-end lengths determined from the distance distribution histograms by Gaussian fits showed good accordance with the expected theoretical values. In principle this method can also be used to resolve the distance of more than two dyes, if a clear photobleaching event for each dye is observed. Whereas this procedure is simple and quick, it has the drawback that only relatively few dye constructs, i.e. those with resolved photobleaching events and without significant intensity fluctuations, could be used for analysis. Furthermore it is not suitable for measuring the distance of molecules in 3D space, but can only determine the distance projections on the x-y-plane.

In a slightly more sophisticated method based on TIR, two-color detection was applied using two different excitation laser (532 nm and 633 nm), and the emitted fluorescence light (maximum at around 580 nm and 660 nm) was splitted in two color channels, which were directed on two different regions of the same camera [274]. This system necessitates highly accurate superposition of each of the channel images, but does not require photobleaching of the dyes, since determination of the dyes center can be made simultaneously for each dye channel. Testing was also achieved with double stranded DNA as molecular ruler and yielded good results with a similar accuracy, a possible distance resolution of two dyes below 10 nm apart with an estimated error lower than 5 nm [274]. Despite these successes, the sensitivity of these system as to imaging within biological systems has still to be investigated. Two major obstacles are expected: especially if using

one color imaging, any non-homogeneous background, as is often observed within cells due to autofluorescence, should distort the Gaussian shape which should influence the accuracy severely. Even for two color detection, within cells, a 3D space has to be investigated which is also problematic, since different from a surface many imaged molecules might be out of focus which leads to distortion of the Gaussian shape. Also, only the 2D projection of the distance can be determined

Scanning confocal microscopy

Scanning confocal microscopy has been studied for high-resolution colocalization of two different chromophores using either spectral or both spectral and lifetime information (SFLIM) lit. The approach is similar to the method presented in to the extent that it uses two color detection with two APDs spectrally separated by a dichroic beamsplitter to determine the respective center of each of the dyes. However, in these experiments two chromophores were used which could be excited at the same wavelength, thus avoiding interference of chromatic abberation.

In the case of colocalization using spectral information only, NC samples of different emission were employed as chromophores [53]. Colocalization was achieved by statistical means, i.e. no model construct as distance linker was used, but NCs were randomly immobilized at comparatively high concentration and the surface screened for suitable events. The used NC samples displayed 80 nm difference in emission (540 nm and 620 nm) and crosstalk from the color channels could be avoided with narrow band pass filters (transmission ranges of 25-35 nm). Distance measurement were successful below 50 nm, albeit with comparatively large errors around 15 nm which was caused by frequent blinking events. Since in scanning microscopy a different pixel refers to a different detection time, blinking causes dark or dimmed pixels which aggravate PSF fitting with a Gaussian intensity distribution.

With the aid of a modified set-up a combination of lifetime and spectral separation was employed to study colocalization with organic dyes [57,58]. The dyes had to meet several standards: (i) excitation with the same laser source (pulsed laser diode at 635 nm) giving similar brightness, but (ii) different emission wavelengths and (iii) different fluorescence lifetimes (Fig. 2.17). Dyes which fulfill all necessary preconditions were found to be very rare, especially since most dyes show similar ranges of excitation and emission wavelengths, which means that the range of excitation is rather too small compared to a rather too broad emission. As most suitable dye combination, the carbocyanine Cy5.5

(excitation/emission maximum $\lambda_{ex}/\lambda_{em}$ = 685/710 nm, extinction ε_{max} = 2.5*10^5 (l/Mcm), lifetime $\tau \approx$ 1.5-2 ns) together with Bodipy630/650 ($\lambda_{ex}/\lambda_{em}$ = 630/650 nm, ε_{max} = 1*10^5 (l/Mcm), lifetime $\tau \approx$ 3.5-4 ns) was found. Due to the broad emission spectrum, a significant amount of channel crosstalk could not be avoided. Nevertheless, the combination of spectral and lifetime information was shown to give comparable results to other methods and was also tested using differently labeled double-stranded DNA constructs, yielding distance measurements well below 50 nm with an error < 10 nm [58]. The most difficult problem in these measurements was the finding that apparently Cy5.5 emission vanished when constructs were immobilized on dry surface, emission was only observed to a significant amount embedded in agarose. Although a mechanism for the "off"-state could not be established, it is most likely connected to other photophysical characteristics of carbocyanines, such as cis-trans-isomerisation or reversible transformation into a photoswitchable state [84,275].

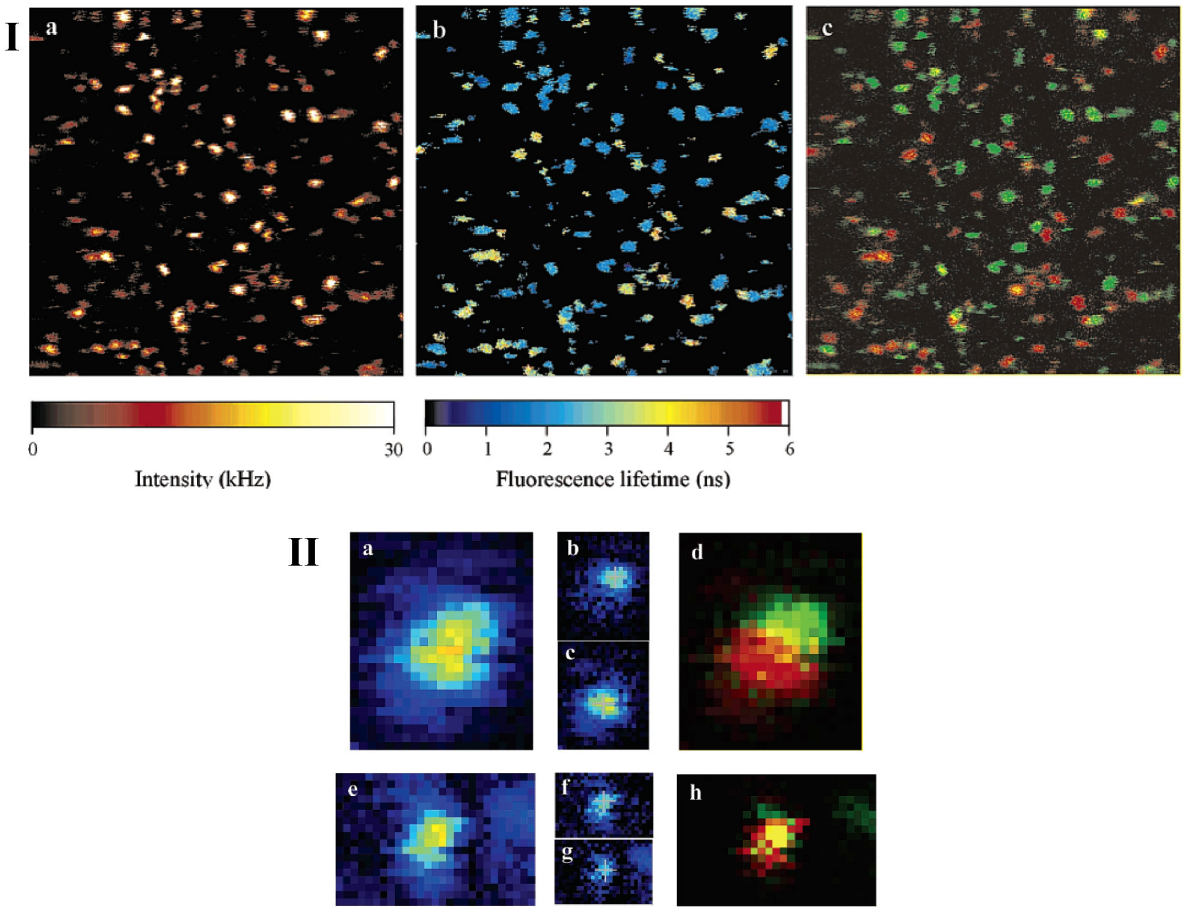

Figure 2.17: ***(I)*** *SFLIM images of a 20x20µm^2 area of a surface covered with two different dyes. (a) The intensity image shows a dense layer of single fluorophores. In the lifetime (b) and the spectrally (c) encoded images, two different populations can be distinguished.* ***(II)*** *(a)+(e) Enlarged intensity images (50 nm/pixel resolution) of two spots with mixed values. By separation and correlation of the information from different lifetimes and spectral values, the separated PSFs of the two overlapping dyes can be calculated and are shown in (b) and (c), as well as (f) and (g). Finally, the relative position of the center-of-mass can be used to calculate the distance between the two dyes. From* [57]**.**

3 Materials and Methods

3.1 Spectrally-resolved fluorescence imaging microscopy (SFLIM)

The presented work centered on PL investigations of single particles and assemblies using modified Spectrally-resolved Fluorescence Lifetime Imaging Microscopy (SFLIM) [55]. The set-up is based on a confocal scanning microscope, as is depicted in Fig. 3.1, and will be outlined before single components are discussed in more detail:

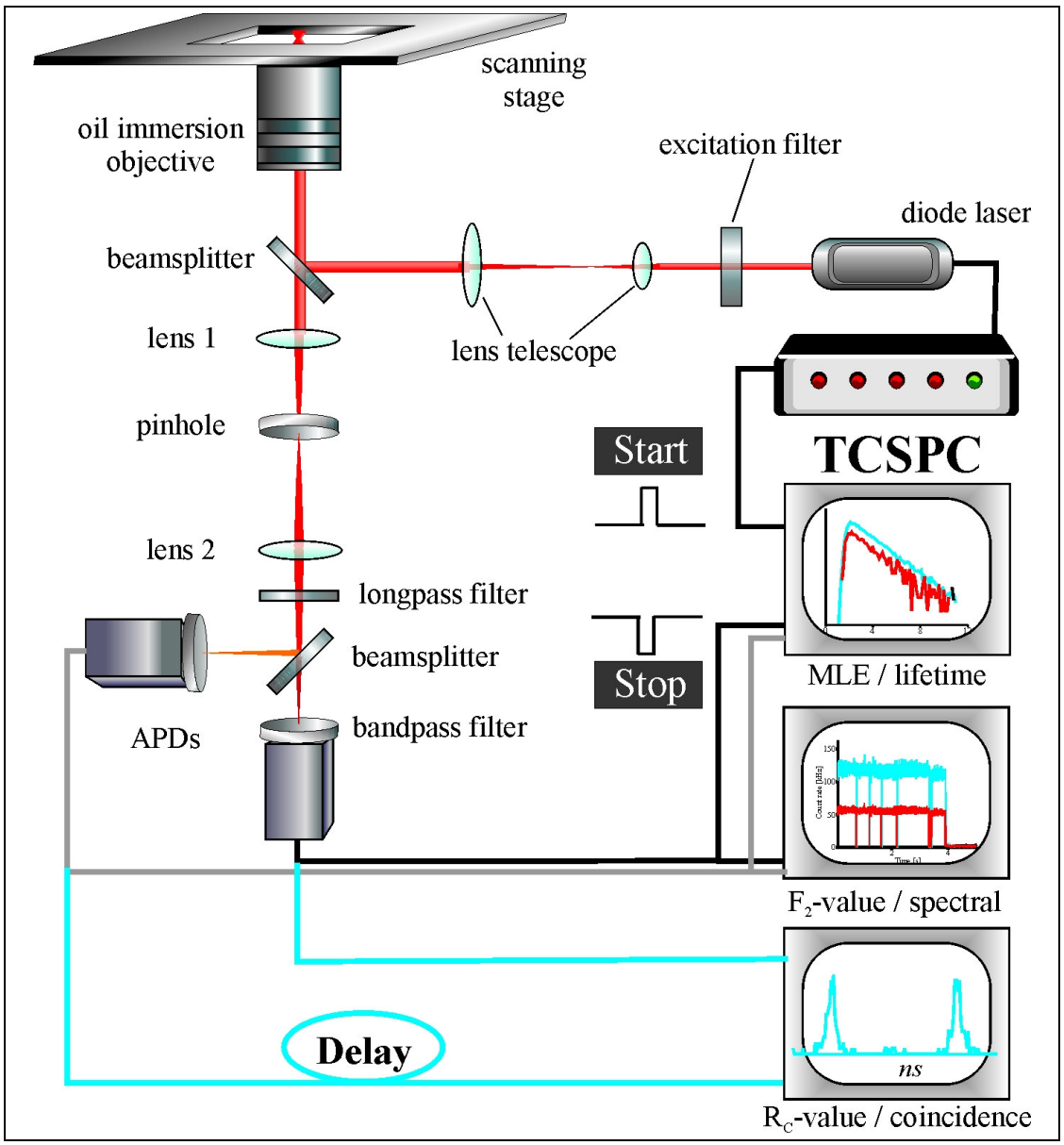

Figure 3.1: *Schematics of the employed SFLIM set-up. After data processing and with a dichroic mirror as beamsplitter before the APDs, apart from the intensity, three further observables are accessible*

It consists of an inverted microscope (Axiovert 200M, Zeiss, Germany) equipped with a 3D scanning stage (PI-509.3CL, Physik Instrumente, Göttingen) which is steered by a servo controller (E509.3A) in combination with a three-channel amplifier (E503.00). The expanded beam of a pulsed diode laser was sent through an excitation filter and coupled into the microscope via the back port. The excitation light was directed with the aid of a dichroic mirror into the back aperture of an oil-immersion objective (Plan-FLUAR 100x, NA = 1.45, Zeiss, Germany) which focused the light through a silica coverslide where the PL probes were immobilized. PL light was collected with the same objective, passed from the dichroic mirror into the base-port and was focused by the tube lens through a pinhole. With the aid of a second lens, the light was focused and split by an appropriate dichroic mirror and optical filters onto two avalanche photodiodes (APDs, SPCM-AQR-14/15, PerkinElmer, USA). For each photon, an electric impulse is fed into a card allowing for time-correlated single photon counting (TCSPC, SPC-630, Becker&Hickl, Berlin) that compares the arrival time with the synchronization (SYNC) signal sent for each laser pulse from the pulse generator (PDL 800-B, PicoQuant, Berlin). For time synchronization, each APD signal is sent through a digital delay generator (DG535, Stanford research Systems, USA) and a router which distributes the signals from the different APDs to the TCSPC card. Synchronization of the scanning stage with the detection hardware was achieved with an analogue output card (PCI-6713, National Instruments, USA) which was addressed using a custom-made software (LabView, National Instruments, USA).

Laser Sources

Two pulsed laser diodes were used: Either fiber-coupled with a circular profile emitting at 635 nm or collimated with an elliptical profile and 445 nm emission. Both lasers were sent through a suited excitation filter (633 DF 10 for 635 nm, 445 DF 20 for 445 nm) and expanded to a diameter of about 1 cm with a lens telescope. Because of the elliptical profile shape, an additional telescope with cylindrical lenses had to be used for sufficient beam expansion of the 445 nm laser. In most cases, the laser light was used without modification of the polarization direction, resulting in about 90% linear polarization.

Both lasers were run at a repetition rate of 10 MHz or 5 MHz, apart from the fluorescence investigations on gold surfaces (section 4.1), where 40 MHz pulsing was used. However, in this case (40 MHz pulse repetition) the lifetime data was of minor importance.

Filtersets

Depending on the excitation source, either a dichroic mirror splitting at 650 nm (635 nm diode) or at 500 nm (445 nm diode) was employed as excitation beamsplitter. Although the use of a pinhole is mandatory for SM microscopy, it was found that it could be omitted in many cases when imaging NCs, since the S/B was not significantly reduced whereas the detected photon rate decreased. Hence, it was only used for instances, where an especially high S/B ratio was of interest, i.e. for investigations of BX emission using a non-polarizing beamsplitter.

PL particle	Section	DC (split/nm)	Filter D1/D2	Filter D1	Filter D2
Alexa633/680	4.1	685	-	667DF30	710DF50
QD655	4.2.1-8	660	500LP+542LP	-	665DF65
QD605	4.2.1-9	600	500LP+542LP+ 610DF75	-	-
QD705	4.2.1-8/11	690	500LP+542LP	-	-
QD655*	4.2.9/10	660	500LP+ 585AELP	-	-
QD655‡	4.2.11	pBS	500LP+ 585AELP		
QD655**	4.3.1-5	50/50	500LP+585AELP +645DF40	-	-
QD605**	4.3.6	50/50	500LP+542LP+ 610DF75	-	-
QD655***	4.3.7	620	500LP+542LP	580DF60	645DF75
QD655***	4.3.7	620	500LP+542LP	605DF55	645DF75
QD655***	4.3.7	635	500LP+542LP	615DF40	665DF40

Table 3.1: *List of the used filtersets throughout the work. * Measuring under saturation conditions; ‡ investigation of emission polarization; ** investigation of BX emission; *** investigation of TX emission*

Different beamsplitters and filters in the detection path were employed for SFLIM, depending on the desired imaging. Table 3.1 lists most of the used filtersets. Note that the set-up could be modified if parameters other than a wavelength shift were subject of investigation. Accordingly, with the aid of a polarizing beamsplitter (pBS), changes of the polarization direction of the PL light could be measured, whereas a 50/50 non-polarizing beamsplitter (50/50) was employed to determine biexciton (BX) emission efficiency. A detailed discussion of the used filtersets for the NC investigations and implications on the obtained data is found in the corresponding sections.

Detectors and Data acquisition

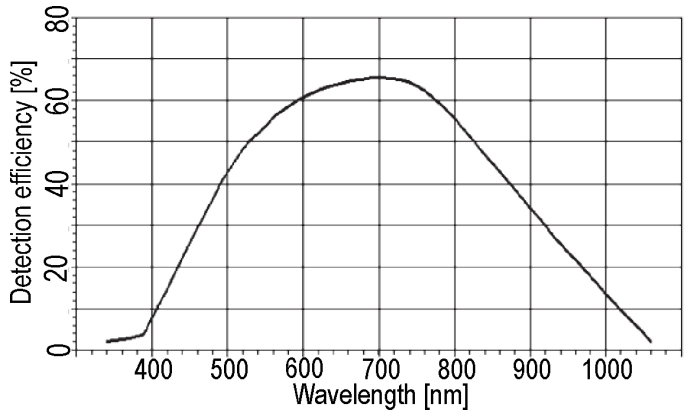

Figure 3.2: *Dependence of the detection efficiency on the photon wavelength for the used APDs. In the wavelength range which was of interest > 600 nm, the efficiency is quite constant.*

The APDs used provide the maximum efficiency for the trade-off of a detector between detection sensitivity and time resolution. Thus, they display a high photon detection efficiency > 65% in the spectral range of interest (> 600 nm) with a moderate dead time of around 300 ns. In addition, they display very small dark count rate, i.e. wrong positive photon signals, which minimizes interference with non-correlated background. In the following, steps central to an understanding of the acquisition will be explained more detailed:

Detected photons are processed by the TCSPC card which uses a Time-to-Amplitude Converter (TAC) to calculate the relative photon arrival time ("microtime", START signal) with respect to the following laser pulse (SYNC or STOP signal). The analog TAC signal is then allocated to one of 4096 microchannels into which the time span between two laser pulses ("TAC window") is divided by a Amplitude-to-Digital Converter (ADC). Two further things have to be considered: Though both laser pulse and detected photon have a well defined absolute time difference, both signals (i.e. from the SYNC and from APD) may have different arrival times at the TCSPC car due to the electronic transmission rate. Thus, to ensure that all photons stemming from the same laser pulse are detected in the same TAC window, both APDs have to be set at a certain delay. Furthermore, if one is interested to check for two-photon events (bunching/antibunching), i.e. emission of two or more photons within the same laser pulse, the dead time of the TCSPC card (about 200 ns) has to be considered. Therefore, the delay unit for one of the APDs has an additional delay time spanning several macrotime intervals, in the present case 1 µs, which ensures that two photons can be detected on the two APDs for the same laser pulse.

Since the absolute arrival time of the photon with respect to the start of the measurement ("macrotime") and the APD channel where it was detected are also recorded, one has for each detected photon three parameters from which the experimental observables can be

deduced (First-in-First-out, FIFO mode). The processing by which this can be achieved will be outlined in the next chapter.

Data processing

The FIFO data was acquired in two different modes using a developed software based in LabView. In the first, the sample was scanned within a certain area in homogeneous x-y steps ("pixels") over the laser focus and the data for each pixel was acquired for a preset time range (integration time). The fluorescence image constructed of the pixels could then be used to address a certain spot within the scanning image by the stage and record the detected photos for this spots for an undetermined period ("transient").

The FIFO files obtained for each measurement are analyzed with a custom-modified software (LabView). Principally, the obtained data consists of single photons detected at different macrotimes, or –expressed in macrotime distances- at different count rates. However, due to the uncertainty principle relevant conclusions can only be drawn from photon statistics, hence for data analysis the count rate is converted into a photon number by integration over constant macrotime ranges ("bins"). Whereas the bin size may be chosen arbitrarily for a transient, it is already defined for scanning imaging by the integration time over the pixel.

From this data, four independent parameters can be obtained for a bin:

- The brightness of the particle is accessible without further processing via the photon number per bin, N_C.
- The spectral information can be obtained since each photon is assigned to one of the APDs which are separated (for SFLIM) by a dichroic beamsplitter. Therefore, the fractional intensity on the long wavelength detector D2 is defined by $F_2 = I_{D2} / (I_{D1} + I_{D2})$, where $I_{D1/2}$ denotes the photon number detected on the short and long wavelength detector, respectively. Thus, an increase of the F_2-value of the particle indicates red shift of its emission spectrum.
- The microtimes of the photons can be used to gain information about the PL kinetics, which is in most cases expected to be a monoexponential decay, the PL lifetime τ. For analysis, all photons detected within the bin are plotted in a microtime histogram, which is exemplary depicted in Fig 3.3. It has to be considered, that the resulting distribution monitors not only the decay of PL, but the convolution of the decay with the laser pulse and the instrumental response function (IRF) (see below). Nevertheless, since the pulse width is generally around 100 ps, i.e. much faster than common PL lifetimes, the decay can be

assumed to be unaffected by the pulse within a very short microtime range after the maximum (laser pulse). If sufficient counts are obtained the decay may be processed by common fitting procedures, however, in most cases lifetime ranges for short bins (low photon number) is required. To answer the demands of efficient data processing and reliable lifetime information, lifetime analysis using the maximum-likelihood estimator (MLE) algorithm has been established [102-105]. This can be used to calculate from the count distribution in the microchannels over a certain time range in the TAC window ("TAC range") the most probable monoexponential decay. Thus, for the lifetime τ holds for a given count number N distributed over m microchannels with a temporal width T within the TAC range:

$$1+(e^{T/\tau}-1)^{-1}+m*(e^{mT/\tau}-1)^{-1}=N^{-1}\sum_{i}^{N}(i*N_i),$$

where i indices the order of the respective microchannel, starting at 1 for the first channel in the TAC range. Note that the MLE yields no information about the quality of the monoexponential fit, thus for every count distribution a lifetime can be obtained irrespective of the actual decay kinetics.

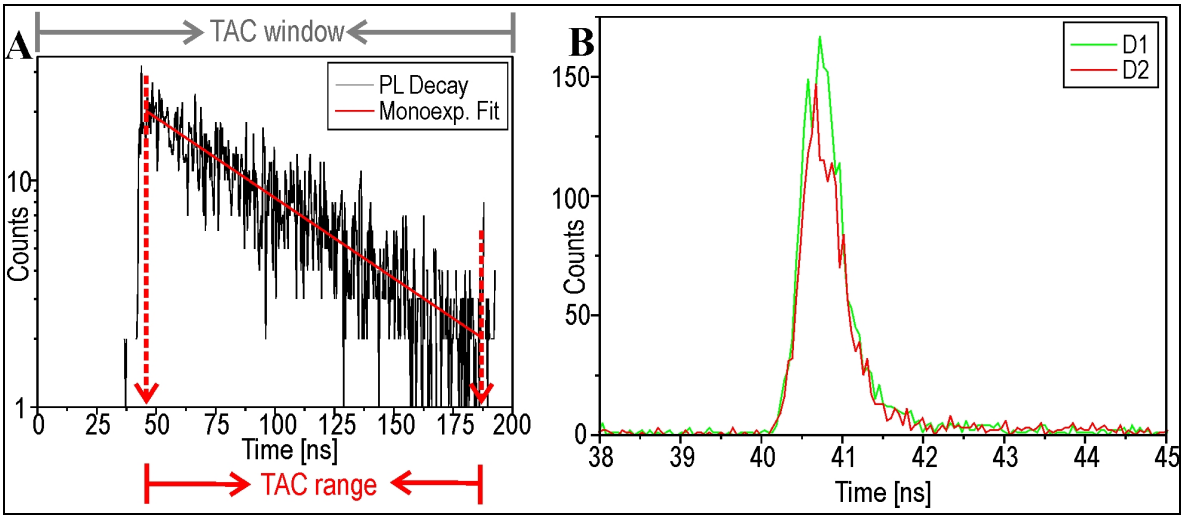

Figure 3.3: ***(A)*** *Resulting TAC window for a laser repetition rate of 5 MHz, i.e. 200 ns interval between the laser pulses. In A, the laser pulse position is at about 45 ns (rise), the section labeled by dashed red lines marks the TAC range, i.e. the section from which the lifetime is calculated by the MLE. In this case (single NC QD705), the MLE of the range yields ≈ 61 ns compared to 62 ns from the monoexponential fit.* ***(B)*** *Instrumental response function with a FWHM ≈ 0.7 ns and a minimum lifetime ≈ 0.25 ns.*

As an intrinsic limitation for the lifetime determination, it has to be considered that due to broadening effects caused by the temporal response of the electronics and limited transfer rates the set-up gives a minimal lifetime, the IRF. Since the IRF has to be considered when interpreting fast decays (< 1 ns), it was determined for the used set-up is displayed in Fig

3.3B and yields a full-width-half-maximum (FWHM) of about 0.7 ns and a "lifetime" as obtained from the MLE of about 0.25 ns. This was determined as the fastest decay that could be detected with the used SFLIM set-up.

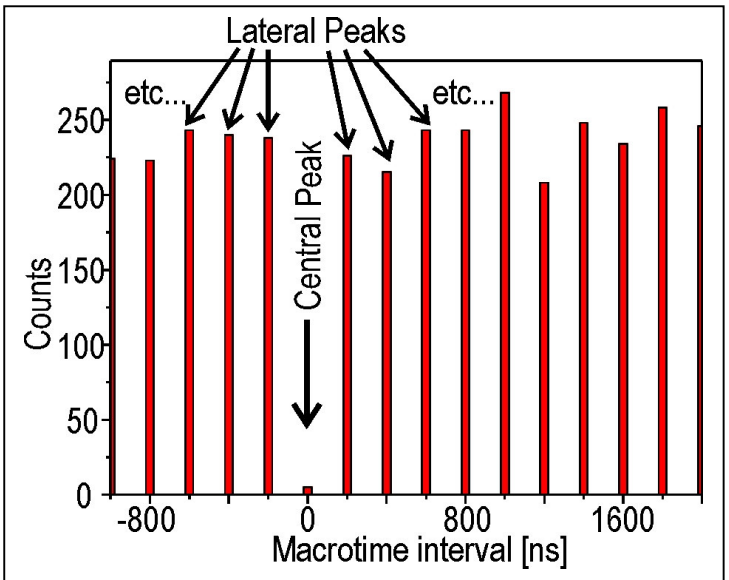

Figure 3.4: *Coincidence histogram for pulsed excitation at a frequency of 5 MHz corresponding to a macrotime interval of 200 ns between two pulses. The peak position is normalized with respect to the delay, so that an interval of zero marks two-photon events for the same laser pulse and corresponds to the central peak counts. As can be seen from comparison of the central to the adjacent lateral (non-correlated two-photon events) peak heights, the sample (QD705 from Fig. 3.3) displays nearly perfect antibunching characteristics with R_C = 0.025.*

- Apart from these obvious photophysical parameters, there is the coincidence ratio which is only of interest when imaging few molecules within the focal spot, but can nevertheless give important information. It is based on the finding that common organic fluorophores can only show radiative decay for the transition S_1-S_0, i.e. cannot emit more than one photon for each laser pulse. To check for this behavior, the data has to be analyzed in view of two-photon events ("coincidences"), where two photons belonging to the same macro time interval (i.e. emitted for the same laser pulse) are recorded. Because of the dead time of the TCSPC and of the APDs this can only occur when a delay is applied to one of the APDs (mentioned above) and when the two photons are detected on different APDs. The number of coincidences for a given measurement ("counts in the central peak") constitutes itself no quantitative information, but has to be related to the non-correlated two-photon events, detected for different laser pulses. Accordingly, all two-photon events are histogrammed with respect to their macrotime interval (laser pulse difference). Note that the histogram has to be corrected for the additional delay set on one of the APDs (1 µs). For a single organic fluorophore, the central peak is visible by a drastic dip compared to the adjacent ("lateral") peaks. This can be put into quantitative information by the coincidence ratio R_C, where the height of central peak N_{cp} is normalized to the average height of the lateral peaks N_{lp}: $N_{cp} / N_{lp} = R_C$.

Spectra recording of single NCs

The SFLIM set-up was modified in several instances to allow for simultaneous recording of PL spectra. For this purpose, the PL light was redirected after passing the dichroic mirror by either a switchable mirror or a 50/50 beamsplitter into the side-port of the microscope. There, it was focused by a cylindrical lens through a slit of variable width and entered a monochromator (spectrograph model SP-150, Roper Scientific, USA) from which it was imaged onto the active area of a Peltier-cooled, front-illuminated charge-coupled device camera (Cascade, Photometrics, USA). Software recording and further processing of the spectra was done with a software provided from the manufacturer (WinSpec, Roper Scientific, USA). Calibration of the wavelength was accomplished using both the 488 nm line of an Argon-ion laser (95 SHG-6W, Lexel Laser Inc., USA) and the 633 nm line of a He-Ne laser (Typ 710, Polytec, Germany). To reduce the noise and obtain spectra of sufficient accuracy, the camera was switched to the highest amplification level and an internal background correction was used. Furthermore, a hardware binning of 1 s was employed.

For the spectra recording of single NCs, a coverslide coated with NCs at low density (< 1 NC/μm^2) was imaged using the standard SFLIM set-up, i.e. light collection on the APDs via the microscope base-port. After redirection of the PL light through the switchable mirror, or –for the F_2-calibration with the wavelength- the 50/50 beamsplitter into the sideport, selected NCs were addressed consecutively with the respective software written in LabView.

Atomic Force Microscopy (AFM)

Atomic force microscopy was performed on a Solver P47H (NT-MDT, Moscow, Russia), equipped with a piezo-driven scanning device (range 50x50x2.5 µm) and corresponding software. Measurements were carried out under air in the non-contact (NC) mode using an aluminium-coated single-crystal silica point probe sensor (LOT-Oriel, Darmstadt, Germany). Typical cantilever specifications were: size = 4x30x125 µm, force constant of 42 N/m with resonance frequencies at 320 kHz. According to the manufacturer, te typ radius was below 10 nm. For scanning, the sample was mounted on a microscope slide.

Ensemble spectroscopy

Absorption measurements of the corresponding NC solutions were performed on a UV/VIS spectrometer (Lambda 25, Perkin Elmer, USA) within solica precision cuvettes (suprasil)

from Hellma (Germany). For the measurements, about 100 µl of a 10^{-8} M solution of the respective NC were filled in a micro cuvette with a path length of 3 mm.
Fluorescence spectra were obtained using a Cary Eclipse spectrometer (Varian, Germany) within the same cuvettes. Both spectrometer allowed measurements in a range from 190-1100 nm.

3.2 Sample Preparation

Gold-Patterns

Patterned samples were prepared and received from the group of Prof. Dr. Armin Gölzhäuser (University of Bielefeld), and the detailed preparation is described elsewhere [64]. Briefly, each consisted of a 2 mm thick silicon wafer with a 30 nm layer of gold. Typical wafer dimensions were 1x1 cm^2 to 0.5x0.5 cm^2. The surface had been incubated several days with 4-Nitro-4'-mercaptobiphenyl (NBT) for SAM-formation. Irradiation was carried out by low energy electron proximity printing using an electron flood gun in a high vacuum system. Patterning was achieved by using a carbon foil with hole pattern as a stencil mask. The hole diameter was 1.5 µm, the resulting patterned surfaced had an area of about 0.1 cm^2. In the case of nanostructures with sizes below 1 µm, a scanning electron microscope was used to write the desired structures on the surface [61,62]. After patterning, samples were shortly treated with a solution containing either KOH or I_2 to remove unmodified NBT from the surface. Finally, the surface was incubated in a solution of alkanethiol terminated poly(ethylene-glycol) [$HS(CH_2)_{11}(OCH_2\text{-}CH_2)_n\text{-}OCH_3$, n = 34-56] (PEG2000-OH) in dimethylformamide (DMF) for several hours.
All modification procedures were carried out at room temparature. The detailed method applied for each surface modification is given in section 4.1. Generally, a drop of 100-200 µl of glutaraldehyde solution 10% in distilled water) was carefully spread on the dry surface for activation with cross linker and covered with a lid to prevent evaporation. After activation, the surface was briefly rinsed with distilled water, dried in an air stream, and treated with the respective protein solution (≈ 10^{-7} M recombinant streptavidin [Roche Diagnostics, Germany] or labeled IgG-antibody [MoBiTec, Germany]) in PBS containing 0.01% Tween 20 and 25-33% glycerol (Sigma-Aldrich, Germany) in the same way. Streptavidin was labeled with the biotinylated dye Cy5 (absorption/emission maximum = 650/665 nm), which was prepared and provided from V. Buschmann in the same group.

Two different types of labeled antibodies were used, goat anti-rabbit IgG labeled with Alexa633 (632/647 nm) and rabbit anti-goat IgG labeled with Alexa680 (679/702 nm). After protein modification the sample was successively rinsed with PBS solution containg 0.01% Tween 20, PBS and distilled water, afterwards dried as before.

For modification with the aminolinker tetraethylene-pentaamine (TEPA, Sigma-Aldrich), the patterned and passivated sample was activated by treatment with 220 mg nitrophenylchloroformiate (NpCF) and 200 µl N-diisopropyl-ethylamine (both from Sigma-Aldrich) dissolved in 15 ml 1,2-dichloroethane (Sigma-Aldrich) for 2.5 h. The sample was thoroughly washed with dichloroethane, dried and immediately incubated overnight in 250 µl TEPA dissolved in 20 ml DMF. This was followed by rinsing with DMF, methanol and subsequent ultrasonication for 15 min in the same solvent at 40°C. Finally, the sample was washed with acetone and dried under air. Modification with labeled protein was accomplished in a similar manner to the procedure described above.

NC-samples

NC stock solutions were provided from the manufacturer (Quantum Dot Corporation, USA) with a concentration of $2x10^{-6}$ M in a solution containing 2% w/v bovine serum albumine (BSA) and 1 mM sodium azide ("storage buffer") and were kept in the fridge at 4°C. Stock solutions were diluted prior to use in the same buffer, stored in the fridge and used within a few days, otherwise they displayed “aging” effects such as unstable and quenched PL (see Fig. 4.2.44). Three types of samples were used, with maximum emission wavelengths of 655 nm (denoted QD655), 605 nm (QD605) and 705 nm (QD705). All constituted core-shell NCs with a CdSe- (QD605 and QD655) or CdTe- (QD705) core and a shell made of ZnS. To ensure water-solubility they were coated with an ambiphilic polymer and had streptavidin attached to the surface. According to the manufacturer, the average size was 10-15 nm diameter with about 15-25 streptavidins per NC on the surface. Transmission electron micrsocopy (TEM) images and the schematic composition as provided from the manufacturer are shown in Fig. 3.5. From the same source stems the average PL quantum yield given as > 40% (QD605) and > 60% (Qd655 and QD705).

Samples suited for imaging of single NCs were prepared by two different approaches: Samples in non-biological medium were adsorbed non-specifically on the silica coverslides and dried, then imaged under air or covered either with a polymer coating or a drop of immersion oil. Samples imaged in a biological buffer were prepared in coverslides

equipped with eight plastic chambers (chamber slides) and immobilized using the streptavidin-biotin bond.

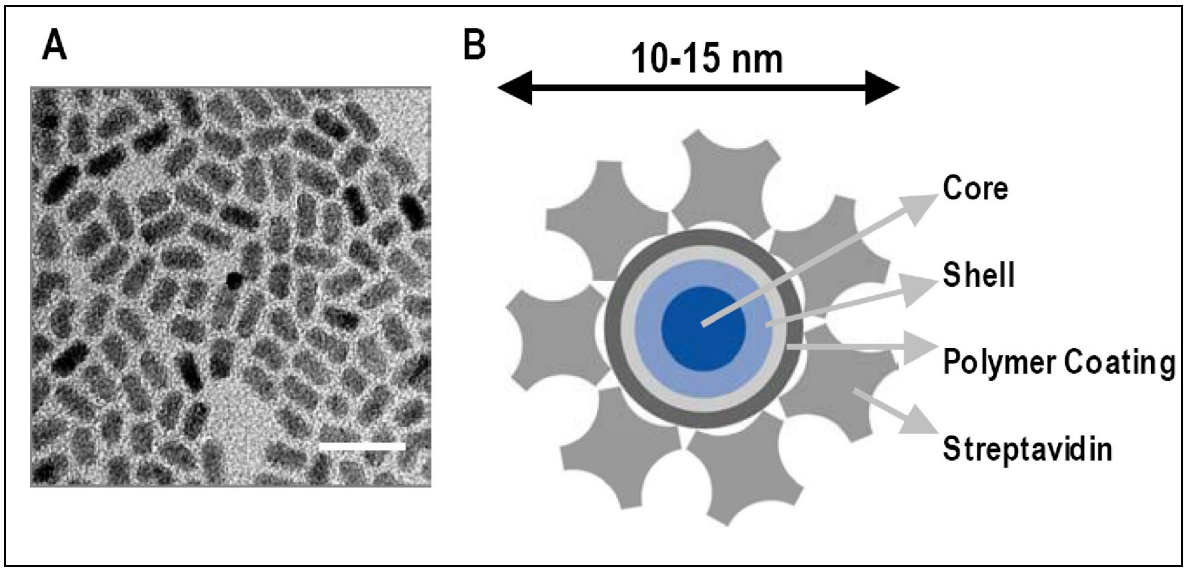

Figure 3.5: ***(A)*** *TEM images provided from the manufacturer, scale bar is 20 nm. Note the slightly elongated shape due to the growth procedure.* ***(B)*** *Schematics of the layer construction of the employed NC samples.*

Coverslides (Carl Roth GmbH, Germany; thickness ≈ 170 µm) were used either cleaned or non-cleaned before modification, depending on the imaging. Generally, when especially high S/B ratios were required, e.g. for coincidence analysis and biexciton imaging (section 4.3), they were cleaned, otherwise they were directly used. Cleaning was accomplished by immersion of the slide in 0.5% hydrofluoric acid for about 30 s, then it was rinsed several times with destilled water and blown dry with compressed air. For non-specific adsorption of the NCs on the surface, the surface was incubated either cleaned or directly as provided in a solution of 2.5% 3-aminopropyl-triethoxysilane (APS, Sigma-Aldrich) dissolved in methanol for several minutes, then rinsed with water and dried as before.

For immobilization of NCs on the slides, the corresponding stock solution was diluted to about 10^{-9} M in the storage buffer (provided by the manufacturer) and about 20-50 µl of the solution spread over an area about 0.5 cm^2. Depending on the required NC density, immobilization was terminated after 10-100 s by rinsing with distilled water and subsequent drying. Note that in this case the surface density is not so much controlled by the concentraion of NCs but of the BSA. This is because BSA has a great tendency to surface adsorption and prevents binding of NCs, thus it is an effective binding competitor to the surface and comparatively few sites are available for NC immobilization. This procedure was chosen since it was found that samples diluted in protein-free buffer showed a tendency of NC agglomeration, so that even for a low surface coverage many NC cluster

containing two or more particles were found. However, by this method only an NC concentration of 10^{-11}-10^{-12} M was required for sufficient NC coverage. Although agglomeration could be prevented using a buffer containing 0.01% Tween 20 this again lowered surface coverage, and NC densities proved to be difficult to reproduce.

For imaging, the slide was mounted upside down on a microscope slide with a mould and fixed to it using adhesive tape. This resulted in much more stable scanning conditions which was especially important when imaging an area over extended periods.

In several cases, samples prepared on a dry surface were covered with a layer of polyvinyl-alcohol (PVA, Sigma-Aldrich) to remove oxygen from the sample. For this case, PVA was dissolved in water at about 1% w/v concentration under heating and ultrasonication. About 500 µl of the solution was then spin-coated onto the prepared sample at 7000-8000 rpm in several drops, using a home built spin coater.

For immobilization under biological conditions, chamber slides were cleaned and coated with APS in a similar manner to the coverslides, with the difference that the surface was treated with APS for 1 h. APS-modified surfaces were then incubated for about 1 h in a PBS solution containing 5 mg/ml BSA (Sigma-Aldrich, Germany) and 0.05-0.5 mg/ml biotinylated BSA (Sigma Aldrich) where each protein bears about twelve biotins. The chamber slides were then rinsed several times with PBS and filled after the last rinsing with about 100-200 ml PBS. Surfaces prepared in this manner could be stored in the fridge for several days, before NC immobilization was carried out.

For binding of NCs, the sample was mounted onto the microsocope and the NC solution added to the PBS to yield a concentration of about 10^{-11} M. After mixing of the solution, scanning was started and the surface coverage monitored by subsequent scanning. This method yielded sufficient coverage of NCs (≈ 50-200/20x20 μm^2 area) usually within five minutes. After the required coverage was obtained, the surface was rinsed on the microscope several times with PBS and 200 µl glucose oxidase buffer were left in the chamber after the last washing step.

The glucose oxidase buffer [276] was prepared from a stock solution stored at -20°C containing the following reagents (per ml): 1 mg Glucose oxidase (Sigma-Aldrich), 0.5 ml Tris buffer (Carl Roth GmbH), 25 mM KCL, 2 µl Catalase 30 mg/ml (Sigma.Aldrich), 4 µl 1 M Dithiothreitol (DTT, Sigma-Aldrich) in PBS, 0.5 ml glycerole. Prior to use, 50 µl of stock solution was diluted in 1 ml of 0.1 g/ml glucose solution in PBS (Sigma-Aldrich).

For the measurements made under MEA, the chamber was filled with a solution containing 150 mM mercaptoethylamine (MEA, Sigma-Aldrich) in PBS.

4 Results and Discussion

The aim of the presented work was to advance and expand the performance of high resolution colocalization microscopy using SFLIM and is divided into two different parts:

1) Section **4.1** addresses the development of fluorescence labeling strategies of nanopatterned gold surfaces to facilitate the application as CPS substrate
2) The investigation of NC photophysics with regard to the use as probes for high-resolution colocalization is split into two further parts: Section **4.2** discusses the results of the photophysical investigation with regard to spectral, lifetime and intensity fluctuations, whereas in section **4.3** investigation of bi- and triexciton emission from single NCs are presented.

4.1 Fluorescence labeling of patterned gold surfaces

Patterned gold surfaces with 1.5 µm circular structures were received from the group of Prof. Dr. Armin Gölzhäuser and prepared using e-beam lithography as described in section 3.2. The irradiation of with electrons results in a reduction of the nitro- to an amino-moiety; the hydrogen stems from the underlying biphenyl-moieties which subsequently saturate by crosslinking of two adjacent aromatic rings (Fig. 4.1.1). Crosslinking has the important side-effect that the bonding of the modified biphenyls in the irradiated region is much stronger to the gold (possibly because of entropic reasons) than in the non-irradiated areas. Therefore, the unmodified biphenyls can be specifically removed from the gold layer by mild oxidizing (I_2) or complexing (KCN) agents without affection of the crosslinked aromatic layer. The exposed gold surface can then be passivated against non-specific adsorption by incubation with a thiol-modified polyethylene-glycol (PEG2000).

Before attempts for a successful fluorescence modification are started, it is worth to consider several critical points, since immobilization takes place near a surface where strong fluorescence quenching is expected to occur (section 2.2). Hence, a lack of or weak fluorescence might either be the consequence of insufficient immobilization or strong quenching of the surface. If one furthermore seeks to reduce the quenching by placing a linker (e.g. DNA) between surface and dye, the flexibility of the linker has to be considered

as third parameter influencing the fluorescence signal (longer extension ⇒ stronger fluorescence by weaker quenching). Thus, for a thorough study and optimization of an immobilization scheme, it is desirable to find ways to differentiate between these three parameters by suitable analysis techniques.

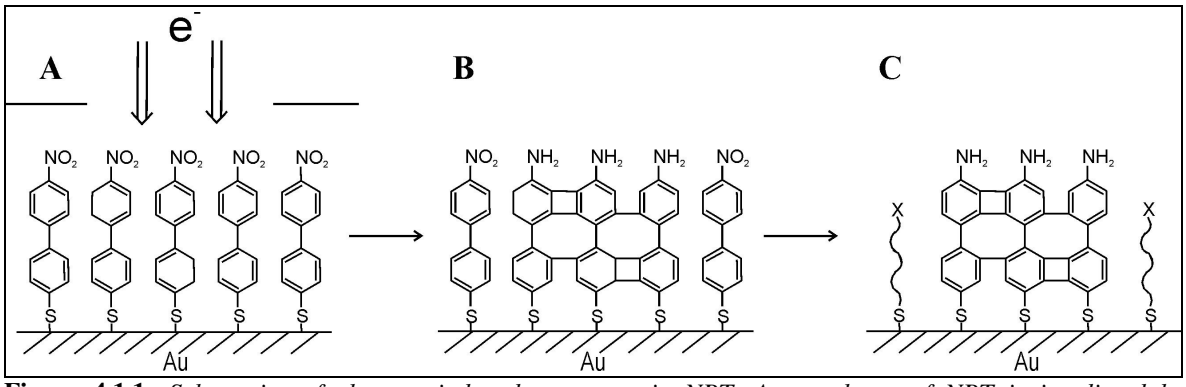

Figure 4.1.1: *Schematics of electron induced processes in NBT. A monolayer of NBT is irradiated by electrons* ***(A)*** *and generates amino end groups while the underlying aromatic system is dehydrogenated and crosslinks with each other* ***(B)****. In a subsequent modifction step, the amino groups can be used for covalent attachement of biomolecules under mild conditions* ***(C)***

For fluorescence modification of the surface, the amine moiety of the irradiated biphenyls suggests a reaction with an activated acid of a suitable fluorescent dye as straightforward reaction. However, several reaction attempts with Lissamine rhodamine B sulfonyl chloride in dimethylformamide did not result in a visible fluorescence pattern, but for the reasons stated above it is not clear if it is entirely due to quenching.

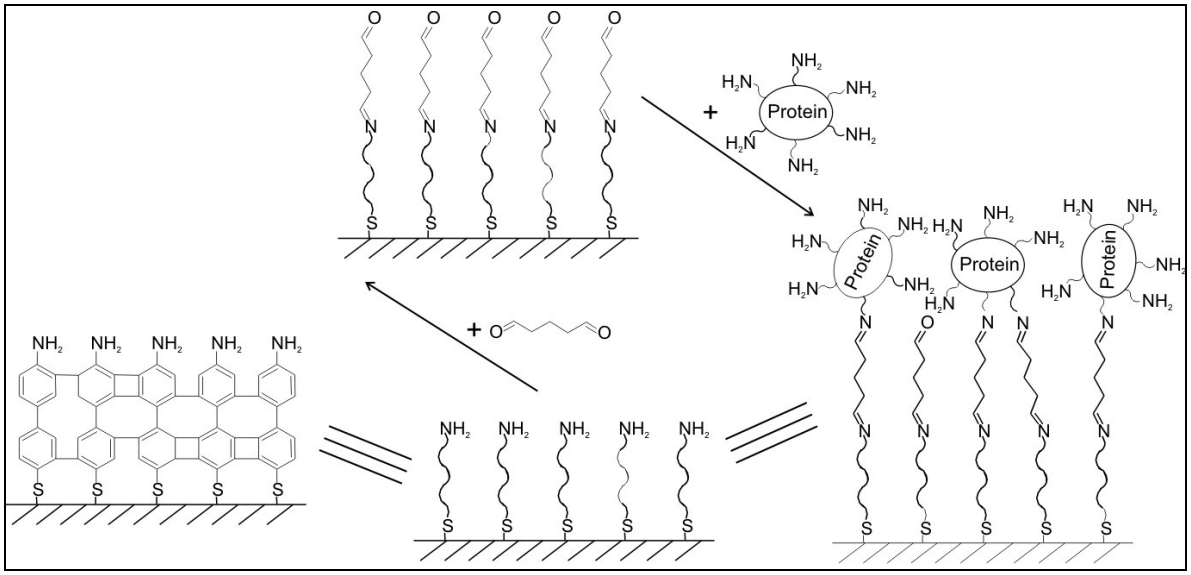

Figure 4.1.2: *Schematics of fabrication of three-dimensional fluorescently labeled protein assemblies on the nanometer scale. The amino groups in the irradiated spots are activated with glutaraldehyde via generation of an imino-bond. The exposed aldehyde groups are then used to crosslink proteins to the surface via the lysine residues. Since proteins exhibit free lysines all over their surface, the modification step can be repeated to produce further protein layers.*

Therefore, a different immobilization strategy was elaborated, e.g. based on the previous finding (using AFM) that streptavidin can successfully be tethered to the surface after treatment with 10% glutaraldehyde. In addition, the concept of using proteins as dye support exhibits also several advantages compared to simpler immobilization schemes in terms of the discussed difficulties (see also Fig. 4.1.2):

- typical proteins (50-150 kD) have sizes between 2-6 nm, with near spherical shape ⇒ rigid spacer for dye molecules
- simple labeling schemes by reaction with free lysines which are usually present in proteins in sufficient number (>10), both for immobilization on surface and modification with dyes efficient immobilization of dyes
- lysines available all over the surface ⇒ top site of immobilized protein can be crosslinked with labeled proteins to gradually enlarge the distance of the dyes to the surface
- height of protein layer can be measured by AFM after immobilization ⇒ information about successful reaction independent of the fluorescence intensity obtained from the quenched dyes

4.1.1 Fluorescence labeling of patterned surfaces using several protein layers

Using a previously exploited method, an irradiated and passivated surface on a silicon plate was treated for about 1 h in 10% aqueous glutaraldehyde solution and after rinsing with distilled water incubated with a solution of about 10^{-7} M recombinant streptavidin in PBS-buffer for further 90 min. After washing, the sample was finally treated with a solution of biotinylated Cy5 (10^{-7} M in PBS), rinsed with 0.15% Tween 20 in PBS, PBS-solution and distilled water and then dried in a nitrogen flow. For fluorescence analysis on the confocal set-up for SFLIM, the plate was mounted upside down on a cover slide.

In the irradiated region, the pattern of 1.5 µm circles is barely silhouetted against the background using high power excitation from the laser diode (635 nm, 40 kW/cm^2). Because of the weak signal intensity it is not possible to ascribe the heightened intensity of the pattern unequivocally to fluorescence of Cy5 bound to streptavidin for example by F2 analysis; however, considering the strong quenching expected from the nearby gold surface it seems the most likely explanation.

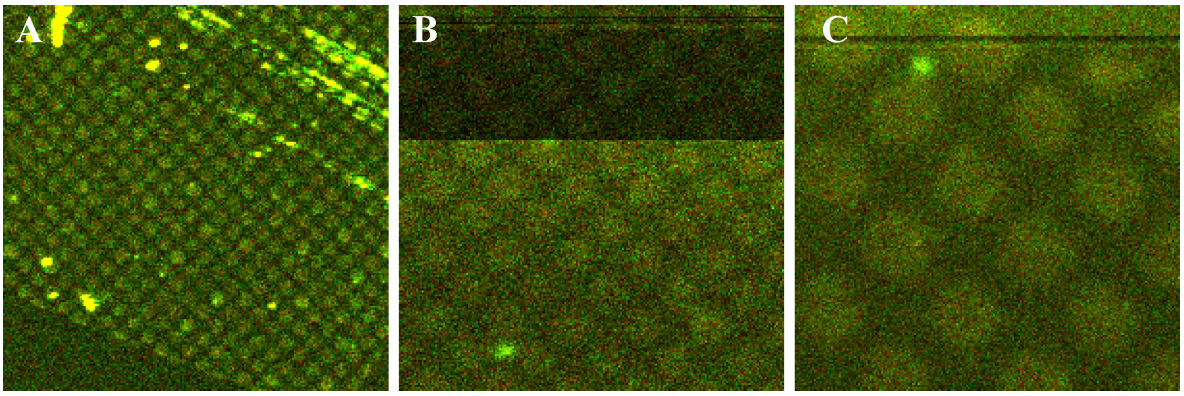

Figure 4.1.3: *False color SFLIM images of irradiated gold surface after modification with one streptavidin layer and subsequent immobilization of biotinylated Cy5 dye. 635 nm irraditaion, 40 kW/cm^2 intensity,* ***(A)*** *50x50 µm with 200 nm/pixel resolution,* ***(B)*** *20x20 µm, 100 nm/pixel;* ***(C)*** *10x10 µm, 50 nm/pixel.*

To test this assumption and to obtain a higher fluorescence signal from the dye, the reaction scheme was repeated with glutaraldehyde as crosslinker for a second streptavidin layer functionalized with Cy5. As imaging is accomplished for the dry surface, the protein was incubated for 2 h in PBS ("rehydrated") before glutaraldehyde treatment. In contrast to the method used for the first layer, the biotinylated Cy5 was bound to strepavidin before crosslinking by incubation of the latter with a 5-fold excess of Cy5 for 15 min. The rationale of this stems from the fact that a streptavidin immobilized on the surface will on average have only two possible binding pockets accessible for the biotinylated Cy5; however, even a streptavidin fully loaded with four Cy5 molecules will be accessible for the crosslinker, since the lysines should not be affected by the Cy5.

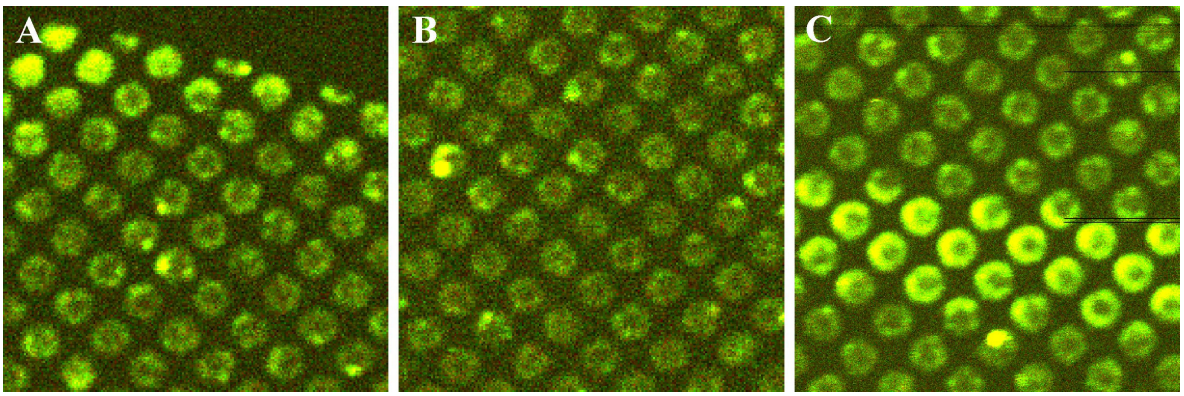

Figure 4.1.4: *SFLIM image of the surface of Fig. 4.1.3 after immobilization of a second strepatvidin layer, which had been treated with biotinylated Cy5. 40kW/cm^2 intensity,* ***(A)/(B)*** *20x20 µm^2, 100 nm/pixel;* ***(C)*** *20x20 µm^2, 50 nm/pixel*

After washing and drying, the pattern shows indeed higher signal-to-background ratio (S/B) compared to the first immobilization step (S/B = 2; Fig. 4.1.4), and the circles can now be easily distinguished from the scattered light. This rise in intensity might simply be due to the higher number of dye molecules bound to the pattern, however it is also expected that

the second dye layer has a greater distance to the surface, thus these dyes should experience less quenching from the gold. To check for this effect the same surface was imaged with an atomic force microscope using the non-contact mode for measurement of the height of the irradiated pattern.

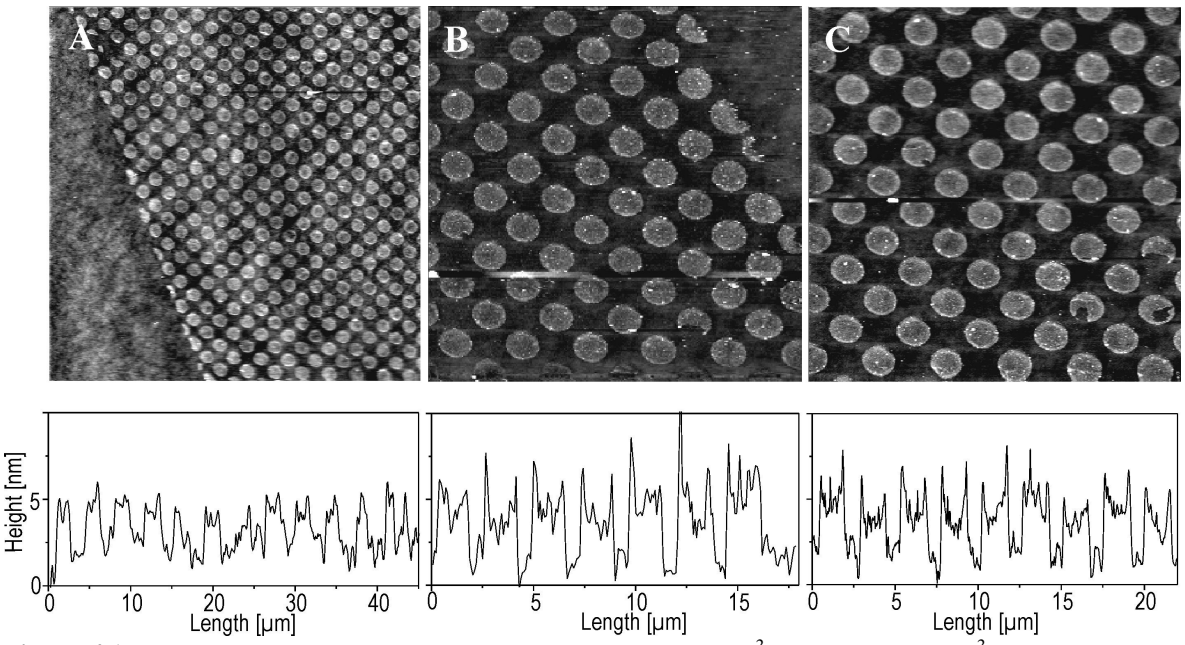

Figure 4.1.5: *AFM (upper panels) height images of* ***(A)*** *50x50 µm², (B)/(C) 20x20 µm² (1024x1024 pixel resolution) and exemplary height sections (lower pannels) ef the corresponding images of the surface in Fig. 4.1.4, i.e. with two streptavidin-layers. Note the brims around the circle structures.*

Although no height measurements had been taken for the first layer, it is known from previous experiments conducted on identical surfaces under similar conditions that the irradiated pattern has about the same height as the surrounding PEG-layer of the non-irradiated region. In contrast, the successful binding of streptavidin could be demonstrated by a significant height increase of about 2-3 nm for the patterned region and is in good agreement from height measurements of streptavidin monolayers on different surfaces [277-279].

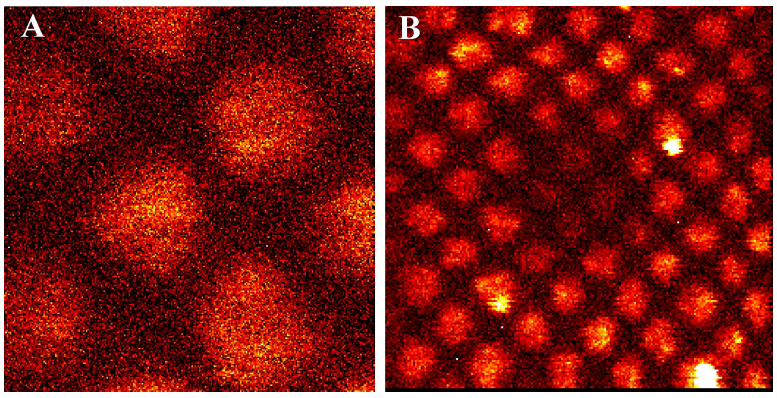

Figure 4.1.6: *Fluorescence bleaching of the surface shown in Fig. 4.1.4.* ***(A)*** *Fluores-cence intensity image of detail scan (6x6 µm², 25 nm/pixel) from region* ***(B)****. After three repeated detail scans, bleaching of fluorescence is obvious by by the darkened spots (center of* ***(B)****) compared to the surroundings in* ***(B)*** *(20x20 µm², 50 nm/pixel, 40 kW/cm²).*

Accordingly, the results after the second immobilization step of streptavidin showed an average height of about 4nm, indicating as expected the existence of two monolayers on the irradiated pattern. The presence of fluorescence in the brighter circles is not only apparent from the F_2–value determined by the spectral characteristics of Cy5, but also from reduced intensity, i.e. bleaching after repeated scanning in the same area with high power excitation (Fig. 4.1.6B, center).

It is interesting to note that the circle patterns are much brighter at the brim than in the center giving them a ring-like appearance. There is no ready explanation for this characteristics, nevertheless it cannot be due to quenching or photophysical aspects since these rings are also apparent from the AFM height images, indicating more densely packed proteins at the brim. In order to test to the stability of the formed layers, e.g. non-specific binding versus covalent crosslinking of the streptavidin, the sample was incubated for 4 h in a solution of 0.05% Tween 20 in PBS, subsequently rinsed with water and dried.

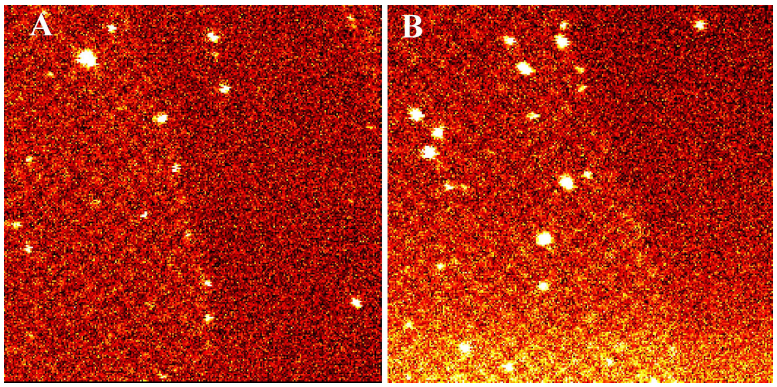

Figure 4.1.7.: *Fluorescence scan image of the surface shown in Fig. 4.1.4 after prolonged treatment with Tween 20 solution. The fluorescence intensity nearly completely vanished, indicating removal of biotinylated Cy5 molecules from the streptavidin.* ***(A)/(B)*** *50x50 µm², 250 nm/pixel, 40 kW/cm²).*

As is obvious from the resulting fluorescence image (Fig. 4.1.7), the distinct fluorescence pattern has nearly completely vanished. The remaining intensity corresponded to the results after the first immobilization. On the other hand, the height of the circles is unaltered (Fig. 4.1.8) indicating that the strepavidin layer was stably attached but Cy5-biotin was removed. Therefore, the labeled biotin has apparently disassociated from the streptavidin for which a denaturation of the latter upon binding to the surface might be a possible explanation. This unexpected results stressed the importance to switch to a different immobilization strategy which circumvents an extra labeling step of the protein. As suitable system a commercially available, covalently labeled antibody, anti-rabbit immunoglobuline type G coupled to the red dye Alexa 633 (Alexa633-IgG) was chosen, and used for building a third protein layer on top of the two strepavidin layers with glutaraldehyde.

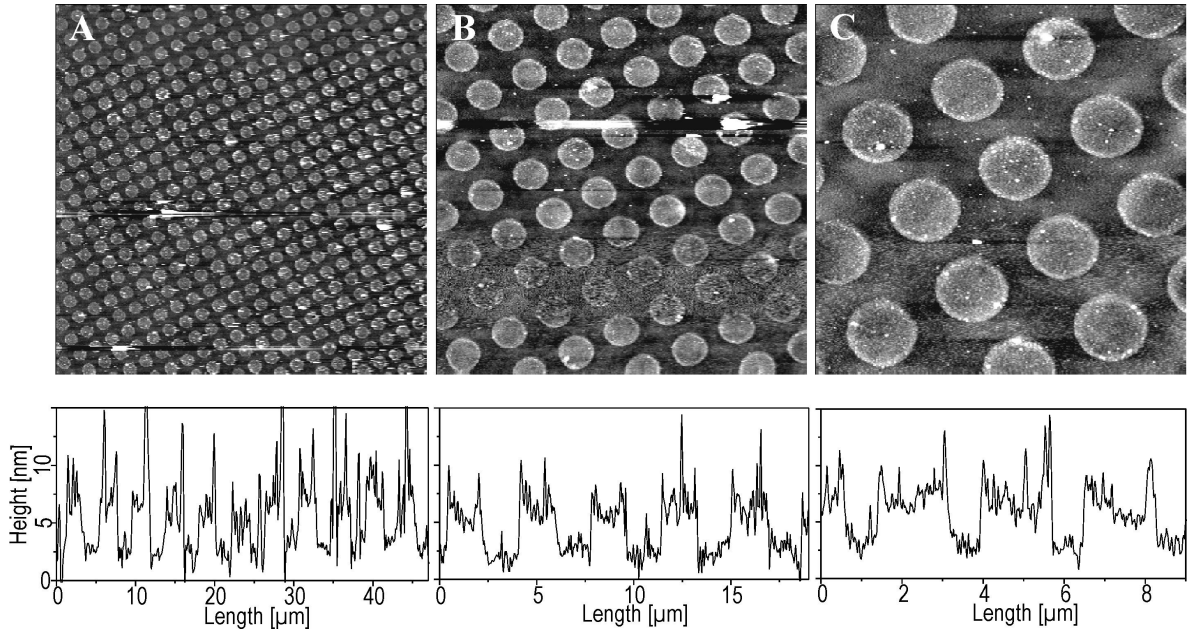

Figure 4.1.8: *AFM height images (upper) and exemplary height sections (lower pannels) of the surface shown in Fig. 4.1.7. Although the fluorescence has been considerably reduced, the height does not indicate significant disattachment of protein from the surface (compare with Fig. 4.1.5).* ***(A)*** *50x50 µm², **(B)** 20x20 µm² and **(C)** 10x10 µm² with 1024x1024 pixel.*

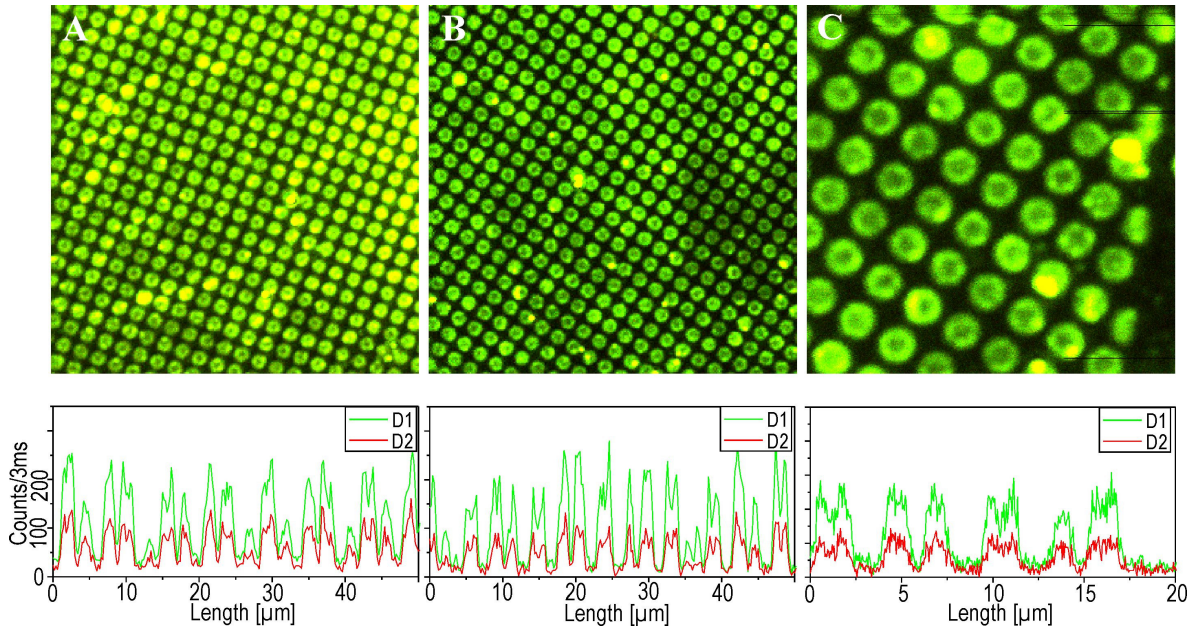

Figure 4.1.9: *SFLIM images (upper) and exemplary intensity sections (lower pannels) of the surface of Fig. 4.1.7 after immobilization of a third protein layer, an IgG antibody covalently labeled with Alexa633. Note the strong increase of the fluorescence and hence of the S/B ratio especially compared to Fig. 4.1.3. 30kW/cm² intensity,* ***(A)/(B)*** *50x50 µm², 100 nm/pixel;* ***(C)*** *20x20 µm², 50 nm/pixel*

The resulting fluorescence image (Fig. 4.1.9) shows a fluorescence increase of more than 10-fold compared to the region before labeling and can directly be compared to the result with two protein layers which displayed only 2-3-fold increase in fluorescence intensity after binding. The large difference cannot be attributed solely to a higher density of bound

dyes (according to the provider each IgG is on average labeled with 2-3 Alexa633 dye molecules) but stems from a significantly lower quenching of the dyes.

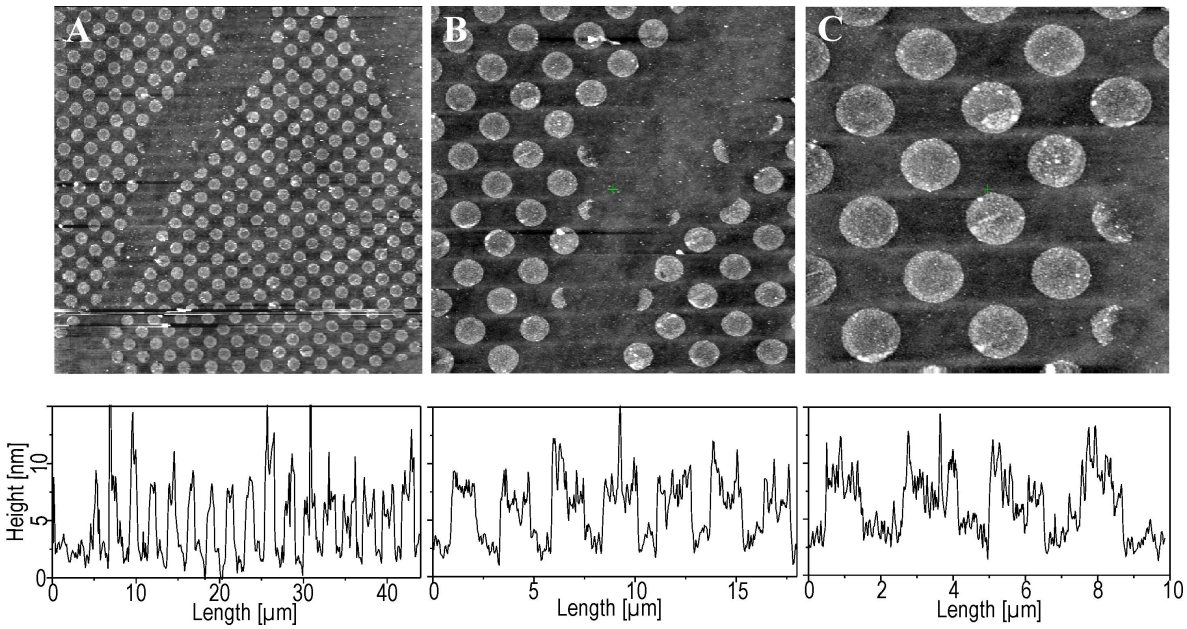

Figure 4.1.10: *AFM height images (upper) and exemplary height sections (lower pannels) of the surface shown in Fig. 4.1.9.The height displays a significant increase to 6 nm which proves succesful immobilization Alexa633-IgG on the two streptavidin layers.* ***(A)*** *50x50 µm², **(B)** 20x20 µm² and **(C)** 10x10 µm² with 1024x1024 pixel.*

Accordingly, the height of the irradiated circles has grown to about 6 nm which again corresponds to a further layer of bound protein (Fig. 4.1.10). However, whereas the S/B rises to about 4 rendering the pattern clearly visible, a significant patchy background fluorescence is discernible, apparently from non-specific binding of labeled proteins. This does not only reduce the S/B but also corrupts the employed technique of growing further protein layers since crosslinking will also occur on non-specifically bound proteins and thus increase both background and specific fluorescence. However, further attempts to remove the adsorbed proteins by 4 h incubation with the detergent Tween 20 at room temperature rather lead to accumulating non-specific background therefore the sample was not further modified.

4.1.2 Fluorescence labeling of nanometer patterned surfaces using several protein layers

In order to test the efficiency of the employed technique, structures with sizes from 1 µm down to 50 nm were patterned with the aid of a remote electron microscope (REM), and

passivated as mentioned above. The pattern consisted of five rows with four line-triplets, respectively, where each triplet had two outer lines of 3 µm and a center line of 5 µm length. The line width was constant for a given row, but decreased from top to the bottom row, so that the width decreased from 1 µm for the first to 500 nm, 200 nm, 100 nm and finally 50 nm for the fifth row (compare Fig. 4.1.12). The sample was specifically coated with streptavidin by subsequent incubation in 10% glutaraldehyde and 10^{-7} M streptavidin solution in PBS, then rinsed with 0.05% Tween 20 in water, distilled water and finally dried with nitrogen. AFM height measurements visualized the pattern and confirmed the existence of a monolayer of protein with an average height of about 2-3 nm (Fig. 4.1.11). After rehydratization two further layers of Alexa633-IgG were immobilized by treatment with glutaraldehyde, then the sample washed and dried.

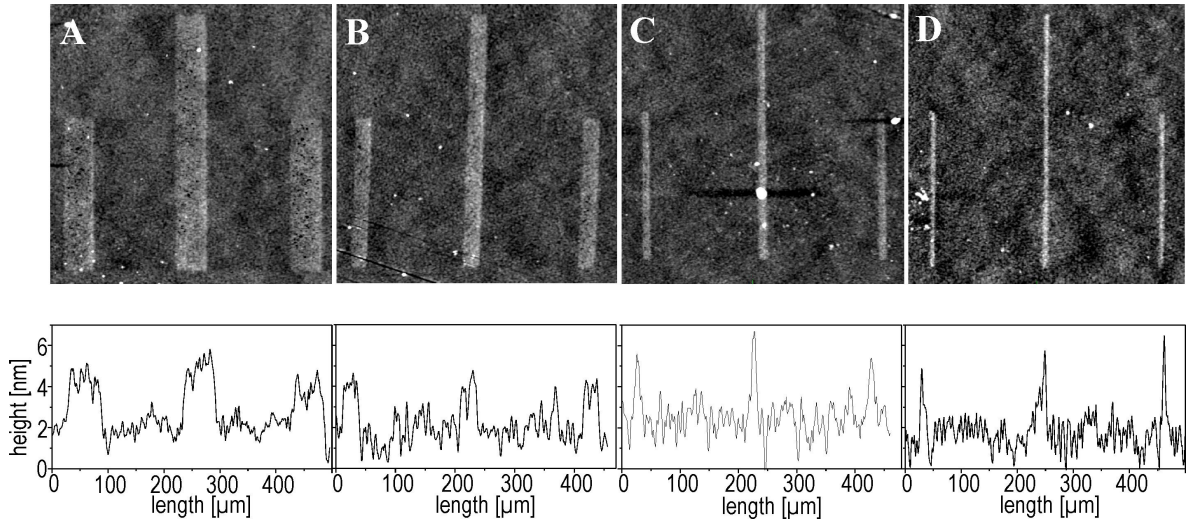

Figure 4.1.11: *AFM height images (upper) and exemplary height sections (lower pannels) of a REM patterend surface showing triplet structures with 500 nm* ***(A)****, 200 nm* ***(B)****, 100 nm* ***(C)****, 50 nm* ***(D)*** *width. The triplets stem from the region shown in Fig. 4.1.12. Note that the largest structures with 1 µm width is not displayed here. Size is in each case 5.5x5.5 µm², 1024x1024 pixel.*

In the fluorescence image of the surface (Figs. 4.1.12B/13) the first row with 1 µm width is clearly visible and yields about the same S/B = 4 as obtained from the 1.5 µm circle patterns. Nearly the same S/B is obtained for 500 nm, whereas S/B decreases rapidly with smaller width, so that the pattern for 50 nm width is hardly discernible from the background. This is because fluorescence intensities of dyes at shorter distances than their PSF will accumulate, which means that for structures of sizes above the PSF the intensity and therefore the S/B is constant, whereas the visible size changes. Then again, for structures smaller than the PSF, the visible size (= width in the present case) remains basically constant whereas the intensity decreases due to a lower number of dyes with overlapping PSF (see section 2.4). Note also that for a line the size reduction occurs only in

one dimension, thus below the PSF the intensity should decrease proportional to the size whereas for a circular structure the reduction would be proportional to the square of the radius.

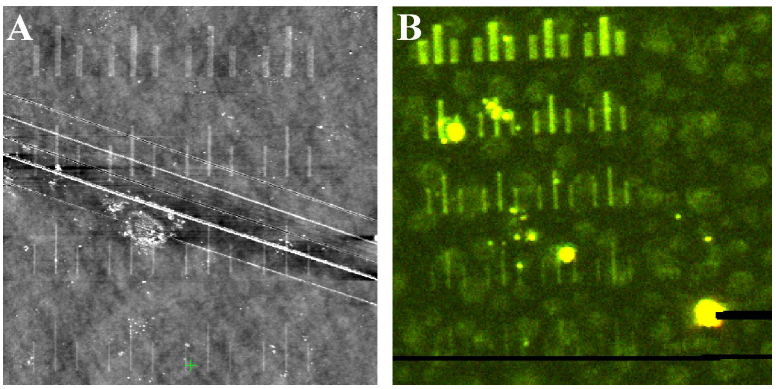

Figure 4.1.12: *(**A**) AFM height image of the REM patterned surface with one layer of streptavidin and (**B**) SFLIM image of the same surface after immobilization of two further layers of Alexa633-IgG. In the AFM image (**A**), the first line with 1 µm wide triplets is not displayed. (**A**) 40x40 µm², 1024x1024 pixel); (**B**) 50x50µm², 200 nm/pixel, 30 kW/cm²).*

Therefore, it can be concluded that the improvements obtained from the protein labeling strategy were still not sufficient for fluorescence imaging of point like structures of 50 nm and below. Furthermore it is also clear that immobilization of further protein layers would not result in better S/B ratios considering the significant amount of adsorbed proteins on the non-irradiated regions. Although as reagents to avoid non-specific adsorption about 30% glycerol and 0.01% Tween 20 were added to the protein buffer solution during incubation, accumulation of background signals poses an upper limit for the number of protein immobilization cycles.

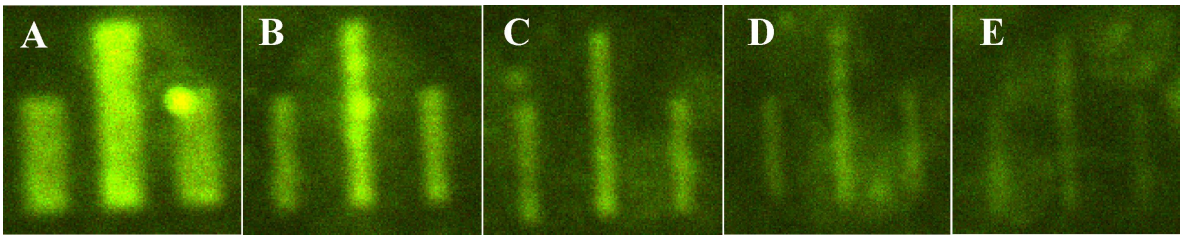

Figure 4.1.13: *Detailed SFLIM images of the surface in Fig. 4.1.12B, showing the triplets with decreasing size from 1 µm (**A**) to 500 nm (**B**), 200 nm (**C**), 100 nm (**D**) and finaly 50 nm (**E**) width. Whereas the S/B for the 1 µm triplet amounts to about the values obtained for the samples in Fig. 4.1.12, it decreases significantly for smaller structures.*

4.1.3 Fluorescence labeling of patterned surfaces using a combination of external linker and protein layers

To obtain higher fluorescence intensity without increasing the background, a complementary strategy was required. In this context the density of immobilized proteins as important parameter has to be considered which is dependent on the binding efficiency.

Though the protein density cannot be determined by the measuring methods employed, chemical considerations suggest that glutaraldehyde though reliable for protein crosslinking is not an optimal reagent for surface immobilization. Thus, glutaraldehyde is supposed to react with primary aliphatic amines via the aldehyde moiety, forming a Schiff base. However, the amine moieties on the patterned surface are much less nucleophilic due to coupling of the electron lone pair to the aromatic system and should display reduced reactivity with glutaraldehyde.

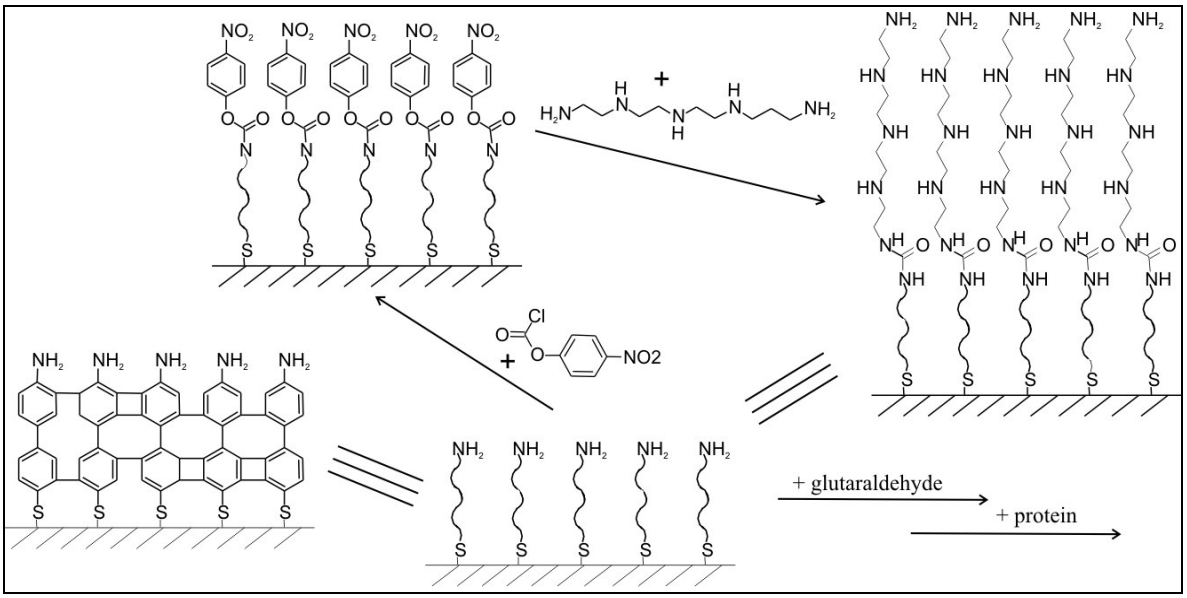

Figure 4.1.14: *Schematic of extension of protein labeling procedure of patterned surfaces (Fig. 4.1.2). The amino-groups in the irradiated spots are modified first with an aminolinker by activation with NpCF. The axtivated surface can subsequently form a stable urea-bond with TEPA. The new surface exhibits also amino-groups and reaction with NpCF with TEPA can be repeated. Finally, the top amino-layer is treated with glutaraldehyde and crosslinked with protein.*

Therefore, a coupling method developed by Hoheisel *et al.*[280] was tested which uses 4-Nitrophenyl-chloroformate (NpCF) and Tetraethylene-pentaamine (TEPA) to couple a linker with free amino-moieties to hydroxy- or amino-functionalized surfaces. The modification consists of two subsequent steps and is depicted as a scheme in Fig. 4.1.14. Briefly, the surface is first reacted with NpCF that will react exclusively by substitution of the chlorine since this is the better leaving group (using dichloromethane as solvent). This is of great advantage since partially hydrolyzed acid might bind to the surface which cannot couple to free amine. This method has also further benefits compared to direct immobilization of proteins used so far:

- NpCF is a highly activated acid thus readily reacting even with aromatic amines
- TEPA not only has a primary amine, it also bears three secondary amine moieties which can react with glutaraldehyde, thus increasing the binding probability

- TEPA is a long molecule (> 1.5 nm extended, ~ 2 nm with acid linker), even if it is not bound fully extended protein distance to the gold will be increased
- the technique can be repeated to build layers further increasing the distance to the surface similar to the labeled protein layers discussed above

Accordingly, an irradiated sample was incubated for two hours in a solution of NpCF in DCM with DIEA as proton catcher and then reacted overnight in TEPA dissolved in DMF. After washing and drying, the surface was lined with Alexa633-IgG by consecutive treatment with 10% glutaraldehyde (75 min) and the protein-solution (75 min).

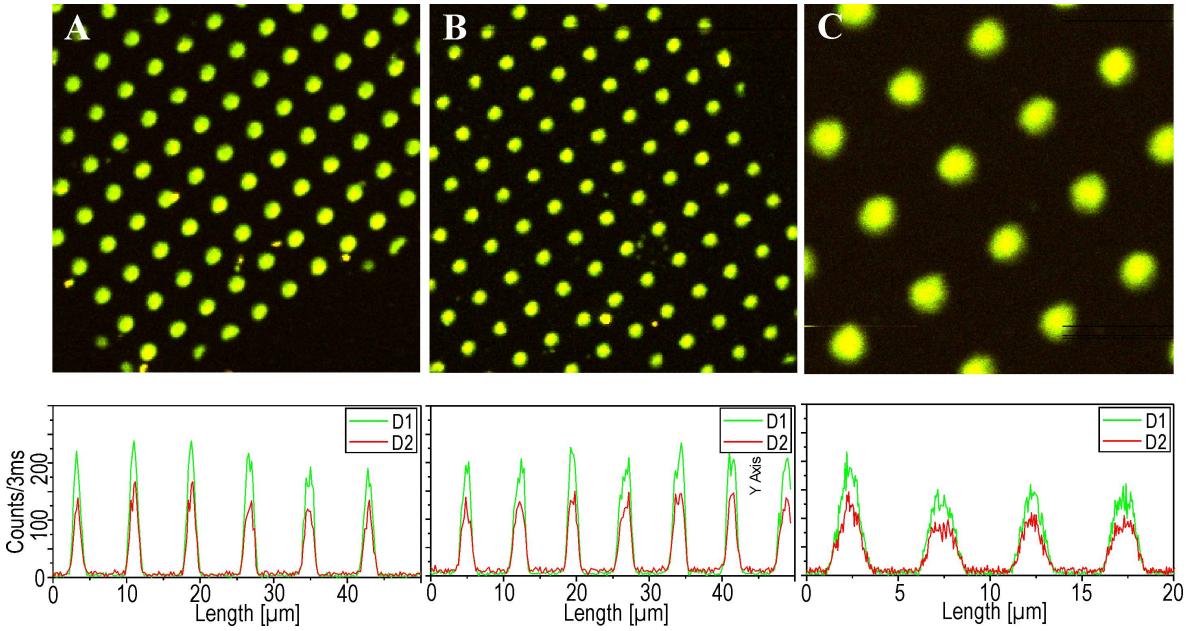

Figure 4.1.15: *SFLIM images (upper) and exemplary intensity sections (lower pannels) of a patterned surface after modification with one layer TEPA and a further layer with Alexa633-IgG. The strong increase compared to the result with three protein layers directly immobilized on the surface in Fig. 4.1.9 is obvious.* ***(A)/(B)*** *60x60 µm², 200 nm/pixel;* ***(C)*** *20x20 µm², 50 nm/pixel, 5 kW/cm².*

To further improve the imaging efficiency, a droplet of immersion oil was placed between the fixed sample and the coverslip for SFLIM. This circumvents loss of both excitation and fluorescence intensity at the glass-air interface by reflection and scattering. After imaging, the oil is easily removed by rinsing with acetone. Though in principle water is a more desirable reagent for immersion of the protein surfaces, this poses the problem of instability of the laser focus due to slow evaporation of the water. On the other hand, the use of immersion oil showed no significant effect on the protein binding efficiency after rehydratisation compared to the dried samples.

The fluorescence images in Fig. 4.1.15 shows a dramatic increase in fluorescence even when compared to the intensity with free protein layers without TEPA, resulting in a S/B >

15. Since AFM measurements (Fig. 4.1.16) yielded ≈ 3 nm feature heights, stronger dequenching compared to previous experiments by greater distance to the gold seems to be only of minor importance.

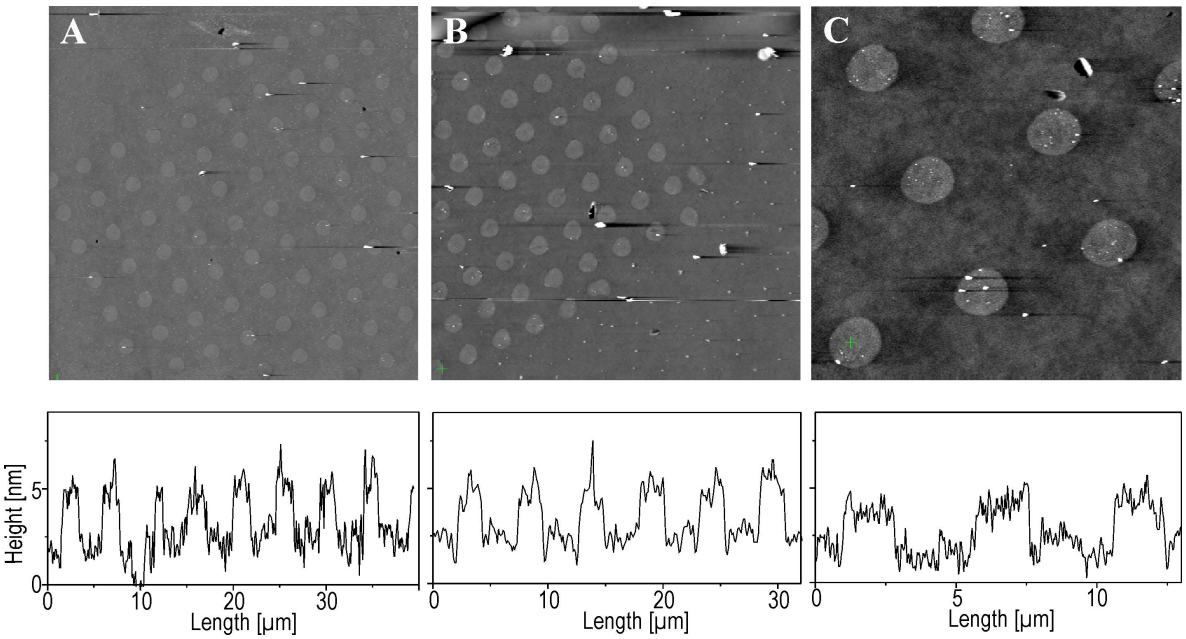

Figure 4.1.16: *AFM height images (upper) and exemplary height sections (lower pannels) of the surface depicted in Fig. 4.1.15. The average height is about 3 nm, thus only marginally higher than observed for a single protein layer, however, the structures seem to be much smoother, e.g. than in Fig. 4.1.5.* ***(A)*** *50x50µm², **(B)** 40x40µm², **(C)** 20x20µm², 1024x1024 pixel.*

But even a more densely bound protein which is indicated by the smoother AFM height images seems insufficient to explain the strong increase in fluorescence. As a further quenching possibility, however, electron transfer from the surface to the dyes has to be considered which has been proved to play a significant role for distances below 5 nm [152]. Since TEPA is an alkylic linker, i.e. has no delocalized bonds, and is expected to be positively charged due to the proton-affinity of the secondary amine moieties, electron transfer should be efficiently hindered by TEPA. Therefore, it can be assumed that the strong dye quenching observed for direct protein modification was in part due to electron transfer which is prevented by TEPA.

After discussion of several essential points for efficient specific labeling, it is necessary to consider further aspects to allow for a more detailed analysis of obtained data. On the one hand, the aim of a specific immobilization method is to ensure maximum fluorescence signal from the labeled structures, i.e. both highest dye density and lowest quenching (greatest surface distance). On the other hand, this is not the only limiting factor since also non-specific signal outside the structures is observed, which originates from two different

sources: a) intrinsic background, dependent on scattering and autofluorescence from the employed surface type; b) extrinsic background due to non-specific adsorption of the labels. The intrinsic background is a principle surface property and cannot be circumvented, thus posing an upper limit to the obtainable contrast, whereas non-specific binding depends on the adopted method and might be reversible. These background contributions can be distinguished by their spatial appearance: background due to adsorption of labels shows for low concentration an inhomogeneous or patchy distribution whereas the intrinsic contribution is evenly distributed.

In order to obtain quantitative evaluation of data for surface modifications under identical conditions, several new parameters are defined:

- signal-to-power (S/P): average fluorescence count rate obtained from the labeled spots divided by the excitation intensity
- signal-to-background (S/B): average signal from the labeled spots divided by the average background signal
- signal-to-scatter (S/S): average signal from the labeled spots divided by the signal from the lowest background

The S/P is under identical imaging conditions a relative measure for the absolute intensity, i.e. the efficiency of different labeling strategies; the normalization to the intensity is done to account for different excitation intensities. Since samples are excited far below saturation intensity and the PSF is constant, the fluorescence intensity should be proportional to the laser power used. Note that due to the wide intensity range displayed from the various fluorescence patterns (> 10-fold) the intensity of the excitation laser has to be adjusted. Thus, for strongly quenched surfaces, the fluorescence intensity and the photon statistics it is too low for a reliable information, whereas high power excitation to obtain a strongly fluorescent pattern is prevented both by strong bleaching (distortion of the true S/B ratio) and the detection limit from the set-up (~ 150 kHz).

From the S/S the maximum contrast, i.e. relative intensity of the pattern versus the scattering background can be derived, whereas the additional background due to non-specifically bound labels is accounted for by the S/B. The S/S can then be interpreted as ideal S/B, that might be theoretically achieved from the obtained specific fluorescence if non-specific contamination with proteins of the passivated regions could be completely prevented or retracted.

The S/P is determined by averaging the count rates within spots over circles of 1.5 µm diameter (size of the hole pattern) and dividing by the excitation intensity (Fig. 4.1.17A).

Only homogeneous spots with medium to low brightness were used for the determination, since brighter and inhomogeneous spots are due to additional non-specific adsorption which distorts the reproducibility of the results. The S/B is obtained in the same manner by dividing the average intensity within the circles by the average background, whereas for S/S only the background spots with the lowest count rates are chosen (Fig. 4.1.17B).

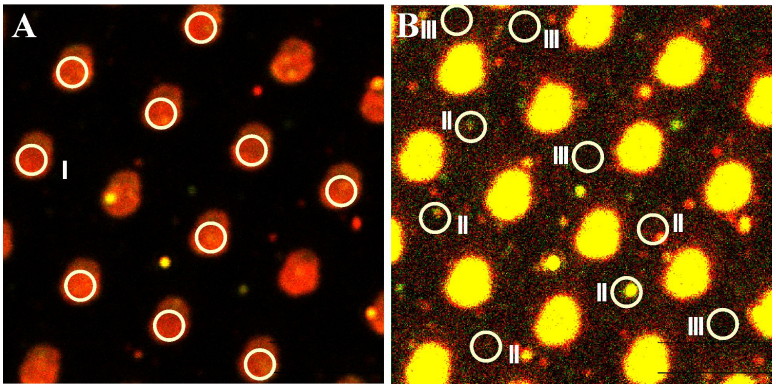

Figure 4.1.17: *(A) Description of the S/P- and S/B determination on a fluorescently patterned surface. Counts within the circle diameter of medium bright spots (I) are taken as absolute S signal. In (B), the procedure for taking both the background (II+III) and the scatter (III) is outlined. The average count rates in the circles is then used to calculate S/P, S/B and S/S.*

Accordingly, one obtains for the surface of Alexa633-IgG on one layer TEPA about 1 MHz/µW for S/P, whereas S/S- and S/B-average values of about 15. The fact that S/S ≈ S/B means that there is almost negligible contribution from non-specific background, suggesting that the ratio might be further increased for immobilization of additional layers.

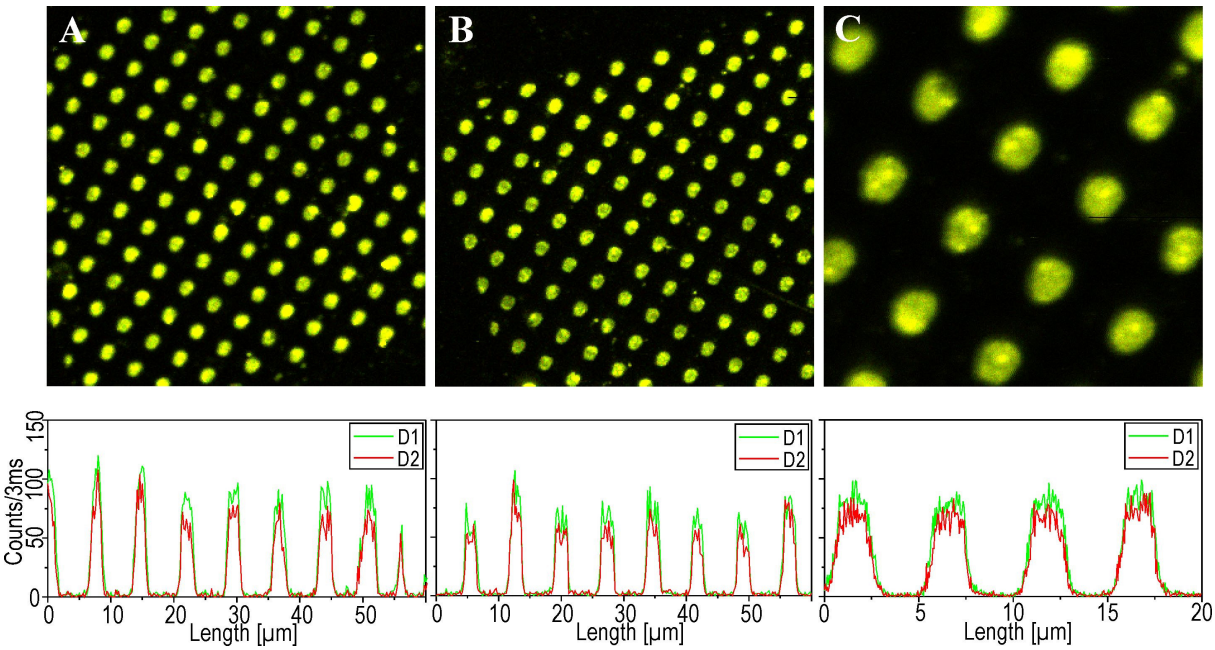

Figure 4.1.18: *SFLIM images (upper) and exemplary intensity sections (lower pannels) of a patterned surface after modification with two layers of TEPA and a further layer with Alexa633-IgG. A further increase of the signal compared to one layer TEPA (Fig. 4.1.15) is observed.* ***(A),/(B)*** *60x60 µm², 200 nm/pixel;* ***(C)*** *20x20 µm², 50 nm/pixel, 1.5 kW/cm².*

Thus a sample was prepared with two layers of TEPA prepared by the same method described above and again modified with Alexa633-IgG (Fig. 4.1.18). The pattern is even more pronounced than for one layer, however also the non-specific background increased slightly. Accordingly, a S/P of 3-3.5 MHz/µW was found, which corresponds to nearly a tripling of the fluorescence intensity and can be attributed to the additional TEPA-layer. Though this increase is quite large, it is modest compared to the rise obtained from direct protein immobilization to one layer and supports the assumption of an additional quenching pathway for dyes near the gold surface.

As expected the S/S increases also significantly to more than fifty, whereas the S/B remains considerably lower (25-30). The discrepancy compared to the similar S/S and S/B values obtained for one TEPA layer is explained by a significant non-specific background. This demonstrates that also TEPA contributes to the latter, thus we tried to further improve the S/B by constructing further protein rather than TEPA layers.

Therefore, the surface with one protein layer was incubated for 2 h with 0.05% Tween 20 at RT both to allow for efficient protein crosslinking and to test the efficiency of the surfactant for non-specific background removal. After rinsing with water, it was treated with 10% glutaraldehyde for 2.5 h and immersed in a 10^{-7} M solution of Alexa680-IgG in PBS with 25% glycerole and 0.01% Tween 20 for 2 h. The use of Alexa680-IgG instead of Alex633-IgG accounts for the fact, that SFLIM facilitates spectral resolution to gain further information about successful protein-binding and lower quenching of a second protein-layer. Thus, bound Alexa633-IgG is visible in the false color image as green spots, which denotes that emission on the shorter wavelength detector 1 (D1, colored in green) is stronger than on the longer wavelength detector 2 (D2, red), with an F_2-value of about 0.4-0.45. This is expected since the light is splitted by a 685 nm dichroic beamsplitter and Alexa633-IgG has an emission maximum of 650 nm, whereas the newly immobilized Alexa680-IgG ($\lambda_{max} \approx 705$ nm) emits predominantly on D2.

The scanning image indeed features red spots in the irradiated area, indicating that the emission intensity is dominated by the Alexa680-IgG layer. Considering that both dyes, Alexa633 and Alexa680, should exhibit the same brightness, since the lower absorption (only 55% vs 100%) of Alexa680 at 635 nm is compensated by its higher extinction coefficient (180000 $M^{-1}cm^{-1}$ vs 100000 $M^{-1}cm^{-1}$) compared to Alexa633, this again demonstrates the weaker quenching of the dyes attached to higher protein layers. From the F_2^* = 0.8-0.85 averaged over the red spots and a measured F_2-value of 0.9 for bulk

Alexa680, the relative intensity of the Alexa680 emission normalized to Alexa633 can be deduced.

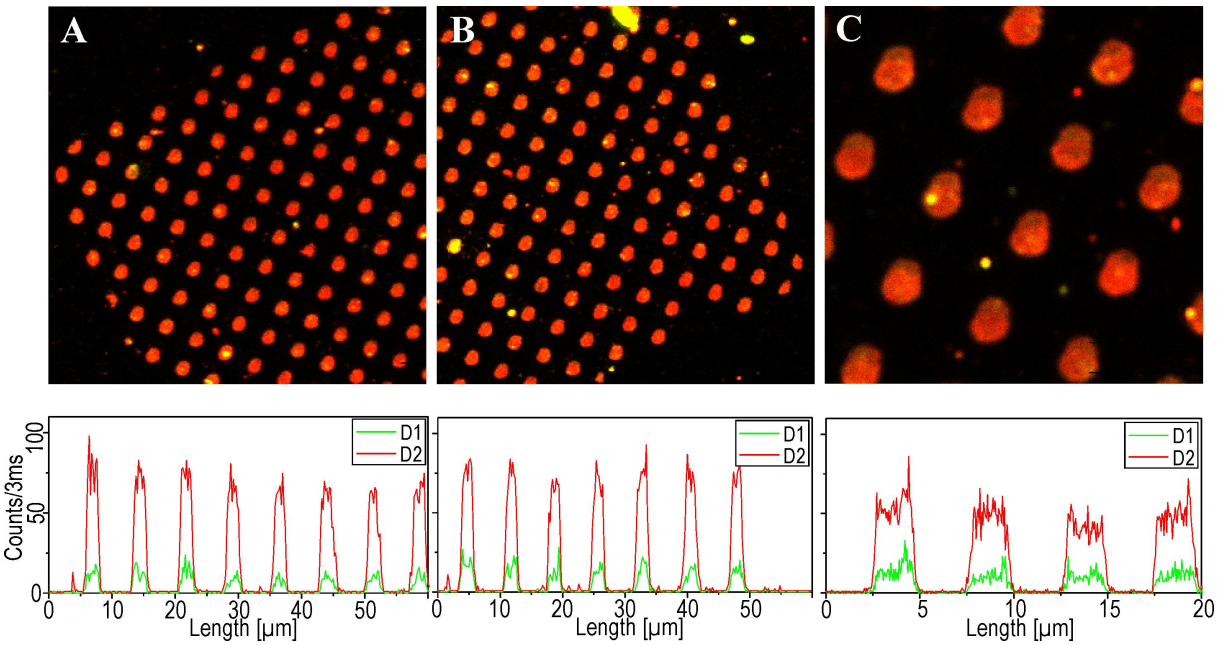

Figure 4.1.19: *SFLIM images (upper) and exemplary intensity sections (lower pannels) of the sample in Fig. 4.1.18 modified with a further layer of Alex680-IgG. Since Alexa680 emits strongly on D2, the red color indicates that it dominates the fluorescence over Alexa633, probably due to dequenching.* ***(A),/(B)*** *60x60 µm², 200 nm/pixel;* ***(C)*** *20x20 µm², 50 nm/pixel, 0.3 kW/cm².*

Thus, if one assumes comparable intensity I for both layers under normal conditions, F_2 can expressed as $F_2 = D_2/I$ and $F_2' = D_2'/I$ where D_2 and D_2' denominate the intensity on the long wavelength detector for Alexa633 and Alexa680, respectively. After immobilization the F_2 has changed to $F_2^* = (D_2 + x*D_2')/(I + x*I)$ with x as fractional intensity factor of Alexa680 to Alexa633. Therefore, the relative intensity increase yields $x = (F_2^* - F_2)/(F_2' - F_2^*) \approx (0.8 - 0.4)/(0.9 - 0.8) = 4$ for the Alexa680 normalized to the Alexa633 intensity. This compares favorably with the an S/P of about 12-16 MHz/µW which indicates a four-fold increase of the intensity upon addition of the Alexa680 layer. The fact that this is somewhat lower than expected from the F_2-analysis (x+1 = 5-fold increase) could be explained by weak FRET from Alexa633 to Alexa680. Nevertheless, the importance of non-specific adsorption is distinct by an S/B = 25-30, much lower than the S/S > 50 and what is expected from the increase in fluorescence. Furthermore, it has to be considered that the S/B is an insufficient parameter to describe the background influence on the identification of small structures below 100 nm. This is because the shape of these structures is dominated by the PSF size. Thus, a certain differentiation of these structures from background spots visible e.g. in Fig. 4.1.19 is almost impossible. The bright spots certainly do not stem from densely packed aggregates, but rather from few labels adsorbed on small

dust particles. Note that the AFM images e.g. in Fig. 4.1.16 show a significant number of spots easily exceeding 20 nm in height which accumulate for each immobilization step and place adsorbed dyes far from the strong quenching regime of the gold surface. These results stressed the importance to adopt more efficient procedures for the removal of non-specific background before further layers of labeled protein can be built. Note, that in principal also the lifetime gives valuable information about the quenching. Nevertheless, in the investigated cases it was always found that the measured lifetimes were too short to be used for unequivocal statements concerning the quenching, i.e. they were limited by the IRF.

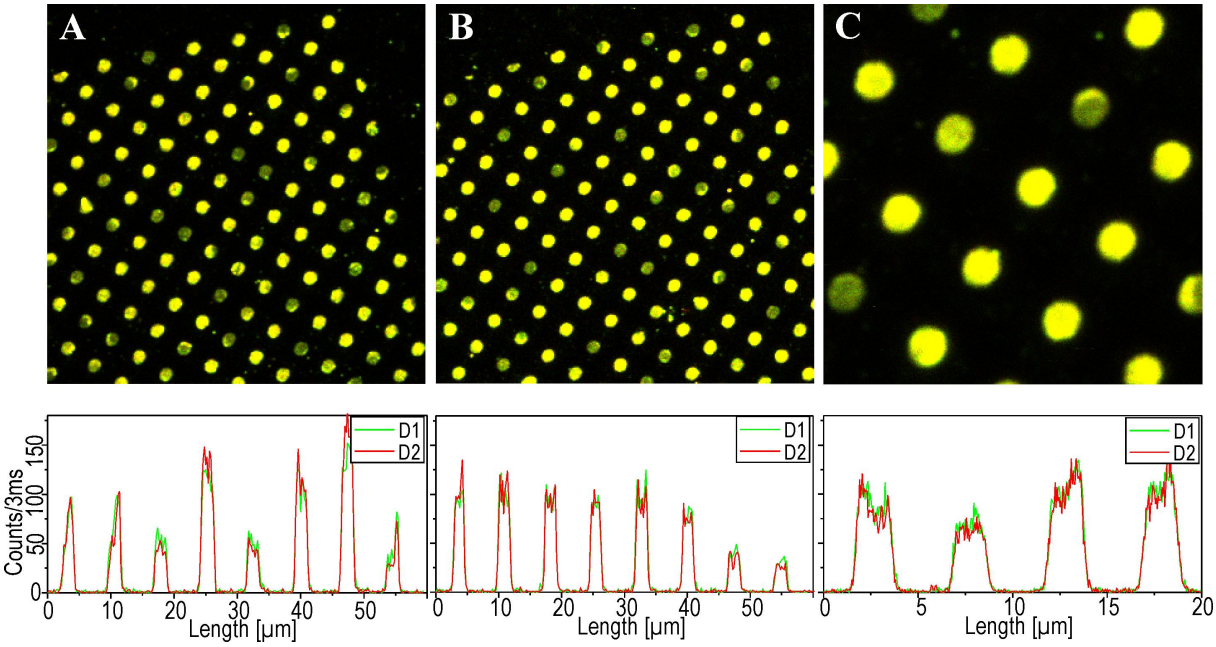

Figure 4.1.20: *SFLIM images (upper) and exemplary intensity sections (lower pannels) of the sample in Fig. 4.1.19 modified with a further layer of Alex633-IgG, i.e. three protein layers in total. The F_2 shows a significant decrease as is expected for a further layer with Alexa633. Note the striking bright and dark spots.* ***(A)****,****(B)*** *60x60 µm², 200 nm/pixel;* ***(C)*** *20x20 µm², 50 nm/pixel, 0.5 kW/cm².*

For this reason, the sample was incubated 2.5 h in PBS containing 0.05% Tween 20 at RT. Since this treatment alone had proved not to be adequate for effective cleaning, the surface was furthermore ultrasonicated in the same solvent while heating to 40°C. After rinsing and 2.5h incubation in 10% glutaraldehyde, the surface was immersed in 10^{-7} M Alexa633-IgG. This label was chosen because the fluorescence from the pattern for two protein layers had been dominated by Alexa680 emission, thus a distinct decrease of the F_2 upon a successful Alexa633 modification is expected.

From the images depicted in Fig. 4.1.20, two features for the patterns after the third protein modification are obvious: the F_2 is now dominated by Alexa633 emission (green color) and the spots show a patchy distribution with few dim among many bright spots. Concentrating on the bright spots we obtain S/I = 25 MHz/µW, S/S > 150 and S/B = 65-70 with an F_2-

value of 0.5. Taking into account the previous discussion, this F_2-value implies an increase of Alexa633- compared to Alexa680 emission of x = (0.8-0.5)/(0.5-0.4) = 3. However, this would mean an expected four-fold increase of the overall emission intensity whereas less than two-fold is obtained (25 MHz/µW vs 12-16 MHz/µW). The deviations of the intensity from the expected results can only be explained by decreased emission from the Alexa680-layer, most probably because of partial removal during the cleaning process. This also explains the dim spots with only half the intensity of the bright spots and accordingly lower S/S- and S/B-values. Since the F_2-value is even lower in these spots (F_2 = 0.45), it can be concluded that the spots with the strongest Alexa680-IgG desorption also show the least binding efficiency for further protein crosslinking. The fact, that significant desorption occurs is not unexpected since glutaraldehyde is known in many cases to form reversible bonds with proteins. For this reason, the cleaning procedure is not accomplished directly after protein immobilization, but rather before building the next layer, since it was found that drying and rehydratisation apparently stabilizes the bound protein layer. Though the detailed mechanism for the crosslinking is not known and supposed to be partially caused by polymerisation products of the reagent, the imine bonds are the most likely source, since they can be hydrolyzed under drastic conditions. This may also be amplified by denaturation of the proteins and subsequent reactions of the lysines which apparently inhibits binding upon treatment with glutaraldehyde. Despite the loss of fluorescence intensity, the effectiveness of the cleaning procedure is apparent by an increase of the S/B-value even for the dim spots (S/B =35) compared to the results for two protein layers (S/B = 25-30). Furthermore, the number of bright background spots decreased also considerably.
To test if complete desorption of the non-specifically adsorbed proteins can be achieved, the sample was again ultrasonicated in 0.05% Tween 20 for 30 min. at 40°C, afterwards left in the solvent at the same temperature for additional 2 h. After rinsing with water and incubation in PBS-buffer overnight, the surface was treated with 10% glutaraldehyde solution for 5 h and finally with Alexa680-IgG for 3 h.
The resulting fluorescence pattern (Fig. 4.1.21) monitors a homogeneous distribution concerning both the brightness of the spots as well as the background distribution. In fact, not only have bright spots completely disappeared from the background, but near complete desorption of any protein has apparently occurred. This can also be deduced from a comparison of the S/S ≈ 120 with S/B ≈ 100, indicating that the non-specific signal stems almost exclusively from intrinsic background scattering.

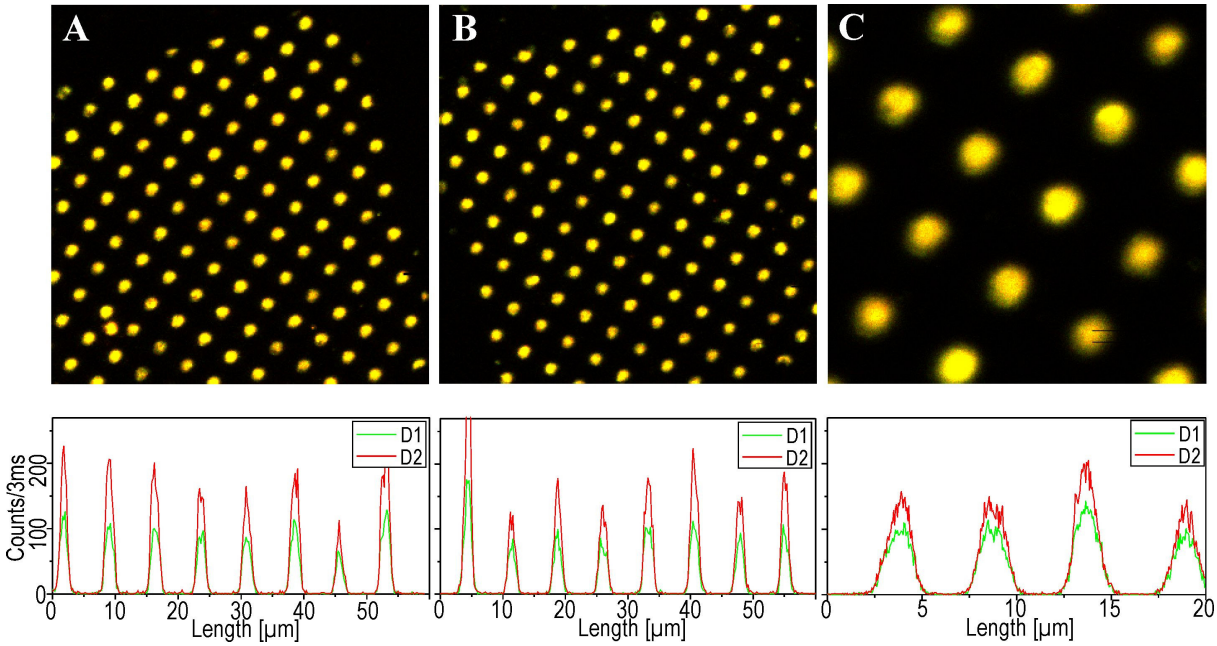

Figure 4.1.21: *SFLIM images (upper) and exemplary intensity sections (lower pannels) of the sample in Fig. 4.1.20 modified with a further layer of Alex680-IgG, i.e. with four layers of protein. Whereas the fluorescence from all spots is homogeneous, it is also apparent, that the circle margins do not show a well-defined borderline.* ***(A)/(B)*** *60x60 µm², 200 nm/pixel;* ***(C)*** *20x20 µm², 50 nm/pixel, 0.3 kW/cm².*

The considerable decrease of non-specific background is better displayed by direct comparison of detail scans of the four protein modifications for this sample, when the brightness is adjusted to the background intensity (Fig. 4.1.22).

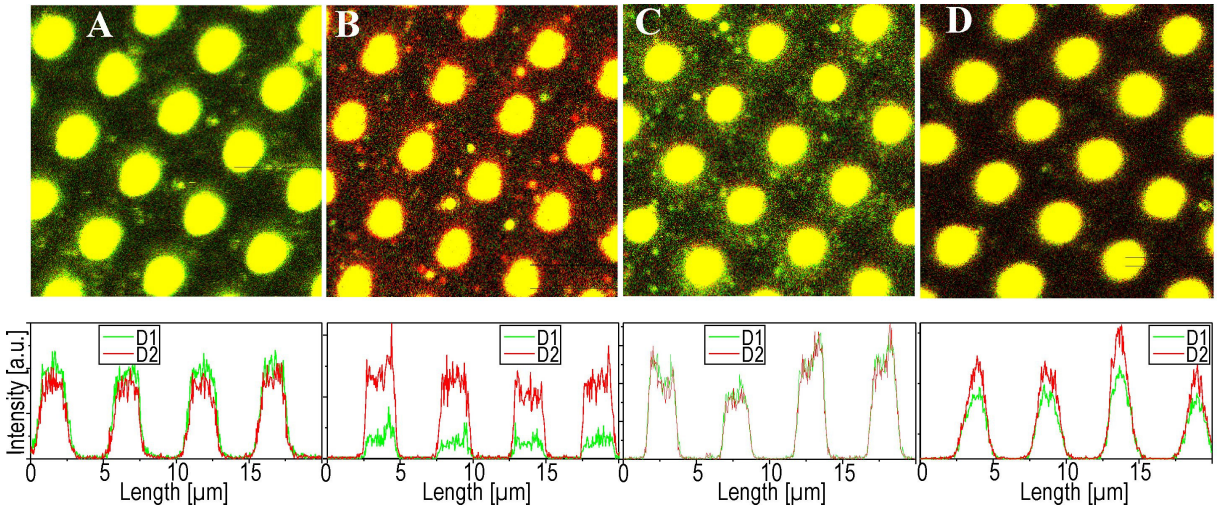

Figure 4.1.22: *SFLIM images of Figs. 4.1.18-21C, i.e. the patterned surface after modification with two layers TEPA and one* ***(A)****, two* ***(B)****, three* ***(C)*** *and four* ***(D)*** *labeled protein layers. For a better comparison of the different amounts of background, the images are displayed with increased brightness than shown above. Thus, it can be seen, that non-specific adsorption is the strongestin caser* ***(B)****, but the weakest in case* ***(D)****.*

However, the only slight increase of the spectral signature ($F_2 \approx 0.55$-0.6) indicates despite the prolonged reaction time only modest immobilization efficiency of Alexa680-IgG compared to the second protein modification (Fig. 4.1.19). Together with an S/I =

20 MHz/µW which is between the intensities obtained from the bright and the dim spots in Fig. 4.1.20, this suggests strongest desorption of the upper layers (bright spots) during the cleaning but only few available free lysines on the remaining proteins for further coupling. Whereas this weak immobilization is overcompensated by the strong background desorption yielding a three-fold increase of the S/B-value, it should be noted that the fluorescence spots show a distinct difference to the previous patterns. Thus the margin of the fluorescent circles is not well defined with a steep increase of fluorescence, but rather diffuse and displays the highest intensity only in the center. It can be concluded that proteins on the margin are more prone to desorption from the surface, because they are exposed to the solution. However, this effect would be detrimental for smaller structures, because the surface-to-volume ratio is much higher than for the 1.5 µm circles. Therefore, the decrease of protein density will be lower on those structures after the cleaning procedure. Thus the obtained S/B for this method cannot be translated to the application on nano-patterns such as used in Fig. 4.1.13.

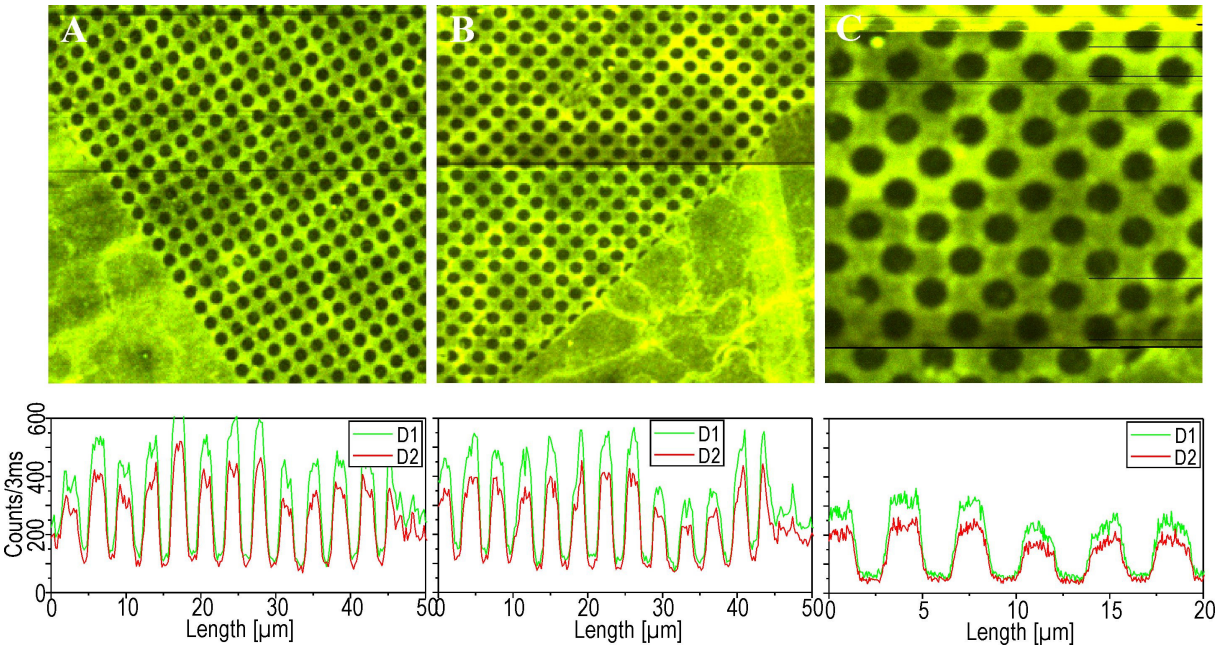

Figure 4.1.23: *SFLIM image (upper) and exemplary intensity sections (lower pannels) of a patterned ITO-surface modified with one layer TEPA and a further layer Alxexa633-IgG. The strong negative pattern demonstrates the dominating non-specific adsorption.*

Note that the achieved fluorescence intensities could be drastically enhanced if it was possible to transfer the electron beam modification of SAMs on other surfaces than gold. Accordingly fluorescence modification of irradiated Nitrobiphenyl-SAMs on Indium-Tin-Oxide (ITO) surfaces were also tested. These surfaces are prepared in an analog manner to

the irradiated gold surfaces, however, it is not possible to passivate the non-irradiated regions since the Nitrobiphenyl-layer cannot be removed from the surface.

The capability of the surface for fluorescence detection was tested by immobilization of one layer TEPA and subsequently a further layer with Alea633-IgG (Fig. 4.1.23). However, contrary to the gold surfaces modified before, which always displayed a brighter fluorescence intensity on the irradiated areas, this procedure results in a homogeneous but negativ pattern. That is, the fluorescence signal obtained from the non-irradiated areas is 3-4-fold higher than for the circular pattern. This can be readily explained by very strong non-specific adsorption of the protein on the hydrophobic Nitrobiphenyl layer. Since these surfaces are also known to result in a denaturing of the immobilized proteins, further binding of proteins is not prevented, thus multiple protein layers may grow in the non-irradiated regions which surpass the single layer fluorescence by far. Though the exact nature of the strong non-specific adsorption and even possible quenching of fluorescence in the irradiated areas cannot be excluded, these results further demonstrate the importance of surface passivation to reduce non-specific signal to a minimum.

4.2 Investigation of radiative and non-radiative rate fluctuations of single semiconductor nanocrystals (NCs) using SFLIM

NCs constitute near ideal chromophores both for application as CPS-labels on the presented surfaces and high precision distance markers using SFLIM. Apart from their favorable emission properties, which prevent bleaching and facilitate multiplexing using one excitation wavelength [75,180], their intrinsic size (> 15 nm) places them far from the quenching surface without additional distance linkers. Thus, compared to the proteins used, they do not only display a much greater size (e.g. than IgGs with ~ 4 nm), but require no labeling with external dyes, either. Commercially available with efficient coupling groups such as multiple streptavidins on their surface, they can both be linked tightly to the surface and crosslinked with each other, e.g. using BSA bearing many biotins to grow multiple layers similar to the protein modifications presented in section 4.1. Moreover, their unusually long PL lifetime > 10 ns makes them suited for the detailed study of non-radiative pathways from the gold, since with a longer lifetime stronger quenching may be resolved without interference from the IRF of the set-up.

On the other hand, high precision colocalization of two chromophores below the Rayleigh criterion requires different lifetimes and/or spectral characteristics when exited with one laser source, a feature that NCs of different size often possess. Their photostability and brightness guarantees high S/B ratios to obtain a sufficient accuracy, which has already been demonstrated before [53]. In contrast to the application as CPS labels, both multiple binding sites and the large size constitute serious disadvantages for SFLIM probes. This is because more than one binding site prevents specific labeling of target molecules with exactly one dye, and a large size implies an intrinsic distance error, depending on the orientation of the label with respect to the target. However, the first problem can be circumvented using NCs modified with HisTAG-linker which facilitates purification of a singly labeled target and has been established recently for protein-labeling [60]. Concerning a potential falsification of measured distances, the extent of this effect has to be tested for model systems (molecular ruler).

It should be repeated here, that alternatively to the distance measurements, the presented method enables the counting of the number of excited fluorophores if more than one fluorophore of the same kind is within the excitation volume. The requirements on NCs as

probes and implications of the accomplished results on the coincidence characteristics of the used NC samples will be presented separately in section 4.3.

Apart from some drawbacks, for successful employment of chromophores in the depicted techniques (especially their use for precision distance measurement on the SM level) further conditions have to be met: the PSF separation of two different fluorophores necessitates the knowledge of the lifetime and F_2-value for both of the dyes. Despite broadening effects on surfaces and fluctuations on the SM level, for organic dyes this can in many cases be achieved by fitting average values measured for many single dyes, which gives good results because of adequately narrow distributions obtained for immobilized molecules [57]. Briefly, the successful application of chromophores for high precision colocalization is only possible for dyes that exhibit well defined and stable spectral and lifetime characteristics on the single molecule level.

For comparison, when using NCs it has to be considered that different from organic molecules, the exact structure and thus emission properties are intrinsically different from NC to NC even after high quality purification. Notwithstanding this dynamic inhomogeneity, on the SM level both the PL lifetime and spectral emission have been known to fluctuate extensively even in homogeneous environment [88,91]. Although general features of these fluctuations have been elucidated in recent years [90,92,235], a thorough understanding of the influencing and controlling parameters has not been accomplished so far.

In summary, whereas the homogeneity of the spectral, lifetime and coincidence characteristics is ascertained for most single organic fluorophores [57,58], this is not the case for colloidal NCs. Therefore, to check for the suitability of NCs as probes for high precision colocalization measurements, one has to

1. analyze both the occurrence and extent of fluctuations of spectral and lifetime fluctuations for single NCs
2. correlate the interplay and identify the environmental parameters that drive these fluctuations
3. if possible, establish imaging conditions which suppress the observed fluctuations

Apart from the application as high precision marker, these investigations are also of fundamental interest for a thorough understanding of NC photophysics on the single-molecule level. This is of great importance since up to now properties of newly synthesized samples are checked by ensemble measurements analogous to synthesis assessment of

organic dyes. However, it has to be considered that organic fluorophores are made up of covalent bonds and display a well-defined structure, where subpopulations can be accounted for by different nanoenvironments. In contrast, NC samples are intrinsically heterogeneous, i.e. each NC will differ to a more or less extent from another NC with respect to the exact number of atoms or its shape etc (section 2.3.2). Especially the effect of subtle variations such as the shape or stacking faults on the NC emission remain to be solved, but there have been indications for a significant influence of the latter on spectral diffusion properties [281]. Thus, for an evaluation of a synthesis route, it is not only important to study the efficiency in terms of the ensemble properties, i.e. spectral bandwidth and PL quantum yield, but also the homogeneity of the sample, i.e. how much do the photophysical properties of one NC differ from another? Analytical methods apt to disentangle different photophysical regimes and their interplay with time and might be used for efficient assessment of different synthetic procedures. With sophisticated modification procedures nowadays at hand such as growing multiple insulating layers on the NC surface, this might open novel pathways for fine tuning of photophysical parameters apart from the spectral characteristics.

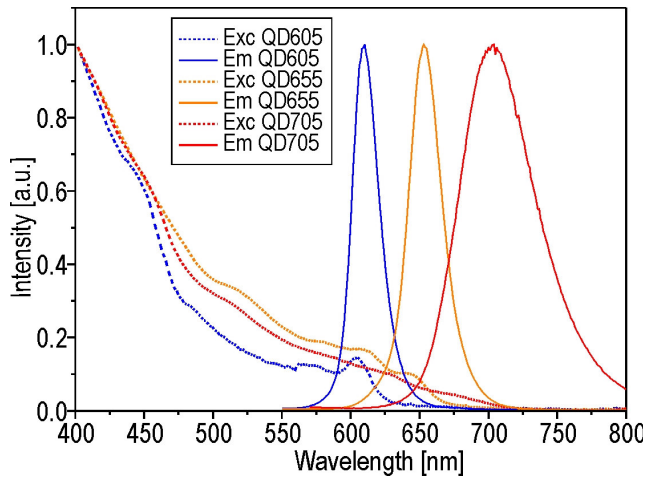

Figure 4.2.1: *Absorption (dashed) and emission (full line) spectra of the applied NC-samples. Note that the band edge feature diminishes for higher wavelength samples.*

In the presented work, measurements and analytical methods were developed for the photophysical investigation of three different samples of commercially available NCs. Briefly, these samples consists of core-shell NCs with the core made up of either CdSe (QD605 and QD655) or CdTe (QD705), coated with a ZnS shell. An ambiphilic polymer coating facilitates both water solubility and functionalisation with streptavidin.

Fig. 4.2.1 depicts both the normalized excitation and emission spectra of the different samples taken in a fluorescence spectrometer at a concentration of about 10^{-8} M. Note that according to the manufacturer the extinction coefficient at 400 nm is as high as about 4×10^{6} L/(Mcm) for QD605 and about 5×10^{-6} L/(Mcm) for both QD655 and QD705. It is

obvious that the characteristic band edge feature for the 1 S transition seems to be stronger for shorter wavelength emission, so that it is very distinct for QD605 but hardly discernible in the homogeneous rise at 700 nm for QD705, due to the higher bulk properties of larger NCs.

For data collection on the SM level, the described confocal microscope (section 3.1) together with a pulsed laser as excitation source and two APDs for detection was used. When a dichroic beamsplitter is placed in the detection path to spectrally split the PL light onto the two APDs and an electronic delay is applied for the signal from one of the APDs, four parameters for single NCs can be determined :

1. the photoluminescence (PL) intensity per time interval N_C, defined as the number of photons ("counts") detected on the two APDs within a certain integration time ("binning")
2. the spectral signature F_2, defined as the number of photons detected on the long wavelength detector D_2 divided by N_C for a given binning
3. the PL lifetime τ, determined from the microtime histogram with the aid of the maximum likelihood estimator (MLE) within a certain time range ("TAC range") after the laser pulse (rise at the beginning)
4. the coincidence ratio R_C, defined as the number of counts in the "central" peak (one count event on each APD for the same laser pulse) divided by the average number of counts in the "lateral" peaks.

In the following paragraph, the correct acquisition and interpretation of the data is discussed in more detail in order to explain their implication on the results. It has to be borne in mind that since the aim is to investigate single molecules, not absolute but relative shifts of initial values are of importance. This is because they contain information about the influence of the microenvironment on the luminescence properties and thereby provide insight into the underlying fundamental photophysics.

4.2.1. PL intensity information

Whereas the PL intensity N_C is the most important parameter, since it determines the photon statistics required for correct assignment of the other observables, it is also the most difficult to interpret. This is because it depends both on intrinsic, i.e. inherent to the photophysics of the NC, and extrinsic factors, i.e. properties of the employed detection set-

up. Principally, it is determined by three factors, a) the probability of NC excitation, b) the probability of NC emission (the photoluminescence quantum yield ϕ) and c) the probability of detection of the emitted photons. Factor c) depends only on the set-up (extrinsic) and b) is a property of the NC, whereas a) depends both on extrinsic and intrinsic factors, e.g. excitation intensity and extinction coefficient. Especially the extrinsic factors are difficult to determine and cannot be derived with certainty. Considering as an example the excitation intensity, a misalignment during the PL detection of only 500nm, -typically more than the PSF radius- of the center of the NC with respect to the focal spot results in less than two-fold lower power the NC is actually exposed to. Although extrinsic factors should be constant during the measurement and allow for a determination of the relative change of photophysical parameters of the NC, the possible interrelation between extrinsic and intrinsic factors have to be considered. Experimental approaches which might allow for the disentangling of these factors and yield more information about the NC photophysics require a thorough investigation of the respective set-up and are discussed in more detail in section 4.3.

4.2.2. Single NC spectra and F_2-calibration

In the past years, the F_2-value has been proven to be an adequate tool to gain information about spectral shifts and subpopulations of chromophores with high temporal resolution. This is more important for NCs which display an dynamic spectral inhomogeneity independent of the environment and have been shown to be subject to spectral diffusion. A prerequisite for the correct interpretation of the obtained F_2-values is the knowledge of the spectral characteristics. Generally, a change of the F_2-value might be caused either by a) a spectral shift, b) a change of the spectrum shape or c) a relative increase or decrease of a second component with different spectrum. However, due to the photostability and brightness of NCs, it is possible to obtain PL spectra emitted from a single NC and which can be investigated with respect to fluctuations of shape and peak-positions. The SFLIM set-up was accordingly modified to facilitate recording of the detected PL photons both with the APDs and a camera equipped spectrograph. In the latter, the light was focused through a slit aperture of variable width, dispersed by a grating of the suitable wavelength range. The intensity distribution was imaged with a Peltier-cooled front-illuminated electron multiplying (EM)-CCD camera (section 3.2). To obtain maximum sensitivity and

spectra of sufficient photon statistics, camera exposure times of 1 s per image were used. Generally, spectra from single NCs were recorded for one minute, i.e. consisting approximately of 60 bins, which allowed for the observation of spectral diffusion. The long integration time was necessary because the effective collection time of the PL is significantly diminished by blinking events. This was important, as high power excitation was necessary (> 10 kW/cm^2) to collect sufficient photons for a spectral analysis, but also aggravates blinking. Hence, only a fraction of the bins recorded provided enough PL intensity for analysis.

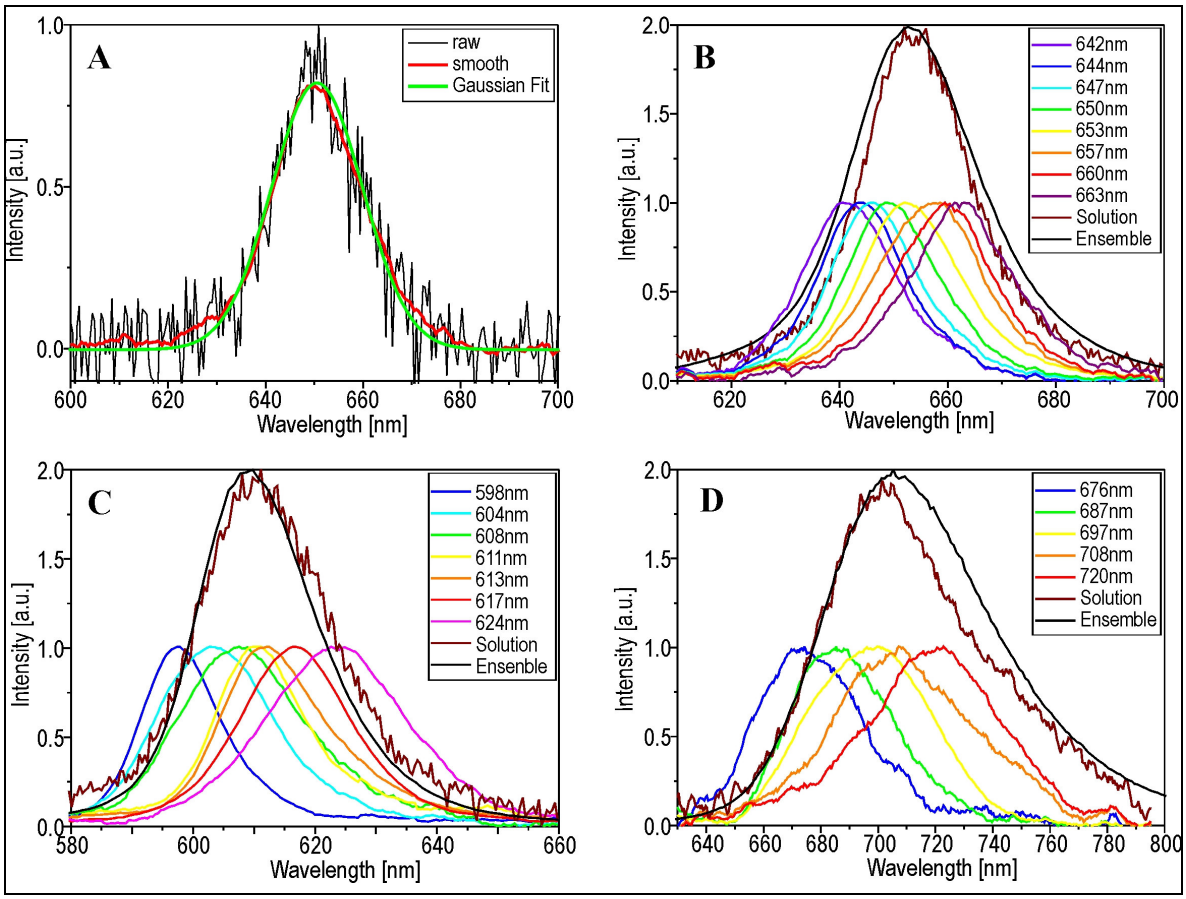

Figure 4.2.2: ***(A)*** *Spectrum of a single NC (sample QD655) integrated over one minute. The noise can be significantly reduced by smoothing with adjacent avering (20 data points, red curve) without significant shape alteration. The curve is well described by a Gaussian distribution fit (green).* ***(B)-(D)*** *Ensemble spectra measured in the spectrometer (black curve) and with the CCD spectrograph (brown curve) for QD655* ***(B)****, QD605* ***(C)*** *and QD705* ***(D)****, respectively. In all cases, the colored curves with arbitrary maximum intensity of one show examples of smoothed single NC spectra taken over one minute.*

An exemplary spectrum obtained from a single NCs of QD655 averaged over one minute is shown in Fig. 4.2.2A. Note that the remaining photon noise can effectively be overcome by smoothing over 20 data points by adjacent averaging, without alteration or distortion of the original spectral shape. For quick quantitative analysis the data can also be fitted in very good approximation by a Gaussian distribution, from which both the emission maximum

wavelength and the spectral linewidth can be obtained (in the presented case yielding 650.6 nm and about 19 nm FWHM, respectively). The spectral inhomogeneity of the samples is obvious from the distribution of maximum emission wavelengths for different single NCs immobilized on dry cover slides (Figs. 4.2.2B-D). The accuracy of the employed spectrograph is demonstrated by the resulting spectra of 10^{-9} M solutions of the respective sample, which is in good agreement with the ensemble spectra taken in the fluorescence spectrometer (brown and black curves, respectively, in Fig. 4.2.2B-D).

On the basis of these spectra, the unique features of SM spectroscopy can be demonstrated: From the ensemble measurements it is not possible to decide whether the observed width of the ensemble spectra is caused by a) a broad distribution of different but narrow single NC spectra, b) a narrow distribution of broad single NC spectra, or c) by a contribution due to both factors. With the aid of the SM spectra, it can be deduced that case c) gives the best description since the typical line widths (≈ 18-20 nm for QD605 and QD655, respectively; 35-45 nm for QD705) are comparable to the observed differences of the maximum emission wavelengths (21 nm for QD655, 26 nm for QD605 and 46 nm for QD705). It has to be considered that the actual size distribution is narrower (< 5 % according to the manufacturer) than deducible from the last values since these depict seldom events of strongly red- or blue-shifted emission. This also accounts for the fact, that the actual spectral width measured in solution (22 nm for QD655, 23 nm for QD605 and 57 nm for QD705) is only slightly broader than the average FWHM from single NCs of the respective sample. Due to the low statistics of only 35-40 SM spectra per sample, the actual spectral dispersion and the resulting FWHM could not be obtained. By comparison of the different samples it is obvious, that both QD655 and QD605 show comparable dynamic heterogeneity (≈ 20 nm each) whereas the dispersion for QD705 is much broader for both the size distribution and the average

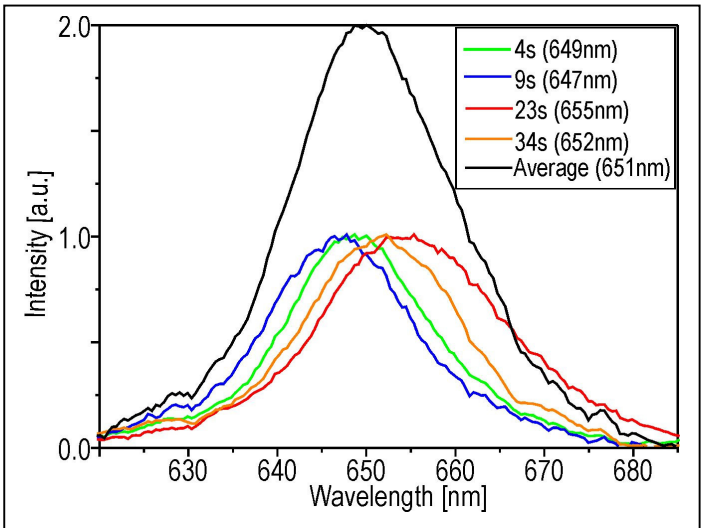

Figure 4.2.3: *Resolved spectral diffusion (SD) for the NC shown in Fig. 4.2.2A. The colored curves show smoothed 1 s portions of the spectrum averaged over 1 min (black curve).*

linewidth. This non-trivial effect can only be deduced from single NC spectroscopy and is apparently caused by the different core material (CdTe for QD705 instead of CdSe).

For the interpretation of single NC spectra, it has to be considered that the linewidth obtained is not the ideal limit derived from temperature broadening (section 2.3.5), but is also broadened by the slit width which was chosen to gain best signal-to-noise ratio. Furthermore, the actual linewidth is considerably concealed by spectral diffusion (SD): Only on timescales longer than 1 s and for significant spectral jumps the spectral diffusion can be resolved as is discussed below. Since, these spectral shifts can also be considerably faster, their influence on the measured values cannot be derived with any certainty. For a demonstration of the observable SD, i.e. on timescales > 1 s, Fig. 4.2.3 shows extracts of bins for the spectra of a single NC of QD655 (same NC as in Fig. 4.2.2A).As is expected, the amplitude of the spectral shift (6 nm) is much lower than that caused by the static heterogeneity (21 nm). It is also noteworthy that the observed FWHM of the linewidth broadens for a spectral red-shift and amounts to 18.5 nm for a λ_{max} of about 647 nm (after 9 s) compared to 21.5 nm at 655 nm (after 23 s). This confirms the trend observed within different samples where the broadest NC linewidths are also found for the strongest red-shift. This behavior is well-known from literature and has been accounted for by increased coupling with LO phonons [90].

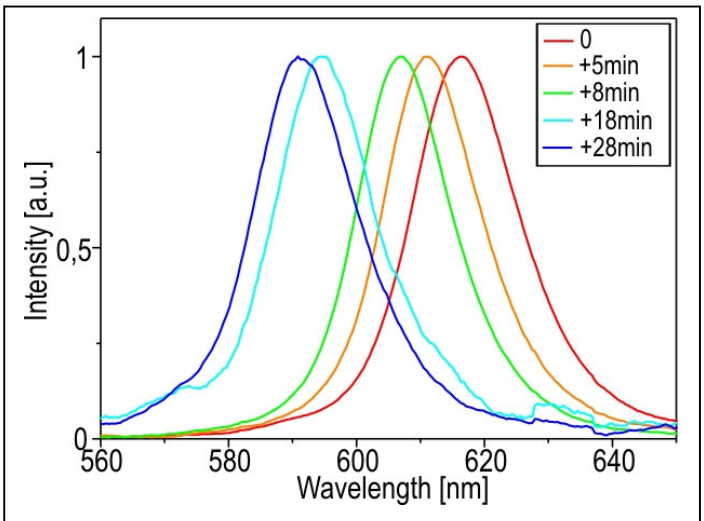

Figure 4.2.4: *1 min spectra of a QD605 on a dry coverslide with high excitation power (≈ 20 kW/cm²). The spectrum shifts within less than 0.5 h irreversibly from 618 nm maximum emission to 592 nm, i.e. a blue shift of 26 nm*

Note that apart from SD, spectral shifts might also be caused by "blueing", i.e. photooxidation of the NC leading to a cumulative blue shift of the emission under continuous excitation [282]. Blueing can be distinguished from SD by the fact that the shift is irreversible, and furthermore requires long excitation under saturating conditions even for old samples on dry surface (shown for a NC of QD605 in Fig. 4.2.4).

Since the homogeneity of the spectral characteristics for the three samples has been verified, i.e. no significant shape alterations and other components have been detected, the application of the spectral signature F_2 as correct indicator of SD is guaranteed.

Furthermore, a combination of the spectrograph within the SFLIM set-up allowed for a calibration of the F_2-values acquired for the appropriate beamsplitter and filter set-up with the spectra. Therefore, a 50/50 non-polarizing beamsplitter within the confocal microscope was used to divide the PL intensity between the APD detection path and the spectrograph (section 3.2). To ensure simultaneous recording of the spectrum and the F_2-value for single NCs, a coverslide coated with the respective NC sample was imaged using the SFLIM scanning program. Suitable spots were then selected for detection and subsequently addressed with the scanning stage while simultaneously recording the transient and collecting the spectra for 60 s each.

For calibration, spectra were analyzed in bins of 1 s with a home-built program written in LabView, in which the maximum emission wavelength was determined by fitting with a Gaussian function. For each NC, the emission maxima were plotted versus the calculated F_2-value which was simultaneously obtained from the SFLIM set-up. Since it was not possible to start both measurements at the same time and because there was also a slight delay between consecutive frames of the camera, both transients had to be processed for synchronization. This was achieved using the intensity fluctuations from different bins, which were superimposed by adjusting the timescales of the camera frames. The accuracy attainable by the parallel detection can be estimated from comparison of the intensity and spectral transients for both the camera and the confocal set-up, exemplary shown in Figs. 4.2.5.

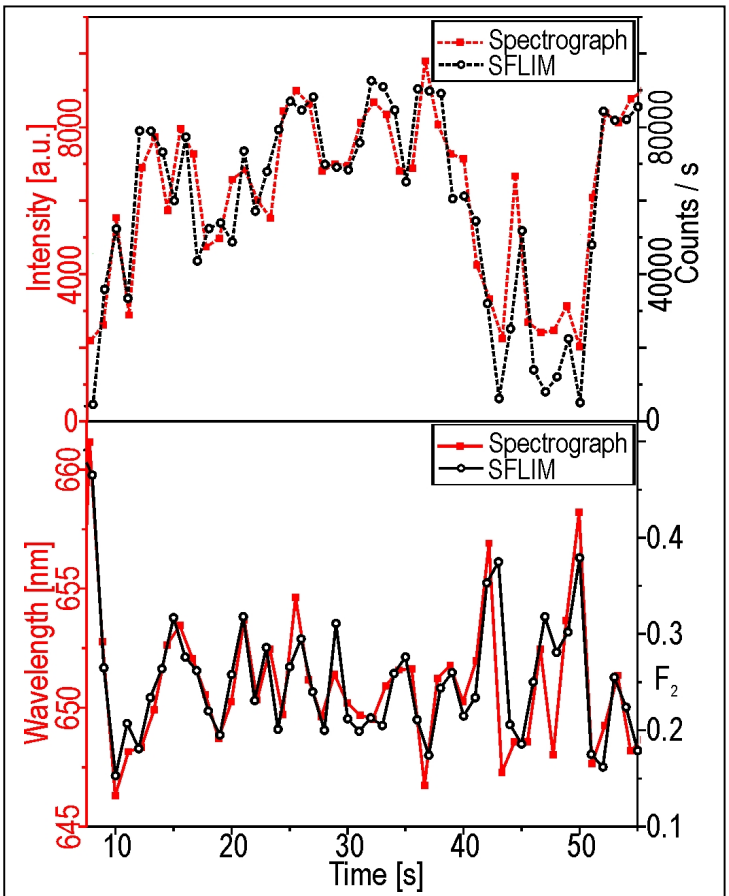

Figure 4.2.5: *Intensity (upper) and spectral information (lower panel) for the NC depicted in Fig. 4.2.2A/3 both determined for the spectrograph (red) and SFLIM set-up (black).Both curves show nearly parallel course, only for low intensity are major derivations of the wavelengths because of statistics.*

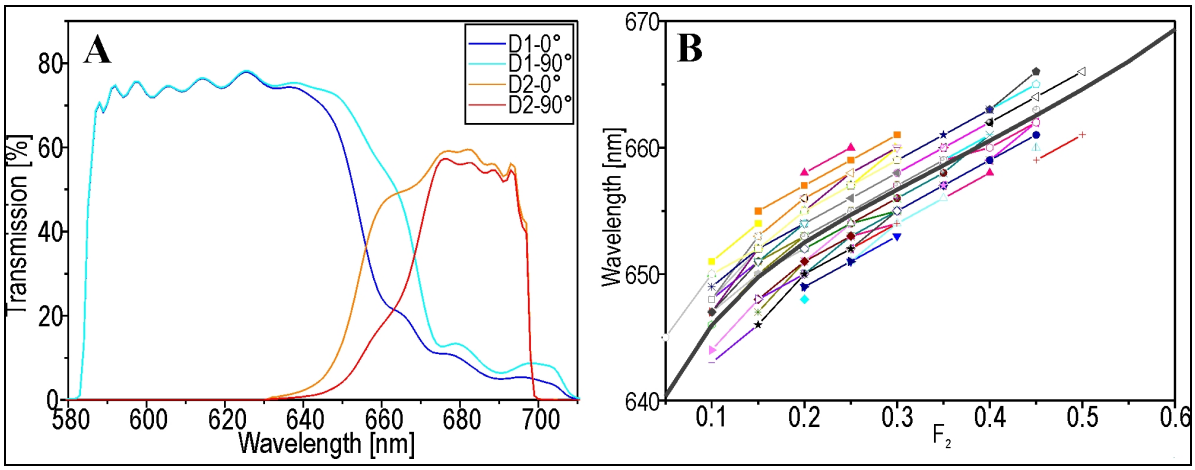

Figure 4.2.6: ***(A)*** *Calculated transmission of the SFLIM set-up on both detectors for QD655 using a 660 nm dichroic beamsplitter. Note the difference between light that is polarized horizontally (0°) or vertically (90°) with respect to the beamsplitter.* ***(B)*** *Calibration data and resulting* F_2-λ_{max}*-calibration curve (black line) for QD655.*

From the good correlation of the wavelengths with the F_2-values in Fig. 4.2.5, it can be deduced that the F_2-value is fairly proportional to the maximum wavelength for the depicted NC. As at the high excitation intensities the PL emission was seriously corrupted by blinking, only those bins with sufficient photon statistics were considered for calibration. Because of statistical errors the obtained wavelengths and F_2-values are given only with an accuracy of 1 nm and 0.05, respectively (see Fig. 4.2.5). The plots with the calibration data of 40 NCs for each sample are displayed in Fig. 4.2.6B. Depending on the extent of spectral diffusion each NC is represented not only by a single spot but a line. Whereas the distribution of lines implies that for a measured F_2-value the emission maximum wavelength of two different NCs might differ more than 5 nm, the course of the lines is predominantly parallel and they almost never cross each other. These findings indicate that relative wavelengths shifts can be obtained from the course of F_2 with high accuracy. The cause for the observed deviations of the absolute values is the slight sensitivity of the beamsplitter to the polarization orientation of the light. The effect can be estimated from the corresponding transmission curves, which show a distinct wavelength shift depending on the polarization of the light (Fig. 4.2.6A).

The calibration data for each sample was then used to construct density plots of the emission wavelength versus the F_2-value from which an averaged calibration curve was obtained by fitting of a polynomial function (black line in Fig. 4.2.6B). For comparison, the theoretical calibration function was exemplary calculated for the QD655 set-up. This was done by calculating the respective overlap of a Gaussian curve with FWHM of 18 nm (simulated NC emission of QD655) with each of the transmission curves of the QD655 set-up shown in Fig. 4.2.6A. The overlap represents the transmission of the simulated PL on

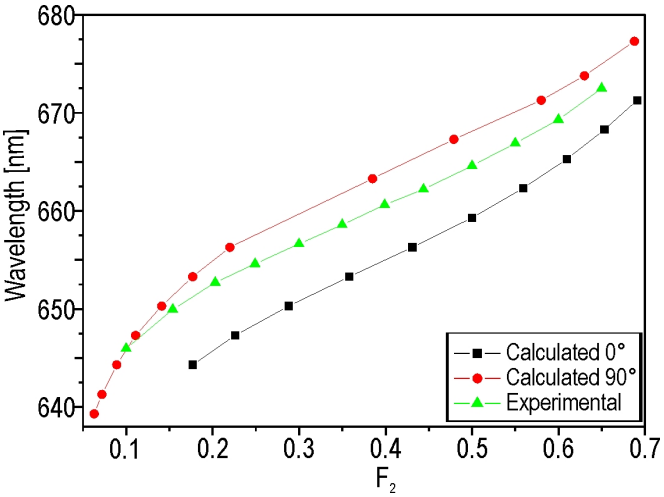

Figure 4.2.7: *Comparison between the theoretically calulated* F_2-λ_{max}*-calibration curves with parallel (black) or vertically polarized (red) light and the actually fitted curve (green) of QD655.*

the respective detector, i.e. long- and short wavelength detectors D1 and D2, both for vertically and horizontally polarized light (denominated D1/2-90° and D1/2-0°, respectively). Thus, for a given maximum emission wavelength (center of the Gaussian curve), the fractional intensity F_2 as overlap with D2 normalized by the overlap-sum with D1 and D2 could be derived. SD was simulated by shifting the maximum emission wavelength with constant FWHM and the resulting calibration curves plotted for the corresponding polarization orientation (red and black graph in Fig. 4.2.7).

The experimental fit (green curve in Fig. 4.2.7) shows very good agreement with the theoretical graphs and is located between them as is expected, since the averaged emission of single NCs should not display a preferred polarization under the employed circularly polarized laser excitation. The slight discrepancy towards low F_2-values might be caused by weak triexciton emission which will be discussed below in more detail. However, since the main attention is centered on spectral fluctuations of NCs with F_2 around 0.5 where the greatest sensitivity is obtained, this seems to be only of minor importance.

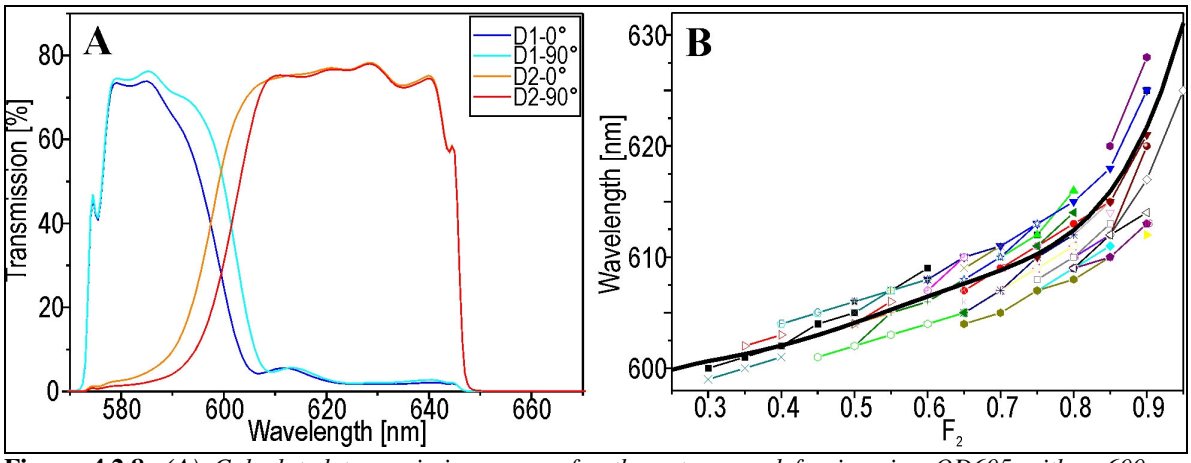

Figure 4.2.8: ***(A)*** *Calculated transmission curves for the set-up used for imaging QD605 with a 600 nm beamsplitter.* ***(B)*** *Corresponding fitted* F_2-λ_{max}*-calibration curve (black line) and the single NC data.*

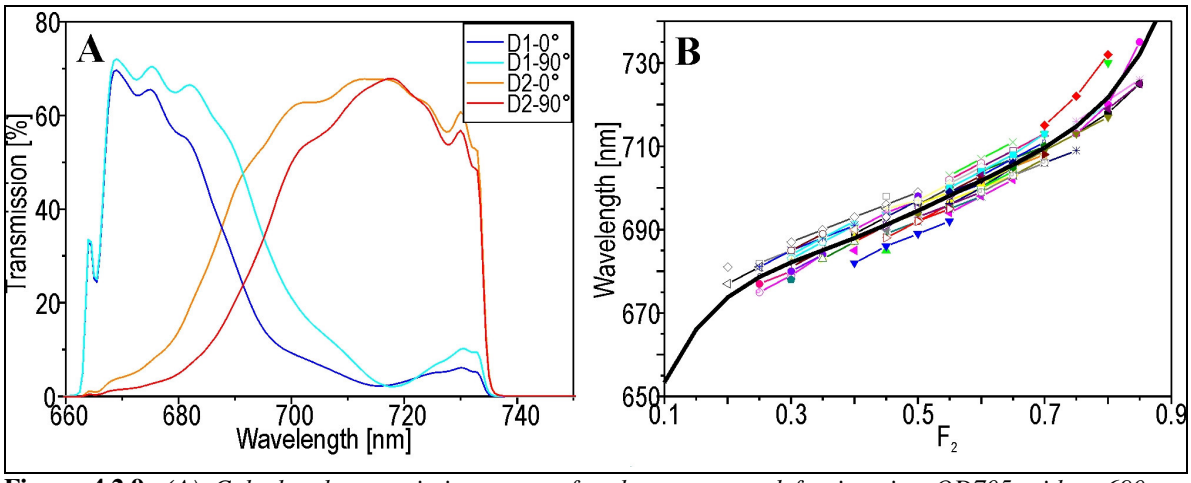

Figure 4.2.9: ***(A)*** *Calculated transmission curves for the set-up used for imaging QD705 with a 690 nm beamsplitter.* ***(B)*** *Corresponding fitted* F_2-λ_{max}*-calibration curve (black line) and the single NC data.*

Similar calibration curves were obtained for the other two NC samples, QD605 and QD705 and their corresponding filter sets using beamsplitters at 600 nm and 690 nm, respectively. (Figs. 4.2.8 and 4.2.9). Altogether, it could be assured that the F_2-value analysis allowed for an accurate determination of PL emission maximum and relative wavelength shifts.

4.2.3 Lifetime approximation using TCSPC with the MLE algorithm

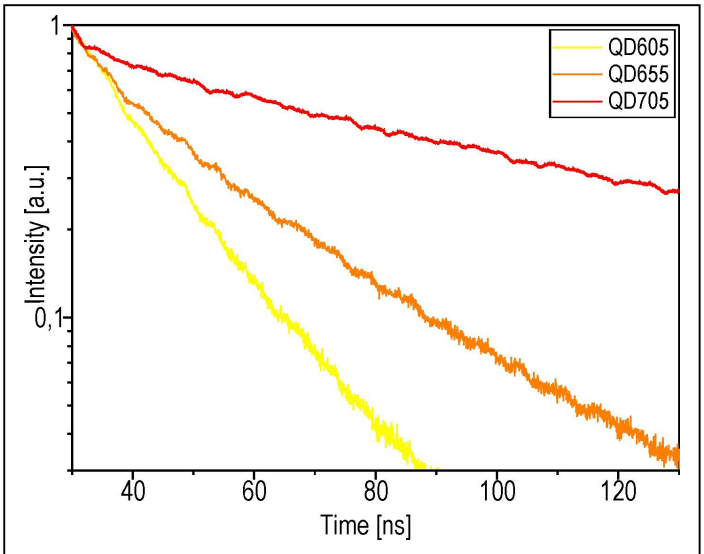

Figure 4.2.10: *Lifetime measured via TCSPC for the three sample solutions imaged on the SFLIM set-up.*

The employed set-up facilitates lifetime resolved PL measurements with the aid of the TCSPC technique, which determines the microscopic arrival time of each detected photon with respect to the following laser pulse. In principal, this method provides measurement of PL lifetimes with a similar accuracy as ensemble methods under the condition of sufficient photon statistics

Normalized PL decay curves obtained from 10^{-9} M solutions of the three NC samples used are displayed in Fig. 4.2.10. The lifetimes of the different samples obviously vary and are not monoexponential. The fact that the decays are multiexponential is most likely due to

sample heterogeneity; however, it has to be considered that also single NCs are known for complicated PL decay characteristics (section 2.3.6), thus the ensemble data is ambiguous about this question. Nevertheless, the mono-exponential fit for QD605 gives a lifetime of about 15 ns while QD655 and QD705 yield 27 ns and 94 ns, respectively, which should be interpreted as mean value from a distribution of the possible lifetimes. Two things are notable about this finding: first, there is apparently a correlation between the PL lifetime and the maximum emission wavelength, since QD605 display the shortest and QD705 show the longest lifetime; second, the lifetime difference is much larger from QD655 to QD705 than from the former to QD605. This implies that not only the emission wavelength but also the NC core material might control the radiative decay.

For accurate fits of the underlying photophysical kinetics, all measured decays would require analysis with a multiexponential approach. However, since one aims to monitor fast lifetime fluctuations with the TCSPC data, elaborate multi-exponential fitting of the decays is prevented by the low photon statistics and the demand of efficient computer processing. Thus, the maximum likelihood estimator (MLE) analysis was employed (section 3.1) for simple lifetime analysis, as it gives reliable results using simple processing of the data [102,103]. The drawback of this approach is that it presumes mono-exponential decay kinetics and will lead to wrong conclusions if multi-exponential decays are analyzed. Therefore the calculated lifetime changes if photons from different time intervals ("TAC range") after the laser pulse are examined. This is especially important for NCs which have been known to show multiexponential kinetics even on the single NC scale.

Previous publications already demonstrated that the multiexponential decay characteristics are not intrinsic to NC PL, but rather the result of external trap states causing fluctuations of the PL quantum yield by changes of the non-radiative rate constant. This means that the non-exponential characteristics of the PL decay converges to mono-exponential behavior when only photons from regimes with similar emission intensities are analyzed. To test these characteristics and justify the use of the MLE for lifetime analysis of NCs, Figs. 4.2.11A/B shows a typical transient of a QD605 under high power excitation and the resulting decay obtained from all detected photons. Both the mono-exponential fit (Fig. 4.2.11B), with a lifetime of 10.1ns (0.96) and the logarithmic scale in Fig. 4.2.11C reveal the expected non-exponential behavior. The MLE shows different lifetimes depending on the limits of the TAC range, so that the resulting lifetime gets longer, when photons within a longer time interval after the laser pulse are examined. Hence, the lifetime apparently increases by about 20% (9.6 ns for the decay range as indicated by the arrows compared to

11.6 ns) when the TAC range is increased from 17 ns to 47 ns after the laser pulse. This can be explained by "time gating" effect, i.e. after a longer time interval short time components will not contribute to the decay any more and long time components dominate the decay for larger TAC ranges.

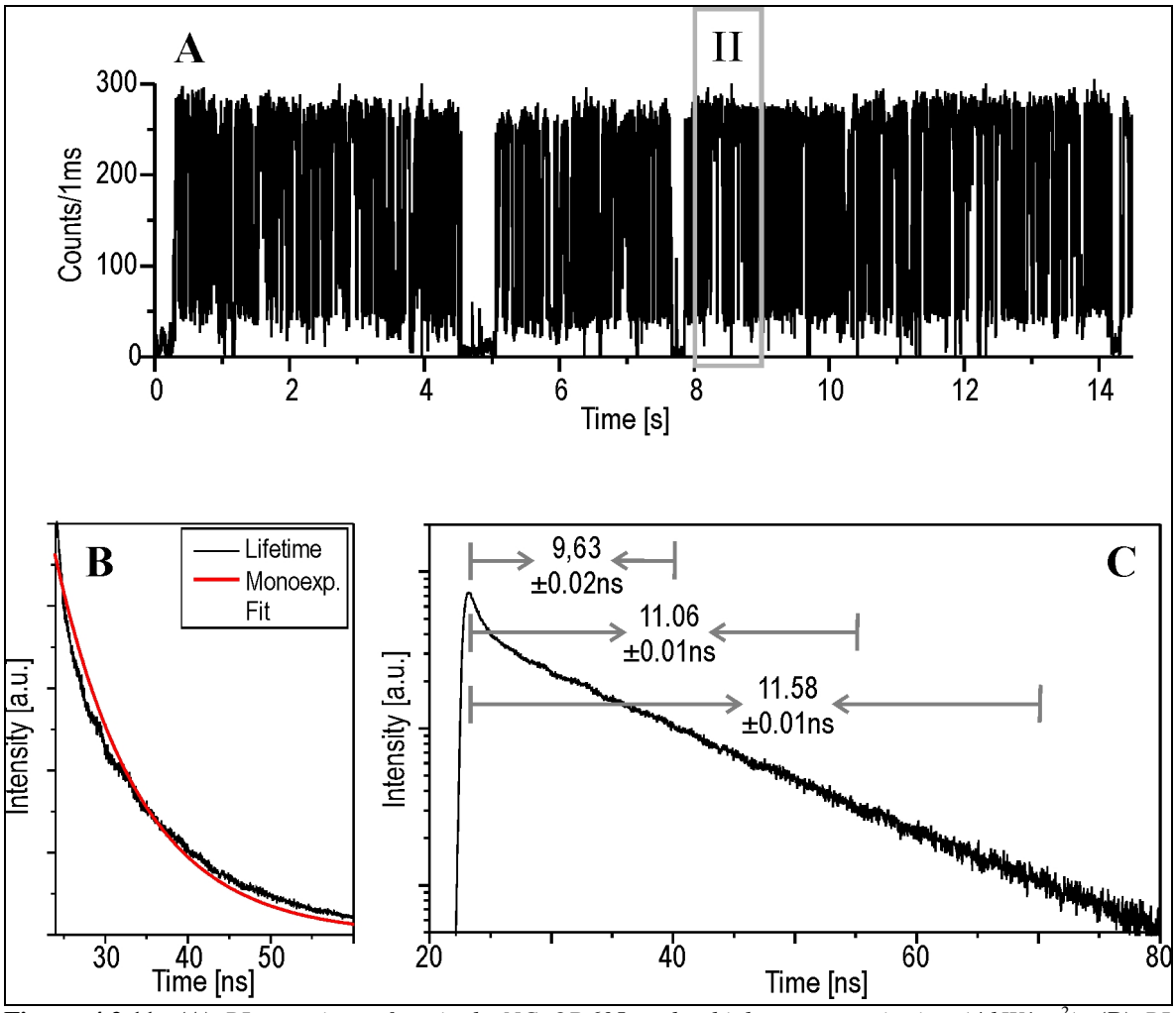

Figure 4.2.11: ***(A)*** *PL transient of a single NC QD605 under high power excitation (4 kW/cm²).* ***(B)*** *PL lifetime for the whole transient in* ***(A)*** *on linear scale (black) and the best monoexponential fit (red).* ***(C)*** *Same decay as in* ***(B)*** *on logarythmic scale with three different TAC window ranges (gray arrows) and the corresponding lifetimes calculated with the MLE.*

In contrast, if one focuses on a small section of the transient (as indicated in Fig. 4.2.12A/B II and III) from 8.245 s to 8.298 s, the count variations are reduced to less than 10 % for the different time ranges. The resulting PL decay can then be well fitted with a mono-exponential model (τ = 12.4 ns), and the discrepancy of the lifetimes obtained for different TAC window ranges are within the experimental statistical error (< 2 %, see Fig. 4.2.12C/D). This strongly supports the assumption that NC decays can be described as a sum of mono-exponential regimes if the intensity fluctuations can be resolved, i.e. for short enough time intervals NCs exhibits mono-exponential PL decays.

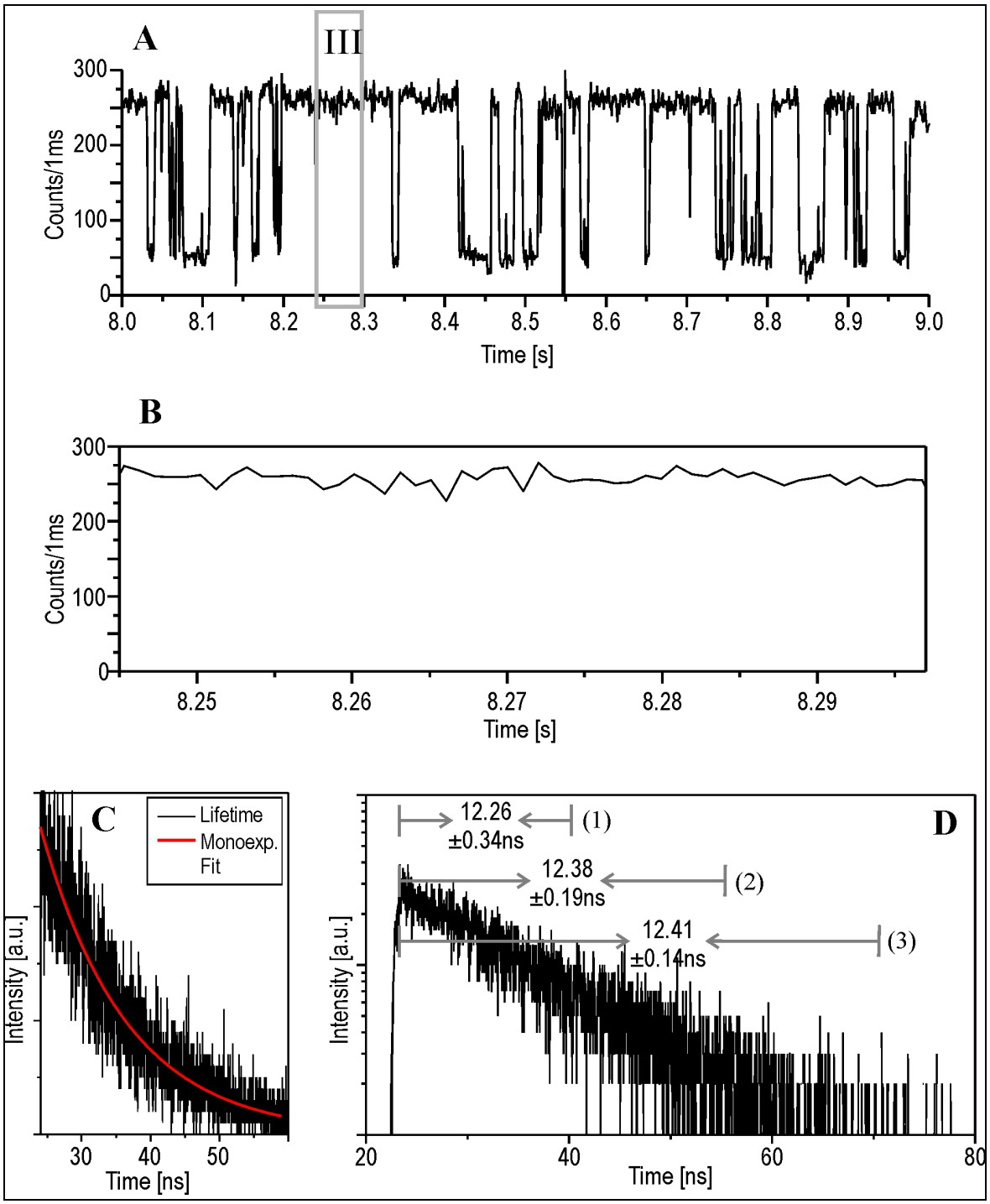

Figure 4.2.12: ***(A)*** *Magnified portion of section II in the transient shown in 4.2.11.* ***(B)*** *Magnified portion of section III in the transient shown in* ***(A)****.* ***(B)*** *PL lifetime of section III on linear scale (black) and the best monoexponential fit (red).* ***(D)*** *Same decay as in* ***(C)*** *on logarythmic scale with three different TAC window ranges (gray arrows) and the corresponding lifetimes calculated with the MLE.*

At this stage several points influencing the lifetime measurement have to be discussed in more detail. It is the aim to achieve a high time resolution with optimal accuracy and to minimize interferences from the background as much as possible. In the analysis the PL transients are divided into constant macro-time intervals ("bins"), for each of which measurable parameters are calculated, i.e. intensity, spectral signature F_2 and PL lifetime.

To obtain a high temporal resolution of the photophysical fluctuations a short binning time is desirable, although it leads to fewer photons per bin, and accordingly a larger statistical error for the calculated observables. Therefore, there is a trade-off between the statistical error (limited by the photon number) and an averaging error (limited by the binning time), if fluctuations are faster than the bin time. Concerning the statistical error, the lifetime determination by the MLE constitutes the limiting factor, because it is calculated from a photon distribution broadly spread over 4096 microchannels, due to the long lifetimes >10 ns. For this reason, lifetime values determined from bins below 100 counts already display a large statistical error, whereas bins with fewer than 50 photons generally are not suited for lifetime analysis, since the error often is larger than the expected lifetime [283].
Furthermore, it as to be considered that not all of the photons within the bin can be used for the MLE calculation. This applies to photons detected near the laser pulse (rise time) of the decay as well as to photons emitted late in the decay. The influence of a too long TAC range can be understood by the following consideration: The maximum likelihood estimator is based on a sum over all microchannels derived from the product of the number of the channel after the TAC start channel multiplied with the counts detected within this channel (see section 3.1). Assumng the theoretical case of an extreme fast decay, where the PL is exclusively detected in the first channel consisting of 4000 photons, it is obvious that one photon in the 4000^{th} channel will result in the doubling of the sum, so that comparatively few photons can have a large influence on the estimated lifetime. As every APD has a certain number of dark counts due to shot noise, i.e. with the same probability of detection for every channel, it is apparent that for short lifetimes calculated with the MLE with a large TAC range, only a few background photons detected in the higher channel might distort the actual result. This effect is aggravated by the fact that short lifetimes are usually observed for quenched states, i.e. with intrinsically low photon counts, which renders the decay even more sensitive to shot-noise.
This is exemplary shown for a section of the transient shown in Fig. 4.2.13 from 1.493 s to 1.530 s (Fig. 4.2.13A), where the intensity drops drastically and the PL lifetime is significantly reduced (“dim state”). Accordingly, the PL decay within this section displays a maximum intensity at 23 ns (temporal position of the laser pulse), while the intensity after 30 ns already faded to nearly the background level. Thus, if a TAC range from 23 ns to 33 ns is chosen, which includes more than 90% of the detected photons (1611 compared to overall 1778 counts) the MLE yields a lifetime of 1.05 ns. In comparison, when the TAC range is extended from 33 ns to 70 ns, the additional 57 photons in the microchannels after

33 ns, i.e. less than 4% more compared to the first TAC range, result in an increase of the calculated PL lifetime to 1.82 ns, i.e. more than 70% increase.

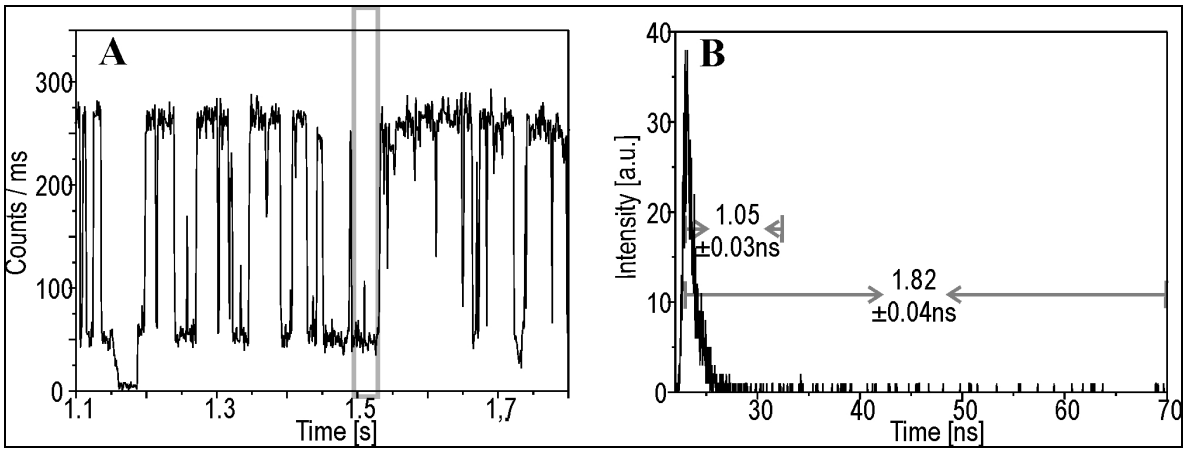

Figure 4.2.13: ***(A)*** *Portion of the transient shown in Fig. 4.2.11A with normal emission, blinking and a "dim" state.* ***(B)*** *Microtime histogram of the framed portion of the "dim" state in A. The short TAC range from 23 to 33 ns, after which the decay obviously is on background level, yields 1.05 ns compared to a result 1.82 ns if the background counts from 33 to 70 ns are included.*

On the other hand, it is also obvious that for long decays, a significant number of photons is lost if the TAC range is too small, thereby leading to an increased error. Generally, the TAC range was adjusted depending on the typical lifetime of the investigated sample, i.e. the TAC range was chosen to at least three times of the typical lifetime, resulting in less than $e^{-3} \approx 5\%$ photon loss (Note that for QD705 this cannot be achieved due to its long lifetimes of about 100 ns). Furthermore, for QD655 biexciton effects had to be considered, i.e. under medium to high excitation power the appearance of a new, short component, not caused by quenched states of the exciton (see section 4.3). To exclude distortion effects to the monoexciton photophysics, the TAC range start was chosen about 4 ns after the laser pulse for QD655, where biexciton effects are negligible [267].Taking these considerations into account, the method facilitates determination of PL lifetime fluctuations with very high temporal resolution. To demonstrate its potential, the lifetime fluctuations monitored by the MLE lifetime are exemplary displayed for the transient A in Fig. 4.2.12. It is obvious that the “dim states”, i.e. drop to a reduced intensity level, (black line) are closely correlated to a drastic decrease in PL lifetime (red squares). However, whereas the intensity is quite constant apart from these “dim states”, the lifetime shows significant fluctuations distinct from the statistical error of about 0.6 ns. Furthermore it shows a homogeneous lifetime distribution around 8.3 s, justified by the good mono-exponential lifetime fit received in this region (Fig. 4.2.12D). Note that this intensity region, where the lifetime remains

reasonably constant for more than 50 ms and which thus displays a mono-exponential decay has been found with the aid of the MLE analysis.

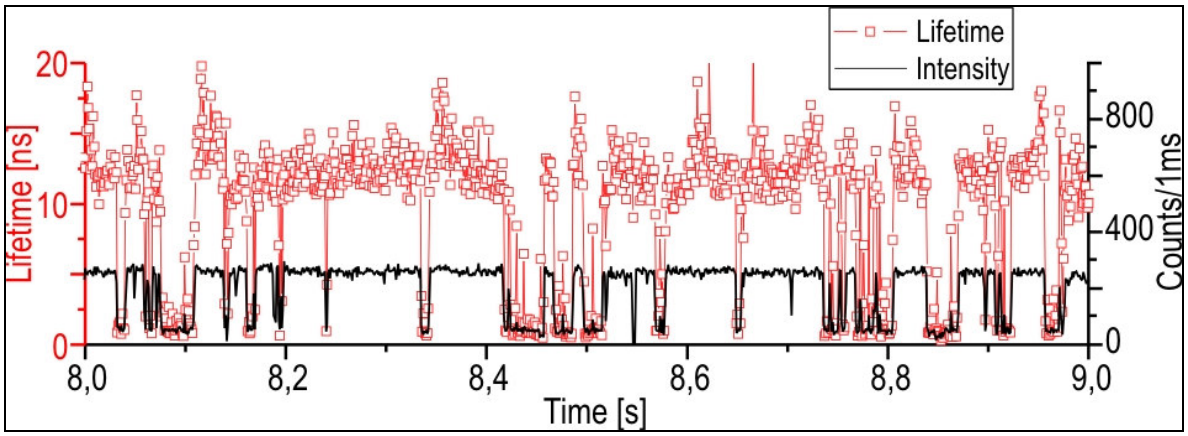

Figure 4.2.14: *Transient of Fig. 4.2.12A (black line) with the lifetime fluctuation as calculated by the MLE shown as red squares. Note the quenched states with strong reduction of both* N_C *and* τ *and the constant region around 8.3 ns.*

4.2.4 Coincidence ratio as single particle indicator

If one aims to investigate photophysics of single photoluminescent particles, one of the crucial aspects is the proof for the existence of only one particle within the detection volume. As has been mentioned in section 4.2.2, a spectral shift might either be caused by spectral diffusion or the presence of two NCs with different emission wavelengths in the detection volume which show intensity fluctuations. Whereas for organic fluorophores often indirect indicators such as the occurrence of bleaching, blinking and spectral jumps are used to assure the detection of fluorescence from a single molecule [284], the complicated photophysical fluctuations observed for NCs do not permit such statements.
Nevertheless, the recently developed methodology allows for the determination of anti-bunching as unequivocal proof of the presence of a single emitter within the focus [59]. As has been discussed in the experimental section, this is done by counting the events (coincidences) where a photon is detected both APDs simultaneously, i.e. for the same laser pulse/macrotime interval (central peak). This can then be compared to the number of the non-correlated coincidences, i.e. those detected for different laser pulses. Quantitative information can be deduced from the ratio of the central to the average lateral peak counts, the coincidence ratio R_C [59]. Theoretically, R_C is given for n independent emitters as $(n-1)/n$. Thus, for one emitter R_C is zero, since one emitter can emit only one photon per laser pulse even when excited into a higher singlet state S_N due to rapid non-radiative

transition into the first excited state S_1. Accordingly N_C is 0.5 for two emitters in the detection focus, which is explained by the fact, that the probability for the two photons to encounter the same APD (which can detected only one photon per macrotime interval) is equal to that they are detected at a different APDs. In Fig. 4.2.15 photon-antibunching is demonstrated for the organic dye Atto647, a red dye excited with the pulsed 635 nm diode and imaged using a non-polarizing 50/50 beamsplitter by two APDs. The transient in A shows a significant drop to about half of the initial intensity at 11.5 s, which is accompanied in the coincidence histogram by a drastic relative decrease of the central peak coincidences compared to the lateral peaks. Thus, the coincidence ratio R_C yields 0.47 for the high intensity regime (3-11.5 s) , but drops to below 0.1 (0.06) after 11.5 s (see Fig. 4.2.15B).

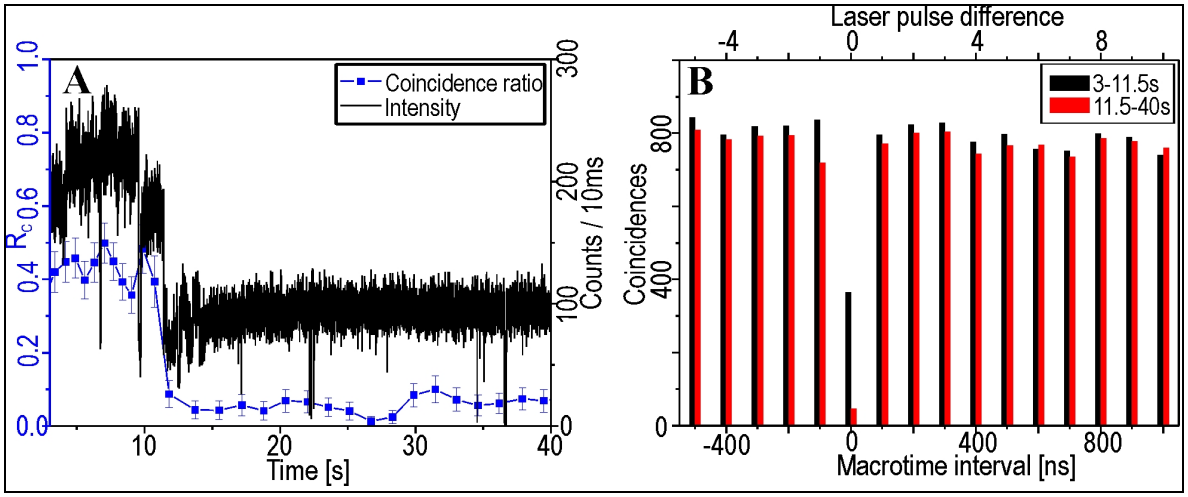

Figure 4.2.15: ***(A)*** *Transient of the dye Atto647, were two molecules were detected nearly equal within the same laser spot. After 11.5 s the intensity drops due to photobleaching of one of the dyes, accompanied by a drop of* R_C *(blue squares).* ***(B)*** *Coindidence histograms for the transient in A before (black) and after the photobleaching event (red columns).*

This decrease can be accounted for by two dyes within the detection volume, one of which was photodestructed after 11.5 s. To better display the correlation of the coincidence ratio, it might be also useful to calculate the coincidence ratio at certain time intervals. However, it has to be considered that the number of coincidences depends on the square of both the excitation intensity and the overall detection efficiency of the set-up, which is typically in the range of a few percent. Therefore, two-photon events are much less frequent than the photons detected even for saturating excitation powers. In contrast to the lifetime and F_2-value, R_C is not calculated for a given time interval but for a constant photon number, which in addition has to be significantly larger than for calculation of the former. As can be deduced from the blue transient in Fig. 4.2.15A which monitors the coincidence ratio for every 100000 photons, the statistical error of R_C is significant, while the time resolution is

on the second time scale, i.e. only 1% of the temporal resolution achieved for the spectral and lifetime information. Nevertheless, the previous assumption about the photodestruction of one dye at 11.5 s is confirmed since the transient shows a parallel course with R_C, which drops from more than 0.4 to less than 0.1. The fact that R_C is slightly different from 0.5 is explained by a weaker emission of one of the dyes; likewise, the residual coincidence after 11.5 s can be ascribed to the background, which increases the apparent coincidence ratio since it is detected independently. These effects and their possible interference with obtained results will be discussed more further in the multiexciton experiments in section 4.3.

Additionally, for the set-up used it has to be considered that a dichroitic beamsplitter is employed instead of a 50/50 beamsplitter. This influences the coincidence measurement in such a manner, that for a single molecule the S/B ratio on one detector is decreased with increasing deviation of the F_2-value from 0.5. Thus, the number of coincidences may be decreased considerably and the influence of the background increases, i.e. it is more difficult to obtain sufficient antibunching information if the F_2 is strongly deviating from 0.5, e.g. (>0.9) or low (<0.1) [59].

4.2.5 Determination of static heterogenity on the SM level

As mentioned above, single molecule spectroscopy enables the disentangling of sample heterogeneity smeared out in the ensemble measurements. For NCs, one has to deal with two kinds of heterogeneities: static, i.e. due to slightly different sizes and shapes of the NCs within one sample, but also dynamic, i.e. caused by photophysical fluctuations of single NCs. For a thorough understanding of NC photophysics, investigation of both factors, and their influence on the photophysical observables is important. The most important observables in the discussed case are the spectral signature F_2 and the PL lifetime τ, whose interrelation was first studied in solution.

Fig. 4.2.16 contains the PL decay curves for the three samples in solution from Fig. 4.2.10, this time shown with spectral resolution by using the corresponding beamsplitter sets. The spectra are normalized, i.e. the relative intensity on each detector given by the average emission wavelength with respect to the splitting wavelength is not displayed. The measured F_2-values for the solutions are 0.8, 0.3 and 0.8 for the samples QD605, QD655 and QD705, respectively. It is obvious that the lifetime is significantly shorter on the short

wavelength detector D1, which means that the NCs with shorter emission wavelengths on average also show shorter lifetimes and vice versa. This confirms the trend observed for the different samples and is expected, since e.g. QD605 and QD655 might even stem from different purification steps of the same batch.

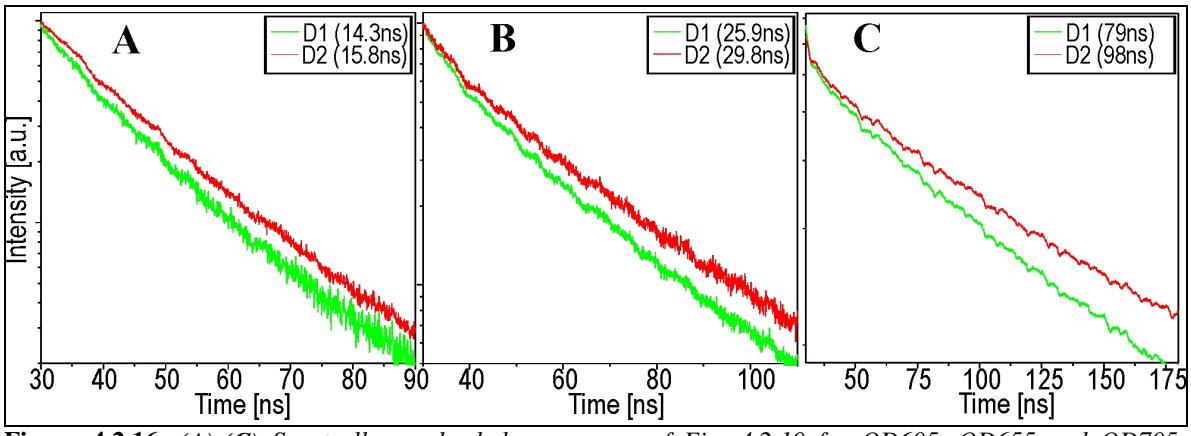

Figure 4.2.16: ***(A)-(C)*** *Spectrally resolved decay curves of Fig. 4.2.10 for QD605, QD655 and QD705, respectively. The PL decay is for all samples significantly shorter on the short wavelength detector D1 (green).*

To study these findings more closely, one has to circumvent the averaging experienced due to particle diffusion, therefore NC samples were immobilized at low concentration (< 1 particle/μm^2) on an APS-coated glass cover slide and imaged in air at RT.

Fig. 4.2.17 shows representative PL intensity images of all three samples excited at 445 nm, with false color encoding of the F_2-value (upper) as well as lifetime encoded representation for comparison (lower pannels). The patched spots indicate blinking, i.e. intermittent dark states. Since the scanning is done horizontally from top to bottom, adjacent pixels to the left and right show a temporal difference of only 3 ms while a difference of one line up or down amounts to 600 ms. Hence, in the image of QD705 many "spots" are made up of only a few horizontal lines, indicating a very strong blinking for these NCs, while QD655 spots show only modest and QD605 negligible PL intermittences.

The F_2 encoding in Fig. 4.2.17, shows that most of the NCs emitted stronger either on the long wavelength (predominantly red color for QD605 and QD705) or on the short wavelength detector (green spots for QD655), respectively, reflecting the average F_2-value measured in solution. In contrast, the lifetime encoding demonstrates broad dispersion of PL lifetimes for the respective samples, with fairly narrow ranges for QD605 (typically 5 ns < τ < 25 ns) and QD655 (15 ns < τ < 50 ns) whereas the distribution is much broader for QD705 with a range from less than 50 ns to more than 200 ns for a single NC.

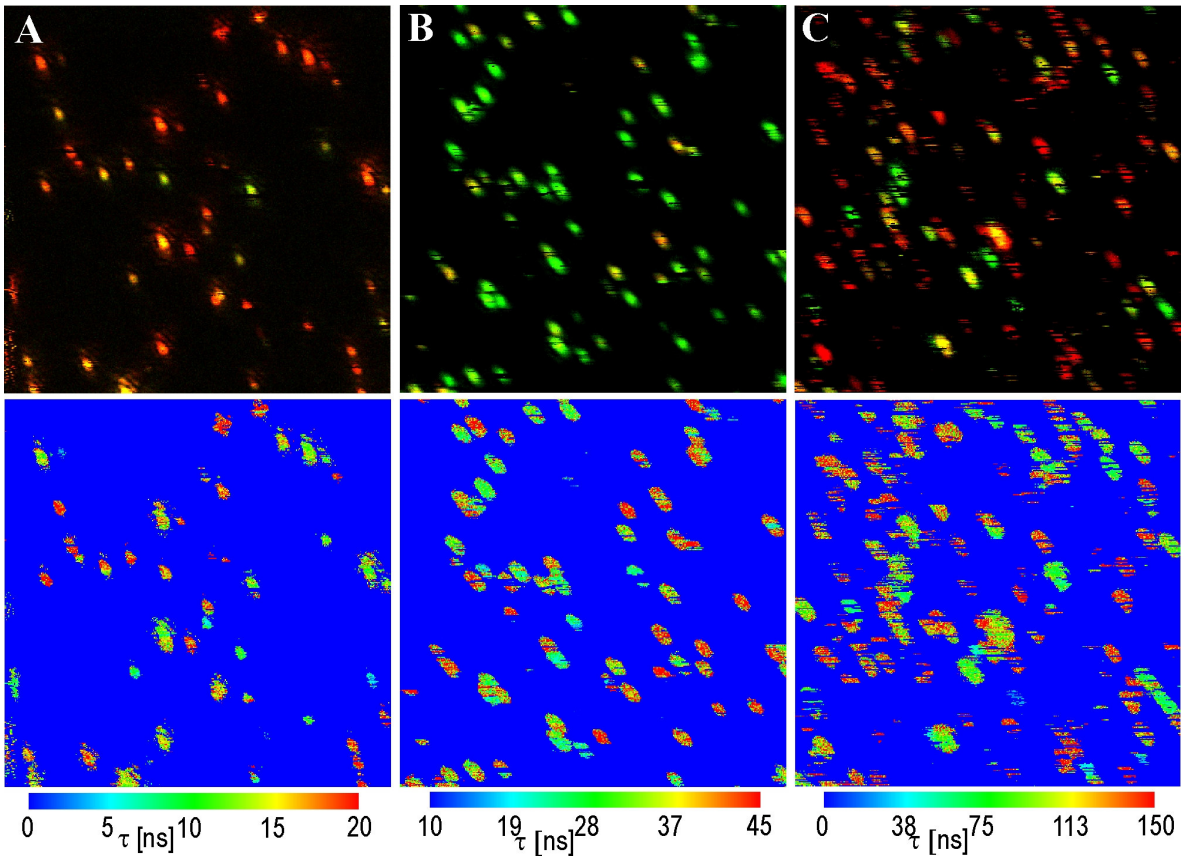

Figure 4.2.17: ***(A)-(C)*** *False color intensity image (upper pannels) of single NCs of type QD605, QD655 and QD705 respectively, excited at 445 nm with about 0.5 kW/cm^2. The scan area is in all cases 20x20 µm with a pixel resolution of 50 nm. The green and red color stands for counts on detector D1 and D2, respectively. The lower pannels display the same images with lifetime encoding. The spectral and lifetime heterogenity is obvious.*

As the measurements made in solution suggested a correlation between lifetime and emission wavelength, i.e. a red shift of the emission leads to a longer lifetime, it is interesting to compare this with the results on dry surfaces. Since it is difficult to discern the correlation from the color-encoded images which do not allow a straightforward conclusion, the photons from the visible spots were summed and both F_2-value and PL lifetime determined. The obtained lifetimes for several scan images of all three samples were than plotted versus the respective F_2-values yielding scatter plots for each of the samples which are shown in Fig. 4.2.18.

Quite different from what is observed in solution, the populations are very broad and only for QD655 and QD705 a weak correlation between emission wavelength and PL lifetime is observed. The measurements in solution (Fig. 4.2.16) show a clear indication that NCs with red-shifted emission display a longer lifetime, since the lifetime τ_2 on the long wavelength detector should be dominated by red-shifted NCs. To obtain a quantitative comparison between the data measured in solution and on dry surface, the average lifetimes on each of the detectors was calculated. If we assume that the contribution of each NC to the lifetime

τ_2 on the long wavelength detector D2 is given by its relative intensity on a detector, $\tau_2 = \sum_{i=1}^{N} \frac{(\tau_{2i} * I_{D2i})}{(I_{D2})}$ is derived, where I_{D2} is the average photon number detected per NC on D2, N the total number of investigated NCs, values indexed with i denote the partial contribution from each NC. The average lifetime τ_1 on D1 is derived analogously with $F_1 = 1 - F_2$. The calculated lifetimes τ_1/τ_2 were obtained as 13.4/15.1 ns (compared to 14.3/15.7 ns measured in solution, Fig. 4.2.16) for QD605, 33.8/39.8 ns (vs 25.9/29.8 ns) for QD655 and 99/119 ns (vs 79/98 ns) for QD705.

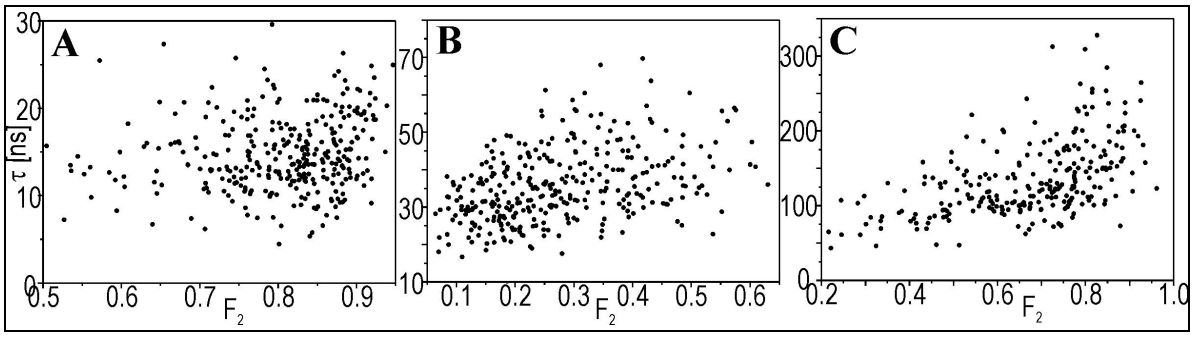

Figure 4.2.18: *(A)-(C) Distribution of the lifetime* τ *versus the* F_2*-value for single NCs of type QD605, QD655 and QD705, respectively, immobilized on a dry surface.*

From these findings two things can be concluded: the difference of the lifetimes for the two detectors is smaller on the surface which has already been concluded from the scatter-plots. Moreover, for QD655 and QD705 the lifetimes are significantly longer on the surface than measured in solution (about 30% for QD655 and 25% for QD705). For the explanation of the latter effect it has to be considered that the measured lifetime does not stem from an NC imaged in vacuum, but near a dielectric interface. However, it is well known that any dielectric interface will increase the radiative rate proportional to its refraction index dipole if the oscillating dipole is not orientated vertically with respect to the imaging surface [285,286]. In the case of a dry surface it is difficult to calculate the effect of the two dielectric media (glass with n ~ 1.55 and air with n ~ 1) and its effect compared to a homogeneous water layer (n = 1.33) is obviously weaker, so that in the latter medium the lifetime is shortened by an effective increase of the radiative rate. The broadening of the distribution on the surface which conceals the correlation of a longer emission wavelength with a longer PL lifetime τ can be explained by two factors: since the strength of the effect of the dielectric layer on the radiative rate depends on the dipole orientation, and the NCs should display all possible orientations on the surface, this leads to a broader lifetime distribution even for NCs with similar emission wavelength. Moreover, it has already been

found (section 4.2.2) that a different orientation of the dipole and thus different polarization of the PL light also results in a dispersion of the observed F_2-value for identical emission wavelengths. Whereas these broadened distributions might complicate the study of the static heterogeneity, it should have no influence on our investigations since we aim to investigate relative changes of the observables from single NCs.

4.2.6 General emission regimes of NCs investigated on the SM level

The ultimate goal of the experiments is the understanding of photophysical fluctuations measured from single NCs. Of special interest in this context are fluctuations of the F_2-value and the PL lifetime since these values determine the characteristics of the chromophore with respect to their use as high precision colocalization nanoprobes. The prerequisite for proper data analysis is the presence of a single NC within the detection volume as proven by R_C (section 4.3). This is examined more carefully for an exemplary case, displayed in Fig. 4.2.19.

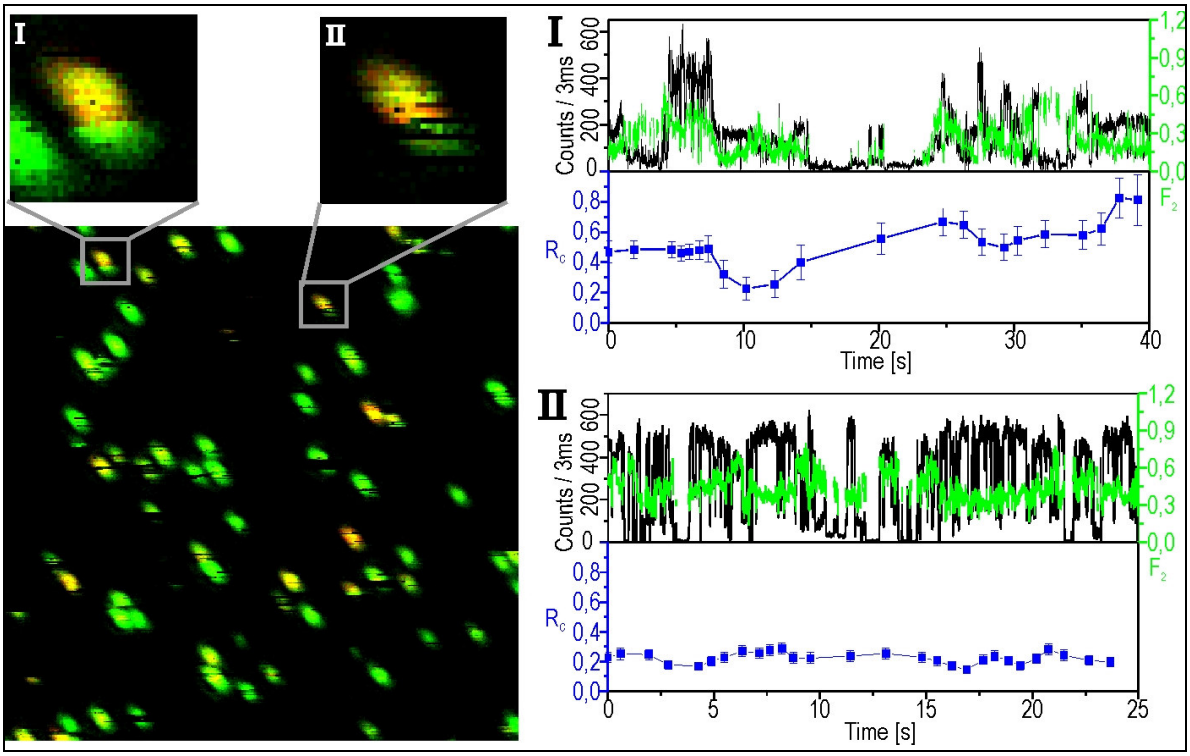

Figure 4.2.19: *Scan image of NCs of type QD655 immobilized on a dry surface (compare with Fig. 4.2.17). The enlarged spots above both show significant fluctuations of the* F_2*-value, visible by color changes within the spots. By analysis of the corresponding transients (right) which depicts intensity (black) and* F_2*-value (green line), as well as the coincidence ratio (blue squares), it can be demonstrated that in case I two NCs are within the focus, whereas II constitutes a single NC.*

The image shows a scan image of surface immobilized QD655 (compare with Fig. 4.2.18B) with the intensities on detectors D1 and D2 encoded in green and red, respectively. Two spots in the upper area, denoted **I** and **II** are of interest since they exhibit significant spectral jumps, i.e. the color changes from line to line. Hence, both these spots indicate strong spectral diffusion which is confirmed by the F_2-fluctuations of the corresponding transients (green line in Fig. 4.2.19) recorded after placing the spots in the laser focus. The calculated coincidence ratio R_C of spot **I** demonstrates that the F_2 fluctuations are not due to SD, but that two NCs of different F_2-value have overlapping PSFs, since R_C fluctuates from 0.2 – 0.8, significantly higher than expected for a single NC. The fluctuations are readily explained by non-correlated blinking and quenched emission from both NCs, i.e. there are periods when only one NC shows significant PL ($R_C < 0.5$). On the other hand, the coincidence transient proofs that the F_2-fluctuations measured from NC **II** are indeed caused by SD of a single NC, since R_C is significantly lower than 0.5.
Here, it should be noted that the latter monitors a constant ration around 0.2, i.e. much higher than expected for a single photon emitter even considering the S/B correction (< 0.1 correction fraction, section 4.3). Similar ratios were found for all QD655 investigated, whereas R_C received from QD705 and QD605 are always < 0.1 after background correction. These characteristics could be ascribed to an unusually high quantum efficiency of biexciton emission and are discussed in detail in a separate section 4.3, since they do not interfere with the intended investigations of SD. In principle, a slightly increased R_C might also be explained from comparatively weak emission of a second NC nearby. However, with the employed set-up one can unequivocally exclude any interference other than background which is too low to explain these features. That is because a nearby NC would show fluctuations of PL intensity uncorrelated to the emission of NC **II** which should result in a fluctuating coincidence ratio, similar to the characteristics observed for NC **I**.

The aim of following investigations is to unravel new interrelations between the photophysical observables, i.e. for the discussed set-up, the PL intensity, the maximum emission wavelength and the PL lifetime, whereas antibunching characteristics are only of minor importance at this point. Therefore the known facts from literature are shortly summed up:
NCs show strong luminescence with frequent near binary interruptions, i.e. sudden drop of PL intensity to or near background level (“blinking”) (section 2.3.4). Furthermore, there might be many levels of emission intensity, decreasing PL accompanied by a shortening of

the PL lifetimes due to increasing non-radiative rate constant (quenched states or "quenching") (section 2.3.6). Finally, the maximum emission wavelength might fluctuate with irregular connection to blinking states (section 2.3.5). This information in mind it is possible to examine the obtained PL transients; for comparison five different NCs for each sample, i.e QD605, QD655 and QD705 are shown:

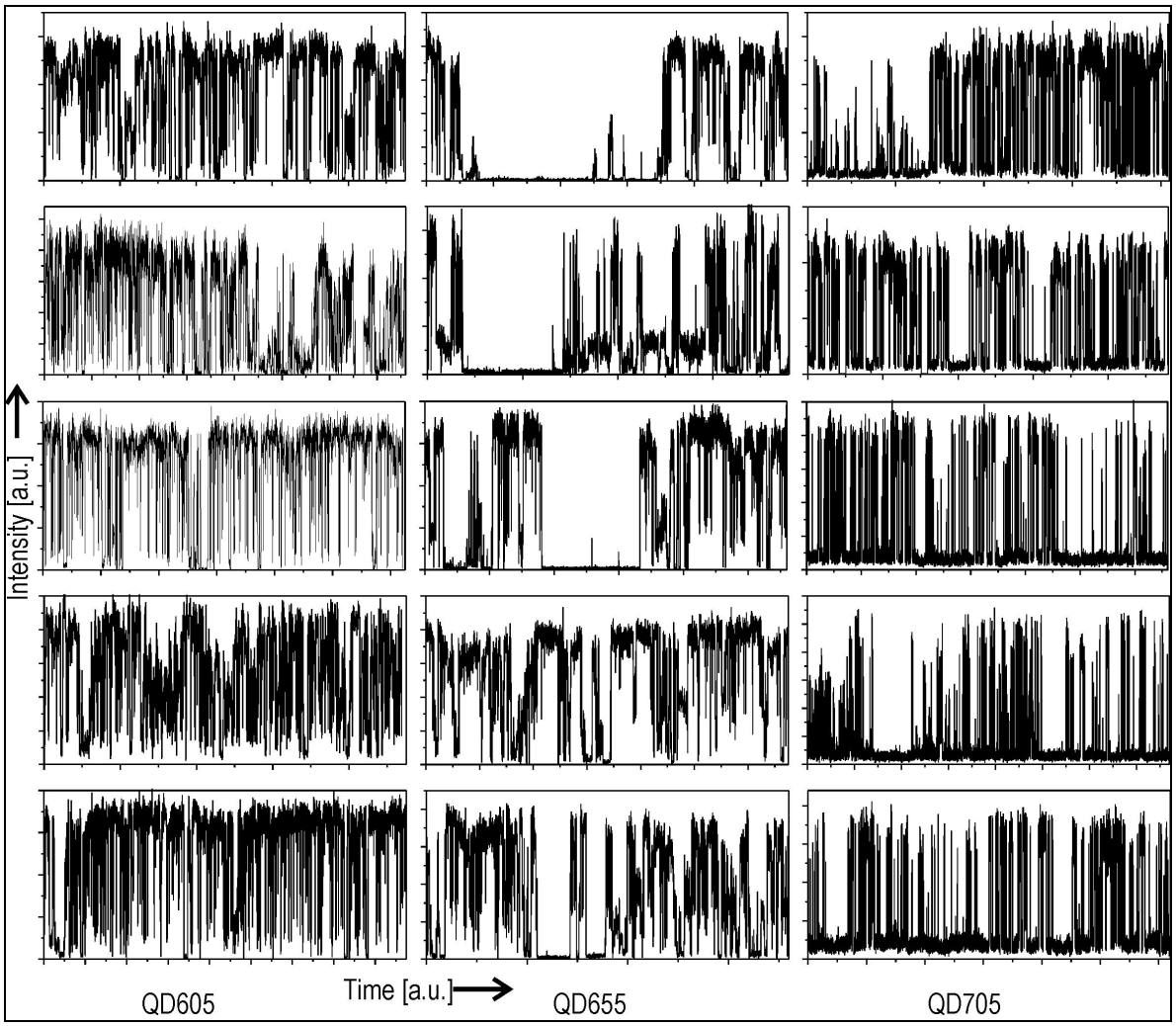

Figure 4.2.20: *Five exemplary intensity transient for each of the investigated samples (QD605 left, QD655 middle and QD705 right). NCs were excited at medium to high power (≈ 0.5-1 kW/cm^2) and transients recorded for 50-100 s with 10 ms binning. Maximum emission rates are all around 30-50 kHz.*

The mentioned regimes are easily recognized, most notably the blinking; since it consists of states with no or negligible PL. Blinking, however, is only of minor importance for the presented investigations. Since it is detrimental for the counts detectable within a certain time range, it is important to note that the extent of blinking, i.e. the average frequency of blinking events, depends on the excitation intensity (Fig. 4.2.21).

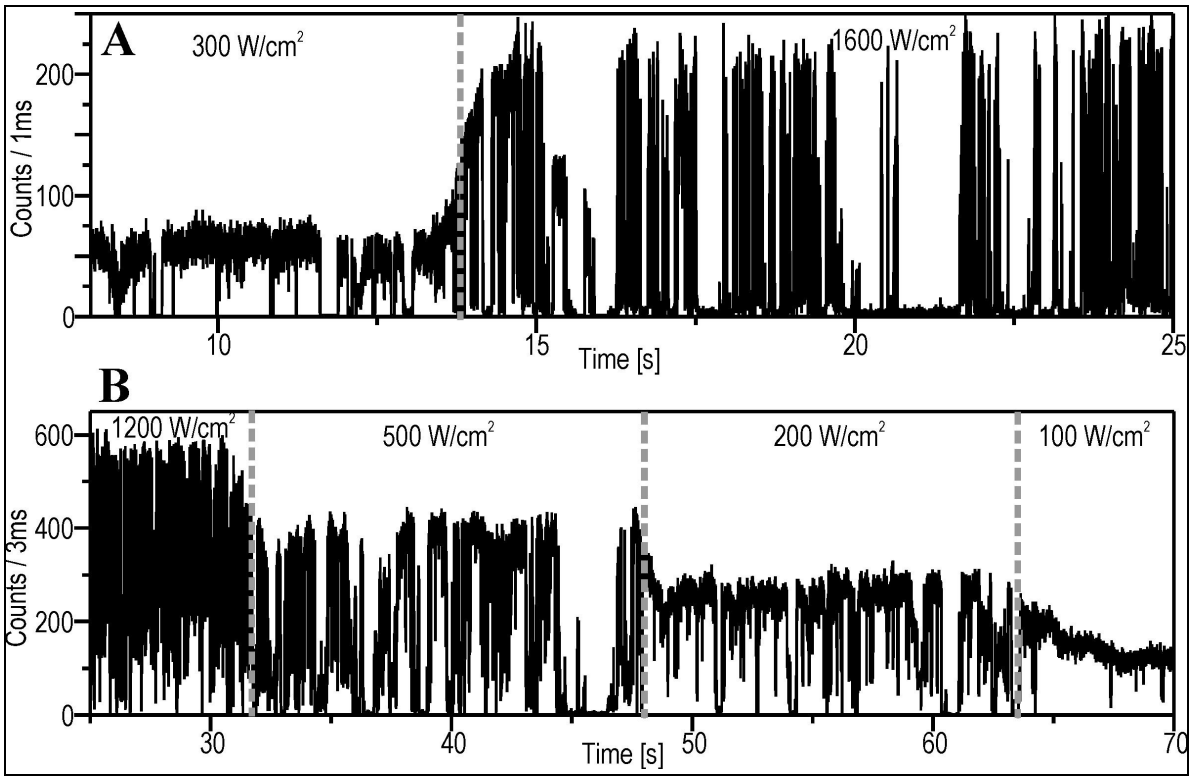

Figure 4.2.21: *Blinking-dependence on the used excitation intensity, exemplary demonstrated for a single NC of QD605* ***(A)*** *and QD655* ***(B)****. The dashed lines separate the regimes with different excitation intensities.*

The strong increase in blinking efficiency with increasing laser power is very pronounced with NCs exhibiting almost continuous emission for low power to few very short emitting periods at high excitation intensity. This feature can be rationalized by the consideration that blinking is caused by a charged NC, which in turn evolves by electron loss from an exciton, i.e. an excited NC (section 2.3.4). Furthermore, multiphotonic processes also greatly enhance the probability of electron loss and thus of blinking events. However, in the measurements it is only of concern in cases of very rapid blinking, as observed especially for QD705. In these cases where the time between two blinking events is shorter than the binning, the PL seems to be reduced as is expected for quenching, but the lifetime is not reduced. Cases of "true" quenching (i.e. count rate reduction above the background intensity) events can also though rarely be seen in the transients.

Nevertheless, it is interesting to note that all NCs show a very homogeneous and well-defined level of or near maximum intensity which indicates that this level is defined by intrinsic properties of the NC. It has been suggested before that NCs exhibit quantum yields close to unity when not subject to external quenching states, i.e. the "intrinsic" non-radiative rate can be neglected compared to the radiative rate (section 2.3.6). Obviously, these states of maximum level might be associated with emission not influenced by external interference from trap states and thus will be denoted „on"-state. If the slight fluctuations

observed for the „on“-state emission are due to weak “quenching” or by other means will be subject of the following investigations.

4.2.7 Investigation of spectral- and lifetime fluctuations on the SM-level

For the observation of photophysical fluctuations, NCs with obvious spectral diffusion as displayed in Fig. 4.2.19 are of major interest. This particular NC has also the advantage that SD occur near an F_2 of 0.5, where the maximum sensitivity of the used set-up is achieved. Fig. 4.2.22A shows the transient of the NC with the course of the intensity (black line), spectral (green line) and lifetime (red line) parameters over time.

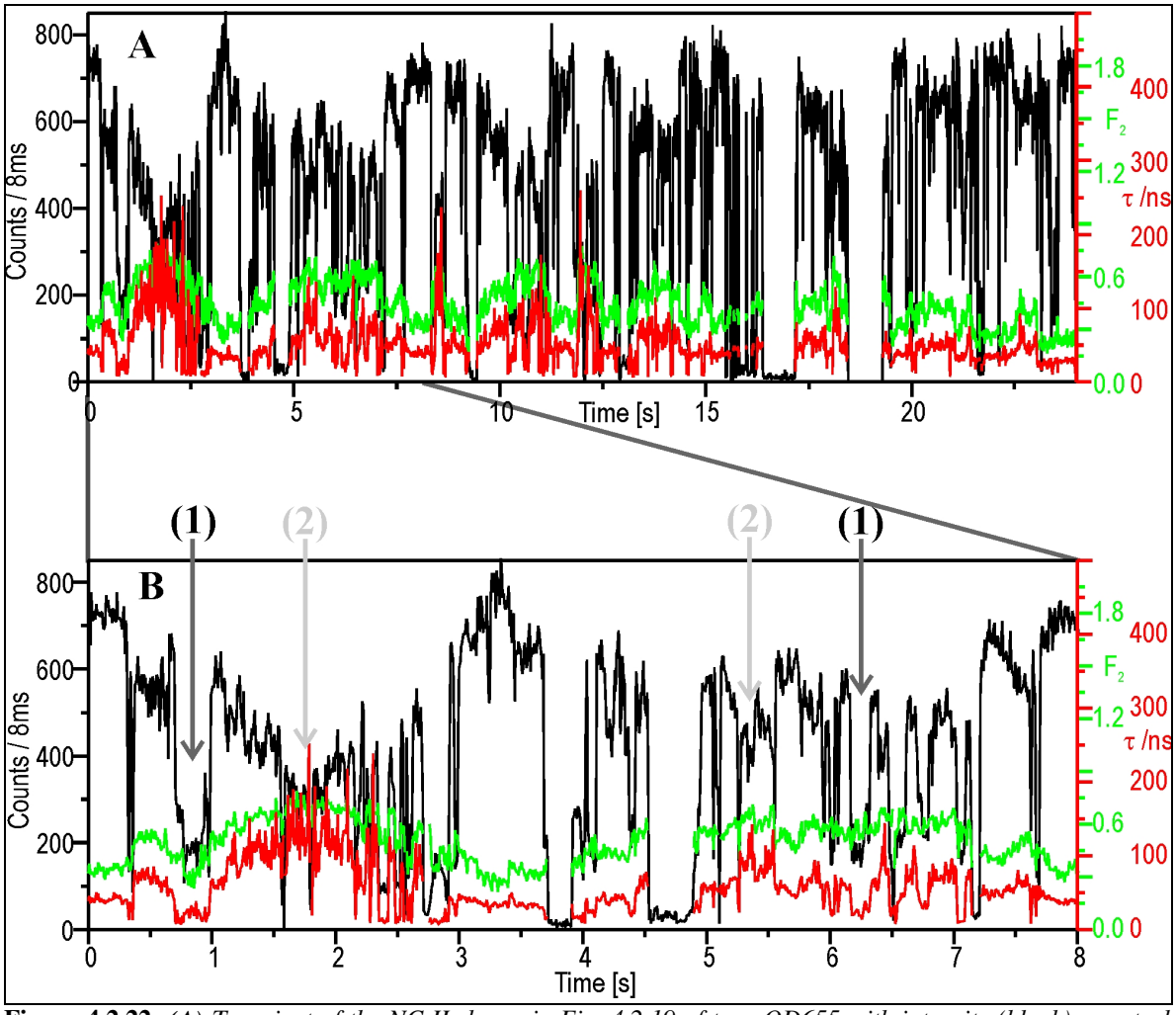

Figure 4.2.22: ***(A)*** *Transient of the NC II shown in Fig. 4.2.19 of type QD655 with intensity (black), spectral (green) and lifetime (red line) information.* ***(B)*** *Portion of the transient in A from 0-8 s where the discussed correlation of* F_2 *with lifetime and anticorrelation with* N_C *are obvious. Note the emission states denoted* ***(2)*** *where low intensity is accompanied by high lifetime and* F_2*-value in contrast to quenched states* ***(1)****, characterized by decreased intensity with shortened lifetime.*

Closer inspection of the SD reveals especially for the expanded part of the transient (0-8 s, Fig. 4.2.22B) that the F_2-value shows in most cases a striking correlation with the PL lifetime, i.e. an increasing F_2-value is accompanied with a longer lifetime and vice versa. Apart from this correlation, the lifetime is also affected by quenching events visble as gaps with reduced intensity (marked in a few cases with arrows, denoted **(1)**, e.g. at 0.8 s and 6.3 s). These quenching events are easily recognized by correlation of a decreased intensity with a shortening of the lifetime. The fact that a correlation between the F_2-value and the lifetime is observed, and that the former is not influenced by the quenching, means that the lifetime is not strongly influenced by any non-radiative rates. Since the emission where the F_2-τ correlation is observed is near its maximum intensity it can be assumed that the NC emits from its „on"-state, which was defined above. Nevertheless, there is apparently a significant fluctuation of the PL intensity for the correlated states, but contrary to what is observed for "quenching", it seems to be anti-correlated to both the F_2-value and the lifetime fluctuations. Hence, at about 0.1 s, 3.4 s and 7.9 s the intensity is at its maximum while both F_2-value and lifetime are comparatively low. For comparison, the gray arrows indicate regimes (denoted **(2)**, about 1.7 s and 5.4 s) where the intensity has dropped to or below half of its maximum level whereas both F_2-value and the PL lifetime increase. This is exactly the opposite behavior as observed in the "quenching" states (black arrows **(1)**).

Due to the superposition of different states it is necessary to develop a different analysis of the observed fluctuations and correlations. One has to consider that the objective of the investigation is not the time course of the observed fluctuations, and the macroscopic time is of minor importance. However, each time bin monitors the NC "frozen" in a particular state which is characterized by its associated observables. Thus, scatter plots were constructed where each data point represents a bin of the time transient, and the three observables were plotted versus each other.

Accordingly, the τ-F_2-plots for the high density distribution (framed gray in Fig. 4.2.23A) demonstrate that a spectral red shift is indeed accompanied by a longer lifetime. The scattered spots below this distribution can be attributed to the quenched states, which show reduced lifetimes. To demonstrate that the strong lifetime fluctuations driven by the SD are no artifact caused by the MLE algorithm, exemplary two decay curves from both detectors, summed over many bins for regions with strong spectral shifts, i.e. 1.3-2.1 s with a strong red shift ($F_2 > 0.65$) and 22.5-22.9 s (high blue shift, $F_2 < 0.3$) are displayed. The decays from 5 ns after the pulse have drastically different lifetimes and can be fitted with mono-exponentials yielding 28 ns and 115 ns, thus a red shift from an F_2 of 0.25 to 0.67 (average

over decays) results in quadrupling of the lifetime. The short component in the red curve is probably due to a combination of biexciton and quenching effects, but not caused by fluctuations within the „on“-state.

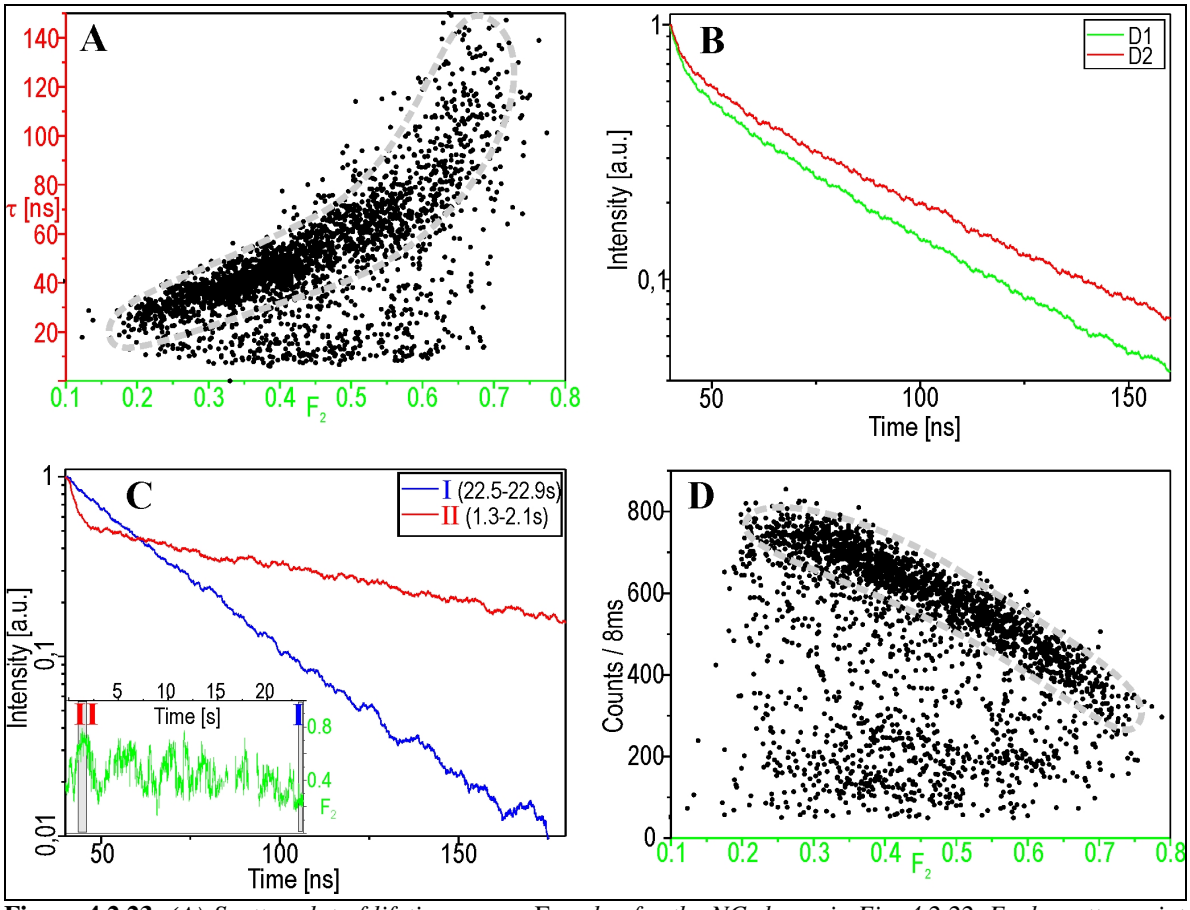

Figure 4.2.23: ***(A)*** *Scatter plot of lifetime versus* F_2*-value for the NC shown in Fig. 4.2.22. Each scatter point represents a bin of the transient. The maximum density population framed gray shows strongly correlated characteristics.* ***(B)*** *Average lifetime of the same transient measured on D1 and D2.* ***(C)*** *Lifetime measured from two different regions of the transient with either a comparatively low (I) or high (II)* F_2*-value, which shows a significantly longer lifetime for the higher* F_2*-value. In the inset depicting the* F_2*-transient, the two regions are indicated by gray areas.* ***(D)*** *The main density ("on"-state) population framed in gray reveals an anticorrelation of the intensity with the* F_2*-value in the plot of* N_C *versus* F_2*.*

These results are in excellent agreement with the average values of the τ-transient derived from the MLE which gives values of 28.5 ns and 118 ns for the same areas, respectively. Likewise, the same effect can be demonstrated for the whole transient by comparison of the decays on detectors D1 and D2. Similar to results obtained from ensemble experiments (Fig. 4.2.16), the decay on the short wavelength detector D1 is considerably shorter than on D2. In contrast to the ensemble measurements the longer lifetime does not stem from particles with a longer emission wavelength, but from red-shifted emission states of one single NC.

Similar to the τ-F_2-plots the framed high density population in the plot of the intensity N_C versus the F_2-value shows a significant interrelation between the observables, this time an anti-correlation, i.e. states with a high F_2-value have a lower intensity. The framed population monitors a well-defined distribution and marks the maximum count rate obtainable for a given F_2-value. This is a good indication that the high density population consists of the „on"-state which is apparently subject to fluctuations independent of quenching states. Fluctuations due to quenched states are seen as scattered spots below this population, consistent with what is observed for the τ-F_2-plots.

Before a thorough understanding of the interrelations can be obtained, one has to crosscheck if these findings are observed for a few NCs, for a special subpopulation or if they even constitute a universal feature of NC photophysics. In this respect it has to be considered that the shown correlations can only be observed for a certain amount of F_2-fluctuations, which makes it best suited for NCs emitting around an $F_2 \approx 0.5$, but not ideal in the present case, where many NCs exhibit a value considerably higher (as observed for QD605 and QD705) or lower (QD655) than this value.

Therefore, it is advisable to use the plot of the lifetime τ versus the detected PL intensity N_C as general correlation analysis of NC states. The resulting scatter plot for the NC in Fig. 4.2.24A shows a somewhat different distribution than observed for the F_2-plots. Whereas there is still the obvious anti-correlation between decreasing lifetime and increasing count rate for the on-state, the scattered "quenched" population is not distributed below the „on"-state but rather shifted versus the origin. Furthermore, there seems to be a higher density regime at lower count rates (marked by a dashed ellipse). Two further issues have to be considered: of interest for an analysis of the scatter plots is both a high time resolution as well as significant spot statistics. The former is especially important if one takes averaging effects into account as discussed for very rapid blinking, i.e. two or more different states (SD, quenching, blinking) overlap within one bin, and averaged values of the observables are obtained which might lead to wrong conclusions. Hence, the aim was to use the lowest binning before construction of the scatter plots possible, which is limited by the statistical error of the MLE. Since this is significant for $N_C < 50$ counts, the bin width was chosen so that typically a few hundred counts were obtained in the highest intensity bins (The binning chosen in the transient in Fig. 4.2.22 is larger to reduce the statistical error for a better visualisation of the observed correlations). As the spectral information provided by the F_2-value as third parameter is still valuable, it is represented in the τ-N_C-plots as color encoding with the color changing from blue to red for increasing F_2.

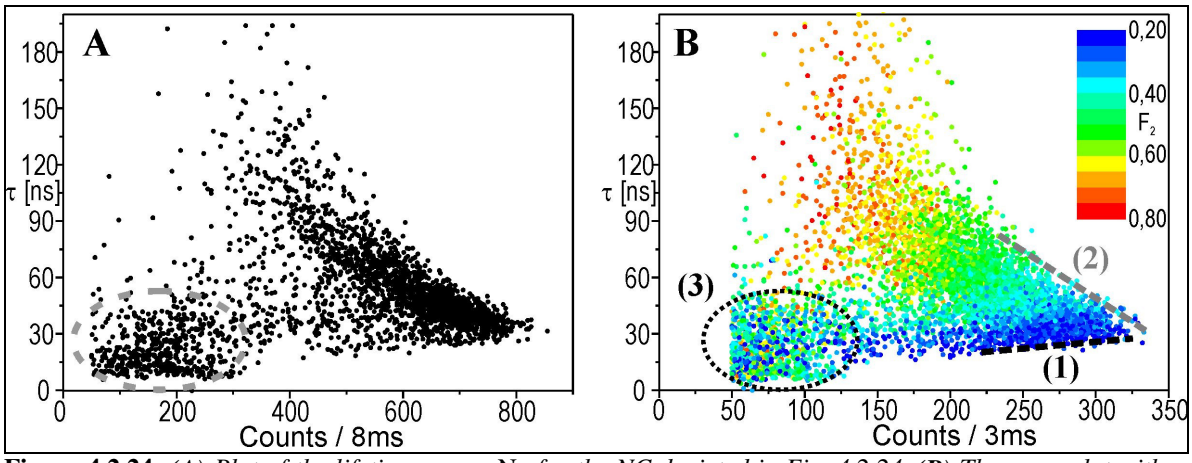

Figure 4.2.24: ***(A)*** *Plot of the lifetime versus* N_C *for the NC depicted in Fig. 4.2.24.* ***(B)*** *The same plot with a higher binning (3 ms versus 8 ms in* ***A****), resulting in a better statistics. Both plots show a "wedge"-like feature with a lower (1, black line) and upper bound (2, gray line). The observed correlation of the lifetime with the* F_2*-value can be observed from the fact, that the blue color (low* F_2*) are predominantly found in the lower "wedge"-part where a higher maximum* N_C *is found. Note also the second population for quenched states which is indicated by the dashed ellipse.*

The resulting plot in Fig. 4.2.24B with a reduced binning time of 3 ms displays similar features as shown in 4.2.24A, however, it presents more distinctly a “wedge”-like appearance with a clearly defined lower (dashed black line denoted **(1)**) and upper bound (dashed gray line **(2)**) of near linear shape. By comparison with the plot for the binning of 8 ms and from the fact, that for each lifetime it gives the population with the highest count rate, it can be concluded that the upper bound stems from the „on“-state population. In contrast, the lower bound made up by states with reduced intensity and lifetime, should be associated with quenching, as is discussed below. Hence, the above mentioned subpopulation is apparently a specific state of quenching and is denoted **(3)** (dashed ellipse). The correlation of the lifetime with the SD is distinct as a change of color from blue to red when moving upwards (= increasing lifetime) along the upper bound (“on”-state).

After it has been clarified how to distinguish between the newly discovered photophysical correlations from the “wedge”-plot, it has to be investigated whether these characteristics are also observed for other NCs and the other samples. Fig. 4.2.25A-D show four exemplary τ-N_C-plots for each of the investigated samples, QD605, QD655 and QD705, imaged under dry conditions.

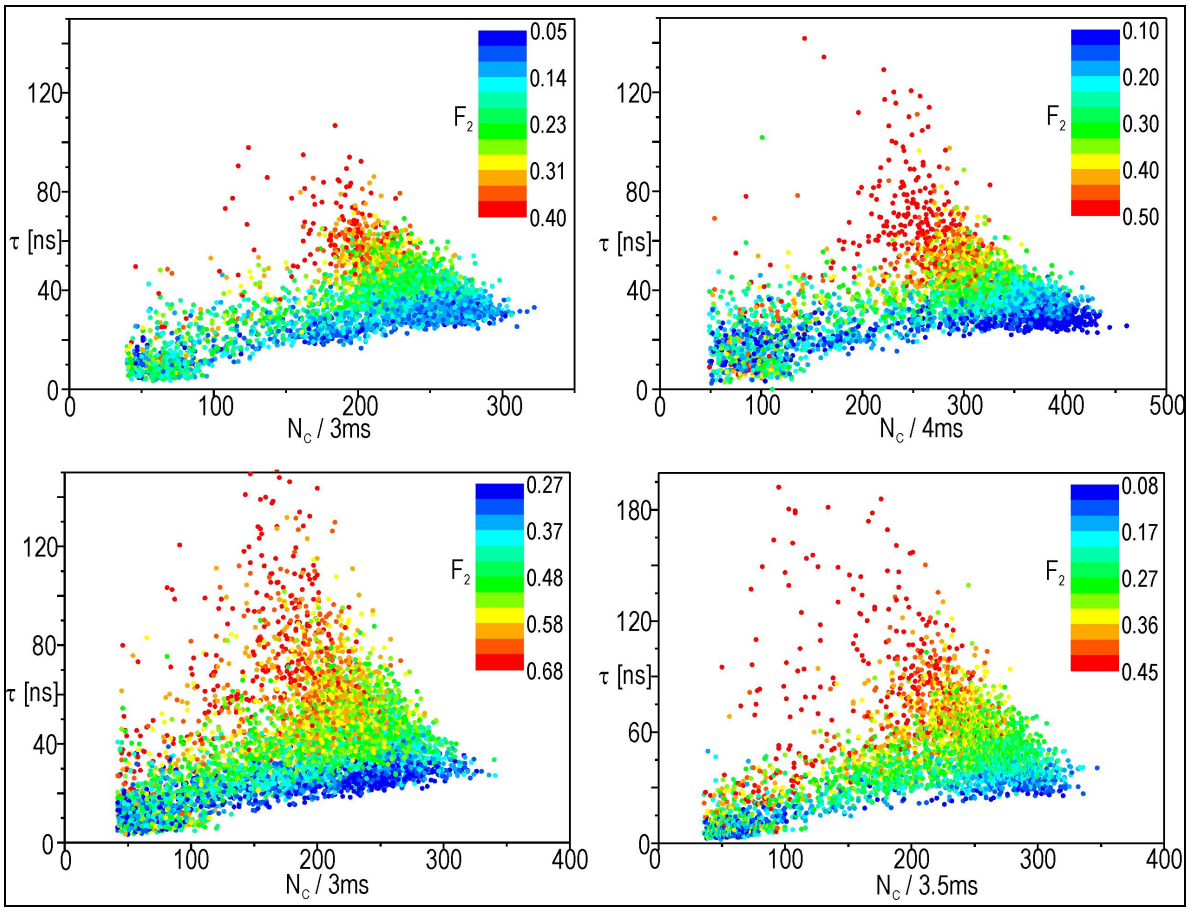

Figure 4.2.25: ***(A)-(D)*** *Scatter plots of* τ *versus* N_C *with color encoding of the* F_2*-value for four different single NCs of type QD605. It is obvious that apart from the shorter lifetimes the plots feature similar characteristics to the NCs of type QD655.*

To obtain plots of statistical significance, only NCs which showed sufficient emission from the „on"-state and a certain amount of SD (which do most of the NCs) were considered. In this respect, QD705 is for several reasons difficult to investigate: As could be deduced from the transients depicted in Fig. 4.2.20, QD705 is very susceptible to blinking events, hence longer periods of uninterrupted blinking are rare and long detection times on the minute scale necessary for sufficient photon statistics are difficult to measure. Though the blinking can be reduced by using lower excitation power, this diminishes the count rate which can be collected from „on"-state emission. The bin time, and thus the temporal resolution as well as the number of data points (= bins) in the scatter plots are then significantly reduced. These effects are aggravated by the long lifetime of typically more than 100 ns, necessitating a higher count rate for a satisfactory confidence level and a further increase of the bin time. Therefore, for QD705 a maximum N_C of about 600 /bin is required compared to 400 /bin for QD605 and QD655. The influence of a decreased binning time on the distribution is depicted for a QD705 in Fig. 4.2.28. Especially the more diffuse appearance of the "wedge" and the large vertical dispersion of the lifetimes caused by the increased

statistical error is noteworthy. In this case also the bins below 50 counts are shown, monitoring the shot-noise distribution to the lifetime.

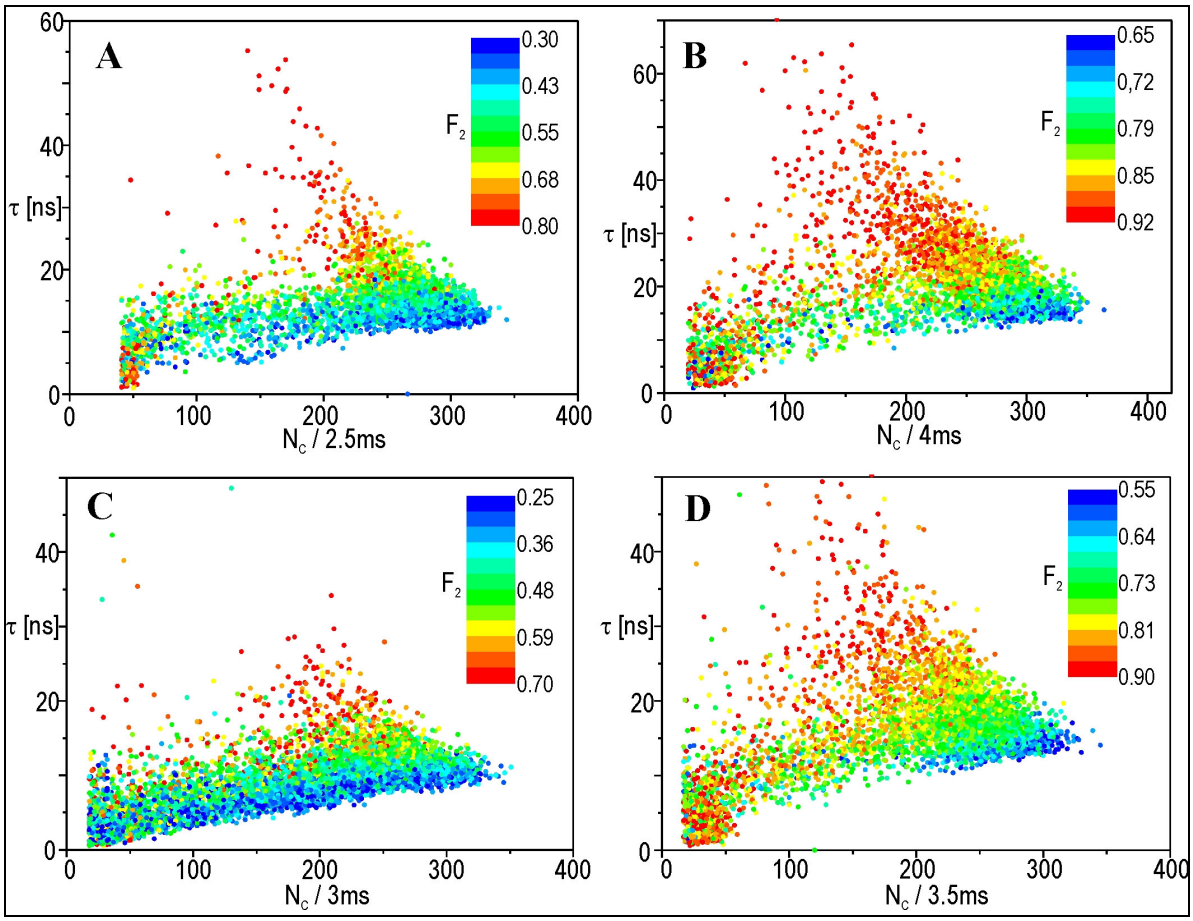

Figure 4.2.26: ***(A)-(D)*** *Scatter plots of* τ *versus* N_C *with color encoding of the* F_2*-value for four different single NCs of type QD605. The NCs show similar characteristics to those of type QD655.*

All plots show to a different degree a "wedge"-like shape as well as the correlation of the PL lifetime with the F_2-value, i.e. the states with the longest lifetime also display a large red shift. Furthermore, in most cases, especially for QD605 (Fig. 4.2.27) and QD655 (4.2.26), a high density population for low emission intensities, i.e. strong quenching is discernible similar to the subpopulation denoted **(3)** in Fig. 4.2.24B.

When interpreting the shape, one has to consider that these plots are made up by superposition of many different photophysical regimes to which the NC was exposed during the measurement, typically a range of 20-100 s. Since it was not possible to control the photophysical fluctuations of the NC during the measurement, the NC might randomly emit from all possible states.

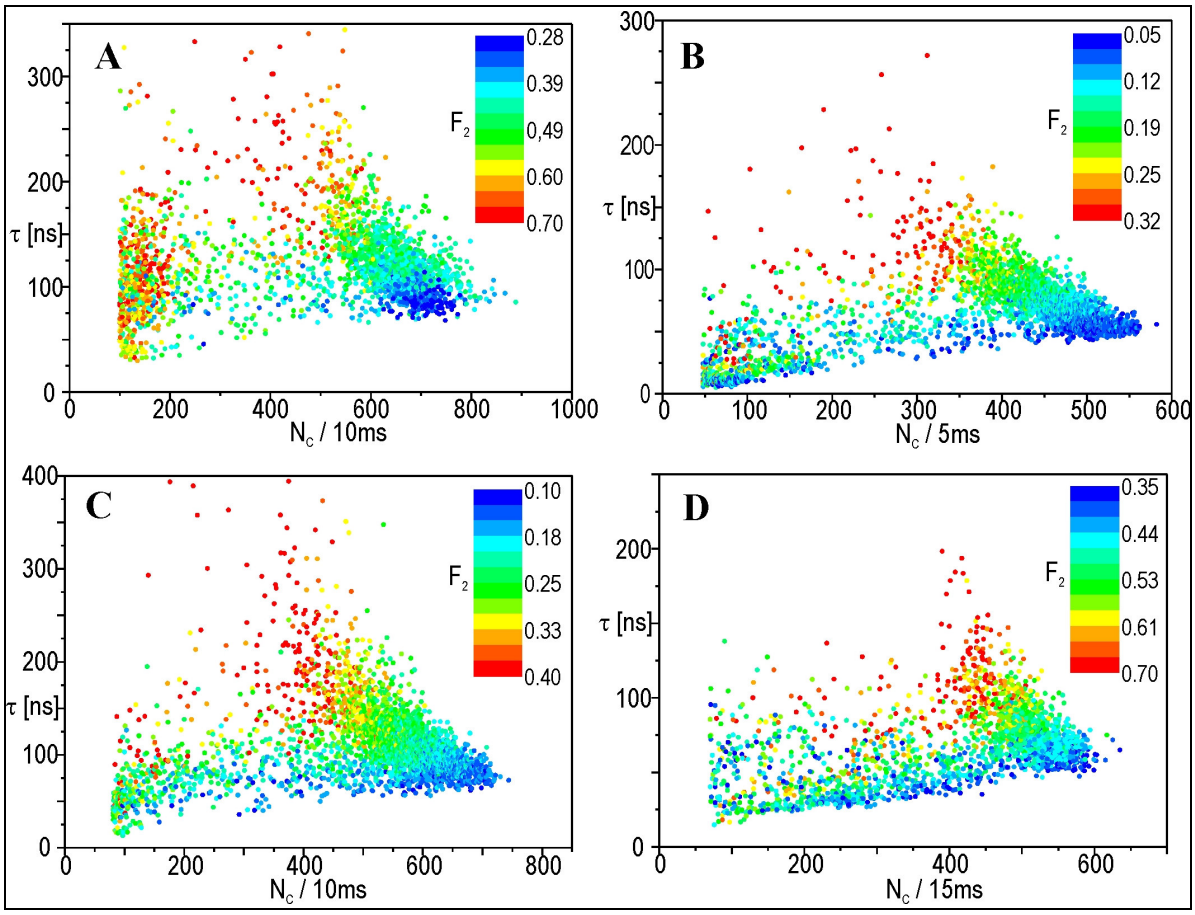

Figure 4.2.27: ***(A)-(D)*** *Scatter plots of* τ *versus* N_C *with color encoding of the* F_2*-value for four different single NCs of type QD705. The major difference to the wedges in Figs. 4.2.26/27 is a scarcely populated lower bound, i.e. the NCs emit predominantly from the "on"-state.*

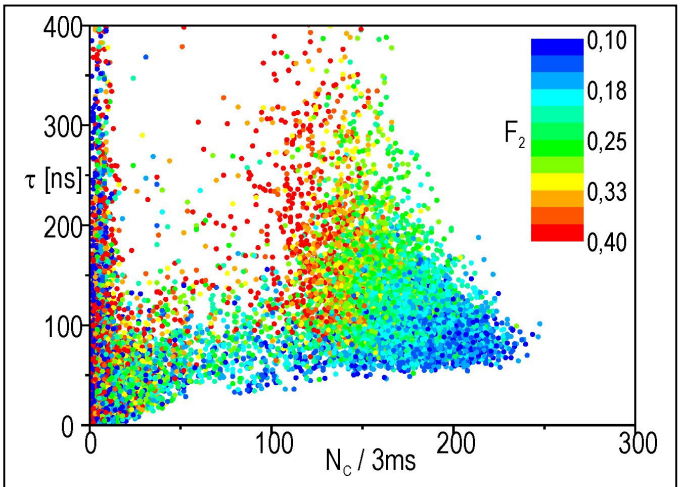

Figure 4.2.28: *The plot of* τ *versus* N_C *for the NC shown in Fig. 4.2.27C (QD705) with reduced binning time and without lower count limit.*

Therefore, the fact that the scatter plots display no statistical but a well defined shape for upper and lower bounds indicates that these bounds are defined by limits intrinsic to the NC photophysics. Therefore, one might expect slightly different shapes for different NCs, dependent on their photophysical properties. To be able to identify these specific borders, certain statistics is necessary which might in cases of seldom events not always be achieved. In this context it is noteworthy that the lower bound is not well defined or even diffuse for the QD705, which apparently means that this type of NC is rarely subject to quenching events.

4.2.8 Investigation of intensity fluctuations driven by SD

Since it has been verified, that the "wedge" shape in the τ-N_C-scatter plots is a general characteristic of NC photophysics and the course of its bounds are characteristic for the respective NC, it is crucial to unravel the key factors of these features and extract quantitative information from them. It has already been demonstrated that the PL decay analysis obtained with the help of the MLE yields correct lifetimes. Then, the factors determining the N_C fluctuations have to be found, and the contributions intrinsic to the NC photophysics must be disentangled from extrinsic factors due to the experimental set-up.
It has already been mentioned in section 4.2.1 that the number of extrinsic parameters is greatly reduced since only relative and not absolute changes of the N_C are of interest for the measurement. Further simplification is achieved by the fact, that a distinct temporal correlation between the changes of the PL lifetime τ, the F_2-value and the count rate N_C is observed. This excludes any factors such as possible imaging instabilities, variation of the excitation power and other non-correlated sources. The remaining factors that depend on the other two fluctuating observables, i.e. the PL lifetime τ and the spectral signature F_2 are driven by the spectral position of the emission curve. The decisive parameter of the set-up that might be influenced by fluctuations of these observables is the photon detection efficiency D_E defined as the ratio of detected to emitted photons. Under the described experimental fluctuations of the maximum emission wavelength constitute the only extrinsic source that might influence D_E. Generally, any chromaticity, i.e. spectral sensitivity of D_E, might interfere with the result, but due to the small spectral shifts of below 20 nm for SD (see Fig. 4.2.3) chromatic aberration can be neglected.
The main influence results from the applied filter sets and the two different detection channels, and their change of transmission over the range of the experienced SD. Thus, if the transmission of the optical components decreases strongly with increasing wavelength, a similar behavior to the observed anti-correlation of F_2 with N_C (Fig. 4.2.23D) would be produced which is also notable in all wedges (Figs. 4.2.25-27). That is, a red-shift results in a loss of intensity. The most critical factor causing such a behavior is a narrow band-pass filter, cutting off the red tail of the NC emission spectrum. Then, a red shift leads to blocking of a larger portion of the emission from detection. Therefore, it was checked if and for which wavelength range such behavior of the employed filter-sets could be expected. For this purpose, a Gaussian fit of a typical NC of the respective sample (FWHM of 18 nm,

20 nm, 45 nm for QD605, QD655, and QD705, respectively) was used and compared with the overall transmission on both detectors, i.e. the sum of D1 and D2 (see also Figs. 4.2.6, 8/9). As it was stated that a requirement is a partial cut-off of the spectrum, spectra for both the short and long wavelength end of the transmission curve were determined, where the maximum blocking amounted to 10% of the maximum intensity, i.e. with overall less than 2% loss due to cut-off.

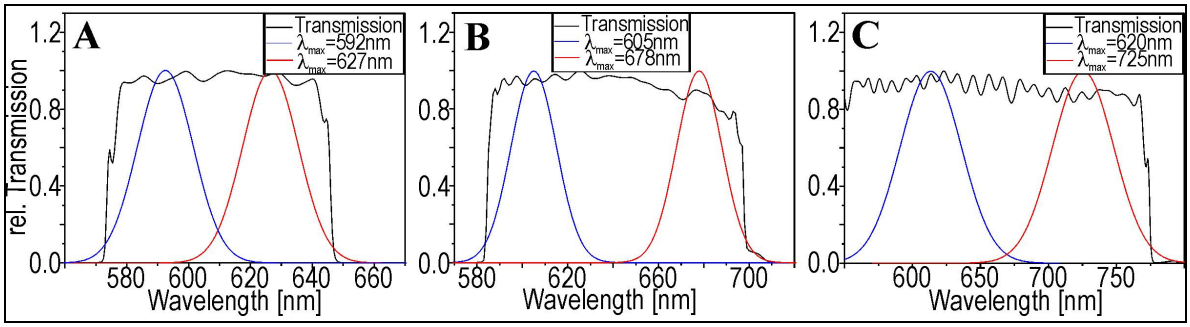

Figure 4.2.29: ***(A)-(C)*** *Overall transmission curves (black line) of the employed set-up for imaging of samples QD65, QD655 and QD705, respectively. The blue and the red curves display the spectrum with the highest blue- and red-shift, for which the detection efficiency due to cut-off is not yet effected.*

The two spectra, shown with the respective transmission curves in Fig. 4.2.29, were considered as the lowest and highest emission wavelengths for which photon loss driven by a spectral shift was negligible. For QD605, significant influence of D_E on the detected counts N_C could be excluded from 592 nm to 627 nm, i.e. according to the calibration curves yielding a F_2-range of < 0.05 to about 0.9. The ranges for the other two samples are 605 nm-678 nm ($0.02 < F_2 < 0.75$) for QD655 and 620 nm-725 nm ($0.02 < F_2 < 0.85$) for QD705, respectively. When comparing these results with the F_2 ranges in which the anticorrelation of τ with N_C is observed (Figs. 4.2.25-27), the results cannot be explained as an artefact due to the cut-off of the spectrum. However, other effects of weaker influence have to be considered as well, e.g. it is discernible from the overall transmission curve for QD655 that the sensitivity decreases towards longer wavelengths before the cut-off occurs (Fig. 4.2.29B). This is mainly caused by the additional bandpass filter used in front of detector D2, which has a maximum transmission of about 90%. Hence the photon detection probability on D2 is 10% less than on D1 and a red shift causes a slight decrease of D_E. This effect was calculated similar to the simulated F_2-wavelength calibration curve introduced in section 4.2.2. Briefly, the relative transmission for a Gaussian curve of fixed FWHM (20 nm) was calculated depending on the position of λ_{max}. A relative decrease of D_E of about 10% was calculated when λ_{max} shifted from 652 nm (according to an F_2 of

about 0.2) to 674 nm (F_2 ~ 0.65). However, in the same F_2-intervall the wedge depicted in Fig. 4.2.24 shows a relative decrease of N_C for the upper bound of about 50%.

Apart from the optical filters, the remaining contribution of major importance is given by the photon detection efficiency of the used APDs, for which the sensitivity curve has been displayed in the experimental section (Fig. 3.2). It is obvious that the detection efficiency in the range of 600-750 nm is not only quite constant, but moreover it increases from 64% at 600 nm to ~70% at 700 nm, thus for QD605 and QD655 the effect would be the opposite of the observed feature. Altogether one can conclude, that the anticorrelation of N_C and τ cannot be accounted for by extrinsic factors due to the experimental set-up, but it is due to photophysical fluctuations within the NC.

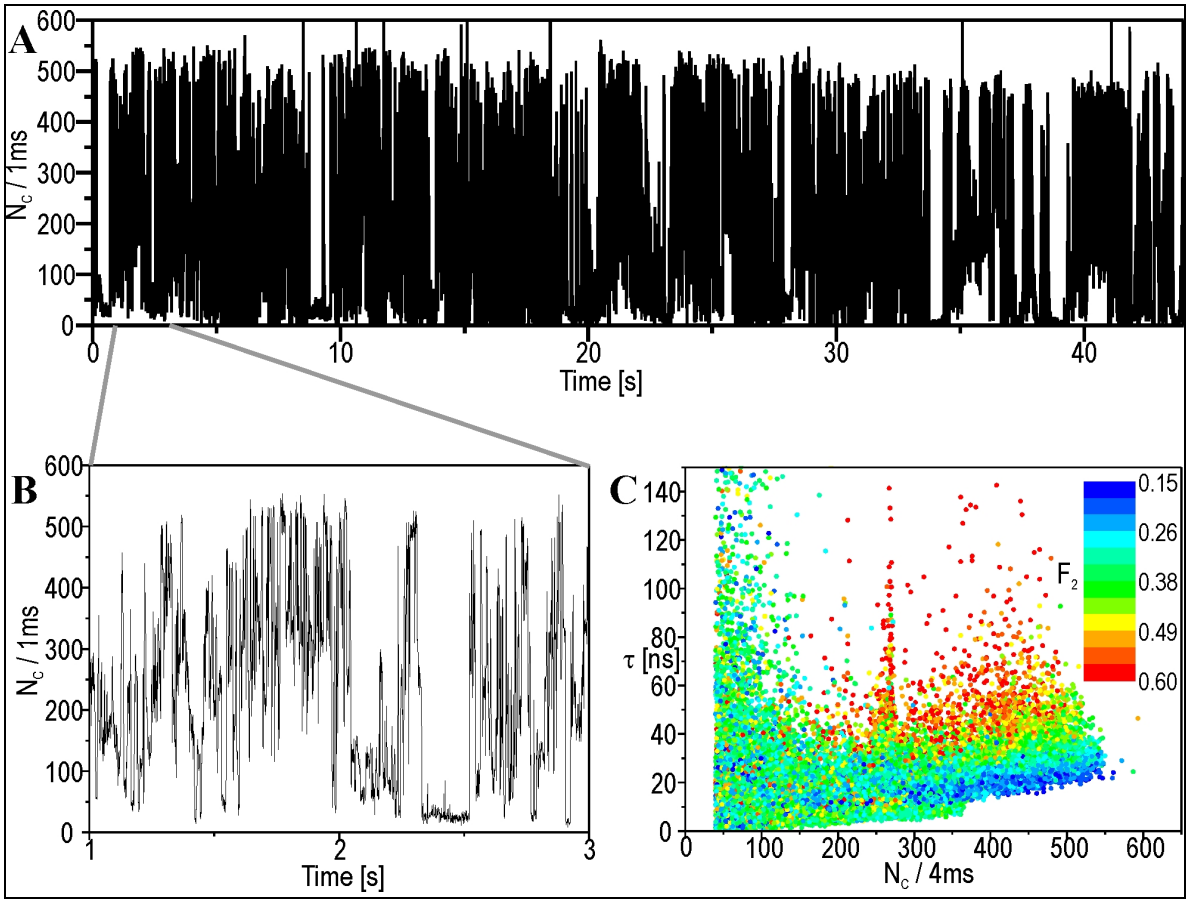

Figure 4.2.30: ***(A)*** *Transient of a single NC (QD655) under saturating conditions, displaying more than 500 kHz PL rate with 5 MHz pulse repetition rate under 3 kW/cm^2 excitation.* ***(B)*** *Portion of the transient in A which reveals the strong fluctuations between different intensity levels. Accordingly, the "wedge" in the* τ-N_C*-plot in C is rather difficult to discern.*

Thus, the observed intensity fluctuations might depend on two intrinsic terms, the absorption coefficient σ, influencing the probability of excitation and the PL quantum yield ϕ, determining the probability of photon emission. To extract the maximum information out of the measurements it would be desirable to eliminate the dependence of N_C on one of the

factors to ascertain whether these fluctuations are driven by changes of σ, of ϕ, or both. This can be done by measuring under saturating conditions, i.e. using high laser powers so that the probability of excitation is close to unity per laser pulse. Under these conditions, even significant variations of the absorption cross section will cause only marginal changes of N_C.

Saturation measurements were first carried out for QD655 which proved to be the most suitable type of NC for such measurements because it is quite stable with respect to both blueing (problematic for QD605, see below) and excessive blinking (QD705). Several adjustments were made to allow for optimal imaging conditions. These included changes of the filter set-up by exchanging the band pass filter 665DF65 in front of D2 versus a long pass filter 585AELP for both detectors, thus circumventing any effect of D_E on N_C. The substitution should have no significant influence on the F_2-λ_{max} calibration since the beamsplitter constitutes the dominating factor for the course of the F_2. Because of the high PL quantum yield obtained from the NCs combined with the set-up, a neutral density filter blocking about 20% of the emitted photons was inserted into the detection pathway to avoid saturation due to high count rates (500 kHz) and subsequent electronic data loss. This reduces the maximum count rates obtained from single NCs of type QD655 excited with 5 Mhz repetition rate from >500 kHz (!) to about 400 kHz. The power was generally adjusted for each NC to ensure that a sufficient degree of saturation (> 90%) was achieved while avoiding too high excitation intensity. The reasons for this procedure was the rapid blinking observed for many NCs that prevented meaningful resolution of the photophysical states due to an average “on”-state duration below 1 ms. Furthermore, other interfering effects such as increased occurrence of quenched states and multiexciton emission should be reduced to a minimum (compare Fig. 4.2.30).

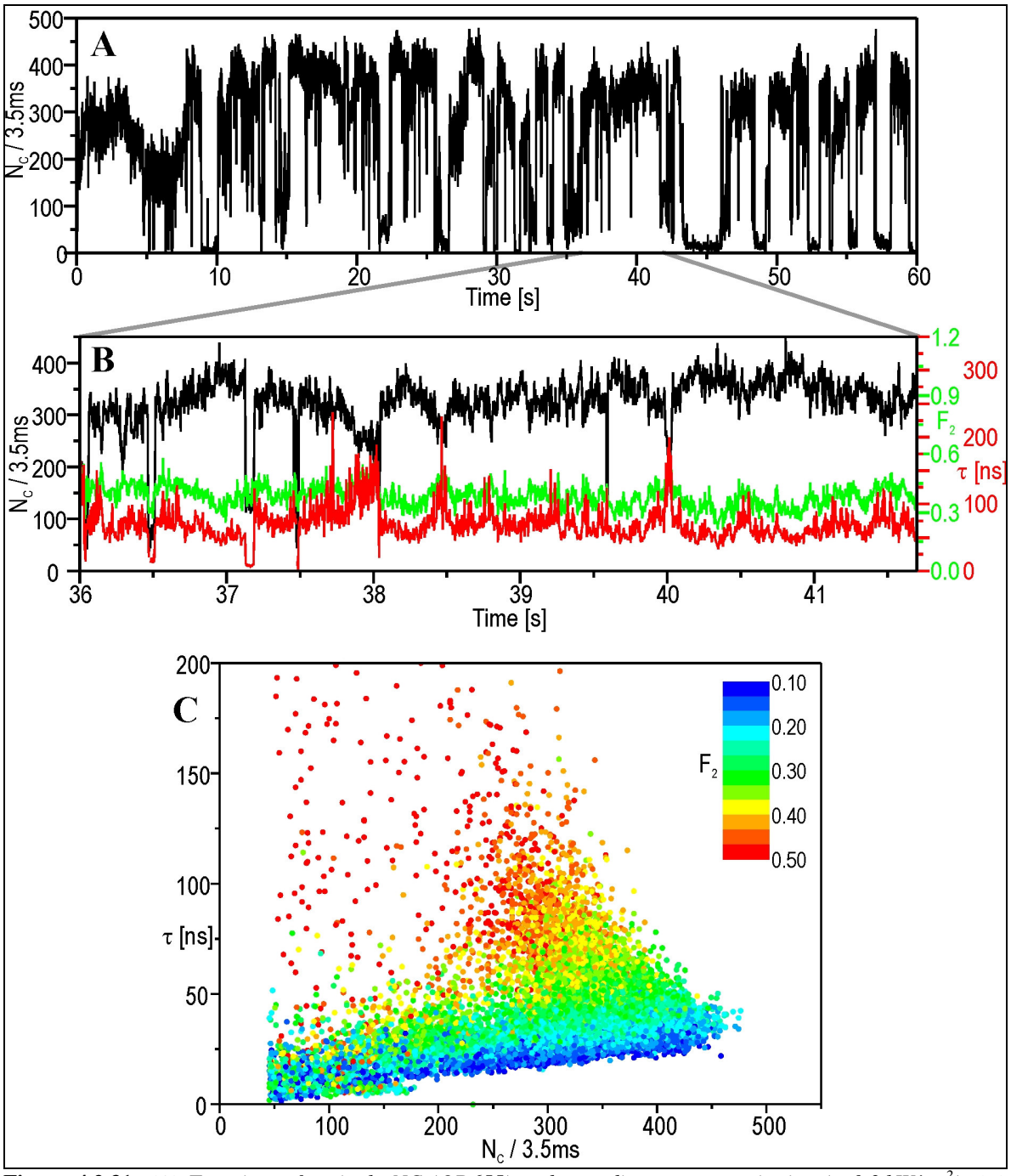

Figure 4.2.31: ***(A)*** *Transient of a single NC (QD655) under medium power excitation (≈ 0.3 kW/cm²).* ***(B)*** *Portion of the transient A from 36-41.7 s with intensity (black), spectral (green) and lifetime information (red line). The interrelations between the different observables during SD are distinct.* ***(C)*** *Resulting* τ-N_C*-plot shows typical "wedge"-like features.*

Figs. 4.2.31/32 show a single NC imaged under the described conditions at medium and saturation power. Both τ-N_C-plots show similar distributions with the characteristic "wedge" shape with well defined upper and lower bounds especially for the saturating excitation. Because of the saturating conditions, influences of the absorption cross section should be negligible, and the fluctuations of N_C reflect changes of the PL quantum yield ϕ, i.e. $N_C \propto \phi$. The count number per bin may then be written as $N_C(\phi) = m * \phi$, where m is

denoted as the constant of proportionality. This can be simplified by considering that there is a maximum detectable photon number per bin N_{max} since the quantum yield cannot exceed unity. With $N_C(\phi = 1) = m = N_{\max}$ the quantum yield can then be expressed as $\phi = N_C / N_{\max}$, where N_{max} is interpreted as the detected count number for an NC emitting with 100% quantum yield. It is important to realize that N_{max} is a constant that depends only on the experimental set-up and the imaging conditions of the respective NC, thus it might vary from NC to NC, but is independent of any photophysical process.

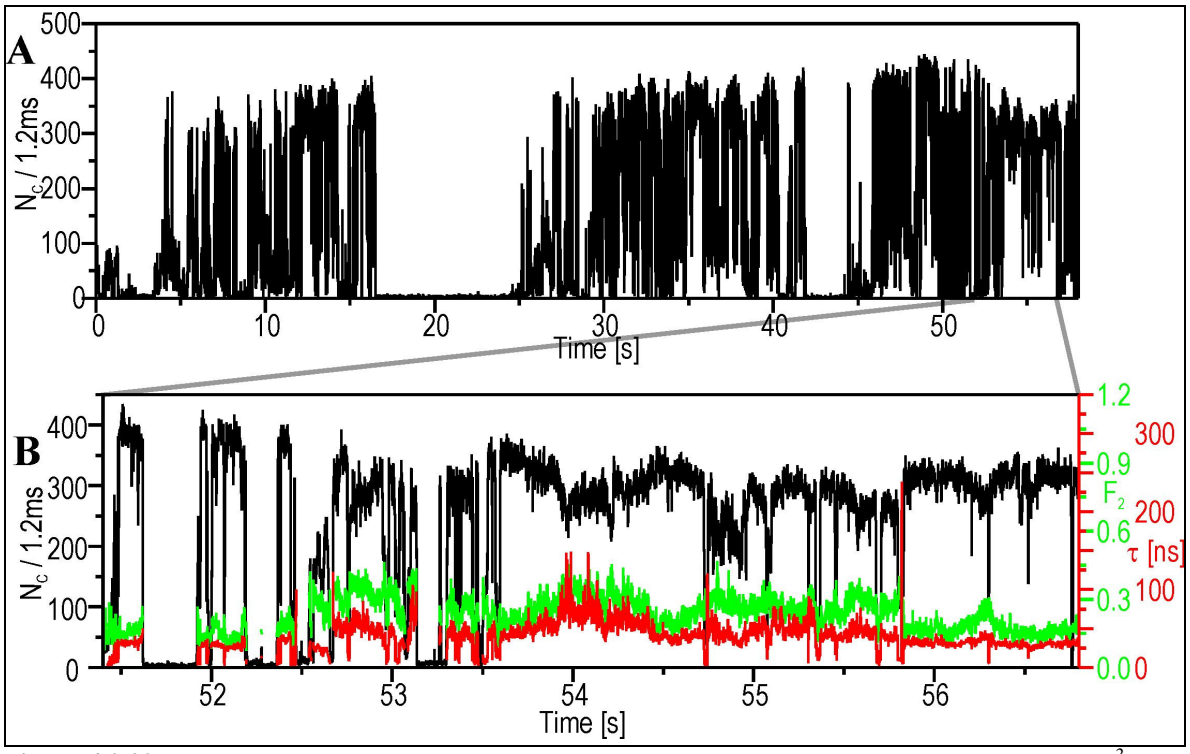

Figure 4.2.32: ***(A)*** *Transient of a single NC (QD655) under saturating power excitation (≈ 1.4 kW/cm²).* ***(B)*** *Portion of the transient A from 51.3-56.8 s with intensity (black), spectral (green) and lifetime information (red line).*

Together with the measured PL lifetime τ this offers the possibility to extract quantitative information about NC photophysics. The basics behind this consideration is the fact that both τ and ϕ depend solely on two parameters central to NC photophysics, the radiative and the non-radiative rate constants, denoted k_r and k_{nr}, respectively. Thus, the lifetime is given by $\tau = 1/(k_r + k_{nr})$, whereas for the quantum yield $\phi = k_r/(k_r + k_{nr})$ holds.

In order to understand the relation of parameters, one has to recall the photophysical regimes, which influence ϕ. In the literature, quenching events are mentioned, for which PL is reduced by increased concurring pathways to a "trap" state, accordingly the non-radiative rate k_{nr} is increased [91,92]. Therefore, depending on the strength of quenching, the quantum yield may fluctuate by means of changing k_{nr}. To understand the consequence of

such behavior within the τ-N_C-plot, the mathematical connection between these two observables has to be found. Since only states are considered where ϕ depends on k_{nr}, the radiative rate k_r can be assumed to be constant, and ϕ can be written as $\phi = k_r * \tau$. Together with the previous definition of ϕ, one obtains for the quenching regime:

(I) $$\tau(k_{nr}) = (k_r * N_{\max})^{-1} * N_C$$

Although in the scatter plots N_C and not k_{nr} is the variable, the expression $\tau(k_{nr})$ is used to emphasize that the fluctuations of N_C for this regime are determined by variations of k_{nr}.

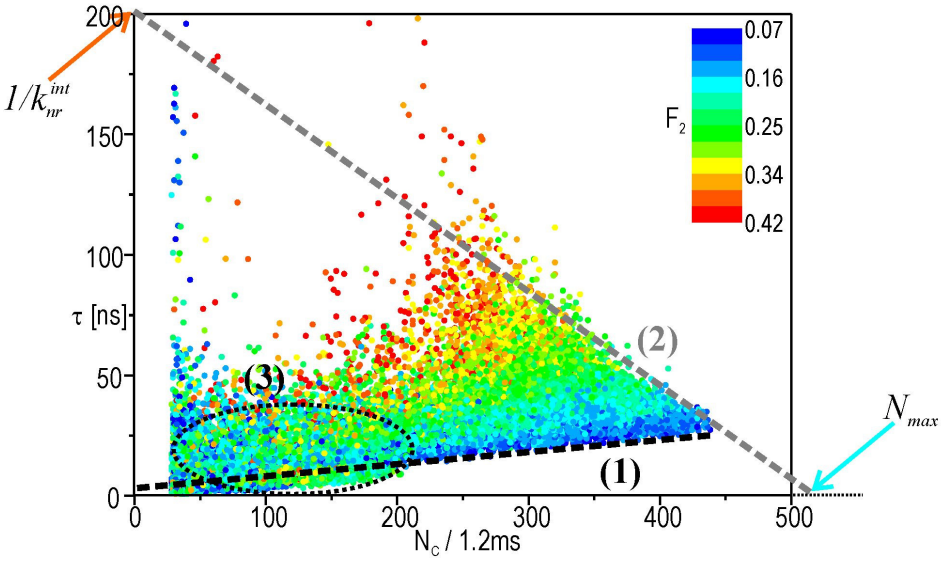

Figure 4.2.33: *Resulting τ-N_C-plot from the transient in 4.2.32 shows a distinct "wedge" shape with clearly defined, near linear lower (1,, black) and upper bound (2, gray line). Notable is the quenched population (**3**, dotted black) starting at N_C = 200/1.2 ms, which is visibly sillouetted against the lower bound.*

Since both N_{max} and k_r are constants, the quenching regime is characterized by a linear function through the origin and can be associated with the lower bound **(1)** observed in the "wedge", explicitly labeled (dashed black line) in Fig. 4.2.24 and in Fig. 4.2.33. The fact that the line matches the first part of the lower bound (dashed black) intersects with the abscissa slightly above the origin can be explained by the long TAC range and the fitting delay of four nanoseconds after the laser pulse. While the latter is used to exclude biexciton effects on the monoexciton decay, this method tends to fit short decays because of a stronger background fraction not correctly (section 4.2.3). Note that this relation in (I) apparently does not hold for the second, strongly quenched population for intensities below 200 counts/1.2ms (Fig. 4.2.33), which takes course below this linear function. Nevertheless, the shape of the lower bound is in good agreement with the course derived from eq (I).

However, it is clear due to the existence of an upper bound (2) and also the found anti-correlation of τ with N_C that quenching cannot be the sole cause for intensity fluctuations.

Since the fluctuations driven by the SD are opposite to the behavior observed for quenching which is dominated by changes of k_{nr}, the existence of a second regime is proposed which stems from fluctuations of the radiative rate constant k_r. In this case, the quantum yield might be expressed as: $\phi = 1 - k_{nr} * \tau$, since in this case, the non-radiative rate constant is regarded to be constant. Together with the N_C, one obtains for the interrelation between the PL lifetime and PL intensity:

(II) $$\tau(k_r) = (k_{nr})^{-1} * (1 - N_C / N_{\max})$$

This dependence also represents a linear function, in contrast to the quenching with a negative slope and without intersection through the origin. Thus, there is a clear indication that (II) is connected with the upper bound **(2)** (dashed gray in Fig. 4.2.33C) which means that the N_C fluctuations observed most notably during the „on"-state are indeed caused by changes of the radiative rate constant k_r. Several issues have to be discussed here more thoroughly: It is interesting to note that at least near the edge of the "wedge", the upper bound can be fitted satisfactorally with a linear function, with the deviations for lower count rates (below 350 counts/1.2 ms) to higher values of τ attributable to increasing errors of the MLE-routine for longer lifetimes and smaller photon statistics.

From these findings it can be concluded that over a large range, both k_{nr} and k_r are basically independent parameters, i.e. even for moderate to strong quenching the radiative rate constant is not affected and vice versa. It furthermore means, that in the presented regimes **(1)** and **(2)** the gradients are really constant and equations (I) and (II) are always fulfilled.

This result can be exploited to draw several important conclusions concerning the NC photophysics. For example, it presents for the first time evidence for radiative rate fluctuations for colloidal NCs. So far, the color encoding of the F_2–value has not further been investigated, though it contains important information. It was already mentioned that especially for the upper bound the F_2-N_C anti-correlation is pronounced since the highest N_C at the edge is always found for the lowest F_2-value, while N_C decreases for a spectral red-shift. Nevertheless, a closer inspection reveals that this relation does not only hold for the upper bound, but even for moderately quenched states. This means that there is not only a linear function for the discussed lower bound which is made up entirely of states with minimum F_2-value, but that for each F_2-section (= each color) there exists a separate linear function. These functions are not parallel but tilted for higher F_2-value, i.e. after extrapolation to the abscissa they seem to intersect near the origin.

Conferred to theoretical quenching regime relation (I) this means that for a lower F_2-value a higher gradient of the linear function is found, from which a decrease of k_r can be deduced,

since the gradient is inversely proportional to the radiative rate. From the course of the distribution for different colors (= spectral shifts) it can thus be concluded that the SD influences the radiative rate constant k_r in such a way that a spectral red shift is accompanied by a decrease of k_r and vice versa.

4.2.9 Determination of the PL quantum yield for single NCs

Concerning the upper bound, the near linear features observed and the well defined boundary were discussed as indication of a property inherent of the respective NC. As it is characterized by the maximum N_C which might be detected from the NC for a given wavelength, it should display the NC at its maximum quantum yield, i.e. with a minimum non-radiative rate constant k_{nr}. Therefore, it is important to notice that a significant tilting of the upper bound is observed, which together with equation (II) suggests that the minimum non-radiative rate constant is not negligible, since the gradient is inversely proportional to it. Because this non-radiative rate k_{nr}^{int} seems to be an intrinsic property of the N_C and is not due to external "trap" states that cause quenching, we can separate the overall non-radiative rate constant into $k_{nr} = k_{nr}^{\text{int}} + k_{nr}^{ext}$, where k_{nr}^{ext} denotes the extrinsic contribution to the non-radiative rate constant caused by traps.

Extrapolation of the outlined linear course of **(2)** then allows estimation of two important parameters: as can be deduced from equation (II), the intersection with the abscissa ($\Rightarrow N_C = 0$) yields $1/k_{nr}^{\text{int}}$, while the intersection with the ordinate gives N_{max}. The data can be used to obtain information about the PL quantum yield, e.g. the average PL quantum yield of the NC when emitting in the „on"-state ϕ_{av}. Since k_r fluctuates within the "on"-state, an average value of the quantum yield, ϕ_{av} , is calculated for the most probable F_2-value of NC emission. The respective most probable count rate $N_{C(av)}$ within the "on"-state is found by extrapolating a line from the origin through the most probable count rate to the upper bound. As it was found that quenching does not affect fluctuations of k_r and SD, the most probable quenched state should also display the same emission wavelength as the most probable "on"-state. For the NC presented in Fig. 4.2.33 it was found $1/k_{nr}^{\text{int}} \approx 200$ ns, $N_{max} \approx 520/1.2$ ms and with $N_{C(av)} \approx 400/1.2$ ms the average quantum yield was calculated to $\phi_{av} \approx 78\%$.

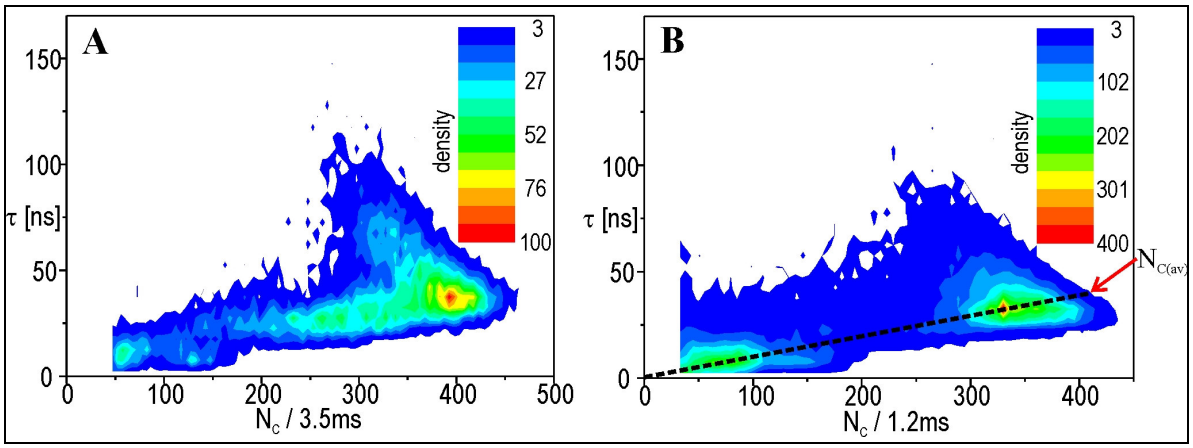

Figure 4.2.34: *Density plots of the "wedges" obtained under medium (**A**, compare Fig. 4.2.31C) and saturating power conditions (**B**, Fig. 4.2.33). The "wedge" in **A** shows the highest density for both upper and lower bounds, whereas the highest concentration (= most probable emission) is found under high power excitation in the center and for the quenched subpopulation denoted **(3)** in Fig. 4.2.33.*

It is interesting to compare these values with those obtained from the wedge of the medium power data (Fig. 4.2.32C). Although the upper bound in this case is not well defined, the slope seems to be steeper, indicating a lower non-radiative rate (i.e. a higher $1/k_{nr} \approx 250$ ns). However, together with an estimated $N_{max} \approx 560/3.5$ ms and $N_{C(av)} = 440/3.5$ ms the average quantum yield under these conditions is comparable to $\phi_{av} \approx 79\%$. The discrepancy of a lower intrinsic non-radiative rate with identical quantum yield can be explained by the overall increased lifetimes measured for the medium power wedge, i.e. 45 ns at the state with $N_{C(av)}$ compared to only about 40 ns for the saturation data. It is also obvious that the density plot in Fig. 4.2.34A monitors a distinct separation between upper and lower bound, whereas under saturation conditions the distribution is much more homogeneous, with the highest density for states between these two regimes. From these findings it can be concluded that not only blinking but also fluctuation between different photophysical states are accelerated under high power saturation. This means that despite shorter binning, the probability of an intermixing between different regimes is increased and leads to an averaging effect, i.e. reduced resolution of the states. These differences, i.e. the fact that the calculated average quantum yield shows no significant dependence on the excitation power, indicates that the absorption cross section σ is, in contrast to the quantum yield ϕ, not affected by SD.

Apart from the homogeneous distribution, the density plot for saturating power reveals a much more distinct subpopulation of quenched states denoted **(3)** (Fig. 4.2.33) which was already discernible for QD655 excited at low power (see Fig. 4.2.24B). The quenched sub-population is also interesting, since the correlation derived for the lower bound **(2)** does not

seem to be valid anymore, so that the distribution of the population **(3)** exceeds significantly below the lower bound.

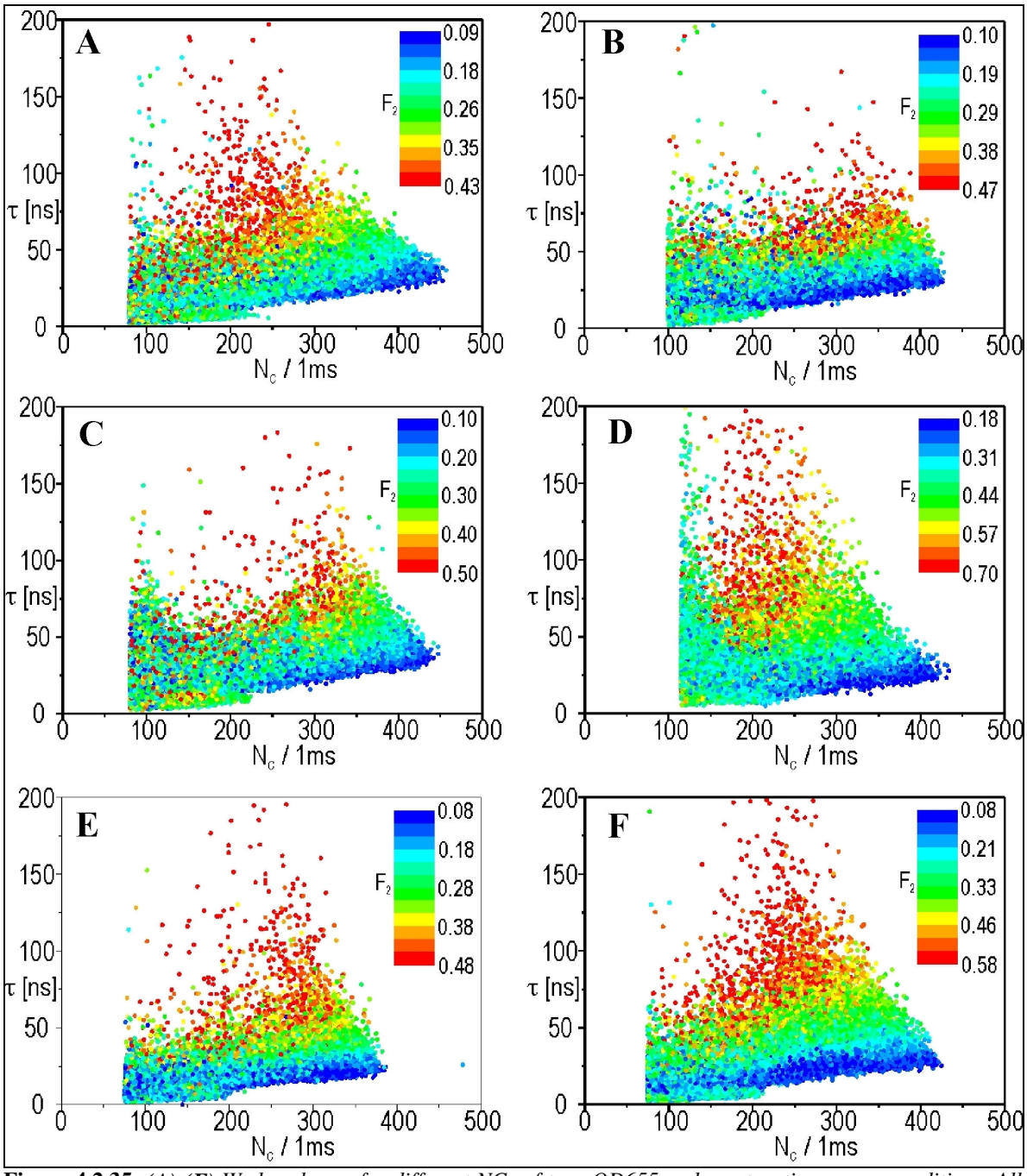

Figure 4.2.35: *(A)-(F) Wedge shapes for different NCs of type QD655 under saturating power conditions. All display near linear upper and lower bounds as well as a significant subpopulation of the quenched state. The following values were extrapolated for each dot:* ***(A):*** $N_{max} \approx 540$ */ms;* $k_{nr}^{int} \approx 1/270$ *ns;* $N_{(C(av))} \approx 420$ */ms* $\approx\Rightarrow$ $\phi_{av} \approx 78\%$. ***(B):*** *480 /ms; 1/300 ns; 400 /ms* $\Rightarrow \phi_{av} \approx 83\%$. ***(C):*** *500 /ms; 1/310 ns; 410 /ms* $\Rightarrow \phi_{av} \approx 82\%$. ***(D):*** *490 /ms; 1/230 ns; 390 /ms* $\Rightarrow \phi_{av} \approx 80\%$. *(E): 430 /ms; 1/320 ns; 360 /ms* $\Rightarrow \phi_{av} \approx 84\%$. *(F): 470 /ms; 1/310 ns; 390 /ms* $\Rightarrow \phi_{av} \approx 83\%$.

Similar wedge features were observed for all QD655 in those cases where the „on“-state fluctuations could be resolved. Several samples for QD655 imaged under saturating conditions (notice the count rates) are shown in Fig. 4.2.35. Typical features of the “wedge”

are discernible similar to the plots obtained under medium to low power conditions. Especially also the quenched subpopulation **(3)** mentioned before is much more prominent. Despite the mentioned limitations concerning the resolution of the „on"-state regime caused by rapid photophysics, about 25 of the investigated NCs allowed for an estimation of the respective average quantum yield, with values ranging from 75% to 90% , but typically 80-85% (Note that for a better perceptibility of the F_2-N_C-anticorrelation, an NC with comparatively low ϕ_{av} was chosen in Figs. 4.2.33). The plots give an idea of the accuracy which might be achieved by this technique and the error is assumed to be around 5%, mainly due to uncertainty concerning the exact course of the upper bound. The values compare favorably with an ensemble quantum yield given by the manufacturer of more than 60%, considering the possible amount of dark particles in solution [217,219]. The fact that it is still somewhat lower than previously measured for similar NC samples using a different technique (> 95%) [241] cannot be answered without further investigation, i.e. if it is due to slightly different types of samples or contributions of other factors. Nevertheless, our method does not rely on external perturbation and exploits intrinsic fluctuations of photophysical properties. Note also, that for the measurement not even spectral resolution is a requirement, i.e. it might be carried out on each set-up equipped with a single APD, a pulsed laser and a TCSPC card, as is demonstrated below.

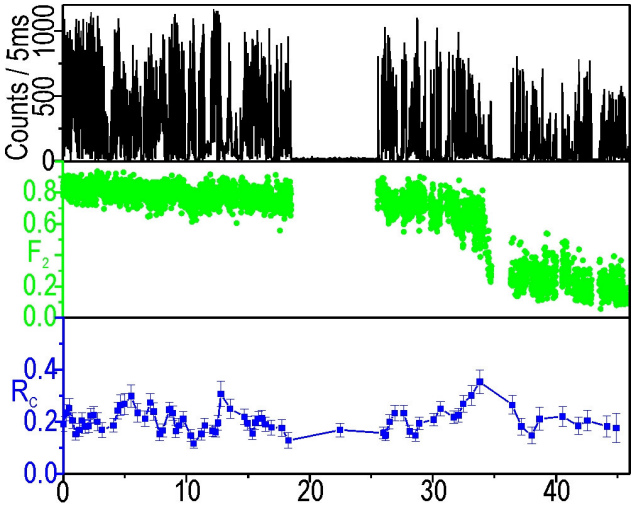

Figure 4.2.36: *Blueing of a NC type QD605, identified by the intensity (black), spectral (green) and coincidence information (blue). The F_2-value first gradually, after 35 s rapidly declines from > 0.8 to < 0.2. For the given S/B, the almost constant ratio significantly below 0.5 indicates a single NC.*

To investigate the effects of high power excitation, and for the determination of ϕ_{av}, also QD605 and QD705 NCs were measured under saturating conditions. Because of the high tendency of QD605 for blueing under high excitation power (Fig. 4.2.36), a newly prepared batch of QD605 with slightly different composition was used for the experiments. Despite problems with blueing, which was still frequently observed, this type of NC also featured reduced SD which made it more

difficult to discern the bounds of the "wedge" (Fig. 4.2.37). Because of these difficulties, the set-up was simplified to allow for a quicker screening of NC samples by using only one APD, thus abandoning the spectral resolution.

The results obtained with the changed set-up gave similar results and also disproved a significant effect of the spectral separation on the "wedge" shape. In the same manner as for QD655, quantum yields for both QD605 and QD705 were determined. Both samples yield average quantum yields comparable to those obtained from QD655, i.e. typically between 80-85%

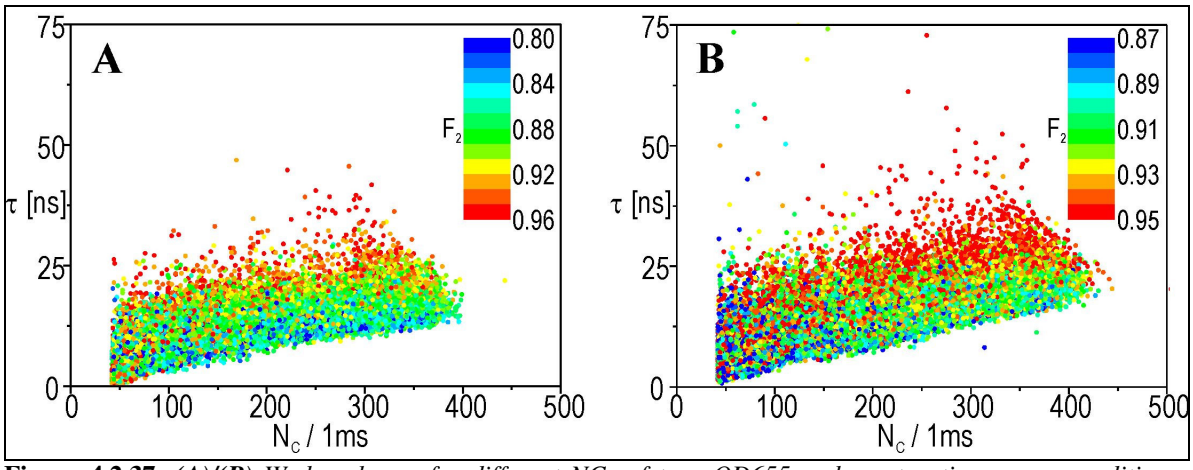

Figure 4.2.37: ***(A)/(B)*** *Wedge shapes for different NCs of type QD655 under saturating power conditions. Though the wedge shape is discernible, the high* F_2*-values and the rapid photophysics aggravate the observation of the typical color pattern. Data* ***(A)****: 470 /ms; 1/100 ns; 380 /ms* $\Rightarrow \phi_{av} \approx 81\%$. ***(B)****: 510 /ms; 1/115 ns; 400 /ms* $\Rightarrow \phi_{av} \approx 78\%$.

In the case of QD705, these values should be interpreted rather as a lower limit of the actual PL quantum yield. The underestimation is caused by the long lifetimes of QD705 (i.e. of 50-100 ns) and the fact that the lower limit for the laser repetition rate is 5 MHz limiting the TAC window to 200 ns per laser pulse. To understand the effect of long lifetimes, it has to be considered that for a state with a PL lifetime of τ, the probability that the NC is still in the monoexciton state after the elapse of 200 ns is given by $e^{(-\tau/200\ ns)}$. If the measurement is made under saturating conditions, it can be assumed that the following laser pulse will excite the NC into the biexciton state, which nevertheless decays non-radiatively back into the monoexciton state due to strong quenching of BX emission (see section 4.3). The result is an overall loss of PL since two laser pulses lead independent of the NC quantum yield only to the generation of a single photon. Hence, in states of longer lifetime the probability of photon loss via this route is more probable and results in a reduced N_C even if ϕ is not affected. Explicitly, a state with an "on"-state lifetime of 60 ns results in a detection loss of

about $e^{(-4)} \approx 4\%$ to 19% if the lifetime increases to 120 ns which means that the relative reduction of N_C amounts to 15%.

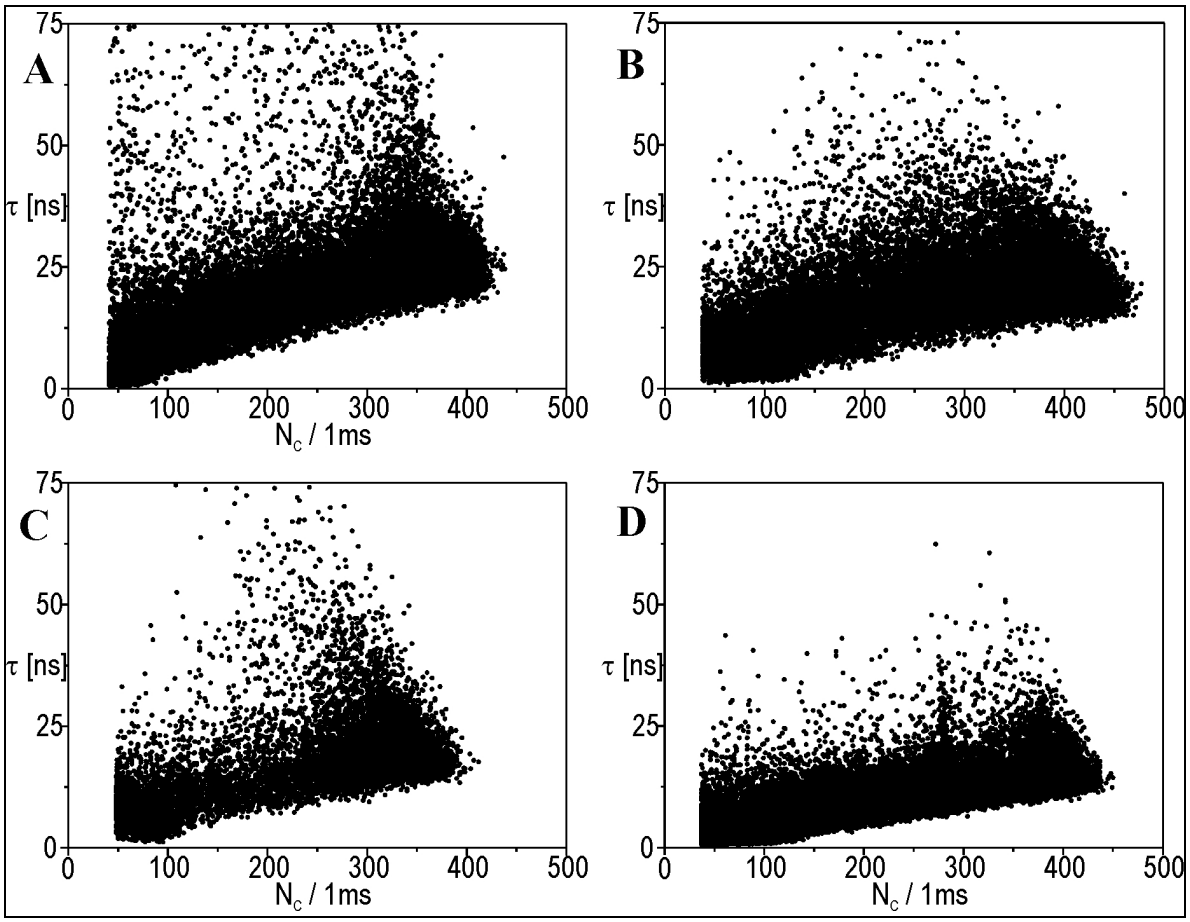

Figure 4.2.38: *(A)-(D) Wedge shapes for different NCs of type QD655 under saturating power conditions using only one APD without spectral information. The wedge shape is obviously not affected, even the quenched subpopulation might be discerned from the distortion of the lower bound versus low count rates. Data* ***(A)*** *490 /ms; 1/180 ns; 400 /ms* $\Rightarrow \phi_{av} \approx 82\%$. ***(B)****: 530 /ms; 1/150 ns; 440 /ms* $\Rightarrow \phi_{av} \approx 83\%$. *(C): 440 /ms; 1/140 ns; 370 /ms* $\Rightarrow \phi_{av} \approx 84\%$. ***(D)****: 500 /ms; 1/130 ns; 410 /ms* $\Rightarrow \phi_{av} \approx 82\%$.

This value can be compared to the NC shown in Fig. 4.2.38D which shows in the same lifetime range a decrease of the maximum emission counts from about 450 /ms to 400 /ms, i.e. a reduction of 11% which is exactly the theoretical difference calculated above. However, the calculation holds only for 100% saturation and an effective PL quantum efficiency of unity, so the actual influence cannot be obtained without further experiments. Although the wedge shapes obtained under saturating conditions displayed no significant effect concerning the boundaries, the most notable effect is apart from a somewhat stronger subpopulation **(3)** which was found most often for QD655 and QD605, a generally much more prominent lower bound. This is especially apparent for QD705 which displayed under normal excitation conditions a prominent upper bound while only few quenched states can be discerned. In contrast, imaging under saturating conditions leads to a dominating lower

bound, i.e. independent of accelerated blinking (for a significant differentiation of blinking and quenching in the wedge see section 4.2.11) emission from quenched states is much more frequent. An explanation can be found by Auger-related multiexciton relaxation pathways where one of the excited electrons might be lifted into much higher energy states than possible from the excitation wavelength. From these excitied states, tunneling of a carrier (electron) into a trap state with increased non-radiative relaxation is much more probable and has been recently verified in ensemble measurements [287].

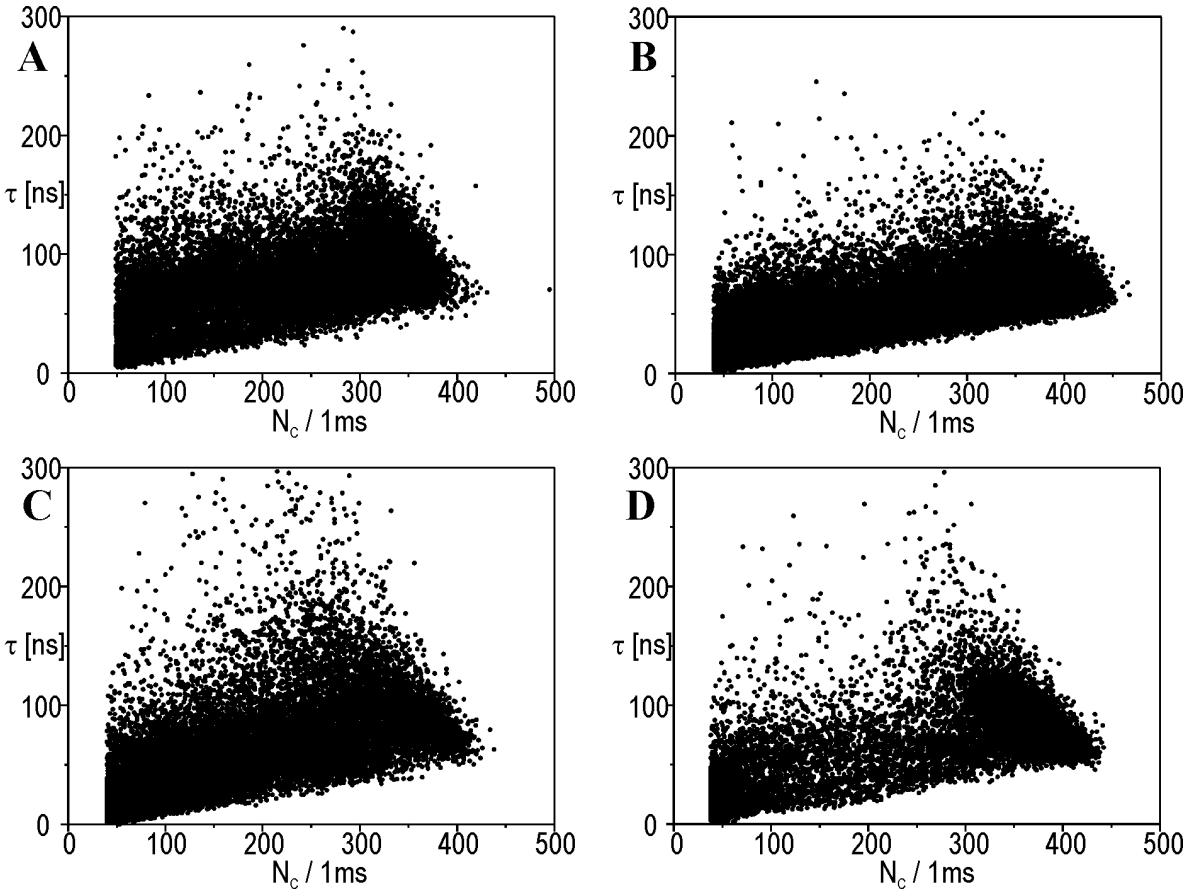

Figure 4.2.39: ***(A)-(D)*** *Wedge shapes for different NCs of type QD655 under saturating power conditions using only one APD without spectral information. Whereas the wedge features principally are identical to those obtained under normal conditions (Fig. 4.2.28), it is noteworthy that the lower bound, i.e. quenched states are found much more frequently compared to medium excitation data. Data* ***(A)*** *480 /ms; 1/500 ns; 380 /ms* $\Rightarrow \phi_{av} \approx 79\%$. ***(B)****: 490 /ms; 1/650 ns; 430 /ms* $\Rightarrow \phi_{av} \approx 88\%$. ***(C)****: 480 /ms; 1/600 ns; 390 /ms* $\Rightarrow \phi_{av} \approx$ *81%.* ***(D)****: 500 /ms; 1/550 ns; 400 /ms* $\Rightarrow \phi_{av} \approx 80\%$.

4.2.10 Determination of the radiative rate constant for a single NC

From the course of the upper bound and the observed F_2-distribution, it was deduced, that the SD driven fluctuations of the radiative rate constant, i.e. a shift to higher energy at the band edge will increase the radiative rate. Both of these parameters are accessible from the

observables: from the F_2-λ_{max}-calibration curve, the maximum emission wavelength is obtained and gives the band edge energy as $E = h * c / \lambda_{\max}$. The radiative rate can be derived with the aid of the extrapolated N_{max} by

(III) $$k_r = N_C / (\tau * N_{\max}) .$$

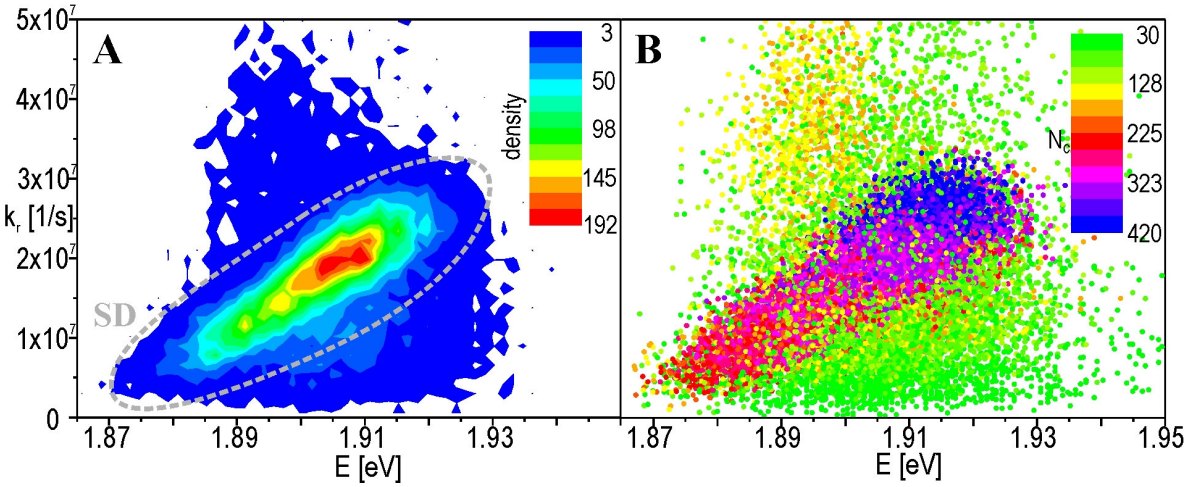

Figure 4.2.40: *Density* ***(A)*** *and scatter plot* ***(B)*** *of the distribution of the radiative rate* k_r *versus the band edge energy* E. *From the density plots it can be deduced that most of the radiative rate fluctuations are driven by the spectral diffusion indicated by the correlation of* k_r *with* E. *This SD population is outlined in* ***(A)*** *by the borders derived from Fig.* ***(B)*** *where it is visible as being dominated by states with higher intensity (red and blue colors).*

Fig. 4.2.40 shows the density plot of E versus k_r calculated from the data of the NC depicted in Fig. 4.2.33. The homogeneous high density population confirms the assumption, that a shift to higher energy results in a strong increase of the radiative rate constant, e.g. a shift from 1.875 eV to 1.92 eV (corresponding to a wavelength shift from 646 nm to 661 nm) yields a more than 5-fold increase of k_r ($5*10^6$ s^{-1} to $2.7*10^7$ 1/s). The finding that the large majority of states (denoted SD population, indicated by the dashed ellipse in Fig. 4.2.40A) follow this pattern is a strong indication, that the made assumptions in eq (I) and (II) about the different regimes are correct. However, interesting information can also be gained from the low density distribution above and below the "SD population". This can be deduced from the scatter plot of the same data, where the bin counts are encoded by different colors. In the plot (Fig. 4.2.40B), the SD population is visible as red to blue spots (medium to high intensity emission), whereas strongly quenched states (orange to green) seem to follow a significantly different relation.

For a better perceptibility of the different regimes, the scatter plot is split into three different parts, namely the distribution of k_r versus the band edge energy E for low, medium and high count rates (Fig. 4.2.41A-D respectively). Thus, the distribution for strongly

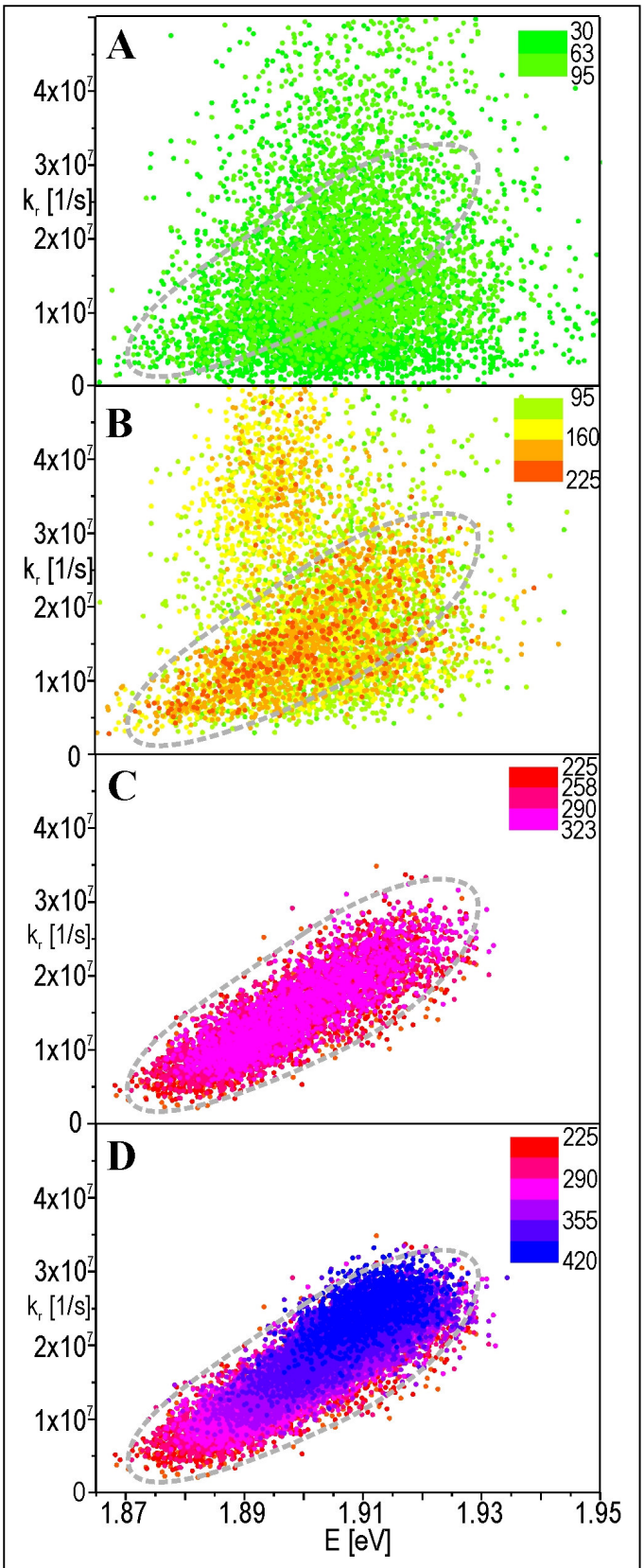

Figure 4.2.41: *Sections of the scatter plot of* k_r *vs* E *in Fig. 4.2.40B for low* ***(A)****, low-medium* ***(B)****, medium* ***(C)*** *and medium-high counts rates* ***(D)****. The color palette is identical to 4.2.40B and for comparison also the outline of the SD population from Fig. 4.2.40A is shown.*

quenched states (30-90 counts/1.2 ms) lies predominantly below the SD population (indicated by a dashed line) and shows no apparent correlation of k_r with the energy shift.

Rather, the distribution of k_r-values seems to be evenly distributed around the most probable emission energy at about 1.91 eV (= most probable F_2-value, from which the average quantum yield ϕ_{av} was obtained). In contrast, for the medium intensity spots (Fig. 4.2.41B, 90-205 counts /1.2 ms), two different populations can be distinguished. The first matches with the distribution of the SD population, whereas a second shows distinctly higher radiative rates and is found predominantly at lower band edge energies < 1.91 eV. The fact that this population is found at higher radiative rates than observed for the SD population at medium intensities (predominantly yellow and orange, 120-200 counts/1.2 ms), means that it consists of the quenched subpopulation **(3)**. More precisely, it is the part of **(3)** which protrudes below the lower bound, since a higher radiative rate results in states with a shorter lifetime for the same

count rates measured. It should also be noted that the separation of the populations of SD and **(3)** proofs that state **(3)** is not only a changed emission observed for strong quenching, but that the NC emits from a fundamentally different state, since for the same N_C-values also spots with the "normal" SD correlation can be found. At this stage it is not possible to define the nature of this novel emission more clearly, or to decide if there exists a different correlation which also includes the strongly quenched states observed in Fig. 4.2.41A to the subpopulation **(3)**. At least the homogeneous distribution of **(3)** in the density plot of the wedge (Fig. 4.2.40A) which is made up of states seen in Fig. 4.2.41B and C supports the latter assumption. However, it has to be mentioned, that features such as comparatively stronger emission under high power excitation, increased radiative rate and lowered band edge emission remind of biexciton emission (section 4.3).

The scatter plots for medium to high counts (Fig. 4.2.41D, orange to blue, > 205 counts/1.2 ms) monitors the homogeneous SD population without discernible deviations of the correlation between k_r and E deduced from the wedge-like appearance. It is worth to discuss several aspects of its appearance in more detail: First, one has to consider that the homogeneity is the measure for the accuracy of the model systems, since for a measured energy E (corresponds to the measured F_2-value) the same radiative rates are obtained nearly independent of the quenching. This can be deduced by comparing the SD distributions for low, medium and high count states (yellow to blue spots in Figs. 4.2.41B-D), which display near complete overlapping of the populations. Thus, for a strongly quenched state, the reduced lifetime can be "corrected" in eq. (III) through a proportionally decreased count rate to yield for a given F_2-value the same radiative rate. The finding that states with higher count rate can only be found above a certain band edge energy (with increasing "blue"-coloration, the left bound of the distributions recedes to the right), is rationalized by taking into account the intrinsic non-radiative rate: Because of the decreasing quantum yield with decreasing E, the maximum count rate obtainable also decreases, whereas the quenching shows no upper limit, i.e. the highest emission energies have no lower limit for N_C. Although the populations observed for different count rates show a broadend distribution, which is most probably caused by statistical errors and averaging effects due to fast photophysics, the distribution for all populations is similar and homogeneous. The only systematic deviation is a small shift to higher radiative rates for states with higher count rates, e.g. the center of the blue population in Fig. 4.2.41D is significantly above the center of the dashed ellipse. This is explained by the previous findings that the lower bound for the wedge of the analyzed NC does not proceed through

the origin (Fig. 4.2.33), as is predicted by eq. (II), but has an intersection with the y-axis slightly above it. This deviation to longer lifetimes, which was attributed to the long TAC range and the exclusion of biexciton influences, yields an underestimation of the actual radiative rate in eq. (III), i.e. for medium and strong quenching, the SD population is shifted to lower k_r-values.

Since these results demonstrate that the SD is intrinsically connected with the novel lifetime fluctuations, the basic knowledge about the SD is recapitulated. Thus, it is assumed that the distribution of electric charges in the environment of the NC creates electrical fields and lead to a distortion of the energy levels by means of the Quantum-confined Stark effect (QCSE) [89,232], most notably at the band edge. The parameters, that determine the energy band shift are the dipole moment $\vec{p}$ and the polarizability α of the respective NC, leading to a linear and quadratic Stark effect, denoted lSE and qSE, respectively:

$$\Delta E = -\vec{p} * \vec{F} - \frac{\alpha}{2} * \vec{F}^2$$

The energy band shift ΔW due to the lSE is dependent on the orientation of the NC dipole $\vec{p}$ with respect to the electrical field $\vec{F}$ either negative or positive, whereas the qSE is always negative. Typical colloidal NCs of type CdSe display both a dipole moment and polarizability of significant strength, but generally the polarizability is in comparison much larger. Therefore both effects are notable, however, already for fields of medium strength ($\approx$ 100 kV/cm) the qSE will dominate the band shift [89]. Explicitly, there exists a maximum blue shift, where, even when dipole and field are antiparallel to each other and thus cause a maximum ΔE, a further increase will lead to a predominating qSE and a relative red shift (decreasing energy). These findings are in agreement with what is observed in the present study and will be discussed in the following for the "on"-state of the measured τ-N_C-plots: If one assumes that significant electric fields build up in the NC environment statistically, one will observe a certain range of achievable field strengths $\vec{F}$ with the most probable occurrence at medium strength. Since there is no preferred field direction with respect to the dipole moment of the NC the average field on the NC should be zero. Thus, the most probable F_2-value observed is denoted "zero-field" (zf) F_2. The zf F_2-value corresponds to the most probable band edge energy which is found for the discussed NC of type QD655 at about 1.91 eV. If the lSE would be the dominating effect, one might expect both shifts from "zero field" to higher or lower F_2 with the same probability. But because of the qSE, shifts to higher F_2 will be observed predominantly. Furthermore, a maximum blue shift will occur since for fields above a certain strength the

qSE will always dominate, independent of the relative orientation of field and dipole. This gives a natural explanation for the finding that the "red end" (region of the upper bound with the longest lifetimes and highest F_2-values) of the "on"-state consists of broadly distributed and comparatively few spots, whereas the "blue end", where the maximum N_C-values are observed, is well defined.

For the obtained results, the dependence of the radiative rate on band edge shifts induced by the Quantum-confined Stark Effect (QCSE) is of special interest, since it is the first time this has been reported for colloidal NCs. However, from the general photophysics of NCs it is deduced that a red shift of a transition leads to a larger spatial extension of the electron- and hole-wavefunctions [255,288,289]. This results in a reduced overlap of the transition wavefunctions and a decreasing oscillator strength and explains qualitatively also the decreasing lifetime with increasing emission wavelength from QD605 to QD705. A similar characteristic is also found for organic fluorophores with the Strickler-Berg-Equation. Although for the used samples up to date no calculations of the quantitative amount of such shifts has been calculated, theoretical investigations of the effect of the QCSE on similar systems are in good qualitative agreement with the obtained results [290,291].

In this respect, it is surprising that e.g. in the case of the NC shown in Figs. 4.2.31/33 no significant alteration of the upper bound of the wedges is observed when changing from medium to saturating power excitation. Thus, a de- or increasing oscillator strength is expected (section 1.1) also to have an influence on the absorption cross section and therefore on the wedge shape, as has been discussed in section 4.2.9. This discrepancy can be explained by the excitation wavelength of 445 nm used for the experiments, i.e. excitation occurs into much higher energy states than the band edge energy, for which PL is detected. Apparently, the polarizability of these states is greatly reduced, so that influences of an electric field result only in marginal changes of the cross section. This seems to be very likely since wavefunctions of higher energy states are supposed to have the highest amplitude near the center of the NC, where effects of the electric field should be much weaker. A similar effect is also observed for smaller NCs (higher band edge energy) which are less sensitive to the QCSE.

Concerning the finding of an intrinsic non-radiative rate, the situation is more complicated. So far, NCs have been viewed as artificial atoms displaying negligible non-radiative rates if not regarding external quenching, i.e. a quantum yield close to unity [92,241]. Thus, reports about the estimation [241] or calculation of non-radiative rates have been rare [252] and further investigations are required to uncover the nature of this energy dissipation

mechanism. In principal the intrinsic non-radiative rate constant might shift with the QCSE, possibly via LO phonon coupling [90], which would explain the comparatively low PL quantum yields obtained for the dots.

4.2.11 Determination of the influence of media and polarization orientation on SD fluctuations

At this stage, it is of importance to check whether the described shifting mechanism has an additional influence on other observables that might interfere with the measurement. Thus, one feature of NCs is a comparably high polarizability α which together with an exerted field $\vec{F}$ in the environment results in an induced dipole moment $\vec{p}_{ind} = \alpha * \vec{E}$. This will lead to a change of the overall dipole orientation of the NC if ground-state and induced dipole moment are not parallel. However, it has been mentioned in section 4.2.5 that different orientations of the dipole of an emitter at a dielectric boundary influences the radiative rate constant. Since the NCs are generally measured immobilized at a glass-air-interface, it cannot be excluded that the fluctuations of the induced dipole moment cause the observed fluctuations of the radiative rate constant. Furthermore, the interface and the dipole orientation with respect to it also has a strong influence on the fraction of PL light that is emitted back into the half-space of the microscope objective [292,293]. This means that the detection efficiency might depend on dipole orientation changes induced by SD and would also give a possible explanation for a fluctuating.

Thus, it was examined whether a) a shift of the dipole orientation is observed and b) if the correlations, i.e. the wedge-like τ-N_C-distribution of states, are also observed in a homogeneous dielectric medium, since then a different dipole orientation will have only minor influences, on both radiative rate constant and the detection efficiency.

The influence of the first consideration was tested by substituting the dichroic by a polarizing beamsplitter, where light polarized parallel to the plane of in- and outcoming beams (p-polarized) is transmitted but for perpendicular (s-polarized) polarization, it is reflected. In this case, to excite all NCs homogeneously without photoselection of a certain polarization orientation, the near linearly polarized laser light of the diode (445 nm) was converted to circular polarization by insertion of a $\lambda/4$-plate. To exclude any interference of the dipole orientation on the glass surface, immobilized NCs of type QD655 were covered

with a drop of immersion oil (n = 1.55) which effectively means that the NC is embedded in a homogeneous dielectric medium and any influences of interfaces should be removed.

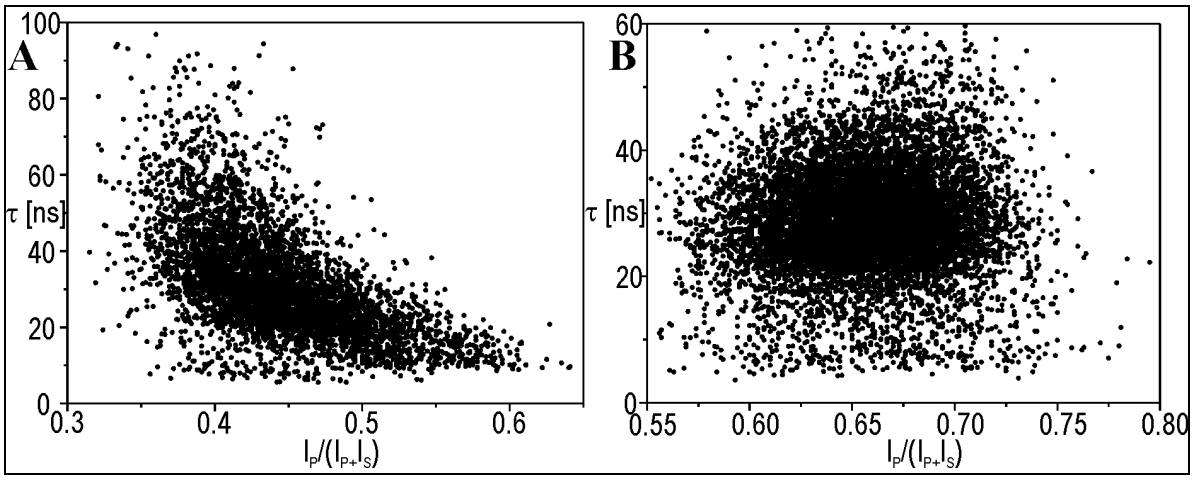

Figure 4.2.42: *Scatter plots of τ versus the polarization factor for two different NCs (QD655). Interestingly, for the NC shown in* ***(A)*** *a clear (anti-) correlation between both observables exists whereas this is not the case in* ***(B)****.*

Fig. 4.2.42 shows the distribution of the lifetime versus the relative polarization factor measured for two different NCs of type QD655. The latter is obtained similar to the F_2-value by calculating for each bin the counts detected on the parallel polarization detector (I_P) and dividing it by the sum of counts on both detectors (I_P+I_S). The distributions show significant fluctuations of the polarization compared to the observed fluctuations of F_2. In some cases even a correlation of the lifetime with the polarization change is observed, see Fig. 4.2.42A, which proofs that the change of polarization direction is indeed caused by SD. However, interpretation of the data apart from the qualitative depiction of the polarization orientation is very difficult: It has to be considered, that by examination of the PL light not the direct dipole orientation of the excited state (exciton) is observed, but the transition dipole moment, i.e. the difference of the dipole moment of exciton and ground-state, even though influences of the latter might be neglected due to weak polarizability. Additionally, the dipole moment of wurtzite type CdSe NCs is not linear, but displays a 2D degenerated dipole or as has recently been found is rather described as superposition of even three perpendicular oriented dipoles with varying emission strength [242]. Hence, an analysis of the observed presence or absence of a correlation of the polarization change with other observables requires a more detailed analysis.

However, it can be concluded from the weak change of the PL light polarization that its influence on other parameters such as the measurement of the F_2-value is of minor importance. This finding is also in agreement with the F_2-λ_{max}-calibration curves which

show a similar slope for the SD of different NCs, whereas a steeper or shallower slope would be observed when the SD is accompanied by significant polarization changes.

When imaging NCs covered with immersion oil under normal SFLIM conditions, i.e. with spectral and time-resolution, the wedge shape with the normal interrelations of F_2-value, lifetime τ and count rate N_C is observed. This data finally disproves considerations that the fluctuations of the polarization direction interfere significantly with the deduced correlations, neither by changes of the radiative rate nor through the detection efficiency. As only effect, a slight decrease of the average lifetime with immersion oil (e.g. Fig. 4.2.43B) compared to the measurements made under air (Fig. 4.2.25) is notable, caused by the higher refractive index of immersion oil (1.55).

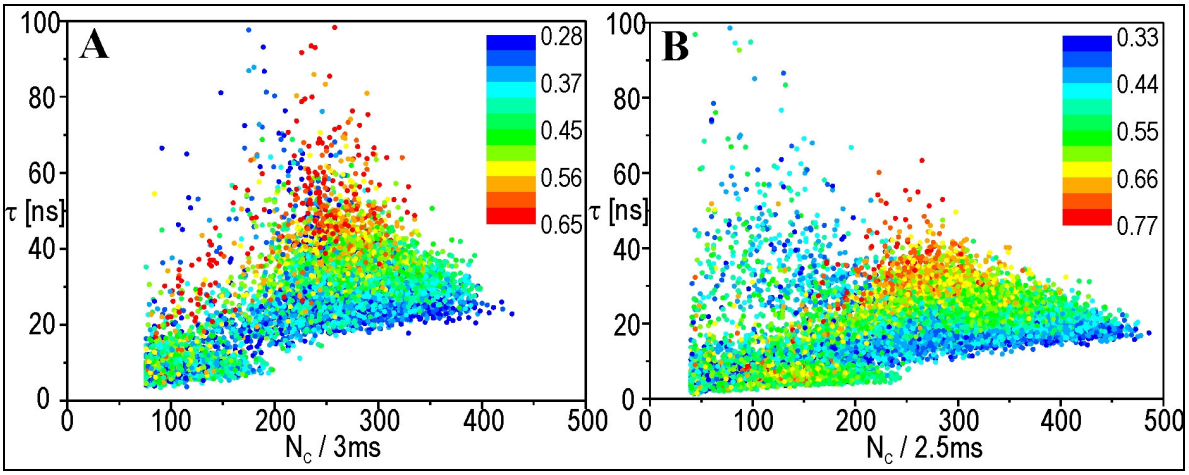

Figure 4.2.43: τ-N_C-*plots for two NCs (QD655) imaged with the SFLIM set-up and covered with immersion oil. No deviations from the wedge shape are observed, although especially the lifetime of the NC in* ***(B)*** *are significantly shorter (≈ 20 ns) than commonly observed for QD655, caused by the influence of the refractive index on the radiative rate constant.*

So far, the presented data have only dealt with analysis of NC photophysics measured under dry conditions or covered with an artificial polymer-layer. Although these have shown to give consistent results, the final aim of the investigations is a thorough understanding of the photophysics especially under physiological conditions, i.e. in aqueous solution. In this respect, experiments of NCs immobilized on a protein-matrix and immersed in an aqueous buffer solution were carried out.

Since the employed NC samples presented streptavidin-groups on the surface, glass-immobilization was accomplished by covering a glass slide modified with a positively charged silane (amino-propylsilane) with a 10:1 mixture of bovine serum albumin (BSA) and BSA covalently coupled to biotin-moieties. The tight and specific biotin-streptavidin bond facilitates rapid immobilization of biomolecules while retaining their physiological activities, since denaturation is prevented. Reactions were primarily carried out with the

QD705-sample since this proved to be the most stable type of NC in aqueous solution. QD605 was not photophysically stable under these conditions, so that even under modest laser irradiation rapid "blueing" occured. However, these features are rather attributed to the age (> 1 year) of the used samples than to a fundamental instability of these NCs which have already been used as PL probes under biological conditions [73,75].

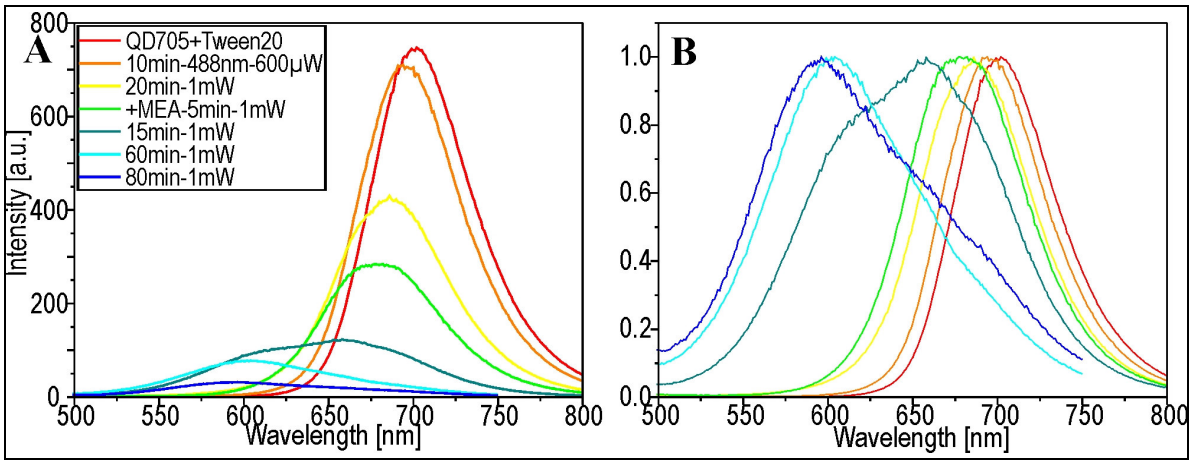

Figure 4.2.44: *Ensemble spectra of a 10˙8 M solution of QD705 in a PBS solution containing 0.1% Tween 20* ***(A)*** *with relative intensity depiction and* ***(B)*** *with normalized spectra. The power refers to the Ar+ laser used for bleaching; after 20 min, MEA was added to give a concentration about 1 M, and the irradiation continued. It is apparent, that the intensity is significantly reduced with consecutive blueing (compare Fig. 4.2.36).*

An "artificial" aging effect could be induced for QD705 samples by addition of 0.1% of the detergent Tween 20 to a several days old 10^{-8} M solution and prolonged irradiation of the ensemble in a cuvette under high power conditions (≈ 1 W at 488 nm). Hence, the spectra displayed under few hours of irradiation not only significant bleaching, i.e. reduction of the PL intensity (Fig. 4.2.44), but moreover a very strong blue shift of the maximum emission wavelength of more than 100 nm. The instability of the older NC samples in aqueous solution is most probably caused by slow irreversible detachment of the underlying ambiphilic polymer from the insulator shell which facilitates diffusion of oxygen into the outer shell and subsequent photooxidation. The effect of Tween 20 can be explained by a corrosion effect on the polymer coating, since it is also ambiphilic and might weaken the linkage of the polymer to the ZnS shell. However, when imaged under normal buffer conditions, QD705 showed no tendency of blueing or quenching.

To ensure stable imaging conditions for the NCs, an oxygen-removing enzyme (Glucose-oxydase) was added to the solution. As can be deduced from the τ-N_C-plots obtained under these conditions from QD705 (Fig. 4.2.45), the basic features of the sample remains with the typical wedge shape. Most notable is a stabilization effect, i.e. the already rare

quenching events under dry conditions (Fig. 4.2.28) and thus the lower bound almost completely vanished for QD705 when imaged in solution. However, blinking which is especially prominent for QD705 (compare Fig. 4.2.20) is only slightly reduced.

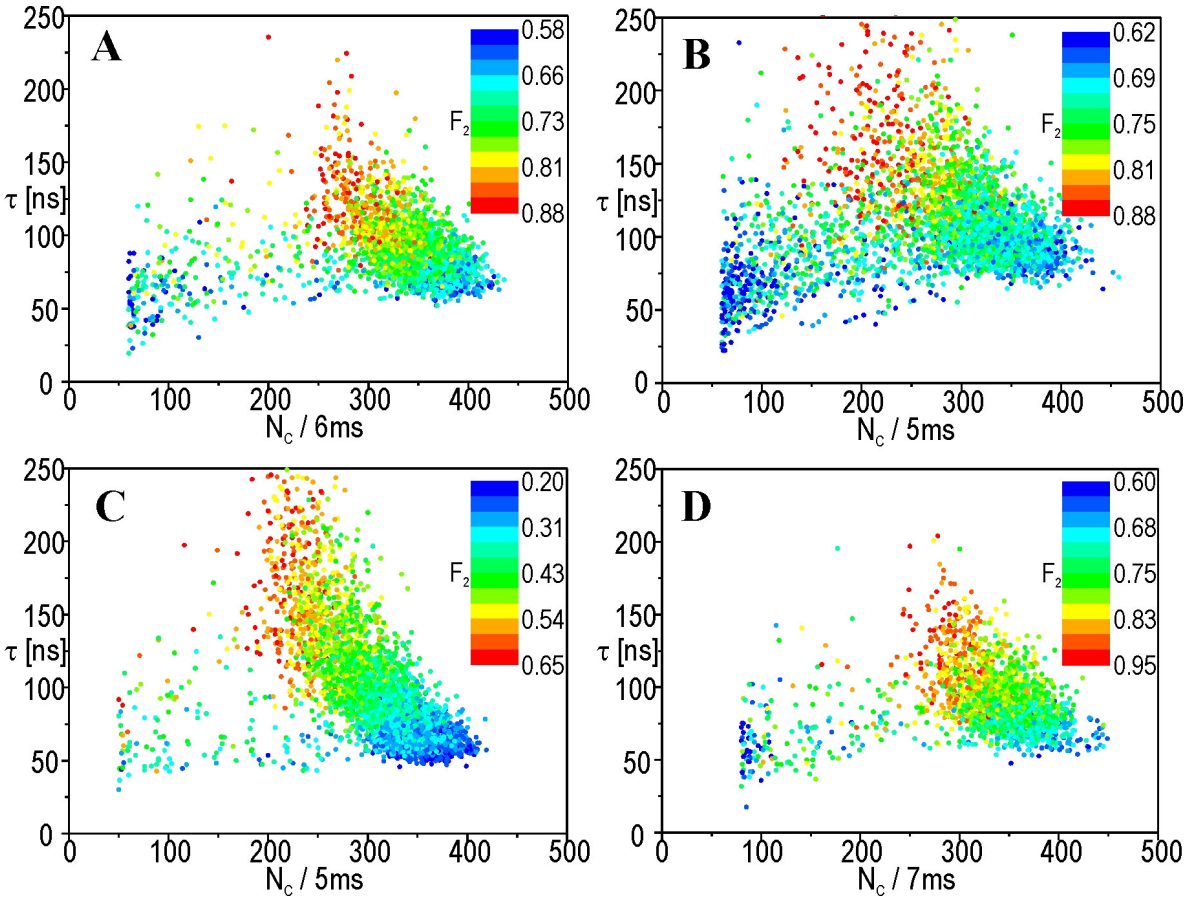

Figure 4.2.45: ***(A)-(D)*** *Scatter plots of* τ *versus* N_C *for four different single NCs of type QD705 imaged in PBS with Glucose-oxidase. The major difference to the results on dry surfaces in Figs. 4.2.27 is that the main emission stems from the "on"-state, i.e. apart from 4.2.45B no quenching occurs.*

As blinking also poses the most serious problems concerning imaging on the SM scale, the application of thiols as anti-blinking agents such as mercaptoethylamine (MEA) [72] and their overall effects on the NC-photophysics are of special interest. Hence, NCs immobilized on a BSA-biotin surface were immersed in a PBS-buffer containing 150 mM mercaptoethylamine. Experiments were again carried out with NCs of type QD705, partly because of the stability, but also because they show a stronger tendency of blinking than the other samples.

The effect of MEA on blinking is obvious in the transients of QD705 by a near-complete vanishing of blinking events for the binning chosen (Fig. 4.2.46), more prominent even when compared to transients obtained without MEA (Fig. 4.2.20). As can be deduced from the course of the lifetime and F_2-fluctuations, the correlation between the latter is still discernible, although not as clear as seen on dry surfaces, and the amount of SD seems to

be reduced. This features can also be deduced from the corresponding τ-N_C-plots in Fig. 4.2.47: whereas the principal "color" correlation is still obvious, i.e. red spots are predominantly found for higher τ and vice versa, the distribution is much broader in the presence of MEA. More obvious is the large lateral dispersion of the spots, so that spots with nearly the same F_2-value and lifetime are found over a wide range of N_C-values. This behavior cannot be explained by quenched states, since in this case the lower bound would be defined by linear functions inclined to the origin whereas the distribution here displays a horizontal shape.

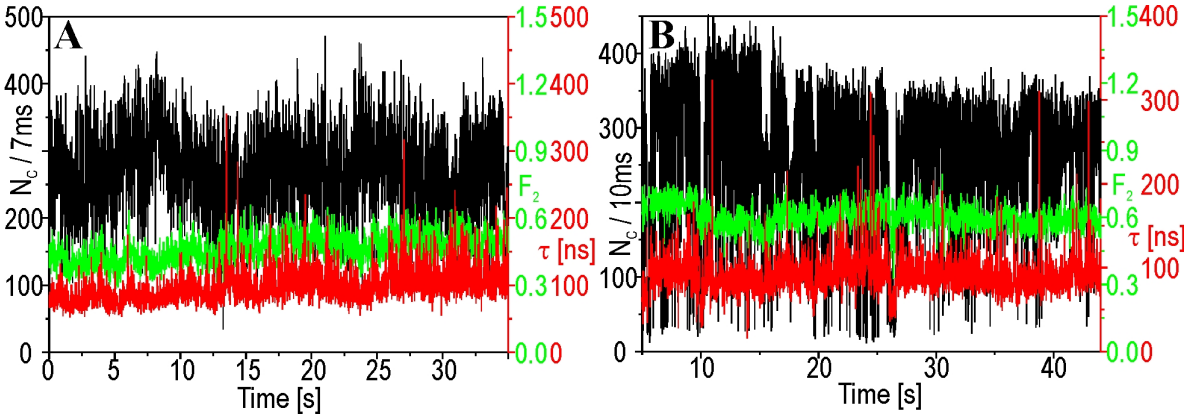

Figure 4.2.46: *Single NC transients of QD705 in PBS containing 150 mM MEA with intensity (black), spectral (green) and lifetime information (red). The blinking is strongly reduced, so that for the NC in* ***(A)*** *no blinking can be observed for the chosen binning. Whereas the correlation of* τ *with the* F_2*-value is still discernible, the fluctuations seem to be reduced.*

Therefore, the broadening is attributed to accelerated blinking events with an "on-off"-intermittency on faster scales than the time resolution provided by the bins. This results in reduced count rates by "off"-periods within the binning while the lifetime is not affected. The distributions seen in the plots do not show the typical wedge feature divided in upper and lower bound regime but rather a nearly statistical distribution where upper and lower bound are hardly discernible. Together with the reduced and blurred SD this not only suggests that both "on"- and "off"-periods are reduced, but moreover a general acceleration of photophysics including SD. Thus, the states cannot be resolved within the bins, but rather averaged values are observed similar to the characteristics observed for high excitation power.

These characteristics strongly support previous assumptions about an intrinsic interrelation of blinking events and spectral diffusion which has been inferred from different experiments before [235]. This can be rationalized by the fact that spectral diffusion is caused by charges in the NC environment, and blinking indicates loss and recapture of a charge (electron) from the NC into its environment.

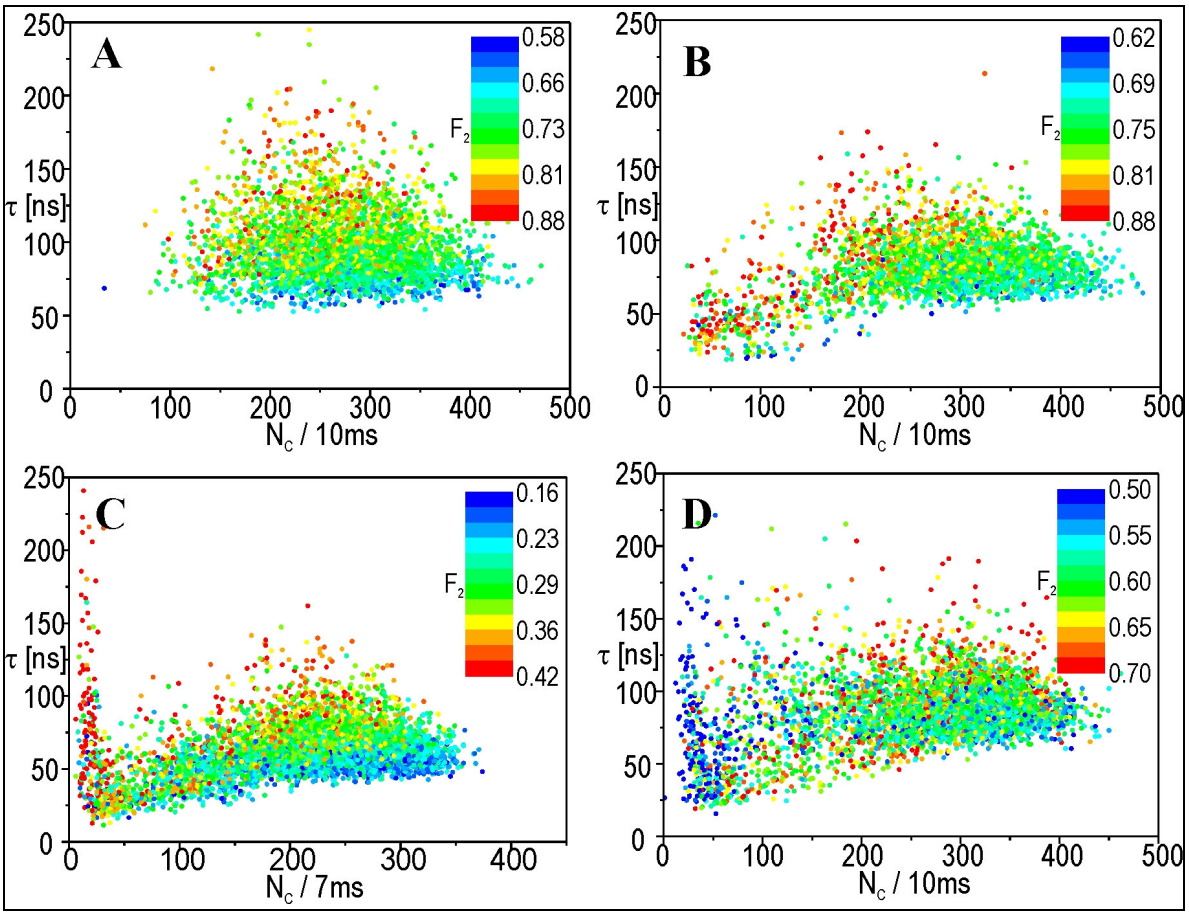

Figure 4.2.47: ***(A)-(D)*** *Scatter plots of* τ *versus* N_C *for four different single NCs of type QD705 imaged in PBS containing 150 mM MEA.. The correlation of* τ *with the* F_2*-value is compared to Fig. 4.2.45 hardly discernible, also the distribution is rather diffuse with no obvious upper or lower bounds. For the NCs in* ***(A)*** *and* ***(C)*** *it is notable, that spots with identical* F_2*-values have a rather horizontal distribution compared to the significant slope seen for the wedges with strong SD (e.g. Figs. 4.2.31/33) or vertically scattered as observed for high statistical errors (Fig. 4.2.28). This characteristics can be explained only by rapid blinking*

4.3 Investigation of Bi- and Triexciton emission from single NCs

The methods which are the basis of high precision distance measurements within cells require the existence of two dyes with significantly different emission properties (spectrum, lifetime) within the excitation volume. Hence, distance measurements with SFLIM are not possible for assemblies of the same dye, i.e. as expected for multiprotein-complexes made up of identical subunits (e. g. for polymerases). It is possible, though, to count the number of dyes and accordingly of subunits within the focus using coincidence measurements. This requires knowledge about the antibunching characteristics of the dyes. Concerning antibunching characteristics, several types of colloidal NCs have already been investigated and established to constitute near perfect single photon emitters due to strong quenching of multiexciton emission [96,97,107,294,295]. On the other hand, epitaxially grown NCs are known to show significant multiexciton emission [98-100,257] and a ready explanation for the discrepancy between differently synthesized NCs has yet to be established. It has already been mentioned in Section 4.2.5 that the coincidence ratios found for NCs of QD655 were unusually high even after background subtraction. In this chapter, investigations concerning the cause of these ratios and the role of multiexciton states is discussed.

4.3.1 General measures for determination of coincidence ratios

The set-up for these measurements is in principal identical to SFLIM with the main difference that a 50/50 non-polarizing beamsplitter is used in front of the two APDs. This is necessary because of the wide spectral dispersion on the surface, since the number of coincidences drops with a deviation of the F_2-value from 0.5 (section 4.2.4) [59].
Although a principal introduction to the coincidence ratio and its application has been given, it is emphasized here, that the application of a pulsed laser provides more information from a Hanbury-Brown-Twiss set-up than using continuous wave excitation [296]. On the one hand, much lower detection count rates are needed in order to extract significant information concerning the antibunching characteristics of the dye. On the other hand, the technique enables measuring of the lifetime of the emitting state(s), i.e. for each

photon not only the relative but also the absolute arrival time with respect to the laser pulse is recorded. Therefore, the macrotime interval can be replaced in the coincidence (two photon) histogram by the absolute interphoton time. For one or more dyes within the excitation volume, a monoexponential decay of the lifetime is observed symmetrically to both sides of the laser start pulse in the lateral peaks, because the first photon after the pulse may be detected on each of the two APDs with the same probability.

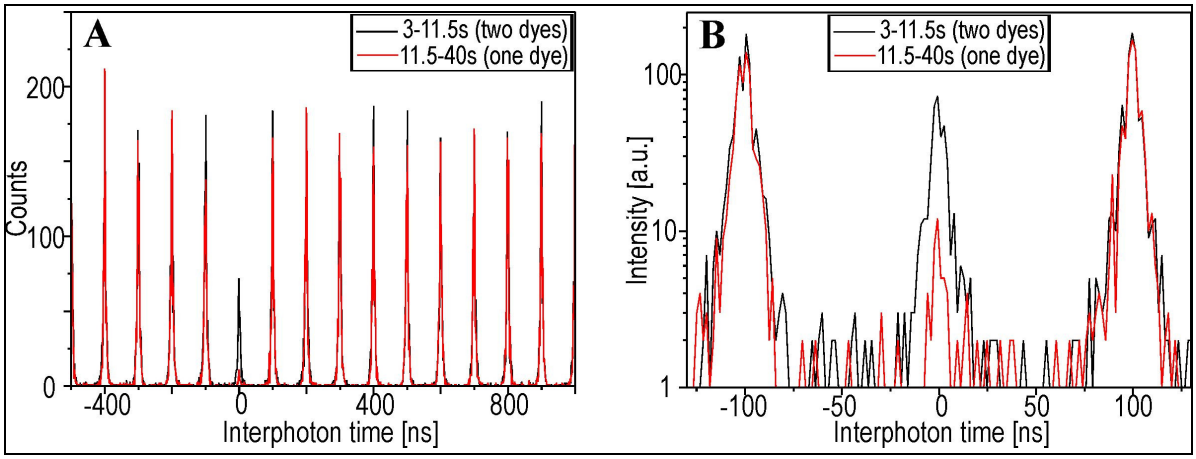

Figure 4.3.1: *Coincidence histogram with the absolute interphoton times shown for the Atto647-dye presented in Fig. 4.2.10.* ***(A)*** *The symmetric peaks seen in the histogram are made up of the monoexponential decay of the dye to both sides of the laser pulse.* ***(B)*** *The monoexponential characteristics of the decay are visible in a zoomed out portion around the central peak of* ***(A)****.*

In the presented case for the dye Atto647 displayed in Fig. 4.2.10, section 4.2.4, in the interval from 0-11.5 s (two dyes, black line), the central peak shows the same decay as the lateral peaks (≈ 3.5 ns), a clear indication, that it stems from a second dye with nearly the same characteristics. In contrast, the decay for the residual counts after the photobleaching event (11.5-40 s) seems to be much shorter and implicates background scattering as source. In the following, it is crucial to distinguish between unusually high coincidence ratios caused either by extrinsic background contributions or by an intrinsic source, e.g. biexciton (BX) emission. Generally, for a known S/B ratio, it is possible to account for the non-correlated contribution to the central peak by a correction amount that can be subtracted from the measured ratio. The dependence on the expected ratio of the central peak to the lateral peaks for a single emitter on the S/B ratio is calculated by $R_C = \frac{1+2*(S/B)}{1+2*(S/B)+(S/B)^2}$. For F_2 = 0.5 [59], and the resulting plot is shown in Fig. 4.3.2A. Although the ratio will slightly decrease when more dyes are in the focus, the error made for the coincidence ratios investigated (normally below 0.5) can be assumed to be negligible. Accordingly, the obtained R_C-value given by the formula above for the

determined S/B ratio was subtracted from the average coincidence ratio to yield the corrected value R_C. Here, two things have to be considered for this correction:

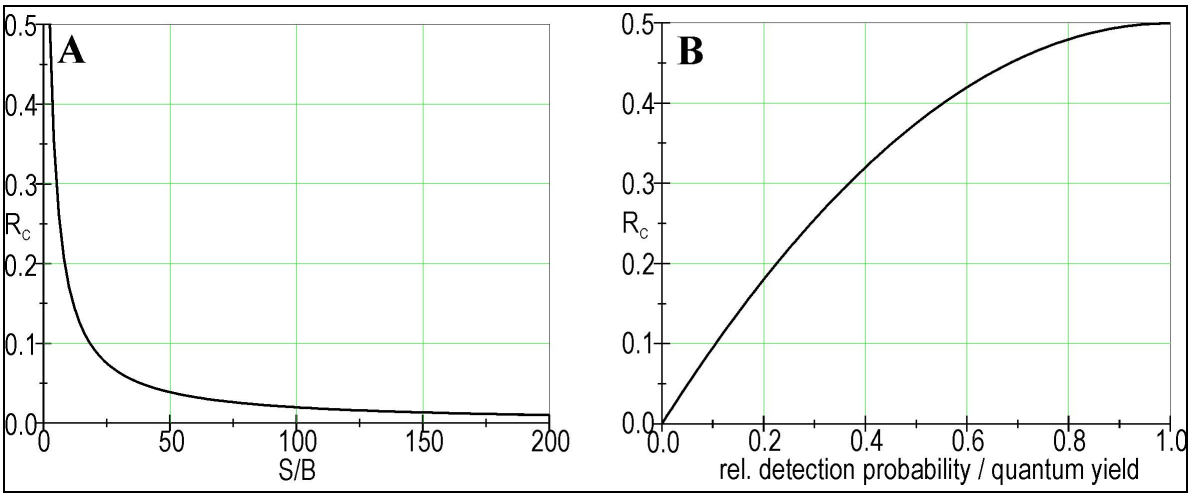

Figure 4.3.2: ***(A)*** *Expected coincidence ratio for a single photon emitter depending on the background contribution.* ***(B)*** *Expected coincidence ratio for two emitters that are not detected equally or exhibit a different quantum yield. No background is considered.*

In most cases, scattered light or autofluorescence from the glass is supposed to create a constant background whose intensity can be measured for different excitation powers and compared with the corresponding emission intensity of the respective chromophore. However, in the present work, it was often found that the background is not homogeneous for an imaging area, but might vary from spot to spot, which corrupts the possibility of a simple background correction. Therefore, the background was directly obtained "on the spot" which is possible due to the frequent blinking events. To differentiate between blinking and strongly quenched states, which might erroneously be taken for a higher background, the emission gaps with the lowest count rate were used for the S/B determination. The most important aspect constitutes the differentiation between a high R_C caused by an intrinsic PL source or by a photoluminescent object, e.g. a second NC nearby. Depending on the relative emission intensity of the NCs, R_C might be quite different from 0.5 and cannot be differentiated from intrinsic factors simply by an average value. This problem can be circumvented by using only spots with a nearly constant R_C, since two NCs emit independently and show intervals with different relative emission. Accordingly, a fluctuating R_C is observed, whereas an intrinsic source should be supposed to emit correlated to the main PL, so that the ratio should stay on a nearly constant level (compare section 4.2.5).

Altogether, if after background correction and the above described examination for independent emitters nearby a significant R_C-value remains, it can be attributed to an

intrinsic source. At first, the most interesting parameter of this source is its relative emission strength to the NC PL which can be ascribed solely to a difference in the PL quantum yield because of equal excitation and detection probability. Since absolute quantum yields are difficult to discern, a relative quantum yield ϕ_R is defined as quantum yield of the intrinsic source devided by that of the normal PL. The influence of ϕ_R on the corrected coincidence ratio is easily derived by: $R_C = \phi_R - \frac{1}{2} * \phi_R^2$, and the course of the interrelation is depicted in Fig. 4.3.2B. The same relation holds also for a different cause of additional PL, e.g. an adjacent NC which is slightly deadjusted with respect to the focus, so that the relative detection efficiency is lower than for the NC in the center of the laser spot.

4.3.2 Increased coincidence ratios as indicators of significant BX emission of QD655

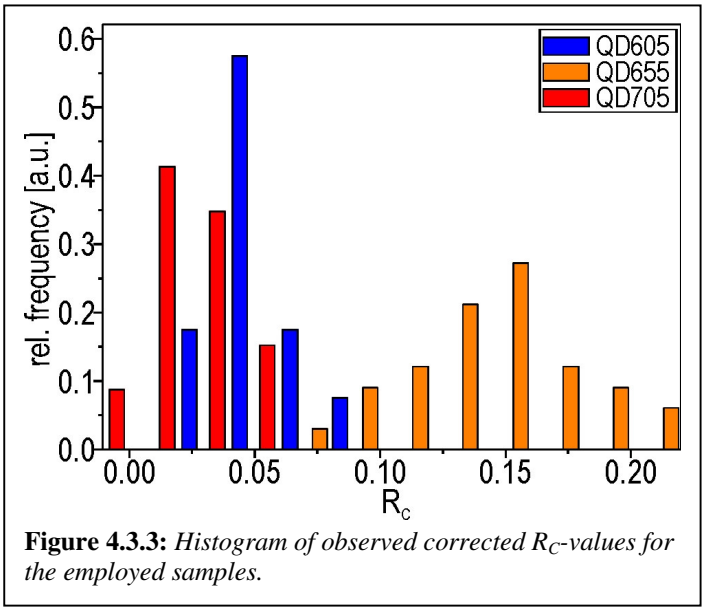

Figure 4.3.3: *Histogram of observed corrected R_C-values for the employed samples.*

Since the average coincidence ratios of QD655 were found to be unusually high, it was necessary to compare these results with R_C-values from other NC samples, to check both the accuracy of the set-up and other NCs for a similar behavior. Hence, the coincidence ratios of about 40 transients of different NCs imaged with a 50/50 non-polarizing beamsplitter and appropriate filters were measured using medium excitation intensities (≈ 1 kW/cm^2). The distribution histogram of the background corrected R_C-values determined by the method described above are displayed for the three samples in Fig. 4.3.3. For QD705, an expected ratio for a single photon emitter with R_C only slightly higher than zero is observed, the residuals being accounted for by statistical errors due to comparatively high background (no suitable bandpass filter for QD705 was available). On the other hand, the ratio R_C of QD655 is much larger for all NCs observed, with an average value ≈ 0.15, whereas the result is ambiguous for QD605, significantly below 0.1 but still higher than for QD705.

As the ratio R_C does not show significant fluctuations over time (compare Fig. 4.2.19), neither interferences from impurities nor from other non-correlated sources can account for the comparatively high R_C-values. Therefore, only an intrinsic emission as cause for the high coincidence ratios remains, for which biexcitons are the most likely explanation.

In order to proof significant biexcitonic emission properties of QD655, the dependence of the coincidence ratio on the excitation energy was investigated. To understand this procedure it has to be recapitulated that biexcitons (BX) are not a higher energy state of a single particle (exciton, X), but two independent particles in the ground state which couple with each other (note that this is possible since excitons are bosons). Hence, a BX can be excited from an X by photon absorption which means that the probability to induce a BX-transition is proportional to the number of X states and the excitation power. Thus, X-creation probability is proportional to the laser power whereas BX goes with the square of the power, and the ratio R_C is expected to increase with excitation intensity.

Fig. 4.3.4-6 show the transients (black) and the coincidence ratios (blue) for three single NCs of type QD655 excited at 635 nm (Fig. 4.3.4) and 445 nm (Figs. 4.3.5/6), respectively, imaged with a 50/50 non-polarizing beamsplitter under variable excitation intensities. For all measurements of BX emission, a bandpass filter from 645-685 nm was employed to exclude any interferences from triexciton (TX)-emission (section 4.3.6) [267]. Even at low intensities (< 0.5 kW/cm^2) and for high S/N ratios (> 50) R_C is sparely below 0.1 and increases slightly when changing to medium intensities (< 1 kW/cm^2). Only when approaching saturating conditions for X-generation, there is a dramatic increase with R_C-values generally above 0.2, but often exceeding 0.3, although the S/N is always > 50. Despite a certain degree of fluctuations which can be explained by statistcal errors, R_C remains constant for a certain excitation intensity which is a good proof of a single NC within the excitation volume.

Since these results give a clear indication that BX emission is responsible for the high R_C ratios observed, it is of interest to further characterize the BX state. An important parameter in this respect is the PL lifetime whereas spectral information cannot be used for a differentiation between X and BX emission, as both show similar PL spectra [267]. On the other hand, the BX should display both a higher non-radiatave rate due to efficient Auger processes and an increased radiative rate because of coupling of the two excitons. Accordingly with increasing R_C the uptake of a short component in the PL decay curves is expected. The resulting PL decays for the regions of different excitation intensities are

displayed for each of the above shown NCs in Figs. 4.3.7A-C (The decays are normalized to about 80ns after the laser pulse, i.e. ≈ 120 ns in the TAC window).

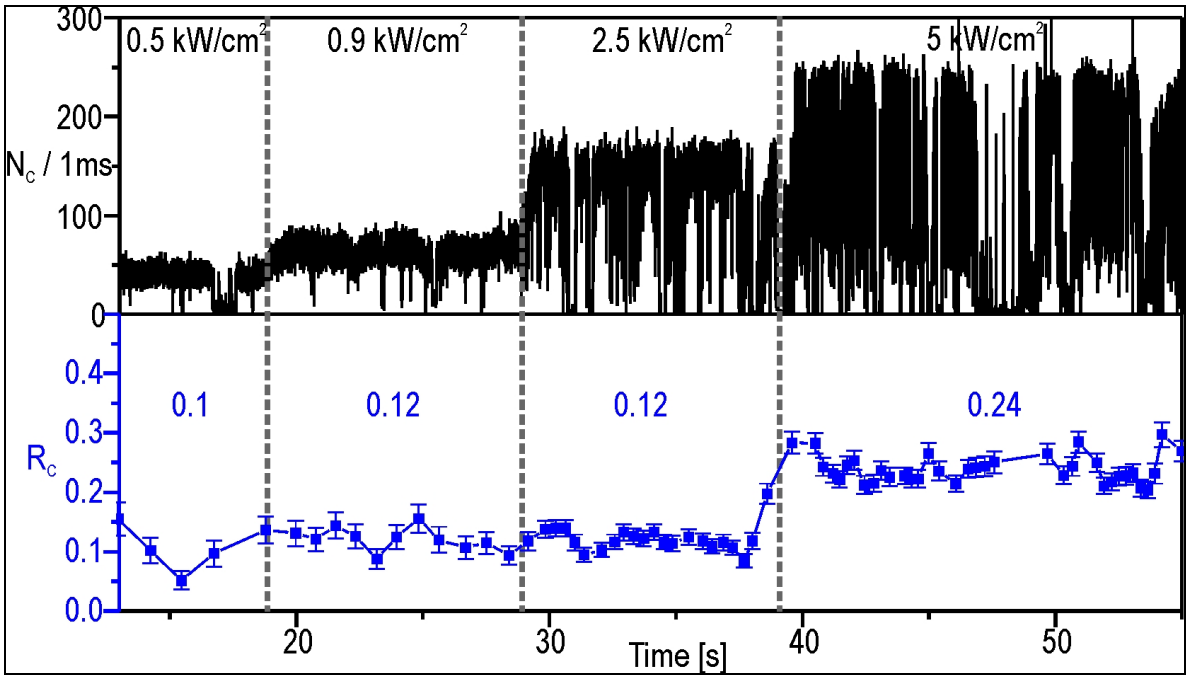

Figure 4.3.4: *Transient of a single NC QD655 excited at 635 nm under various excitation intensities power, with PL intensity (black) and coincidence information (blue) For each section separated by dashed lines, the excitation intensity (black) and the average* R_C*-value are given. The dependence of* R_C *on the laser power is apparent.*

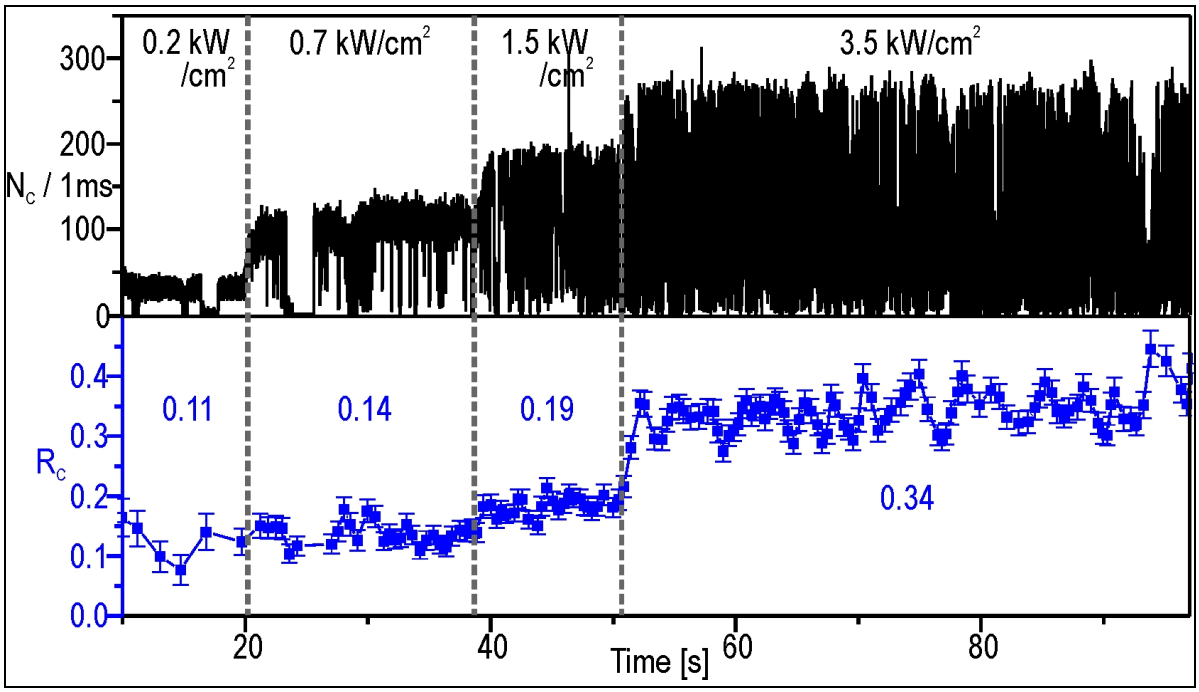

Figure 4.3.5: *Transient of a single NC QD655 excited at 445 nm under various excitation powers, with intensity (black) and coincidence information (blue).*

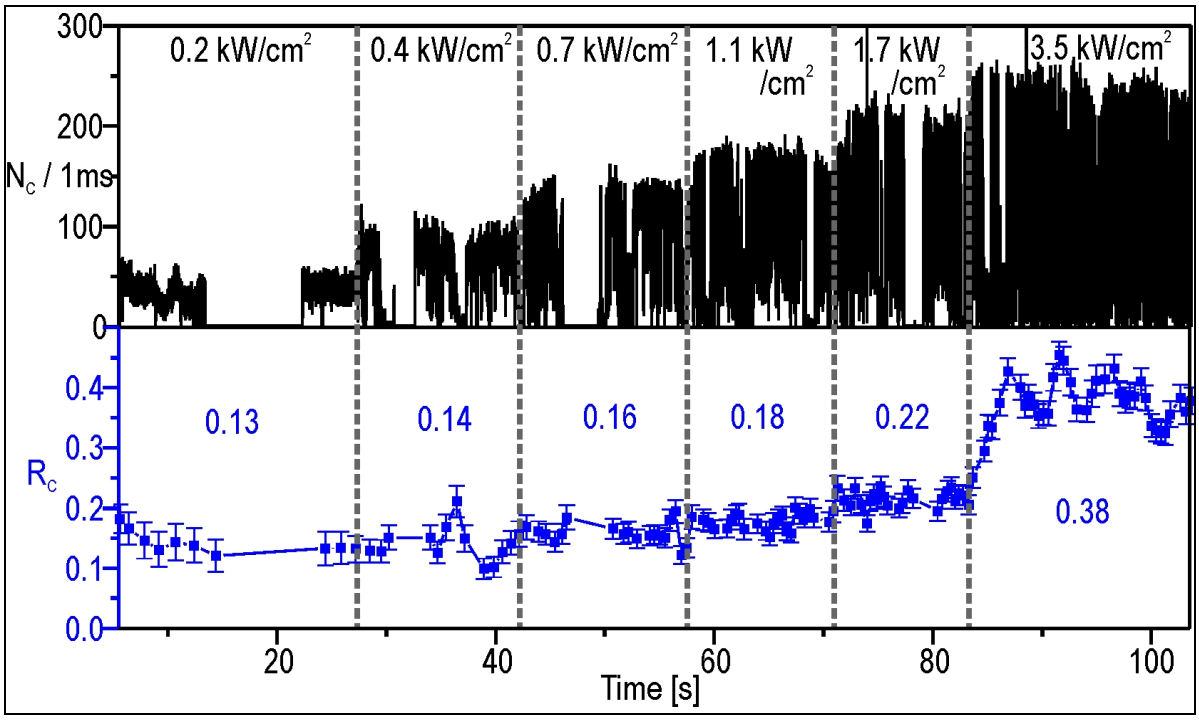

Figure 4.3.6: *Transient of a single NC QD655 excited at 445 nm under various excitation powers, with intensity (black) and coincidence information (blue).*

It is obvious that for low intensities only long decay components are observed and a short component appears with increasing excitation intensity. However, regarding a selective extraction of the BX photons from the overall decay seems to be problematic: The most straightforward analysis of a two-level decay consists of a biexponential fit to extract each of the involved PL processes. This is problematic in the case of NCs which are known to display multiexponential kinetics of the X-decay even under low power excitation for longer times [91,92].

Recently, measurements indicating a significant BX decay for similar NC samples have been reported by Fisher et al. who suggested a different fitting procedure to obtain the BX decay both on ensemble and SM-level [267]. Therein, a sample of NCs or a single NC was imaged under different excitation power and the PL decay was recorded. The decay curve obtained for the lowest power, i.e. with negligible BX contribution was set as decay standard which was fitted into the long tail of the decays measured for higher power. Since it had been found that BX decay was completed 4.2 ns after the laser pulse, fitting was proceeded at this time range. After subtraction the purely mono-excitonic data the resulting decay was defined to consist solely of BX component which was fitted with a monoexponential decay curve with a lifetime about 0.79 ns.

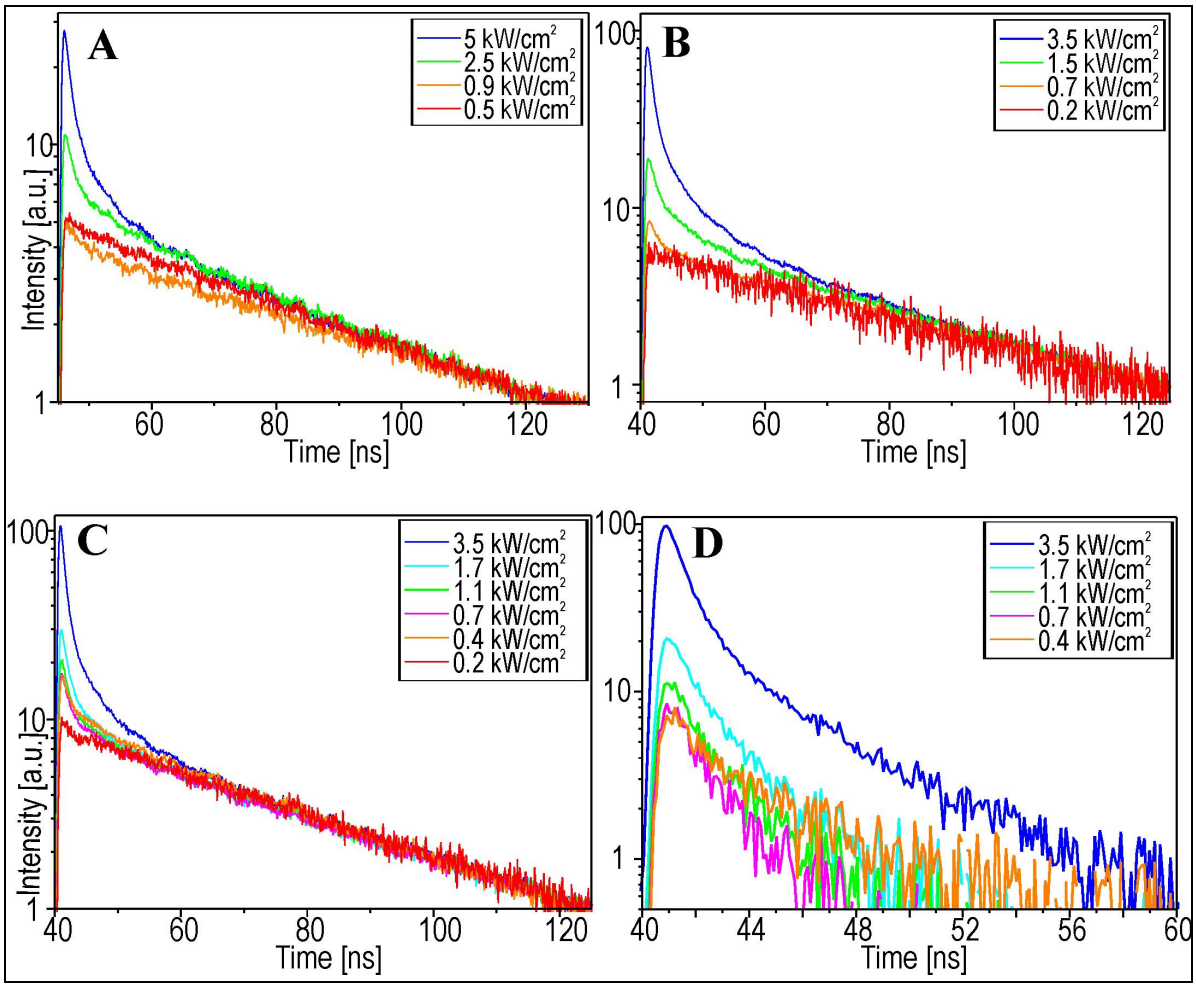

Figure 4.3.7: ***(A)-(C)*** *Ensemble decays of the different power sections for the NCs displayed in Fig. 4.3.4-6, respectively. All decays are fitted to superimpose after 120 ns (80 ns after the laser pulse).* ***(D)*** *The five resulting decays for the NC in Fig. 4.3.6 after subtraction of the fitted, lowest power decay (0.2 kW/cm²). The non-exponential characteristics is obvious.*

However, in the present case this method proved to be problematic for an unambiguous assignment of the BX decay components because of several obstacles: In Fig. 4.3.7D an analog procedure was accomplished using the parts of the transient with different excitation powers to calculate the decay curves of the fast components not present under low excitation conditions. It is quite obvious from the curves, that 4.2 ns after the pulse (at about 45 ns in the TAC window) superimposition of the decays is not achieved, that it takes at least 10 ns, or for the highest excitation power rather 25 ns for complete overlap with the low power decay. Since it is not possible to unambiguously define a complete decay after 4.2 ns the decay was fitted until sufficient superposition was achieved and the high power curves "normalized" by subtraction of the low power decay. The resulting residuals for the five excitation regimes are shown in Fig. 4.3.7D and display obviously multiexponential decay characteristics, although all show similar features. Despite the fact, that there is no rationalization for the existence of a second, longer decay component regarding BX

emission, the curves were fitted with a biexponential model giving reasonably good fits ($0.95 < \chi^2 < 0.98$). The fitted components are shown in Table 4.1:

Nr/Power [kW/cm^2]	short component [ns]	long component [ns]	χ^2
Sum II-VI	0.95±0.05	5.34	0.995
II/0.3	0.86±0.15	6.76	0.920
III/0.5	1.48±0.36	52.4	0.953
IV/0.75	0.98±0.22	3.47	0.971
V/1.2	1.08±0.09	4.01	0.991
VI/2.5	0.93±0.02	5.68	0.996

Table 4.1: *Biexponential fits from residuals of high-power decay curves with the decay measured for the lowest power.*

The data demonstrate, that although the assumed lifetime range of about 1 ns for the BX seems a reasonable value, the method displays several limitations. Thus, the existence of a second (or rather more) lifetime component between the BX and the X decay indicates the upcoming of additional quenching pathways. This is in accord with recent findings which showed that Auger processes accelerated via multiexciton pathways have an important influence on the decay time independent of radiative emission from multiexciton states. This is also in accordance with the results obtained in section 4.2.9 which showed a stronger population of quenched states for all NC samples, even if negligible multiexciton emission was present, e.g. QD705 (see Fig. 4.2.38). Although it may be rationalized that PL of typical X quenching takes place on longer timescales than expected for BX decay, occurrence of strong quenching is expected to interfere with the BX decay. Finally, it would be desirable to actually find a proof that the extracted decay characteristics stem only from BX emission without other interferences.

4.3.3 Specific measurement of PL decay from BX emission

For these reasons, it was envisioned to combine all available information of the BX PL using a different observables, to extract the BX photons from the data. In the present case, the central piece of information about BX emission is the coincidence ratio, or rather the photons of the central peak which were used to calculate the ratios. It has to be considered that the central peak consists of a number of photon pairs, all emitted within the same laser

pulse (macrotime interval). Since X can emit only once per pulse, it was deduced that BX as a second emitter was present to explain the unusually high number of photon pairs. Accordingly, if the background contribution is negligible, each of the photons stems from a photon pair emitted from both the excitonic and biexcitonic state. For a differentiation between each of these photons, it has only to be considered that the BX-state is made up of two excitons within the same NC, and that BX emission -by definition- always occurs before X emission. Summarized, for each of the photon pairs within the central peak, the first detected, i.e. that with the shorter microtime, stems from BX decay and the second from the subsequent X decay.

Therefore, for the analysis of the BX data, the employed coincidence software was modified in a manner that photon pairs detected for the same laser pulse are splitted into a first and a late channel. Since for each photon also the microtime is registered, this was used to construct separated decay curves for each of the channels. Before the results of the BX measurements on NCs are discussed, it is necessary to consider the implications of this analysis on the decay for photons stemming from independent emitters, since also background photons are present in the central peak. In contrast to correlated photon pairs, the effect of the channel splitting on photons stemming from independent emitters results in a distortion of the decays. In addition, the extent of which depends on the lifetime difference of the involved emitters. The most serious interference occurs for two identical lifetimes and is demonstrated in the example of the lateral peaks of a NC QD605 in Fig. 4.3.8.

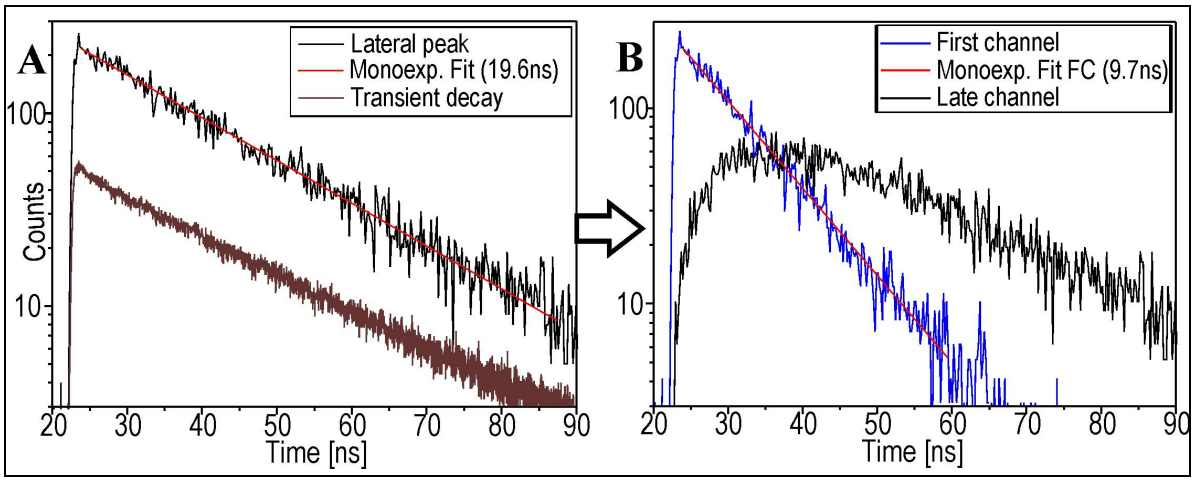

Figure 4.3.8: ***(A)*** *Decay in the lateral peak (black) for an NC QD605 excited at low power displaying nearly monoexponential decay characteristics with corresponding fit (red). For comparison the decay of the whole transient is also shown (brown) with identical characteristics.* ***(B)*** *Decay of the lateral peak photons from* ***(A)*** *divided into a first (blue) and a late channel (black). For comparison, the monoexponential fit of the blue curve is shown with about half the decay time as found for the lateral decay in* ***(A)****.*

Since the NC displays homogeneous emission without significant quenching, the PL decay of both the transient and the resulting lateral peak is well described by a monoexponential decay which yields 19.6 ns for the lateral peak. Since the decay in Fig. 4.3.9A stems from a lateral peak it consists of photon pairs which have been detected at different macrotime intervals, i.e. laser pulses, and hence were emitted independently. If from each of the photon pairs always the first one is picked, it is obvious that the probability to find a photon in the resulting distribution early in the decay has doubled compared to the original lateral peak decay. Accordingly, it is expected that the decay of the resulting distribution in the first channel has doubled compared to the original decay, i.e. the lifetime in the first channel is halved.

This is demonstrated by the PL decay observed in the first channel of the lateral peak from Fig. 4.3.8 yielding monoexponential characteristics with a lifetime of about 9.7 ns, i.e. 50% of the original value. On the other hand, the decay in the late channel is made up by a subtraction of the first channel from the original lateral peak decay, characterized by a slow rise time. This relation only holds for identical decays of the photon pairs and is somewhat more difficult to calculate for unequal decays. However, it is obvious that photons from a state with very short decay characteristics are predominantly found in the first channel compared to a second state with much longer decay.

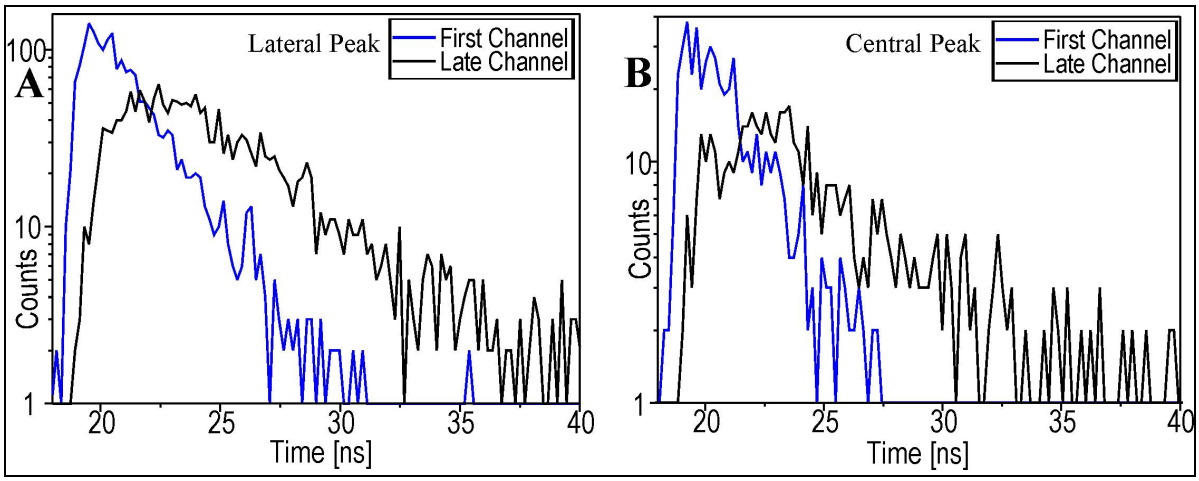

Figure 4.3.9: ***(A)*** *Lateral and* ***(B)*** *central peak decays from the example in Fig. 4.3.1 from 0-11.5 s, divided into first (blue) and late (black) channel. The lateral peak* ***(A)*** *shows the expected features with a shorter component in the first and a long rise in the late channel. Since the decays for the central peak* ***(B)*** *show identical features, it can be assumed that they stem from independently emitted photons, i.e. two dyes.*

It should be considered here, that the characteristics in the lateral peak are similar to the case in the central peak, when two different chromophores are within the focus, since then the detected photons are not correlated, either. This is demonstrated for the Atto647-dye already depicted in Fig. 4.2.15 and Fig. 4.3.1, at the beginning of the transient, where two

dyes are detected with nearly the same intensity (Fig. 4.3.9). Comparison of the first and late channel decays of the lateral peak with the characteristics in the central peak show nearly identical behavior, since both Atto647 dyes have nearly the same lifetime. Thus, comparison of the results obtained from the lateral peak with the central peak decays gives strong hints, whether the coincidences stem from correlated or non-correlated photon sources.

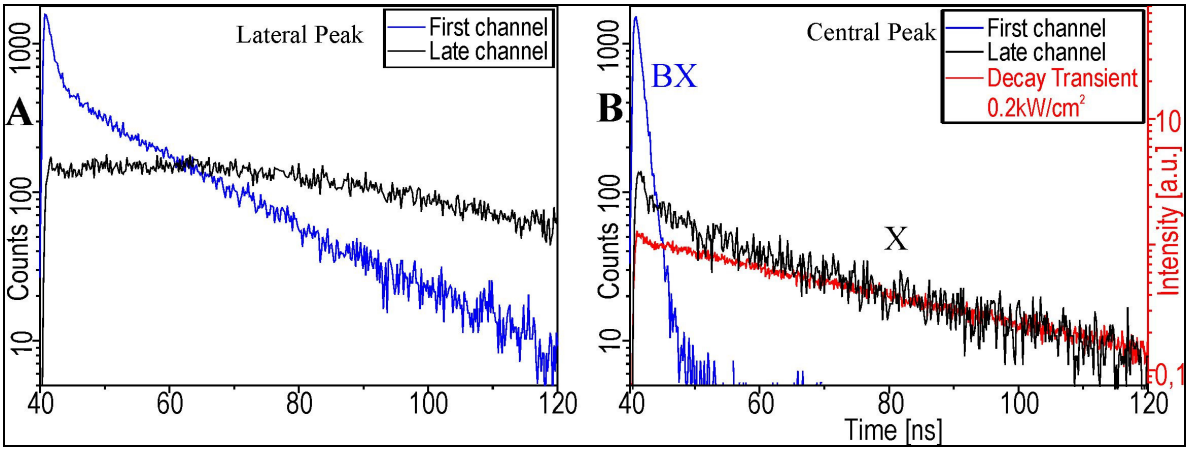

Figure 4.3.10: ***(A)*** *Lateral and* ***(B)*** *central peak decays from the transient of the single NC QD655 depicted in Fig. 4.3.6, divided into first (blue) and late (black) channel. For the central peak* ***(B)*** *the characteristics are strikingly different from the lateral peak with a very short component (BX) in the first channel, compared to a long component without significant distortion features (X). The long component (black) fits almost perfectly with the transient decay of the same NC taken at low powers (red), indicating origin from X decay. Note that the decay binning is reduced in* ***(B)*** *compared to* ***(A)*** *resulting in higher counts per bin.*

With this in mind, the presented method can be used to elucidate the emission characteristics of the investigated NCs. Fig. 4.3.10 shows the channel decays of the lateral peak integrated over the whole transient of the NC depicted in Fig. 4.3.6 and displays the expected features of a slightly shortened decay in the first channel together with the rise-time in the late channel. However, for the same transient, the decays for the central peak have fundamentally different properties with the first channel showing only one significant component with a very short lifetime, whereas the late channel shows a normal decay without significant rise time. If this decay is compared to the NC decay for low power excitation (red curve, 0.2 kW/cm^2, from 7-28 s in transient Fig. 4.3.6), it is almost identical apart from some shorter decay components.

These findings can be readily explained by the expected BX emission characteristics, since then the BX photons are exclusively in the first and the X photons only in the late channel. Although in general, similar features might be expected from a second NC within the focus, this seems highly unlikely since it would mean that a) one NC has to be constantly in a very homogeneous quenched state, b) the other NC should always display stable emission and c)

both NCs must blink synchronously. Otherwise, if the quenched NC shows higher emission states, this would be visible as a longer component in the first channel, whereas a quenching of the second NC would be visible as very short decay component in the late channel. This novel method also helps to explain the feature that decays which were obtained by subtraction of the low power from the normalized high power decay curves had to be fitted with a biexponential function: as has been suspected and can be proved by the novel analysis. The very short component stems from BX emission and the second, slightly longer component, is due to quenched emission of the X induced by high power excitation.

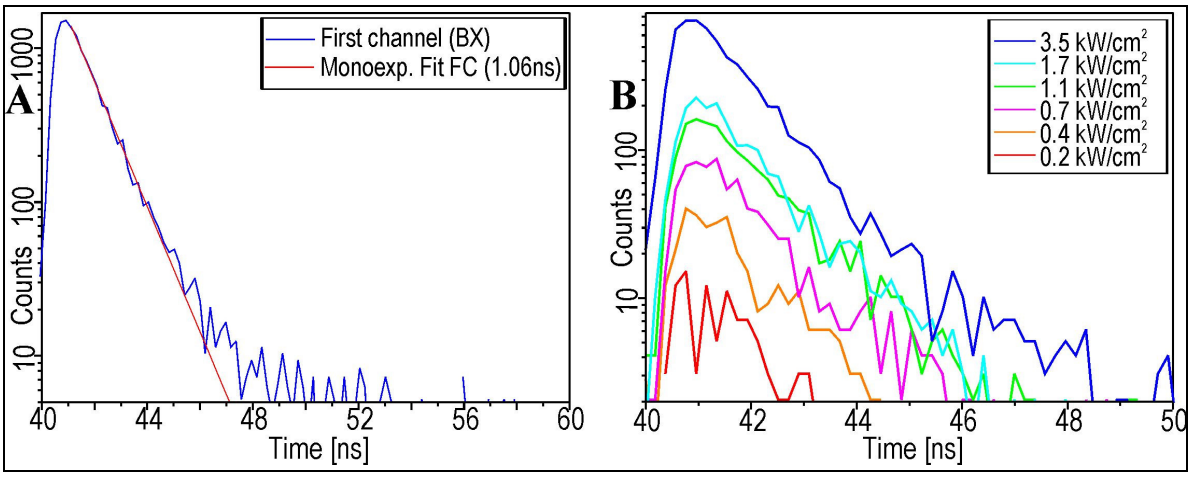

Figure 4.3.11: ***(A)*** *First channel decay for the central peak (blue) and corresponding monoexponential fit (red) for the whole transient of the NC shown in Fig. 4.3.6. In* ***(B)****, the decay in* ***(A)*** *is split into the subsections where different laser powers were used. Apparently, the decays show identical features in all sections.*

To demonstrate the accuracy of the novel method, Fig. 4.3.11A shows the extracted BX decay together with a mono-exponential fit yielding 1.06 ns (χ^2 = 0.996). If this method is applied to each of the six different excitation power sections, the different decays show considering the statistical errors identical decay characteristics, indicating that the BX emission is only marginally influenced by the excitation power (Fig. 4.3.11B). This is a further evidence that the extracted decay is due to BX emission, since fluctuations would be expected if independent emitters were responsible for the short component, and the power is increased. The results of monoexponential fits of each of the decays are shown in Table 4.2 with a narrow range of 1.0-1.2 ns for the BX decay.

Nr/Power [kW/cm^2]	BX decay[ns]	χ^2
Sum I-VI	1.06±0.02	0.996
I/0.15	1.46±0.62	0.54

II/0.3	1.24±0.14	0.90
III/0.5	0.99±0.07	0.955
IV/0.75	0.98±0.06	0.969
V/1.2	1.19±0.05	0.986
VI/2.5	1.04±0.02	0.996

Table 4.2: *Lifetime components from the first channel in the central peak fitted with a monoexponential model. Note that the error is very large for the second decay, hence the value is much larger than the other fits.*

Despite the quality of the fits, the longer tail of the BX decay obviously deviates from the fit in Fig. 4.3.11A to longer lifetimes due to background contributions. Assuming for an average S/B-ratio of 50-100 is assumed which is a reasonable value for the discussed NC, the calculated contribution to the coincidence ratio R_C amounts to about 0.03 (Fig. 4.3.2). This value has to be related to the overall R_C of about 0.25 measured over the transient which means that on average a fraction of 0.03/0.25 ≈ 12% in the central peak stems from background. Since the background has only a very low emission intensity, significant probabilities to form a photon pair within one laser pulse are only expected in combination with the brightest emission state, i.e. the monoexciton X. It follows that in the central peak, two contributions originating in background can be found with decay characteristics of both the background and the exciton. The background consists mainly of autofluorescence from the glass and should be constant over the whole surface.

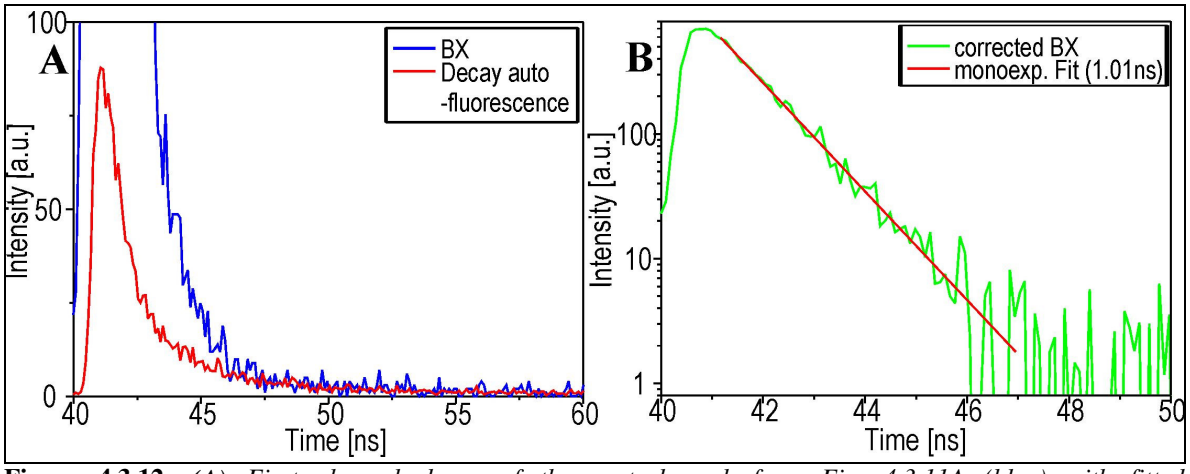

Figure 4.3.12: ***(A)*** *First channel decay of the central peak from Fig. 4.3.11A (blue) with fitted autofluorescence decay from glass surface (red).* ***(B)*** *By subtraction of the fitted autofluorescence, the corrected BX decay (green) is obtained with an excellent monoexponential fit (red).*

Therefore its decay characteristics could be measured on a spot far from emitting NCs and is displayed in Fig. 4.3.12. Though the detailed distribution of both decays on the first and late channel cannot be obtained, it is apparent, that the decay from the glass is much shorter

than the X lifetime. Therefore one can assume that as a good approximation the background contribution from the first channel has the decay characteristics of the glass surface.

In conclusion, the long tail observed in the first channel of the central peak stems from this contribution. Hence, as a straightforward correction from the background, the glass decay characteristics is fitted into the long tail of the first channel decay (Fig. 4.3.12A) and subtracted. In the "corrected" BX decay (Fig. 4.3.12B) the long tail has vanished and it is nearly perfectly described by a monoexponential fit (1.01 ns, $\chi^2 = 0.995$), with the residuals being accounted for by noise. This correction can be checked for validity by the ratio of the curve integrals (= count contribution) from the fitted autofluorescence and the original BX decay in Fig. 4.3.11A which yields about 15%, i.e. in good agreement with the estimated background contribution of about 12%.

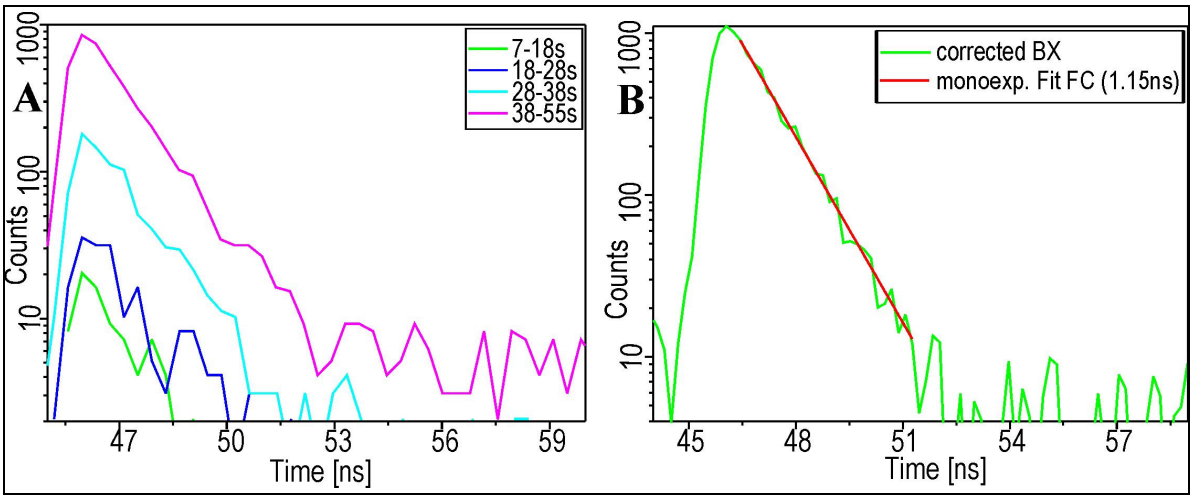

Figure 4.3.13: *First channel decays of the central peak for the NC in Fig. 4.3.4.* ***(A)*** *Non-corrected BX decays for different power sections, displaying no BX dependence on excitation intensity.* ***(B)*** *Corrected BX decay (green) and monoexponential fit (red) for the whole transient.*

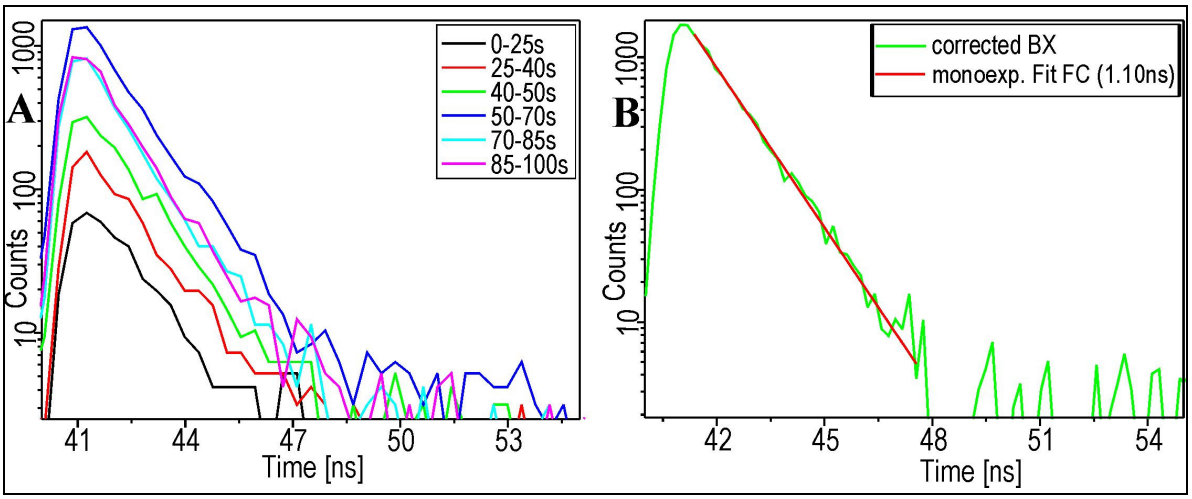

Figure 4.3.14: *First channel decays of the central peak for the NC in Fig. 4.3.5.* ***(A)*** *Non-corrected BX decays for different sections, displaying no BX dependence on excitation intensity.* ***(B)*** *Corrected BX decay (green) and monoexponential fit (red) for the whole transient.*

Even without the correction, which gives only slightly shorter lifetime values (1.01 ns compared to 1.06 ns without correction), the presented method provides an excellent tool to extract and calculate BX decays of single NCs. Fig. 4.3.13/14 demonstrate this for the NCs of the transients depicted in Fig. 4.3.4/5 , respectively. All show identical features, i.e. similar decay curves independent of the excitation intensity (Fig. 4.3.13A/14A), as well as corrected decays which are very well described by a monoexponential model resulting in lifetimes of 1.15 ± 0.03 ns (χ^2 = 0.995) and 1.10 ± 0.02 ns (χ^2 = 0.997), respectively. This also shows that the lifetime of the BX decay might vary from NC to NC significantly.

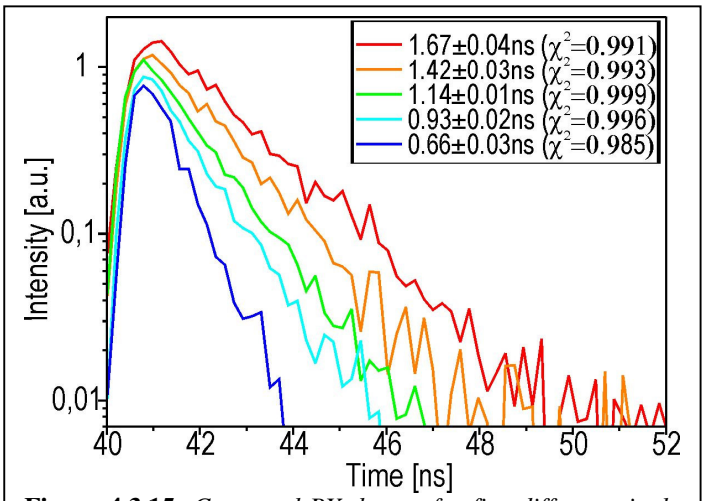

Figure 4.3.15: *Corrected BX decays for five different single NCs, obtained with the above described method. Note that there might be significant differences from NC to NC.*

Analysis of about 20 BX decays from single NCs revealed a large variance ranging from below 0.7 ns to more than 1.6 ns as can be seen from Fig. 4.3.15 depicting five different BX decays. Typically, most lifetimes were found in the range of 1.0 ns to 1.2 ns which is significantly higher than published before for similar samples (0.74 ns). Generally, no apparent interrelation between the observed BX and the X lifetime or the coincidence ratio, or both, could be deduced. Although the method provides a reliable analysis of BX decays, a principal limitation of this method is given by its dependence on the central peak photons. Whereas these carry specific information, they constitute by no means the only BX emission photons detected. In many instances, caused by the limited detection efficiency of the set-up ≈ 5%, detection of a BX photon may not be followed by X detection, even though it has been emitted from the NC. For these reasons, more than 10^4 photons in the central peak which is the range of the presented data require an overall photon detection > 10^6. Nevertheless, it should also be pointed out, that in cases where no spectral separation is possible, this method provides the only specific analysis possible of ordered photon emission.

4.3.4 Investigation of fluctuations of the relative BX quantum yield of QD655

Of further interest are fluctuations of the coincidence ratio measured from a single NC, i.e. fluctuations in the maximum relative quantum yield of BX to X emission ϕ_{BX}. It was already shown (Fig. 4.3.6) that even with background correction the ratio can be significantly higher than 0.3 corresponding to $\phi_{BX} > 40\%$ (Fig. 4.3.2B). This is higher than what has been previously published [267]. However, the prerequisite of obtaining a specific value of ϕ_{BX} for a given excitation power is that the ratio remains constant, i.e. is not dependent on other factors as well. Although the transients shown in Figs. 4.3.4-6 display no dramatic fluctuations for constant power, it has to be checked if the remaining variation is only caused by statistical error or if fundamental photophysical processes also have to be considered.

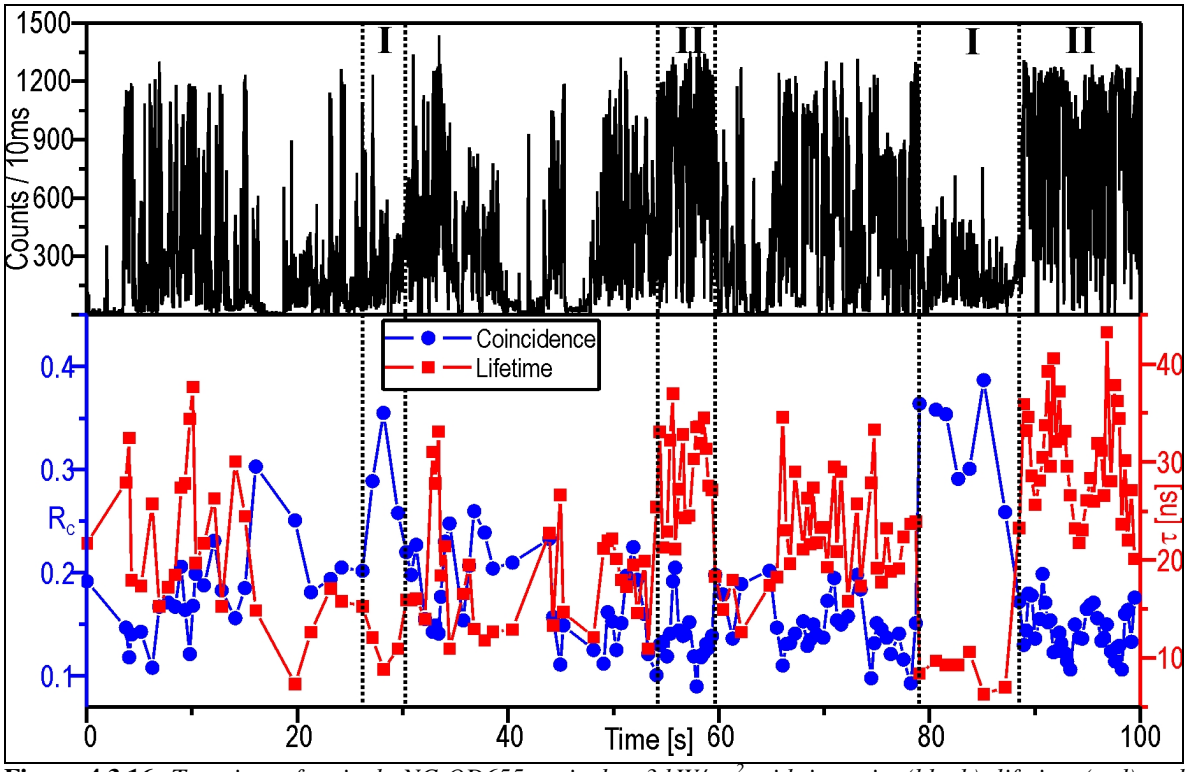

Figure 4.3.16: *Transient of a single NC QD655 excited at 3 kW/cm² with intensity (black), lifetime (red) and coincidence (blue) information. In the sections marked by dotted bars where count rate is low and lifetime short (quenching, denoted **I**), the coincidence is significantly higher than in sections with long lifetime (**II**).*

Fig. 4.3.16 shows an exemplary transient where significant PL intensity fluctuations are observed for a given laser power, depicting intensity, coincidence and lifetime fluctuations. First, the coincidence ratio is especially high in regions with low count rate (denoted as **I**). On the other hand, R_C is low for high count rates (**II**). Since in most cases, a reduced count rate is observed for quenching, the lifetime fluctuations are also shown in Fig. 4.3.16

calculated for the same time intervals as R_C. To exclude interference of BX lifetime, the TAC range was positioned about 4 ns after the laser pulse (compare to section 4.2.3), additionally a comparatively short range was chosen (≈ 50 ns) to monitor the quenched states with higher accuracy. Indeed, throughout the transient a significant anticorrelation is found for the coincidence ratio and the exciton lifetime, indicating that quenching rather than the reduced count rate leads to an increase of R_C and thus to an increased BX quantum yields.

To demonstrate that these characteristics are not exceptional and to show that the lifetime is a better correlation indicator than the intensity, a transient for a different NC is shown in Fig. 4.3.17. Most of the time, the noted anticorrelation of X lifetime and relative BX quantum yield is observed. Of special interest, however, are the sections (**a**) and (**b**): in (**a**) (after ≈ 10 s) the intensity drops significantly from ≈ 900 /10 ms to < 300 /10 ms and recovers within a second back to the initial rate. In the same time range the lifetime rather increases slightly and the coincidence ratio decreases in the intensity dip. A different case is observed after about 40 s (**b**), where the intensity level remains constant for several seconds whereas the lifetime and the coincidence ratios show significant fluctuations in an anticorrelated manner. These findings indicate that quenching is responsible for the observed fluctuations of ϕ_{BX}.

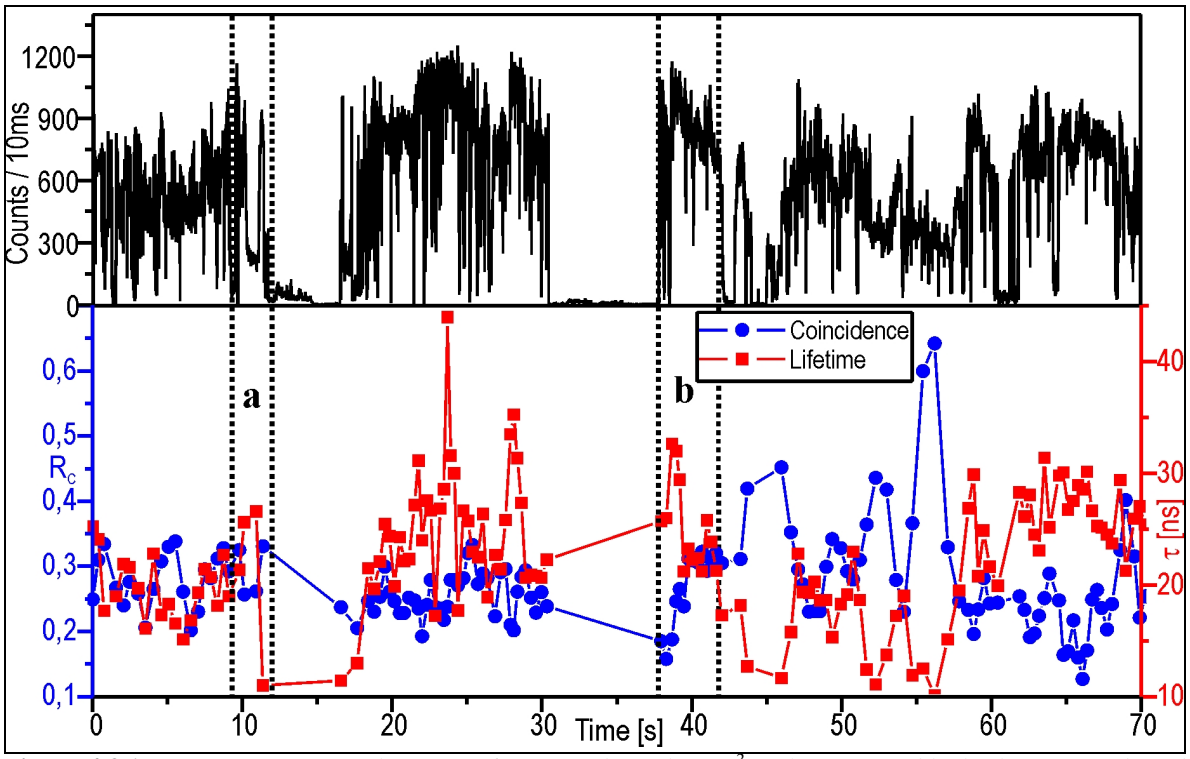

Figure 4.3.17: *Transient of a single NC QD655 excited at 2 kW/cm² with intensity (black), lifetime (red) and coincidence (blue) information. In sections denoted **a** and **b**, lifetime (red) and coincidence (blue) display anticorrelation, with no obvious correlation to the intensity.*

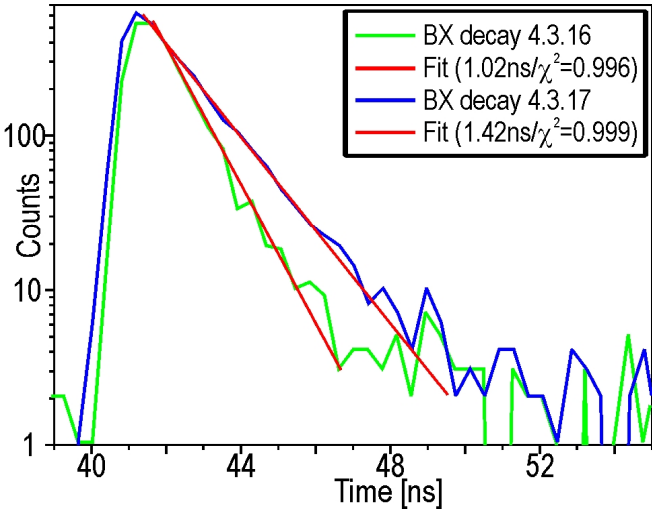

Figure 4.3.18: *Non-corrected BX decays for the whole transients from NCs in Fig. 4.3.16 (green) and 17 (blue), as well as monoexponential fits (red). This demonstrates that the observed features can only be assigned to BX decay.*

Of course it has to be assured that these results are not distorted by influences of weakly emitting NCs nearby. To estimate suchlike influences, Figs. 4.3.18 depicts the first channel decay in the central decay without background correction. Both decays display monoexponential characteristics. The deviations observed at longer times can be accounted for by the background contribution which is comparatively high due to low average coincidence ratios (0.16 for Fig. 4.3.16 and 0.26 for Fig. 4.3.17). The deviations are stronger for the NC in Fig. 4.3.16 since the relative background contribution grows inversely proportional to the absolute value of R_C. Hence, a background correction for R_C of 0.03 amounts to 0.03/0.16 = 19% background contribution to the decay compared to 11% for the NC in Fig. 4.3.17 with R_C = 0.26. This is a further proof that the observed fluctuations are not caused by non-correlated background other than autofluorescence from the glass.

Finally, it should be excluded that the higher coincidence ratio is not an artifact due to the changing S/B-ratio. Thus, if the signal decreases without changes from the background, also the S/B is lower and accordingly the coincidence ratio increases. For the NC in Fig. 4.3.16 a significant effect of the S/B ratio seems rather unlikely since R_C = 0.16 is quite low for QD655 excited at high laser power. Hence, only a small off-set due to the background is expected. The estimation of the background contribution for the NC in Fig. 4.3.16 is much simpler since a long off-time occurs from about 30-37 s. Before the blinking event, the R_C is homogeneously located around 0.25 with a count rate of 70 kHz, during the off-period less than 1 kHz average signal are detected from which an average S/B of at least 70 for the maximum emission follows. If this data is compared to the quenched state around 55 s (sudden increase of R_C) which gives a ratio of more than 0.6 with a count rate > 25kHz, the S/B due to homogeneous background is at least 25. However, comparing these values with the theoretical correction amount accounted for by the background, an increase of R_C from

0.02 (high PL intensity) to 0.09 (quenched PL) is expected, i.e. less than a difference of 0.1 whereas the actual increase amounts to more than 0.3.

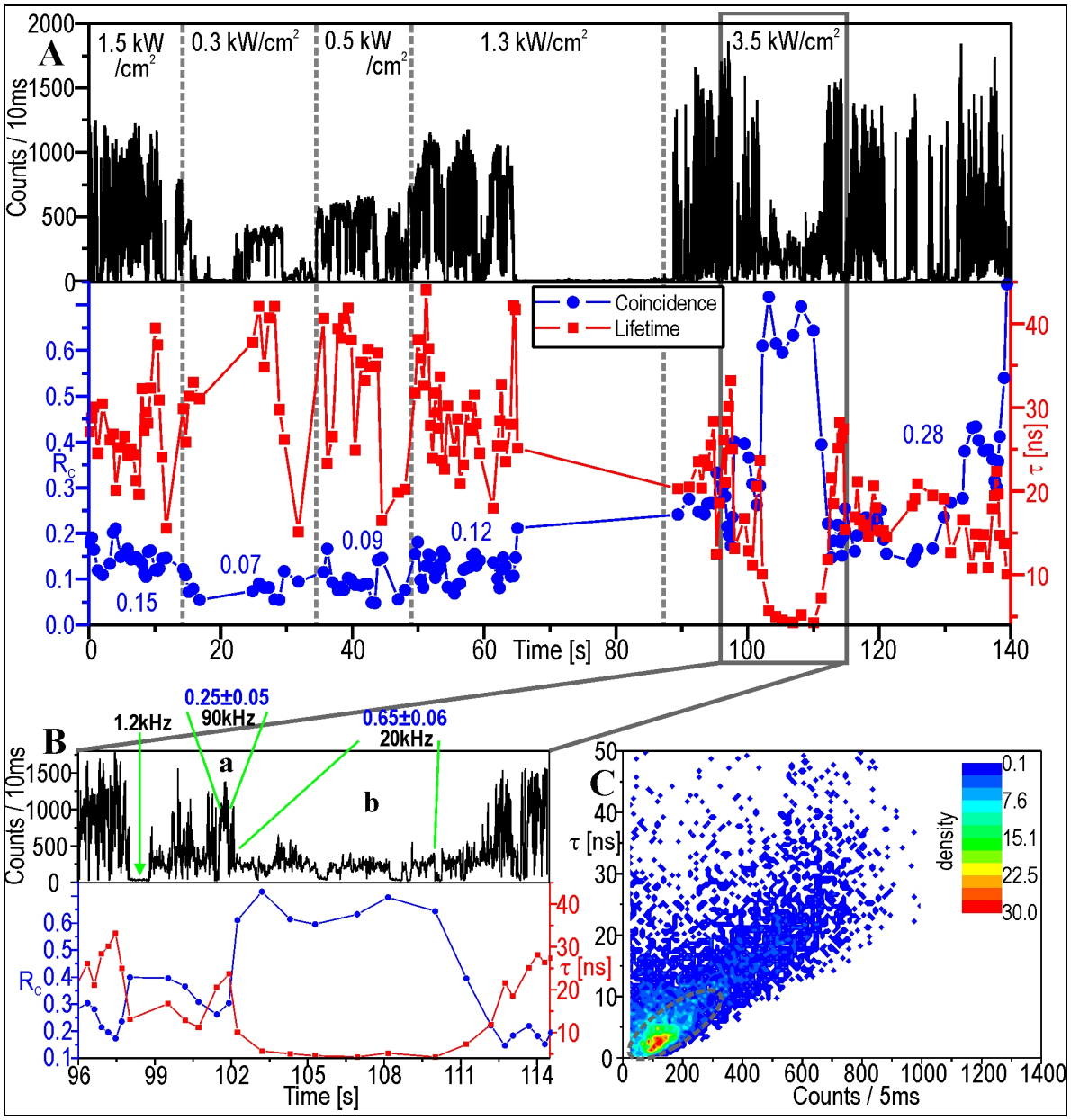

Figure 4.3.19: ***(A)*** *Transient of a single NC QD655 (black) excited at various excitation powers separated by dashed lines. The corresponding laser power is given in black for each section, together with the average* R_C*-value (blue). The blue and red line depict the course of* R_C *and the lifetime, respectively. From 0-100 s the ratio shows the observed dependence on the laser power. However, at about 105 s, a dramatic increase of* R_C *is noted accompanied with decrease of both lifetime and intensity.* ***(B)*** *Portion of the transient in* ***(A)****, with the three observables. At about 98 s, a distinct blinking event occurs, from which the background (green arrow, 1.2 kHz), can be deduced. At around 102 s, the intensity is high and yields an average value in* ***a*** *of about 90 kHz, together with* R_C *(blue)* ≈ 0.25*. In the quenched region (102-110 s,* ***b****), the intensity is much lower (20 kHz) with* $R_C \approx 0.65$*. At around 114 s, the NC reverts back to normal emission.* ***(C)*** *Density histogram of* τ *versus* N_C *for the high power region from 90-140 s. The wedge like feature is hardly discernible due to strong blinking, but the high density population can be attributed to subpopulation* ***(3)*** *identified in section 4.2.9.*

As last example that indicates a significant influence of PL quenching on the relative BX quantum yield, the NC in Fig. 4.3.19 is shown. The NC was excited at varying excitation

intensities (given in the intensity transient of Fig. 4.3.19A) analogous to the procedure in Figs. 4.3.4-6. Additionally, coincidence ratio and lifetime are portrayed. In the range of 0.2-1 kW/cm^2 the ratio shows the expected increase with power from 0.07 to 0.15 (average values given in the transient), with little fluctuation for a given power. When the power is increased to the saturating level the ratio increases significantly to > 0.2 which is similar to the features for the other NCs. Interestingly, after 100 s the intensity drops down from more than 150 kHz (maximum count rate) to below 50 kHz followed by a drastic decrease of the PL lifetime and an increase of R_C to more than 0.6 (see enlarged section in Fig. 4.3.19B). After a few seconds the intensity resumes back to about the initial state with a similar recovery of lifetime and coincidence ratio.

This particular NC and specifically the significant decrease in lifetime at 100 s are interesting for several reasons: For low power excitation, a very low coincidence ratio compared to other NCs of type QD655 is found, indicating negligible BX emission at this stage and low background. For different laser powers used, there was no indication for significant contribution from a second NC leading to non-correlated (to the lifetime) fluctuations of R_C, which also should have been visible in the long off-period from 65-90 s. At around 98 s, a second short blinking event occurs (green arrow in 4.3.19B) which directly facilitates measurement of the background, yielding about 1.2 kHz as an upper value of non-correlated photon contribution. In a small time span around 102 s (indicated by green bars, denoted **a**) the NC shows strong PL with an average count rate of 90 kHz and R_C = 0.25±0.05 (bold blue), whereas in the quenched region (green arrows denoted **b**) only 20 kHz with an average ratio of 0.65±0.06 are detected. Together with the calculated S/B ratios (90/1.2 = 75 for region **a**; 20/1.2 ≈ 17 for **b**), one obtains the off-set as 0.03 (**a**) and 0.11 (**b**). From this data, it can firmly be concluded that this particular NC showed a jump of the coincidence ratio of about 0.32±0.08, which can solely be attributed to a change of the relative BX quantum yield. This finding is not only unprecedented in the literature; it can furthermore hardly be ascribed to common BX emission, since the corrected R_C of an ideal two-photon emitter cannot exceed 0.5.

To find a rational behind this unexpected results, it was tried to analyze the emission state with the aid of the "wedge"-shape featured in the sections 4.2.7-11. Fig. 4.3.19C shows the density plot of the lifetime versus PL intensity distribution taken for the data from 90-140 s, i.e. with constant excitation intensity. Because of the strong blinking and quenching throughout the whole part of the transient, the upper bound is hardly discernible and only the lower part of the lower bound is clearly visible. However, from the high density

distribution for strongly quenched states and also a slight deviation from the linear course, it can be concluded, that the population marked by the dashed ellipse can be attributed to the quenched subpopulation denoted **(3)** in section 4.2.7. This indicates that for this subpopulation even emission of more than two photons might be possible and that it therefore has a strong influence on the power dependence of R_C. It might also give an explanation for a yet uncommented feature which was observed for all coincidence measurements using different powers: The measured coincidence ratios display only low to modest values with little changes (< 0.2) from low to medium power, but only rarely emission regimes with R_C < 0.1 are found. In contrast, when the excitation power is significantly increased above the saturating level, the R_C-value shows a dramatic increase of often more than 30% which cannot be accounted for by the background. From theory, a saturation curve feature is expected for the obtained R_C-values, with the most significant increase at low powers and also a saturating effect on R_C which should show slow transformation to a maximum value. In this respect, the found differences of the coincidence behavior for different emission regimes, especially the quenched subpopulation, might give a new explanation for these findings. Hence, it can be argued that for higher excitation different emission levels are populated, which might have an intrinsically higher quantum yield of multiphoton emission. However, with the limited amount of data at hand and together with the statistical error associated with the analysis of coincidence data, it is not possible to draw further conclusions about these characteristics.

Nevertheless, since it could be demonstrated that quenching significantly affects the relative BX quantum efficiency, it is necessary to find theoretical justification. The most straightforward explanation can be derived from the assumption that both BX- and X-emission experience a comparable quenching, i.e. the additional non-radiative rates induced by the trap state should be of comparable magnitude. The effect of this assumption on the relative BX quantum yield ϕ_{BX} can be demonstrated with the aid of a simple model system:

Generally, the quantum yield is given by $\phi = \frac{k_r}{k_r + k_{nr}}$. Thus, for ϕ_{BX} holds

$$\phi_{BX} = \frac{k_r^{BX}(k_r^X + k_{nr}^X)}{k_r^X(k_r^{BX} + k_{nr}^{BX})}.$$

To simplify the calculation, it will be assumed for maximum PL, i.e. no external quenching that $k_{nr}^X = 0.1 * k_r^X$ (i.e. $\phi_X \approx 90\%$), the radiative rate for BX and X are identical, and that the non-radiative rate of BX is given by $k_{nr}^X = 10 * k_r^X$. One obtains

$$\phi_{BX} = \frac{k_r^X (k_r^X + 0.1 * k_r^X)}{k_r^X (k_r^X + 10 * k_r^X)} = 10\% \text{ without external quenching,}$$

which is in the range of the observed values. If one considers an external quenching, where the additional non-radiative rate k_{nr}^{ext} is of comparable magnitude as the radiative X rate $k_{nr}^{ext} = k_r^X$ (i.e. the intensity of X emission is reduced to about half its initial value), this yields

$$\phi_{BX} = \frac{k_r^X (k_r^X + 0.1 * k_r^X + k_r^X)}{k_r^X (k_r^X + 10 * k_r^X + k_r^X)} \approx 17\% \text{ with external quenching.}$$

Although this is a very rough estimation, it gives conclusive evidence for the observed features.

4.3.5 BX emission from QD605

The same methods presented for the BX emission of QD655 were used to investigate the PL of QD605 under high power conditions, since the average coincidence ratios after background correction showed also slightly higher values than zero (Fig. 4.3.3). Since NCs of type QD605 were found to be sensitive to blueing even under non-saturating conditions (Fig. 4.2.36), prevention of exposure to oxygen was required during the measurement. This was achieved by spin-coating a dried sample with immobilized NCs with a 10% solution of polyvinylalcohol (PVA), which is known to hinder oxygen diffusion [284].

For several reasons, BX investigation of QD605 was more difficult than for QD655: The PVA-coating led to increased background which was aggravated by the fact, that QD605 required higher excitation intensities for saturation (> 5 kW/cm^2). This necessitated the insertion of a 50 µm pin-hole in the detection path of the confocal microscope to obtain sufficient S/B ratios > 50, but reduced the detection efficiency of the set-up by more than 50% (Note that no pinhole was necessary for BX measurement of QD655). Because of these influences and the strong photophysical fluctuations including blinking and quenching, no unequivocal determination of the coincidence ratios attributable to BX emission was possible. In most cases, the estimated ratios were found in a range of 0.05-0.1, but not significantly higher.

Nevertheless, the developed analysis of BX decays allowed for an unequivocal proof of significant BX emission. This could be demonstrated by summation of the central peak photons obtained from 20 single NCs of type QD605, and splitting the photons into the first

and late channel (section 4.3.3). The resulting decays are shown in Fig. 4.3.20 and display similar features to the BX decay of QD655 (compare Fig. 4.3.10), i.e. the first channel is dominated by a very short component with a tail to longer lifetimes, whereas the late channel decay is much longer. These are the expected features of BX emission, i.e. the first channel is made up of counts stemming from strongly quenched BX emission with a certain amount of background contribution (long tail), whereas in the late channel exclusively monoexciton contributions are found, because of high power excitation also sometimes quenched.

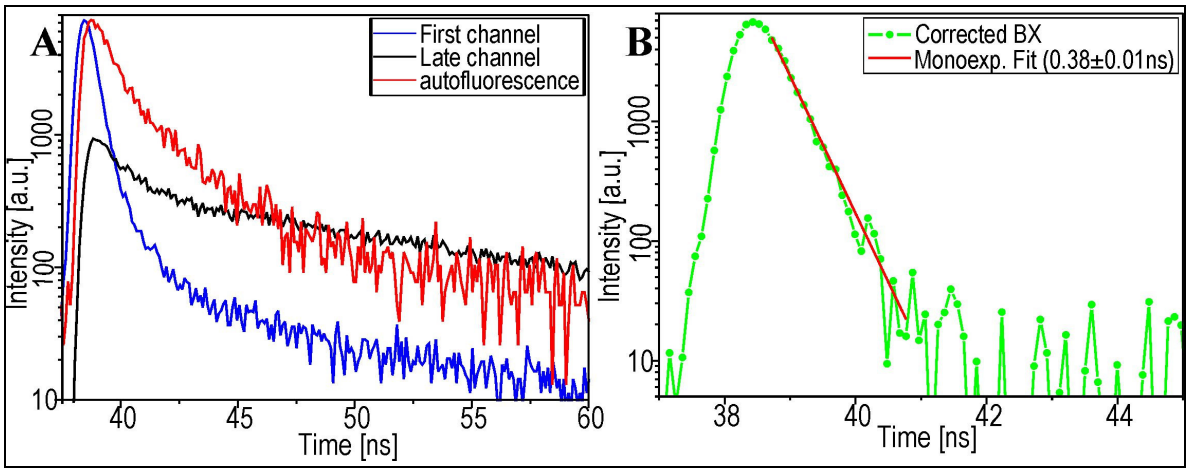

Figure 4.3.20: ***(A)*** *First (blue) and late (black) channel of the central peak summed for ≈ 20 NCs QD605 under saturating conditions. A similar characteristics to the BX emission of QD655 (Fig. 4.3.10) is observed. Note that the short component cannot be attributed to autofluorescence from the glas, which has a longer decay (red curve).* ***(B)*** *Background corrected BX decay (green) from the first channel in* ***(A)****, together with the monoexponential fit (red).*

However, different from type QD655 NCs, the coincidence ratios found for QD605 are much smaller (< 0.1 for QD605 compared to > 0.2 for QD655) which has two major effects for the BX decay component: a) a reduced coincidence ratio results in decreased coincidences, i.e. counts within the central peak, thus rarely more than 5000 photons for a single NC were detected for decay analysis. b) With fewer coincidences, likewise the effect of background emission from autofluorescence is aggravated, hence a correction amount for R_C of 0.02 (accounting for an S/B ratio around 100) and a measured ratio of 0.1 means that 20% of the central peak photons are caused by background signal. Nevertheless, by comparison of the decay from background signal measured on a bare glass surface (red curve in Fig. 4.3.20A) with the short component of the first channel decay (blue curve), it is obvious, that the latter displays a much shorter lifetime. In an analogous manner to the BX decay correction used for QD655, the background signal was then fitted into the long tail of the first channel decay and subtracted from it. The resulting decay can be well described by

a monoexponential function ($\chi^2 > 0.99$) yielding a lifetime of 0.38±0.01 ns, hence much shorter than observed for QD655 (around 1.1 ns, Fig. 4.3.15) which is likely because of stronger quenching for BX emission. In fact, because of the limit of the instrumental response function (IRF) which gives an "artificial" lifetime between 0.2 and 0.25 ns (section 3.), the actual BX decay is expected to be much shorter, i.e. in the range of 0.2 ns.

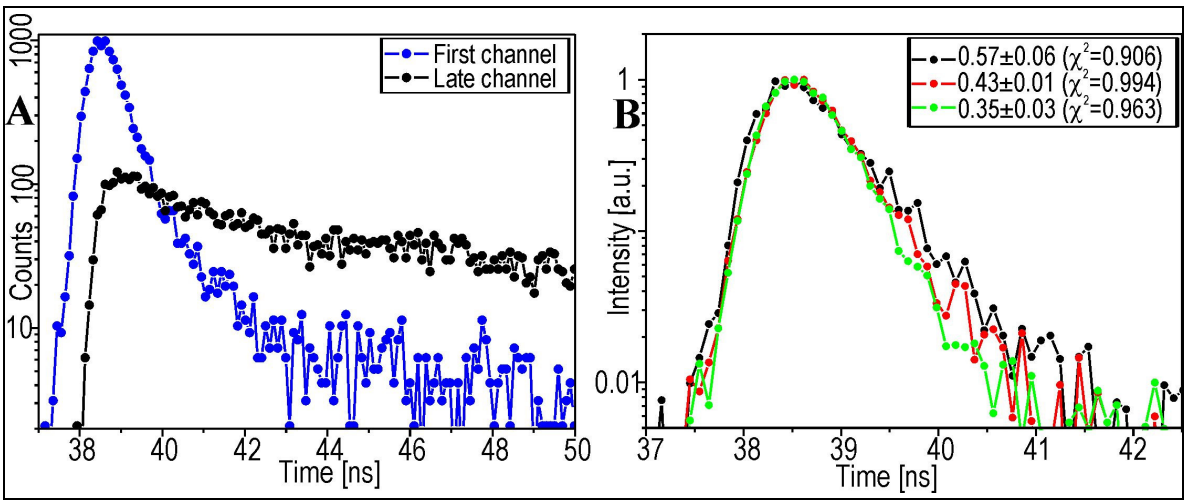

Figure 4.3.21: ***(A)*** *First (blue) and late (black) channel of the central peak for a single NCs QD605 under saturating conditions.* ***(B)*** *Background corrected BX decays measured for three different NCs QD605. The green curve is the corrected decay of the first channel in* ***(A)****.*

In several cases, the method could also be used to correct BX decays of single NCs with satisfactory accuracy. An example is depicted in Fig. 4.3.20A showing near identical behavior to the bulk decays, i.e. a very short component with background tail and a much longer component in first and late channel, respectively. The BX decay after background correction can be fitted with a monoexponential model yielding a lifetime of 0.35 ns (green curve in Fig. 4.3.20B). Two further examples are shown in the same Fig., again demonstrating that the lifetime might exhibit significant differences from NC to NC. Unfortunately, the photon statistics of the presented data did not allow for a deconvolution of the decays using the measured IRF, which could have yielded more accurate information about influences of other parameters on the BX emission from QD605.

Although the methods could have been used to investigate possible BX emission from QD705 as well, these experiments were abandoned since it was found that corresponding to the histogram in Fig. 4.3.3, this type of NC has even a lower relative BX quantum yield than QD705, so that no significant ratio above 0.05 could be found. Even under optimal imaging conditions, i.e. with a S/B ratio > 100, the coincidence off-set of around 0.02, than amounts to at least 40% of the central peak counts. Therefore, no significant BX data could

be produced other than the finding, that the decay is probably even shorter than for QD605, i.e. limited by the IRF.

4.3.6 Measurement of TX emission from single NCs of QD655

The general problem concerning BX analysis stems from the fact that spectral separation is not possible and that in the coincidence analysis many photons are "lost" since only two-photon events give specific information. On the other hand, PL emission is not limited to BX emission, but in principal multiple excitons (MX) can exist within the same NC. Since the carrier concentration and therefore quenching increases and because of the lower probability of excitation, the probability of photon detection decreases for each additional e-h-pair. Nevertheless, recently it has been found that PL from triexciton (TX) emission was sufficient for QD655 to obtain the spectrum and measure the PL lifetime [267]. Although TX emission should be much weaker than BX emission, it features the advantage that the emission spectrum is significantly blue shifted compared to both X and BX emission (maximum emission wavelength ≈ 610 nm compared to 655 nm). This facilitates spectral separation, i.e. as opposed to coincidence analysis, all detected photons can be used for specific analysis which reduces the statistical error significantly. Hence, indicator for absence or presence of significant TX emission is not the R_C- (indicator of BX emission), but the relative intensities on spectrally separated channels, denoted F_2-value in this work. Furthermore, since it is expected that the general features of TX emission are much more similar to BX emission than X emission, it was hoped that the study of TX emission could confirm several assumptions from the BX investigation.

The crucial aspect of the experiment in the case of TX emission is the spectral separation, since it has yet not been studied, whether spectral overlap interferes with lifetime measurements. Previous studies showed that the TX emission band is quite broad, so that a certain amount of spectral overlap or crosstalk between the detection channels D1 and D2 cannot be prevented. Although generally the spectrograph employed for the measurement of X spectra from single NCs was not sensitive enough to allow for TX detection, in very rare cases, a second band blue-shifted with respect to the X emission was observed. One of the examples is shown in Fig. 4.3.22A which was not smoothed to prevent possible distortions of the spectra shape, e.g. by smoothing of the overlap.

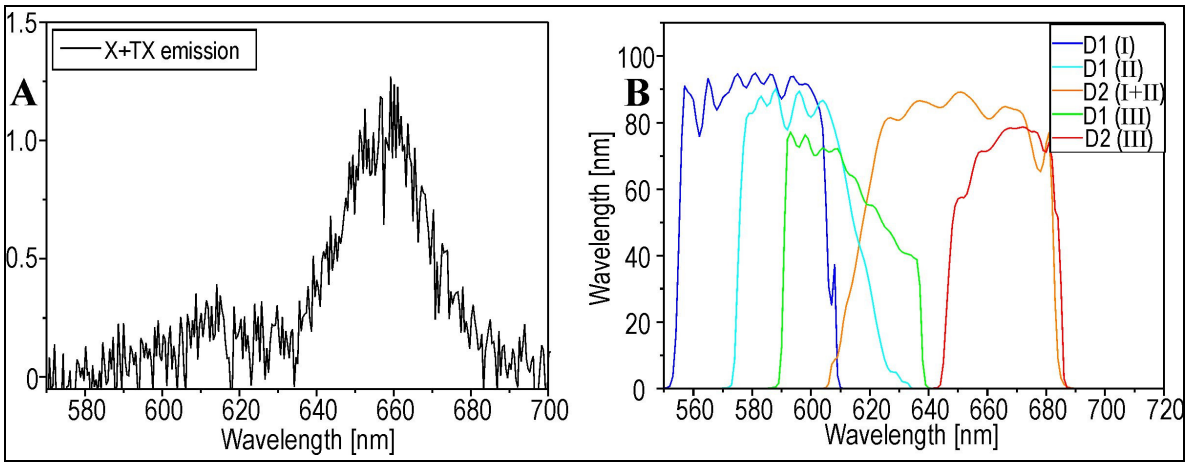

Figure 4.3.22: ***(A)*** *Raw data of a spectrum measured from a single NC QD655 under high power. Apart from the maximum emission wavelength ≈ 660 nm a distinct second component around 615 nm is observed, which can be attributed to TX emission. Spectral separation of X and BX emission is not possible.* ***(B)*** *Transmission curves for the three different filter sets used for the detection of TX emission from QD655.*

The estimated maximum of the blue shifted band is in the expected range (≈ 612 nm) for TX emission. Due to the broad emission, there is a significant overlap of X+BX and TX emission which also prevents determination of the exact shape. Moreover, since only few TX spectra existed, the amount of extrinsic heterogeneity, i.e. the difference of TX emission wavelengths from NC to NC, could not be determined. Therefore, three different filtersets were tested with respect to their suitability for TX imaging, concerning both S/B ratio and spectral separation (Fig. 4.3.22B).

For a first test, denoted set-up I, a dichroic mirror splitting the PL at about 620 nm was used in combination with a bandpass filter in front of each detector (580DF60 for D1, 645DF75 nm for D2); (note that in each of the set-ups, two langpass filters, with edges at 500 nm and 585 nm, respectively, were additionally inserted). Since very high laser intensities are necessary for TX excitation, the set-ups were tested for interference from autofluorescence. In each case, for the maximum power used of about 15 kW/cm^2, less than 3 kHz autofluorescence on each detector were registered with the typical decay characteristics already found for BX investigation (Figs. 4.3.12 and.4.3.20). As in most cases significant TX emission could only be obtained for intensities much higher than X saturation intensity (around 1-2 kW/cm^2), the laser power was rapidly switched between two power states, i.e. near maximum intensity (12-15 kW/cm^2, denoted high power, hp) and an intensity near saturation of X emission (1-1.5 kW/cm^2, denoted here low power, lp), without determination of the exact excitation intensity.

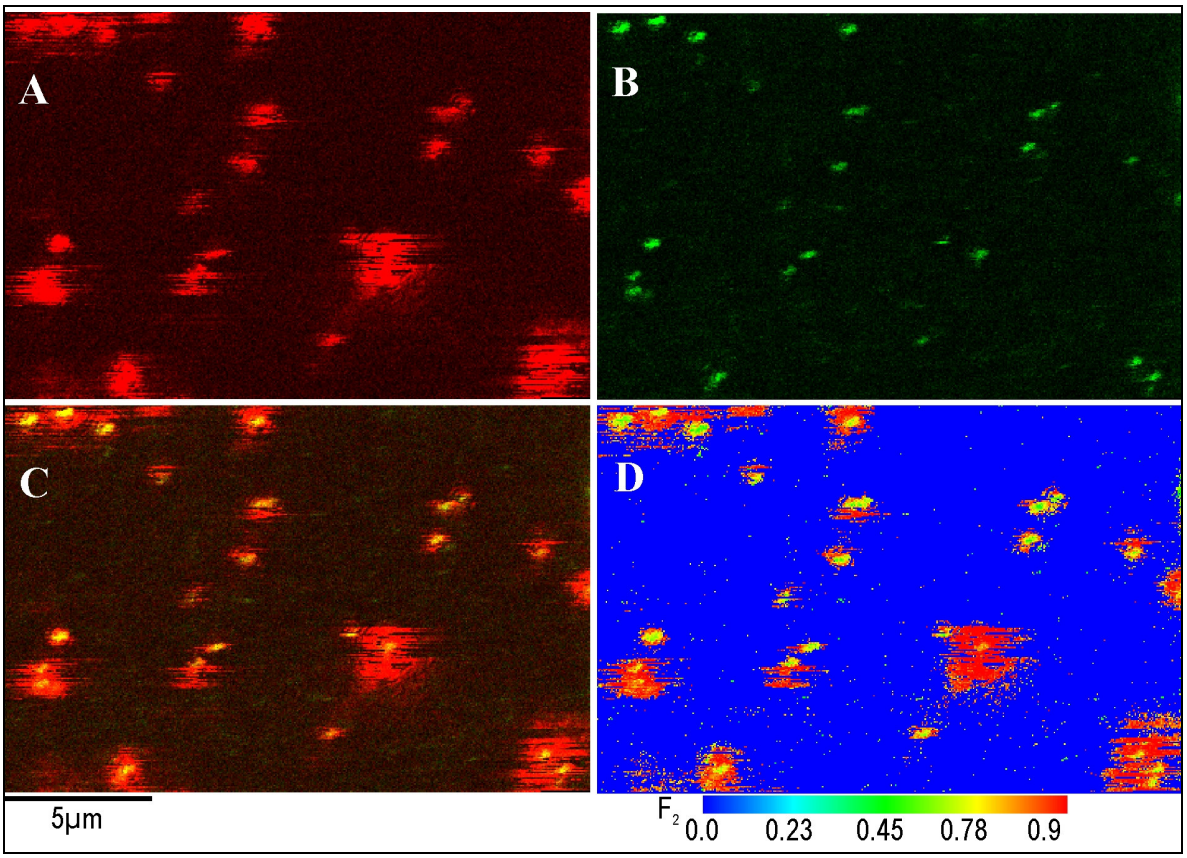

Figure 4.3.23: *Scan image of the detected intensity on the long wavelength detector D2* ***(A)*** *and on D1* ***(B)*** *for NCs QD655 immobilized on a dry coverslide under ≈ 12 kW/cm² excitation power taken with filter-set I. (C) Reconstructed false color image from the sum of* ***(A)*** *and* ***(B)****. (D)* F_2*-encoded image of the scan image in (C). In the center, the* F_2*-value is significantly lower because of higher TX emission.*

Fig. 4.3.23 shows a scan image of NCs (QD655) immobilized on a dry coverslide detected with filter set-up I and excitation near maximum intensity. Depicted are the separated false color images on D2 (A), D1 (B) and the image reconstructed by superposition of (A) and (B) in 4.3.23C. It is obvious, that the images on both detectors show spots at the same positions. Interestingly, the PSFs in A are very large (diameter > 1 µm) and patchy due to strong blinking, whereas the PSFs in B are small (< 500 nm) and display no distinct blinking events. The different PSF size can be proven by calculating the F_2-image from C, where red spots display a high but green or blue spots a low F_2-value. Thus, in the center of each spot, the F_2-value is comparatively low (< 0.8) whereas in the outer regions of the PSFs it is near unity (> 0.9).

This finding is a clear indication of TX imaging on the short wavelength detector (D1): A large PSF on the long wavelength detector (detecting significantly above 615 nm) should stem from X-emission which is already saturated at intensities around 1.5 kW/cm², i.e. much lower than used for scanning. This means, that even the second maximum of the Bessel-function might suffice for an excitation probability of X emission near unity. Hence the PSF is much larger than the Rayleigh criterion. On the other hand, a significant cross

talk of X emission into D1 should result in similar PSF images for B, which is not observed. The PSF is within the theoretical range for excitation at 445 nm indicating that the detected species is in contrast to X emission excited below the saturation level. Following the argumentation for the intensity dependence of BX emission (section 4.3.2), this is exactly what is expected for TX emission, since it should increase with the cube of the power compared to a proportional increase up to the saturation level for X emission.

Despite the successful imaging, measurement of longer transients from single NCs proved to be difficult with this method. The reasons for this were low count rates found on D1 typically below 10 kHz as well as fast blueing as demonstrated in Fig. 4.3.24. To differentiate between TX emission and blueing, the excitation power was alternated between low and high power regimes (lp and hp, respectively) indicated by dashed lines. For the NC shown, before 60 s (denoted section I), the F_2-value (green) decreases only slightly from the change of lp to hp regime, but reverts back to its starting value above 0.95 when the power is decreased again. At the same time, the coincidence ratio shows rather anti-correlated features i.e. is significantly below unity at lp, but increases to the maximum value at hp. To understand this behavior, it has to be considered that the coincidence ratio for spectrally resolved TX imaging does not yield a theoretical value of $R_C = (n-1)/n$ for n emitting species. The latter formula has been derived from the fact that for no spectral separation between the species, there is a certain probability that two simultaneously emitted photons are directed onto the same APD where only one photon within the macrotime range can be detected. However, for TX imaging, this rarely occurs since TX and X (+BX) are detected almost exclusively on two different APDs. Hence R_C should be always unity.

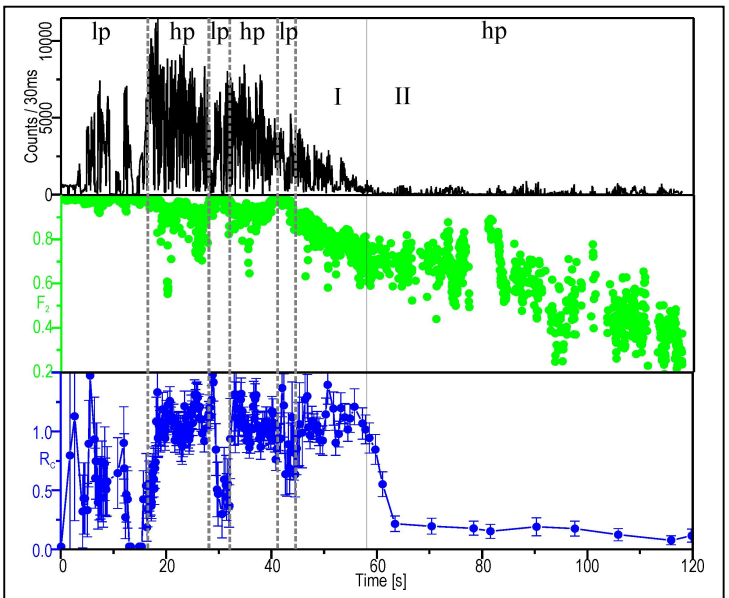

Figure 4.3.24: *Transient of a single NC QD655 with depiction of intensity (black),* F_2*-value (green) and* R_c*-value (blue). Up to 60 s,* F_2 *and* R_C *increase for hp excitation. After 60 s both* F_2*- and* R_C*-value start to decrease irreversibly due to blueing of the NC.*

This feature can also be used for a differentiation between blueing and TX emission, since in Fig. 4.3.24, after the last switching to hp excitation, the F_2 shows a gradually decreasing value together with decreasing intensity. This cannot be due to increasing TX emission, since after 58 s (denoted section II), R_C shows a rapid decrease below 0.3 following the decrease of the F_2-value. Apparently at this stage, the cross talk into D1 from the X emission is strong enough to lead to a sufficient S/B ratio for the distinct increase of R_C. The lapse between the decreasing F_2- and R_C-values is accounted for by the employed filter set-up, where the detection efficiency between 620 nm and 610 nm is very low, so that a blue shift results in a loss of photons on D2 without any gain on D1.

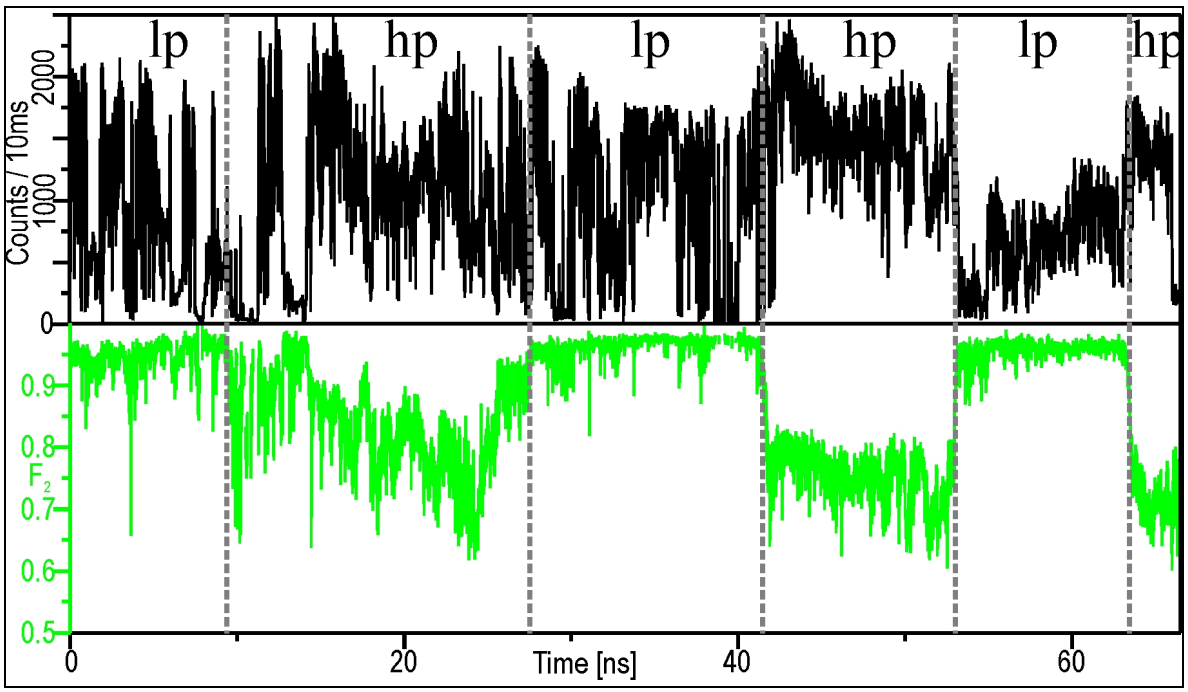

Figure 4.3.25: *Transient of a single NC QD655 with alternating lp and hp excitation. Whereas the switching from lp to hp is hardly discernible from the intensity (black), it is very distinct in the course of the* F_2*-value (green).*

To overcome the mentioned problem of blueing, similar to the BX measurements of QD605, the sample was coated with a PVA layer to prevent oxygen diffusion. Furthermore, the filter in front of D1 was changed, so that the detection range was shifted to red wavelengths (substitution of 580DF60 versus 605DF55, set-up II, Fig. 4.3.22). Although this results in increased cross talk from X emission, Fig. 4.3.25 demonstrates that the increase of TX detection is stronger, so that the observed F_2-values under hp excitation are significantly lower than observed for set-up I due to count rates of up to 40 kHz on D1. Note that the decreased F_2-value cannot be caused by blueing because it rapidly reverts to a value near unity once excitation power goes back to lp. The fact that X emission occurs even under lp excitation near saturation conditions can be deduced from the lack of distinct

correlation between the detected count rate and the emission regimes. Thus, the count rate increase when switching to hp excitation is only caused by the additional TX emission which is weak compared to X emission (F_2 value > 0.7). Furthermore striking is the finding that apparently the relative quantum yield of TX emission, ϕ_{TX}, is not constant for a given excitation power since the F_2 which is proportional to ϕ_{TX} shows fluctuations within the hp section. Possible causes for these fluctuations which seems to be interrelated with variations of the count rate, will be discussed below.

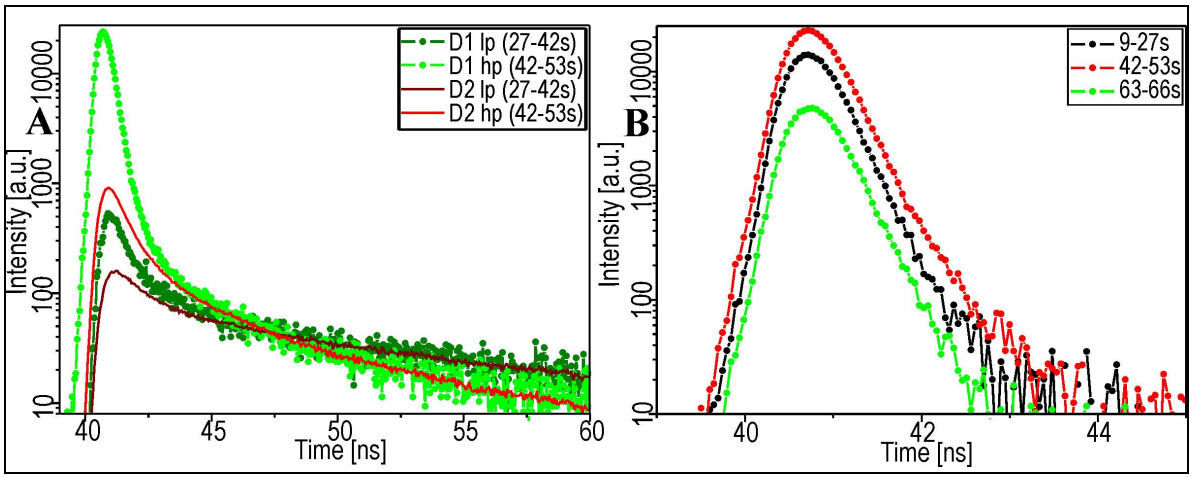

Figure 4.3.26: ***(A)*** *Lifetime on D1 (green) and D2 (red) for the indicated regions in the transient in Fig. 4.3.25 for low (lp, dark) and high power (hp, bright) excitation. The decays for D2 are fitted into the long tail of the decays for D1. A notable increase of the short component under hp excitation is obvious.* ***(B)*** *TX decays for the three hp excitation regions in Fig. 4.3.25, after cross talk correction.*

With the obtained comparatively high count rate, a lifetime analysis of the TX emission is of interest. In Fig. 4.3.26A, the decay curves for both detectors are shown for a lp region (27-42 s, dark green and red for D1 and D2, respectively) as well as under hp excitation (42-53 s, light green and red). The curves within the lp regime monitors no strong deviations for both detectors, only a small contribution of a short lifetime component is observed on D1 compared to D2, attributable to weak TX emission even for 1 kW/cm^2 excitation intensity. This is consistent with the findings under hp excitation, since the short component has increased considerably on D1 in comparison with D2. Both decays show near identical course after 5 ns after the pulse and it is possible to obtain the TX component by fitting and subtraction of the two curves. Although this procedure seems to be similar to the BX analysis on the ensemble level (section 4.3.2), it has to be stressed out that in the present case, both decays (i.e. light green and red curves) stem from X emission within the same macrotime range and thus must have the same decay. On the other hand, comparison of the dark and light red curves reveals even after 20 ns a different course, because of different excitation powers and macrotime ranges.

Decay curves for the three hp regimes in Fig. 4.3.26B are displayed in B and show a very short component with seemingly monoexponential characteristics. However, the resulting decays show similar lifetimes between 0.27-0.28 ns, i.e. only marginally above the minimum lifetime which is found for the IRF (≈ 0.25 ns), thus the actual lifetime is much shorter (around 230 ps [267]) and these values can only be used for comparison. Nevertheless, the finding that correction of the decay measured on D1 under maximum excitation intensity results only in a single, IRF-limited component is unequivocal evidence for detection of TX emission.

Despite the improvement of TX detection by switching to filter set-up II, a major drawback remains because no proof of emission from a single NC exists which leads to ambiguities concerning the interpretation of observed fluctuations. Therefore, a new approach was chosen, allowing for a controlled low amount of crosstalk from X emission into D1. The rationale behind this consideration is the difference of R_C-values for X and TX emission which has been used to differentiate between the two in Fig. 4.3.23. Although with the used set-ups a certain amount of X emission has been detected, it was too low to override the effects of the background. To allow for a stronger X detection, a dichroic beamsplitter with a red shifted splitting wavelength compared to set-up I and II was chosen, about 635 nm compared to 620 nm (set-up III, Fig. 4.3.22B). As bandpass filters, 615DF45 for D1 and 665DF40 for D2 were used, slightly red shifted as well to the filters used before.

With filter set-up III, it was possible to proof that only a single NC was present within the focus while still obtaining all other information, depicted in Fig. 4.3.27. Thus, both F_2- and R_C value show a clear (anti-)correlation with the switching events, i.e. for lp F_2 is high (> 0.9) and R_C is low whereas R_C is near unity at hp with a significantly increased behavior. It is worth to consider several points of these features more detailed: The fact, that R_C is much higher than commonly associated with a single emitter (rarely below 0.5) can be explained by the observation that cross-talk is still very low (F_2 (lp)≈ 0.95) which means that the S/B ratio is quite low as well on detector D1 for X emission.

Apart from the extrinsic noise, also BX emission has to be considered which is significant for the given power around 1 kW/cm^2. The low interference from background can also be deduced from the finding, that R_C is unity at the hp regime even though the F_2-value is decreased compared to lp. Otherwise, an upcoming of crosstalk of X emission on D1 would yield a higher S/B ratio, therefore rather a decrease of R_C compared to the value for lp would be expected.

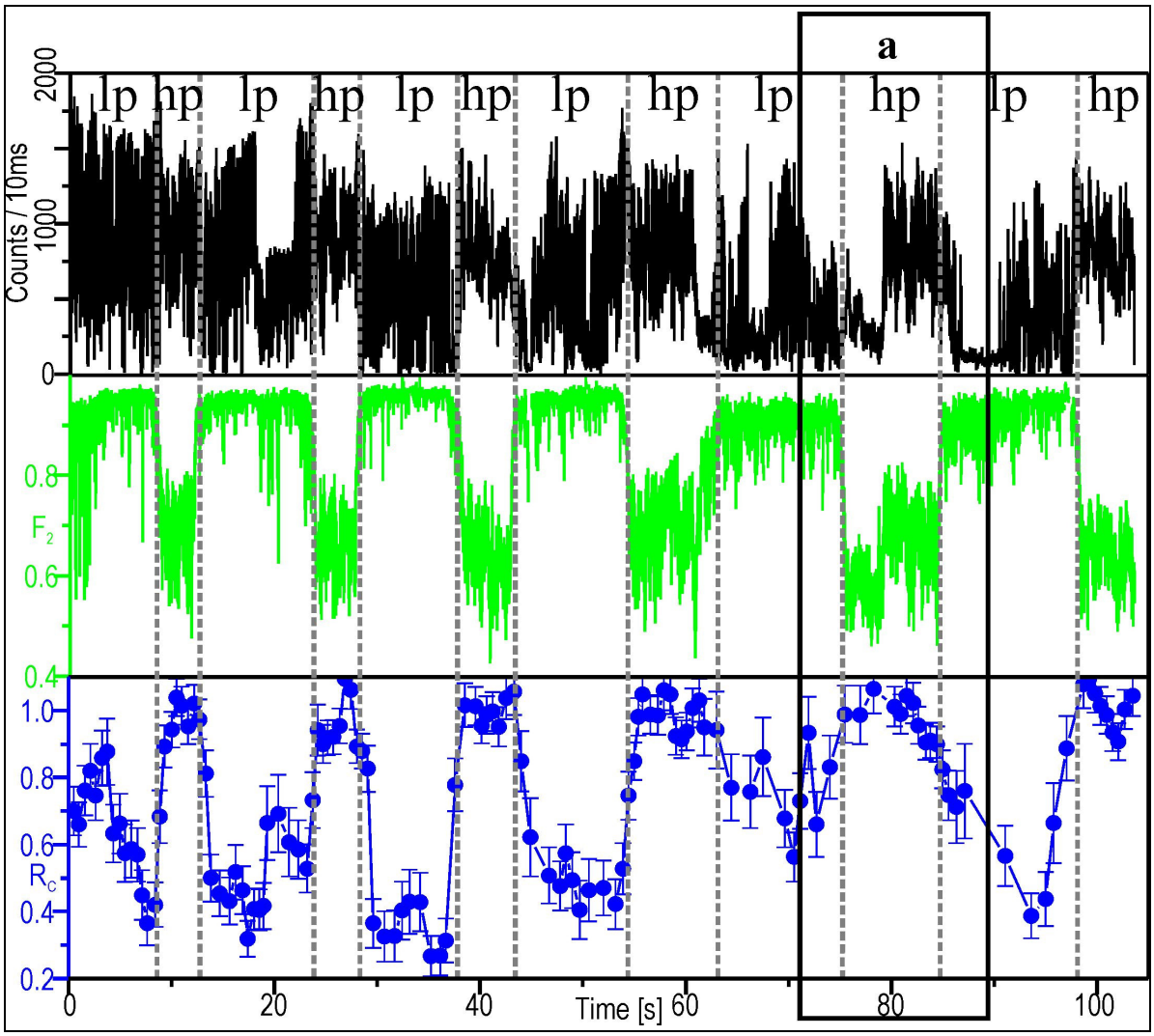

Figure 4.3.27: *Transient of a single NC QD655 with intensity (black), spectral (green) and coincidence information (blue). Because of the small cross talk, the coincidence in the lp sections is < 1.0, but increases to ≈ 1 in the hp sections due to the increasing TX emission. Note the section denoted a, where both intensity and* F_2 *show a significant jump within a hp region.*

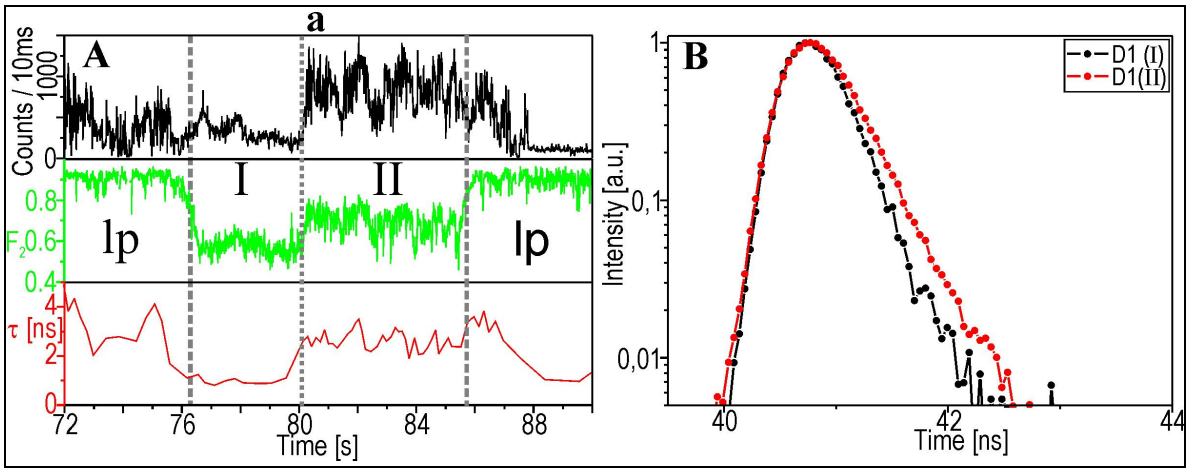

Figure 4.3.28: ***(A)*** *Magnified portion of section a in Fig. 4.3.27.* ***(B)*** *Corrected TX emission detected on D1 for section* ***I*** *(black) and* ***II*** *(red curve), respectively. Note that the decay is significantly shorter in I, indicating that also TX emission is slightly quenched.*

The importance of negligible interference from X emission is of special importance for the discussion of an interesting feature displayed in the section denoted a in Fig. 4.3. Here, in the hp regime, a correlated jump of intensity with the F_2-value is observed although the power remains constant. Since intensity jumps are commonly followed by a change of the lifetime, Fig. 4.3.28A presents an magnified portion of the section a, depicting intensity, spectral and lifetime information (Since in the hp regime the R_C-value is constant, it is of no further interest here). By comparison of intensity and lifetime trace, it is obvious, that at about 76 s, the NC changed to a second long quenching emission, which persisted when excitation was switched to the hp regime (dashed line, section **I**), resulting in a decrease of F_2 from 0.95 to 0.6. At 80 s, still under hp excitation, the NC emission switched back to normal emission, i.e. both intensity and lifetime increased considerably (dotted line, section **II**). Simultaneously, the F_2-value displays a shift to a higher value, but still low compared to the crosstalk level (≈ 0.7). Around 86 s the power is switched back, upon which the F_2 reverts back to about 0.95. Considering, that fluctuations of a single NC are detected, this apparently means that in cases of quenched X emission the relative TX quantum yield, for which F_2 is an indicator, is higher than for normal emission. This would give a strong support to the theory developed from BX emission, that quenching does affect multiexciton emission to a similar amount than X emission. However, since MX emission is already strongly quenched, it is not as sensitive to trap states as is the former.

To check, if the quenching effect does have an effect of TX emission, in Fig. 4.3.28B are displayed the crosstalk corrected decays from D1 for the quenched (**I**) and non-quenched TX emission (**II**). Although it has been mentioned that the lifetimes are strongly influenced by the IRF, it is obvious that indeed the decay is much shorter for section I than for section II and is regarded as good proof for the stated assumptions.

Finally, an example is given were the quenching effect can be observed over a longer duration. This is based on the finding that excitation at very high powers, i.e. significantly higher than the saturation level leads to a decrease of PL. Although the influence is not quite clear yet, it can be argued that high excitation induces multiple Auger steps which can induce occurrence of "trap" states. Since efficient quenching of NC luminescence is often connected with "hole" traps outside the NC, it can be rationalized that negative charges, i.e. expelled electrons are the main cause for trap occurrence. If oxygen has access to the NC, the negative charges will result in a rapid oxidation reaction, which removes the traps but leads to a reduced core, i.e. blueing is observed. In the absence of oxygen, e.g. under PVA,

a high trap concentration apparently leads to an irreversible reorganisation of the shell which results in an increased quenching but does not effect the emission spectrum.

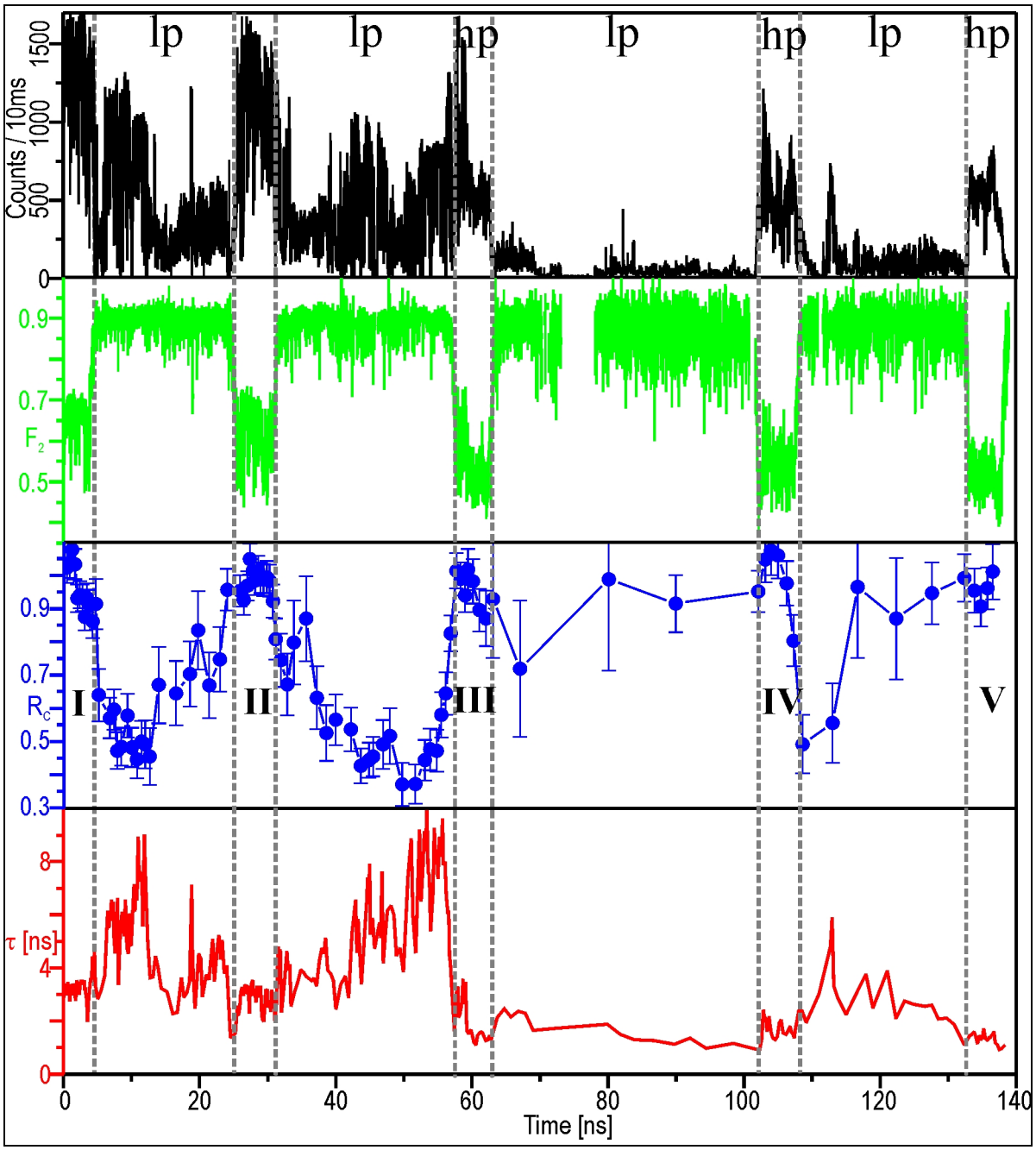

Figure 4.3.29: *Transient of a single NC QD655 with intensity (black), spectral (green), coincidence (blue) and lifetime information (red). In the hp section, it is obvious, that with decreasing X emission from I-V due to bleaching the* F_2*-value increases, since the* ϕ_{TX} *increases at the same time.*

Fig. 4.3.29 shows an NC imaged for more than two minutes with repeated (5x) switching to the hp excitation regime. Since all four observables are shown it can be deduced from F_2- and R_C-value, that a single NC is present and that it exhibits efficient TX emission in the hp regime. If one follows the hp regimes which are numbered I-V, it is obvious, that the PL intensity, F_2-value and lifetime show a gradual decrease. On comparison of section I with

section V one observes more than 50% reduction of the maximum PL intensity, a decrease of the F_2-value from ≈ 0.65 to ≈ 0.51 and for the PL lifetime 7.5 ns compared to 3.7 ns. This is a confirmation to the above made assumptions that upon bleaching of the X emission, the relative quantum yield of TX emission ϕ_{TX} increases. Thus, although also TX emission is slightly affected (visible by the shortened decay in section I compared to II in Fig. 4.3.28B), the impact of an increased non-radiative rate is weaker than on X emission. Analogous to the model calculation shown in section 4.3.4. In conclusion, the experiments obtained for TX emission fully confirm the results obtained for BX emission.

5 Conclusion and Outlook

5.1 Use of patterned gold surfaces as CPS substrate

The presented work focused on the development of a method for high resolution colocalization in biological systems using SFLIM as fluorescent investigation method.
In a first set of experiments, the ultimate aim was to establish gold surfaces nanopatterned by electro-beam lithography for substrates as CPS surfaces. Therefore, labeling strategies on patterned gold surfaces were developed to diminish quenching of the fluorescent labels from the gold layer. In particular, it could be shown that specific protein labeling of the activated surfaces via glutaraldehyde is possible and that subsequent growing of multiple protein layers attached on top of each other enables the synthesis of protein "rods". Efficient growth could be verified both by the height increase per protein layer measured with AFM and increasing fluorescence signal of the labels due to reduced quenching from the surface. Via this procedure, fluorescence signal-to-background ratios of 4 could be obtained from micrometer test patterns crosslinked with three layers of labeled proteins. It could also be demonstrated that the same procedure can be extended to the labeling of smaller structures, so that fluorescence patterns below 100 nm are still visible with the SFLIM set-up.
The fluorescence intensity of the labels could be greatly increased by modification of the irradiated surface with the aminolinker TEPA, so that the S/B-ratio could be increased by almost one order of magnitude. Best results were obtained with two layers of TEPA and two protein layers, which yielded an S/B-ratio of ≈ 30. Since subsequent layers were built with proteins bearing dye molecules with a different maximum emission wavelength (Alexa633 and Alexa680), it could be shown that quenching is reduced for the top layer, since the spectral signature received from the top layer dominated over the spectral signature of the underlying layers. As most serious problem concerning the improvement of the S/B-ratio, non-specific protein adsorption at the non-irradiated areas was observed which prevents unlimited growing of further protein layers. It was demonstrated that more efficient cleaning methods including ultrasonic treatments with Tween 20 solutions results in partial dissolution of non-specifically bound protein layers, so that growth of further

layers was hindered and did not result in a further increase of the S/B-ratio. In particular it was found, that under rigid cleaning near complete removal of the non-specific layer could be induced, however, with serious affection of the patterned areas.

These results demonstrate that subsequent growing of protein layers is an efficient method to overcome quenching of the gold surface which can be greatly enhanced if additional TEPA layers are used. Comparing the results for direct protein immobilization (Fig 4.1.9) with those obtained for two additional TEPA layers (Fig. 4.1.19 and 4.1.20), it can be estimated that the improvement allows for a much more successful visualization of nanostructures (compare Fig. 4.1.13) with satisfactory S/B-ratios.

However, this method is still hampered by several drawbacks: The most serious problem constitutes the protein immobilization procedure by the application of glutaraldehyde as cross-linker. Hence, since disintegration of protein under the described cleaning procedure is unlikely, it is probable that crosslinking induced by glutaraldehyde is reversible. This disadvantage might be circumvented by using a permanent cross-linker such as bis-sulfosuccinimidylsuberate (BS) [297]. If efficient immobilization of protein by this reagent could be accomplished, a more rigid cleaning procedure could be employed which should facilitate immobilization of a larger number of protein layers without significant increase of non-specific adsorption. This should lead to a significant increase of the signal and since it has been found, that also the TEPA layers seem to be responsible for background increase, it might also be beneficial to use also a more efficient cleaning procedure between this immobilization steps.

Independent of these results, the substitution of proteins with NCs is expected to yield much higher PL efficiencies than obtained for labeled proteins. On the one hand, their size is about three to four times larger than that of the used IgG antibodies which will increase the distance to the gold surface and thus the quenching significantly. On the other hand, a growing of further layers is uncomplicated since no additional crosslinking steps have to be employed. Instead, the strength of the biotin streptavidin bond can be used, which is an advantage, since also BSA can be added to the solution as efficient prevention of non-specific adsorption of NCs to the surface. Although in a first step, biotin has to be immobilized either by direct reaction of the amino-modified surface with an activated biotin, or by crosslinking using biotin-labeled BSA, all subsequent steps can be accomplished by alternating addition of BSA-biotin and the streptavidin-modified NCs. The advantage for the use of both the NCs and the biotinylated BSA is that they present multiple binding sites on their surface which results in a large coupling probability.

Furthermore, BSA results also in a distance increase to the surface which is expected to increase the PL efficiency as well. Concerning the observed photophysical fluctuations seen for single NCs in section 4.2, the described strategy should be ideal for the development of a CPS system. This is because at all labeled site, even for a diameter as small as 50 nm, binding of more than ten NCs is expected. Since fluctuations are not correlated, they will be averaged out to a large extent. Furthermore, it should be considered that still significant quenching from the gold surface is expected. However, as was demonstrated blinking can be greatly reduced for NCs near a gold surface. In one instance it was even found that significant emission in the "off"-state could be observed.

Two further problems for the realization of a CPS surface remain: First, it has been stated that for 3D localization of dyes, the label sites also have to display a different height. One solution to this problem would be the use of large (≈ 40 nm) beads as spacer before NCs are immobilized. Finally, it is necessary to allow for a controlled addressing of different labeling sites, since the activation procedures presented lead to a homogeneous immobilization on all sites. This task can be solved by implementation of scanning ion conductance microscopy, which uses an electric field in a very small glass pipette (diameter < 100 nm) to induce or prevent flow of target molecules out of the pipette [298]. In combination with an optical microscope, a labeling site might then be addressed with the tip, which on close contact with the surface can release the desired labeling species. Since by this controlled method, diffusion of target molecules remote from the tip is greatly reduced, it can be assured that the labeling is specific and that only immobilization on the addressed label site occurs.

5.2 Investigation of photophysical fluctuations of single NCs with SFLIM

The aim of the photophysical investigation of single NCs was to gain a principle understanding of the photophysical processes, with a special regard to their use as probes for high precision colocalization. From the obtained results it can be concluded that SFLIM is a suitable tool to study photophysical fluctuations of single NCs on the ms time scale. In particular, apart from minor deviations concerning the MLE fitting procedure and the detection efficiency, generation of artifacts by interferences of the hardware or software processing could be excluded. Furthermore, for analysis of the data, scatter plots of PL

lifetime versus PL intensity (count rate) together with the spectral information as color-encoding was established as valuable information. The results from the measurements on dry surfaces, under immersion oil, and in MEA buffer can be summarized as follows:

- for all types of NCs investigated, more or less pronounced SD is observed
- the SD is correlated with fluctuations of the PL lifetime, i.e. spectral red-shift leads to prolonged lifetimes
- SD and the detected PL intensity are anticorrelated, i.e. spectral red-shift is accompanied by a decrease of the detected count rate. Measurements under saturation conditions reveal that these intensity fluctuations are related to the PL quantum yield
- all the interrelations are independent of quenching due to trap states, i.e. for a constant degree of quenching the described correlations and anticorrelations always hold
- from the analysis of the τ-N_C-plots it can be deduced that the lifetime fluctuations that correlate with the SD are due to changes of the radiative rate constant k_r. This is confirmed by the plots of the calculated k_r versus the band edge energy E which shows a clear correlation for most of the emission regimes.
- by analysis of the τ-N_C-relations for the investigated NCs, the average PL quantum yield was estimated, and the existence of an intrinsic non-radiative rate independent of quenching caused by trap states was revealed
- for some NCs, a quenched state **(3)** with different photophysical properties than the described exists which is generally characterized by a lower polarizability, i.e. in the plot of k_r versus E, a correlation is difficult to discern.
- measurements using a polarizing beamsplitter demonstrated that there are small changes of the PL polarization probably due to induced dipole moments driven by varying local electric fields
- measurements under immersion oil showed no significant changes of the described interrelations, i.e. influences of the dielectric interface and the polarization orientation on the observed interrelations can be neglected
- in the presence of 150 mM MEA blinking is strongly suppressed so that within the binning almost no dark events were detected

- MEA apparently leads to a decrease both of on- as well as off-times, since many bins show a broad distribution of intensities without change of the lifetime
- the spectral diffusion, i.e. the redistribution of charges, seems to be accelerated as well

Given the wealth of new information which has to be considered, these results will be discussed under three different aspects which are connected, but aim in different directions:
1) Suitability of NCs as probes for high resolution colocalization
2) General understanding of NC photophysics
3) Photophysical assessment of NC samples

5.2.1 Suitability of NCs as probes for high resolution colocalization

Concerning an application as probe for high-resolution colocalization, a luminescent particle has to fulfill several criteria apart from brightness and stability. A prerequisite is that both spectral and lifetime characteristics for all NCs within one sample are significantly different from the characteristics of the other sample. Therefore, a dynamic heterogeneity, i.e. large fluctuations of either of the parameters are detrimental for differentiation. Furthermore, for the fitting procedure, presumptions about the characteristics of both NCs present within the focus have to be made for successful colocalization. This means, that also a certain static homogeneity is required, otherwise if the fit is accomplished for each of the NCs with wrong start parameters, a large error is expected even if both display different characteristics. At last, both spots have to display a stable PL quantum yield, since for the localization procedure using either a Gaussian model or a center-of-mass any fluctuations from pixel to pixel lead to a distortion of the PSF and the true distance.

It is obvious from the presented data and the wedge shapes that most of the investigated NC samples are not suitable because they all display significant static (Fig. 4.2.18) and dynamic (Figs. 4.2.25-27) intensity heterogeneity (Fig. 4.2.17). However, there are several possibilities to overcome this disadvantages: The most readiest solution can be found for blinking, since antiblinking agents demonstrate that it is possible to reduce even very long "off"-states to the ms timescale (Fig. 4.2.46). Despite an integration time per pixel (typically 1-3 ms) on a similar scale, it is expected that in most cases the fitting will not be seriously affected, when imaging NCs with an antiblinking agent such as MEA.

Whereas it seems to be much more complicated to overcome the fluctuations caused by SD and quenching, a potential solution for this problem has been already presented. Even if it is not possible to prevent the fluctuations, it has been stated and can be discerned from Fig. 4.2.47 that the addition of antiblinking agents results in an acceleration of photophysical parameters and averaging within one bin. Thus, although the system is intrinsically not static, it is with respect to the pixel integration time and both spectral and lifetime information will not show large differences from pixel to pixel. It has to be considered here that such a procedure has several implications on the lifetime measurement, since an averaged lifetime is not monoexponential any more, as has been discussed in section 4.2.2. This means that a monoexponential fit model cannot be used any more, but that a pattern-matching algorithm has to be used for correct fitting, under the assumption that the averaged values for both NCs still differ significantly. Finally, there remains the problem of the static heterogeneity which is not expected to be affected by the averaging effect of antiblinking agents.

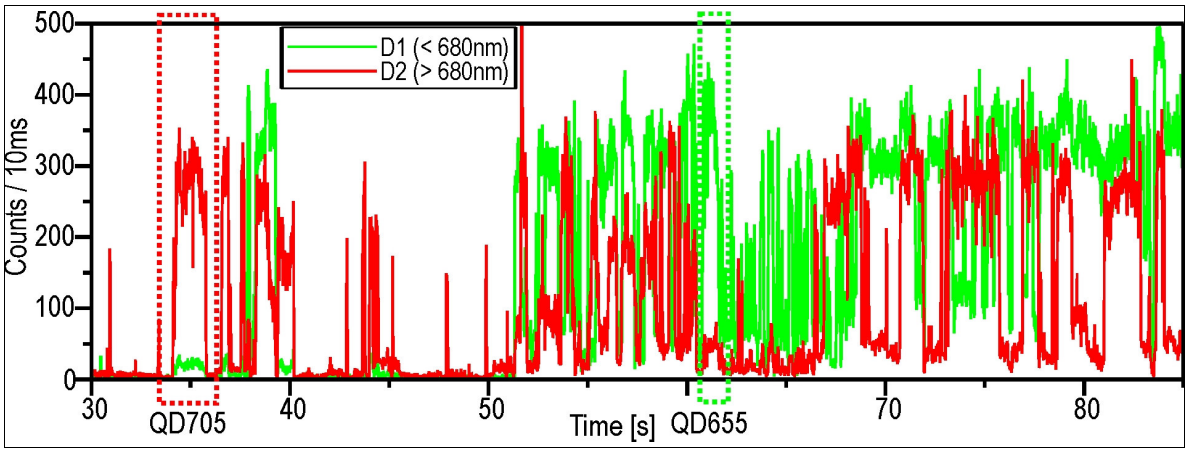

Figure 5.1: *Transient of a construct of a single NC QD655 coupled to a single NC QD705 via BSA-biotin with separated emission on D1 (green) and D2 (red). The 680 nm beamsplitter in the detection path facilitates near complete separation of fluorescence. Note that in the red dotted section at 35 s, only QD705 emits compared to exclusive emission of QD655 (green dotted section at 62 s). These sections can be used to obtain the necessary fit-parameters of the construct.*

Nevertheless, a different approach might be feasible for which blinking of the NCs can be favorably exploited. In general, it is necessary to use averaged values measured from the ensemble to obtain the necessary parameters for the separation algorithm because it is not possible to detect the PL of one dye separately from the other. For NCs, this is possible during blinking events since there is always a chance that during an "off"-event of the first NC, the second is still bright and vice versa (Fig. 5.1). If it is assumed that the averaged values derived from these separated events are representative for the NC characteristics, an individual model system for each NC can be used. Although this approach requires the

recording of a transient and filtering of the necessary parameters for each of the colocalized NC pairs, the increased expenditure will be justified by accurate results.

However, a new difficulty arises concerning the realization of such a procedure. There is the discrepancy that the application of antiblinking agent is necessary in order to circumvent the dynamic heterogeneity, while for recording of the fit parameters blinking is required. Two solutions are suggested: either the transients for each spot are recorded without antiblinking agent and the latter is added for the scanning of the sample. Otherwise, a blinking regime might be found where blinking is generally fast enough to average out the heterogeneity while it is slow enough to facilitate separate recording of the model parameters. Finally, it has to be stated that application of antiblinking agents is prevented in living organisms since thiols are toxic. However, a thorough understanding of the underlying mechanisms might one day allow for the "integration" of antiblinking agent into the dot, so that external addition is not required any more.

5.2.2 General understanding of NC photophysics

Most of the findings stated above have already been discussed in the experimental section, however, there are still a number of questions which remain partially unsolved and require further investigation. Thus, it is intriguing that dynamic heterogeneity might be used to gain quantitative information about the N_C as it has been done to estimate the PL quantum yield ϕ_{av}. It has already been pointed out that the obtained values of 80-90% are comparatively low compared to former measurements and to what is widely assumed in literature. This is the more astonishing since the samples used for these measurements are quite similar to those of previous investigations. Although certain assumptions have been made to derive the exact value of ϕ_{av}, i.e. the postulated intrinsic non-radiative rate constant k_{nr}^{int} was assumed to be constant, there remains the astonishing finding that for red shifted emission always lower maximum count rates were found. Therefore, further tests have to be made in order to find an explanation between the observed discrepancies between the presented work and the reports from literature. Interestingly, similar findings, i.e. red shifts are accompanied by a loss of PL intensity, have been reported before, although they have been assumed to be caused by increasing non-radiative rates by enhanced phonon coupling. Even it cannot be excluded that the non-radiative rate constant k_{nr}^{int} is affected by the band shifts, it cannot constitute the most important cause, since an increase of the lifetime is observed for the red-shift. This is in contrast to what is expected for an influence of the non-radiative

rate which would result in a decreased lifetime with lower PL intensity, as is the case in the quenching regimes. Several experiments might give an answer to these questions: the dependency of the derived ϕ_{av} with regard to different conditions should be tested, e.g. measurements in different solvents, with varying excitation energies and wavelengths, to check whether any systematic changes are observed. Thus, the measurement under immersion oil is expected to increase the radiative rate constant. Hence ϕ_{av} should also increase. Finally, the presented method and the modification procedure from the literature should be exploited on the same surface of NCs, which would give an important check with regard to the accuracies and downfalls of both methods.

A further important point concerns the discovered subpopulation denoted **(3)**. It has been demonstrated that this is a novel emissive state with fundamentally different properties from the "normal" emission (normal is used in the sense that it constitutes the large majority of emission). It has already been stated that some of the observed features indicate some relation to BX emission: In the depicted wedge shapes (Figs. 4.2.25-27) under medium power, it is quite distinct for QD655, but hardly discernible for QD605 and QD705. Under saturating conditions, the subpopulation is not much more prominent for QD655 (Fig. 4.2.35), it also displays a higher relative emission intensity compared to lower power. Although it cannot be explained by BX emission since BX cannot emit independently from X, these similarities indicate that it is connected to Auger processes. This is because, BX emission is dominated by quenching effects through Auger type non-radiative relaxation. Therefore, it might be attributed to a kind of "charged" emission, even though there is at the moment no ready explanation for the fact that within the same NC both blinking and subpopulation **(3)** can be observed although both are connected to charged emission. Further experiments on this field should center on the separate investigation of this state. For this, a novel analysis method which allows for the size separation of bins might be feasible since then mixing with the normal emissive state within one bin could be prevented.

The last point which merits a further discussion is exemplary discussed for the results obtained under MEA. The most interesting feature of antiblinking agents is its acceleration effect on the photophysical parameters which has been deduced from the change of the wedge-shape. Although this allows for an estimation of the average fluctuation rate, i.e. faster than the binning time, there remains the question about the time scales in general. This is problematic since it is acknowledged that blinking occurs on all timescales which makes determination of an absolute value difficult [70]. However, the obvious change

within the plots indicates that some measure for the fluctuation rate might yet be found, although this requires a complex mathematical consideration and is beyond the scope of this work. The measurement of the kinetics of fluctuations is a very important point and has implications on many other investigations. This can be rationalized by the consideration that from each photophysical investigation qualitative and quantitative conclusions are drawn which give a general statement about the investigated NC. This leads to serious problems if fluctuations occur on time scales much longer than the duration of the experiments so that they cannot be detected any more. Although this is not the case for MEA where the fluctuations are rather too fast to be resolved, this can occur under low power excitation (Fig. 5.2). Under these conditions, the fluctuations are very slow since photoinduced ejection and recapture of a charge occurs much more seldom, and charges play for the fluctuations of NC photophysics a dominating role. Therefore, some mathematical evaluation of the fluctuation rate for all parameters, i.e. quenching, blinking and SD has to be found to compare experiments made under different conditions and allow for general statements of NC photophysics.

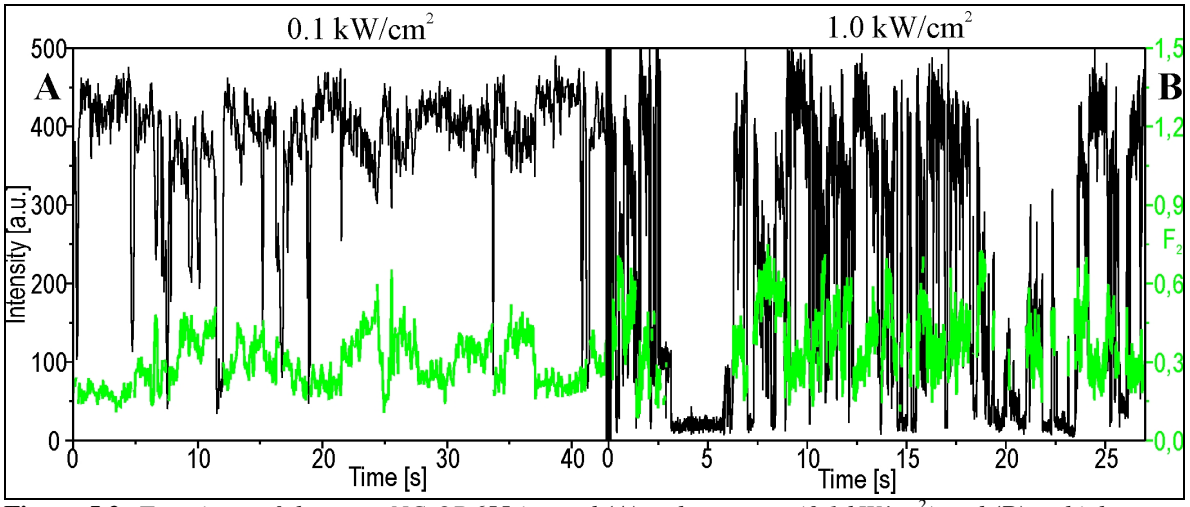

Figure 5.2: *Transients of the same NC QD655 imaged* ***(A)*** *at low power (0.1 kW/cm²) and* ***(B)*** *at high power (1 kW/cm²) with intensity (black) and spectral (green) information. It is obvious that not only intensity fluctuations are much more rapid, but that both the rate and the amplitude of* F_2*-fluctuations increased at high power.*

5.2.3 Photophysical assessment of NC samples

In this work, the depiction method of the τ-N_C-plot has been widely used to draw qualitative conclusions about NC photophysics. In particular, by comparison of typical wedge-shapes of different samples, several differences concerning the general photophysics from sample to sample were elucidated. Therefore, this method seems to be suited to allow

for a kind of assessment of NC photophysics: That is, each sample of NCs is investigated after preparation with regard to several factors, from which the quality of the sample is derived. Up to now, this is generally accomplished using ensemble methods, i.e. the static heterogeneity determined by the size distribution can be estimated from the FWHM of the linewidth of the emission spectrum, whereas the PL quantum yield is derived by comparison with organic dyes. However, as the presented work demonstrated, from the static heterogeneity no conclusions concerning the dynamic heterogeneity can be drawn. In particular, if one aims for the application of NCs on the single particle level, a single particle assessment or qualitative control is feasible to ensure that a prepared sample has the desired quality. The analysis of the wedge shape allows for qualitative statements about the SD, the quenching, the fluctuation rate, and the PL quantum yield, and therefore seems to be a suited tool for such an assessment. Moreover, it can also be used to investigate impacts of a different preparation method on the photophysics. It could be checked if parameters of interest can be influenced by different preparation methods which would allow for a controlled fine tuning of NC properties on a much more sophisticated level.
However, a prerequisite for the employment of the presented method is that it must allow for a quantitative description of the observed differences. Hence, it is desirable to determine how strong quenching is, how large the spectral shifts are, and on what time scales they occur. Before such a method can be developed, it is foremost necessary to check whether the wedge-shape is a characteristic of a certain NC. Thus, if measured under a variety of conditions, its principal features should not change compared to the wedge-shapes of other NCs.

5.3 Investigation of multiexciton emission of single NCs

A number of experiments were carried out concerning the antibunching characteristics of single NCs, especially with regard to both BX as well as TX emission. The results can be summarized as follows:

- a significant increase of the coincidence ratio R_C is observed for QD655, if the excitation power is increased, consistent with characteristics of BX emission, accompanied by the appearance of a short component in the ensemble decays
- the BX emission efficiency decreases in the following order of the samples QD655 >> QD605 > QD705

- separation of photons stemming from BX emission was possible by collection of the photons detected in the first channel within the central peak
- a long component within the BX decay component could be assigned to autofluorescence background and corrected
- for QD655, lifetimes in a large range from below 0.7 ns to more than 1.6 ns could be observed, with typical values around 1.0-1.1 ns
- for QD605, much shorter lifetimes around 0.4 ns were observed, although the IRF is in this case to large to allow for the determination of accurate values
- it was found that even under constant excitation power, R_C may fluctuate significantly, anticorrelated to the PL intensity
- from these characteristics it could be concluded that a quenching of X emission increases the relative BX quantum yield ϕ_{BX}
- spectral separation with suitable filter-sets allowed for TX detection
- observation of TX emission under quenching confirmed that also the relative TX quantum yield increases with quenching of X emission
- investigation of the qualitative change of the TX decay revealed a slight shortening upon X quenching

Although recently a similar report of significant BX emission for the same samples was published, it is noteworthy that the BX decay had been derived from ensemble data [267]. On the other hand, in the presented work it was demonstrated that this method is unequivocal even under strong X emission since a short decay component cannot be assigned solely to BX emission. Therefore, the presented method using pulsed excitation is very efficient for extracting BX decay from single NCs, even though it requires high count rates. A severe drawback of the set-up constitutes the comparatively high IRF > 100 ps which limits determination of BX decay so far to QD655. The most important information stems from the finding that the relative BX emission is not constant, but fluctuates with quenching of NC emission. Thus, it would be of interest if a similar scheme might be used to influence the BX emission at will so that switching from a single to a double photon emitter might be possible. Whereas quenching might be achieved by a number of methods, e.g. imaging near a metallic substance, this is problematic since this would result in an overall reduced emission intensity which is detrimental for the use as double photon source. On the other hand, a relative increase of BX quantum yield might also be accomplished if

the radiative rates could be significantly increased, as is suspected near rough metallic layers [160]. However, the realization of such an enhancement is difficult to achieve.

A very important question concerns the role of the subpopulation **(3)**, for which it has been assumed that even higher coincidence ratios than 0.5, i.e. more than two photons per pulse, might be observed. In this respect, a separation of the photons stemming from regime **(3)** as has been suggested the chapter before, would be also beneficial to allow for a statement.

Altogether, it can be concluded that SFLIM is a highly efficient tool for the investigation of both photophysical fluctuations and multiexciton emission. Thus, the determination of a large number of photophysical parameters is possible with the developed set-up. This is important for a systematic investigation of NC characteristics and facilitates a deeper understanding of the underlying photophysics of these highly interesting probes.

6 References

[1] Lichtman, J. W.; Conchello, J.-A. *Fluorescence microscopy.* Nat. Methods **2005**, *2*, 910-919.

[2] Alivisatos, A. P. *Semiconductor clusters, nanocrystals, and quantum dots.* Science, **1996,** 271, 933.

[3] Kapanidis, A. N.; Weiss, S. *Fluorescent probes and bioconjugation chemistries for single-molecule fluorescence analysis of biomolecules.* J. Chem. Phys. **2002**, *117*, 10953-10964.

[4] Jung, Y.; Barkai, E.; Silbey, R. J. *Current status of single-molecule spectroscopy: theoretical aspects.* J. Chem. Phys. **2002**, *117*, 10980-10995.

[5] Moerner, W. E. *A Dozen Years of Single-Molecule Spectroscopy in Physics, Chemistry, and Biophysics.* J. Phys. Chem. B **2002**, *106*, 910-927.

[6] Orrit, M. *Single-molecule spectroscopy: The road ahead.* Journal of Chemical Physics **2002**, *117*, 10938-10946.

[7] Sunney Xie, X. *Single-molecule approach to dispersed kinetics and dynamic disorder: probing conformational fluctuation and enzymatic dynamics.* J. Chem. Phys. **2002**, *117*, 11024-11032.

[8] Tinnefeld, P.; Sauer, M. *Branching out of single-molecule fluorescence spectroscopy: Challenges for chemistry and influence on biology.* Angew. Chem. Int. Ed. **2005**, *44*, 2642-2671.

[9] Lu, H. P.; Xun, L.; Xie, X. S. *Single-molecule enzymic dynamics.* Science **1998**, *282*, 1877-1882.

[10] Davenport, R. J.; Wuite, G. J. L.; Landick, R.; Bustamante, C. *Single-molecule study of transcriptional pausing and arrest by E. coli RNA polymerase.* Science **2000**, *287*, 2497-2500.

[11] Zhuang, X.; Bartley, L. E.; Babcock, H. P.; Russell, R.; Ha, T.; Herschlag, D.; Chu, S. *A single-molecule study of RNA catalysis and folding.* Science **2000**, *288*, 2048-2051.

[12] Ha, T.; Rasnik, I.; Cheng, W.; Babcock, H. P.; Gauss, G. H.; Lohman, T. M.; Chu, S. *Initiation and re-initiation of DNA unwinding by the Escherichia coli Rep helicase.* Nature **2002**, *419*, 638-641.

[13] Benkovic, S. J.; Hammes-Schiffer, S. *A perspective on enzyme catalysis.* Science **2003**, *301*, 1196-1202.

[14] Shav-Tal, Y.; Darzacq, X.; Shenoy, S. M.; Fusco, D.; Janicki, S. M.; Spector, D. L.; Singer, R. H. *Dynamics of Single mRNPs in Nuclei of Living Cells.* Science **2004**, *304*, 1797-1800.

[15] Raser, J. M.; O'Shea, E. K. *Noise in gene expression: Origins, consequences, and control.* Science **2005**, *309*, 2010-2013.

[16] Cai, L.; Friedman, N.; Xie, X. S. *Stochastic protein expression in individual cells at the single molecule level.* Nature **2006**, *440*, 358-362.

[17] Yu, J.; Xiao, J.; Ren, X.; Lao, K.; Xie, X. S. *Probing Gene Expression in Live Cells, One Protein Molecule at a Time.* Science **2006**, *311*, 1600-1603.

[18] Dahan, M.; Levi, S.; Luccardini, C.; Rostaing, P.; Riveau, B.; Triller, A. *Diffusion dynamics of glycine receptors revealed by single-quantum dot tracking.* Science **2003**, *302*, 442-445.

[19] Kusumi, A.; Nakada, C.; Ritchie, K.; Murase, K.; Suzuki, K.; Murakoshi, H.; Kasai, R. S.; Kondo, J.; Fujiwara, T. *Paradigm shift of the plasma membrane concept from the two-dimensional continuum fluid to the partitioned fluid: High-speed single-molecule tracking of membrane molecules.* Annu. Rev. Bioph. Biom. **2005**, *34*, 351-378, 356 plates.

[20] Lamond, A. I.; Earnshaw, W. C. *Structure and function in the nucleus.* Science **1998**, *280*, 547-553.

[21] Spector, D. L. *Macromolecular domains within the cell nucleus.* Annu. Rev. Cell Biol. **1993**, *9*, 265-315.

[22] Cardoso, M. C.; Leonhardt, H.; Nadal-Ginard, B. *Reversal of terminal differentiation and control of DNA replication: Cyclin A and Cdk2 specifically localize at subnuclear sites of DNA replication.* Cell **1993**, *74*, 979-992.

[23] Pombo, A.; Jackson, D. A.; Hollinshead, M.; Wang, Z.; Roeder, R. G.; Cook, P. R. *Regional specialization in human nuclei: visualization of discrete sites of transcription by RNA polymerase III.* Embo J. **1999**, *18*, 2241-2253.

[24] Cook, P. R. *Review: Molecular biology - The organization of replication and transcription.* Science **1999**, *284*, 1790-1795.

[25] Ha, T. *Structural Dynamics and Processing of Nucleic Acids Revealed by Single-Molecule Spectroscopy.* Biochemistry **2004**, *43*, 4055-4063.

[26] Ha, T. *Single-molecule fluorescence resonance energy transfer.* Methods **2001**, *25*, 78-86.

[27] Weiss, S. *Measuring conformational dynamics of biomolecules by single molecule fluorescence spectroscopy.* Nat. Struct. Biol. **2000**, *7*, 724-729.

[28] Watt, R. M.; Voss, E. W., Jr. *Mechanism of quenching of fluorescein by anti-fluorescein IgG antibodies.* Immunochem. **1977**, *14*, 533-551.

[29] Knemeyer, J. P.; Marme, N.; Sauer, M. *Probes for detection of specific DNA sequences at the single- molecule level.* Anal. Chem. **2000**, *72*, 3717-3724.

[30] Neuweiler, H.; Schulz, A.; Vaiana, A. C.; Smith, J. C.; Kaul, S.; Wolfrum, J.; Sauer, M. *Detection of individual p53-autoantibodies by using quenched peptide-based molecular probes.* Angew. Chem. Int. Ed. **2002**, *41*, 4769-4773.

[31] Heinlein, T.; Knemeyer, J.-P.; Piestert, O.; Sauer, M. *Photoinduced electron transfer between fluorescent dyes and guanosine residues in DNA-hairpins.* J. Phys. Chem. B **2003**, *107*, 7957-7964.

[32] Betzig, E.; Chichester, R. J. *Single Mol. Observed By Near-Field Scanning Optical Microscopy.* Science **1993**, *262*, 1422-1425.

[33] Ambrose, W. P.; Goodwin, P. M.; Martin, J. C.; Keller, R. A. *Alterations of Single-Molecule Fluorescence Lifetimes in Near- Field Optical Microscopy.* Science **1994**, *265*, 364-367.

[34] Hell, S.; Stelzer, E. H. K. *Properties of a 4Pi-confocal fluorescence microscope.* J. Opt. Soc. Am. A **1992**, *9*, 2159-2166.

[35] Egner, A.; Hell, S. W. *Fluorescence microscopy with super-resolved optical sections.* Trends Cell Biol. **2005**, *15*, 207-215.

[36] Bailey, B.; Farkas, D. L.; Taylor, D. L.; Lanni, F. *Enhancement of axial resolution in fluorescence microscopy by standing-wave excitation.* Nature **1993**, *366*, 44-48.

[37] Gustafsson, M. G.; Agard, D. A.; Sedat, J. W. *I5M: 3D widefield light microscopy with better than 100 nm axial resolution.* J. Microsc. **1999**, *195*, 10-16.

[38] Martin, S.; Failla, A. V.; Spoeri, U.; Cremer, C.; Pombo, A. *Measuring the size of biological nanostructures with spatially modulated illumination microscopy.* Mol. Biol.Cell **2004**, *15*, 2449-2455.

[39] Hell, S. W.; Wichmann, J. *Breaking the diffraction resolution limit by stimulated emission: stimulated emission depletion spectroscopy.* Opt. Lett. **1994**, *19*, 780-782.

[40] Klar, T. A.; Jakobs, S.; Dyba, M.; Egner, A.; Hell, S. W. *Fluorescence microscopy with diffraction resolution barrier broken by stimulated emission.* Proc. Natl. Acad. Sci. USA **2000**, *97*, 8206-8210.

[41] Hell, S. W. *Toward fluorescence nanoscopy.* Nat. Biotechnol. **2003**, *21*, 1347-1355.

[42] Dyba, M.; Jakobs, S.; Hell, S. W. *Immunofluorescence stimulated emission depletion microscopy.* Nat. Biotechnol. **2003**, *21*, 1303-1304.

[43] Westphal, V.; Hell, S. W. *Nanoscale Resolution in the Focal Plane of an Optical Microscope.* Phys. Rev. Lett. **2005**, *94*, 143903/143901-143903/143904.

[44] Willig, K. I.; Rizzoli, S. O.; Westphal, V.; Jahn, R.; Hell, S. W. *STED microscopy reveals that synaptotagmin remains clustered after synaptic vesicle exocytosis.* Nature **2006**, *440*, 935-939.

[45] Yildiz, A.; Forkey, J. N.; McKinney, S. A.; Ha, T.; Goldman, Y. E.; Selvin, P. R. *Myosin V Walks Hand-Over-Hand: Single Fluorophore Imaging with 1.5-nm Localization.* Science **2003**, *300*, 2061-2065.

[46] Yildiz, A.; Tomishige, M.; Vale, R. D.; Selvin, P. R. *Kinesin walks hand-over-hand.* Science **2004**, *303*, 676-679.

[47] Gordon, M. P.; Ha, T.; Selvin, P. R. *Single-molecule high-resolution imaging with photobleaching.* Proc. Natl. Acad. Sci. USA **2004**, *101*, 6462-6465.

[48] Qu, X.; Wu, D.; Mets, L.; Scherer, N. F. *Nanometer-localized multiple single-molecule fluorescence microscopy.* Proc. Natl. Acad. Sci. USA **2004**, *101*, 11298-11303.

[49] Lidke, K. A.; Rieger, B.; Jovin, T. M.; Heintzmann, R. *Superresolution by localization of quantum dots using blinking statistics.* Opt. Express **2005**, *13*, 7052-7062.

[50] Betzig, E. *Proposed method for molecular optical imaging.* Opt. Lett. **1995**, *20*, 237-239.

[51] Patwardhan, A.; Manders, E. M. M. *Three colour confocal microscopy using intensity-modulated multiple-beam scanning (IMS) for crosstalk suppression.* Bioimaging **1996**, *4*, 17-24.

[52] Manders, E. M. M. *Chromatic shift in multicolour confocal microscopy.* J. Microsc. **1997**, *185*, 321-328.

[53] Lacoste, T. D.; Michalet, X.; Pinaud, F.; Chemla, D. S.; Alivisatos, A. P.; Weiss, S. *Ultrahigh-resolution multicolor colocalization of single fluorescent probes.* Proc. Natl. Acad. Sci. USA **2000**, *97*, 9461-9466.

[54] Michalet, X.; Lacoste, T. D.; Weiss, S. *Ultrahigh-resolution colocalization of spectrally separable point-like fluorescent probes.* Methods **2001**, *25*, 87-102.

[55] Herten, D. P.; Tinnefeld, P.; Sauer, M. *Identification of single fluorescently labelled mononucleotide molecules in solution by spectrally resolved time-correlated single-photon counting.* Appl. Phys. B **2000**, *71*, 765-771.

[56] Tinnefeld, P.; Herten, D. P.; Sauer, M. *Photophysical dynamics of Single Mol. studied by spectrally-resolved fluorescence lifetime imaging microscopy (SFLIM).* J. Phys. Chem. A **2001**, *105*, 7989-8003.

[57] Heilemann, M.; Herten, D. P.; Heintzmann, R.; Cremer, C.; Muller, C.; Tinnefeld, P.; Weston, K. D.; Wolfrum, J.; Sauer, M. *High-resolution colocalization of single dye molecules by fluorescence lifetime imaging microscopy.* Anal. Chem. **2002**, *74*, 3511-3517.

[58] Heinlein, T.; Biebricher, A.; Schlueter, P.; Roth, C. m.; Herten, D.-P.; Wolfrum, J.; Heilemann, M.; Mueller, C.; Tinnefeld, P.; Sauer, M. *High-resolution colocalization of*

Single Mol. within the resolution gap of far-field microscopy. ChemPhysChem **2005**, *6*, 949-955.

[59] Weston, K. D.; Dyck, M.; Tinnefeld, P.; Muller, C.; Herten, D. P.; Sauer, M. *Measuring the number of independent emitters in single-molecule fluorescence images and trajectories using coincident photons.* Anal. Chem. **2002**, *74*, 5342-5349.

[60] Heinlein, T. *Entwicklung von Methoden zur Struktur- und Funktionsaufklärung in lebenden und fixierten Zellen auf Einzelmolekülniveau mittels Koinzidenzanalyse und Spektral-Aufgelöster Fluoreszenzlebensdauermikroskopie.* Dissertation, Ruprecht-Karls-Universität Heidelberg **2005**.

[61] Geyer, W.; Stadler, V.; Eck, W.; Golzhauser, A.; Grunze, M.; Sauer, M.; Weimann, T.; Hinze, P. *Electron induced chemical nanolithography with self-assembled monolayers.* J. Vac. Sci. Technol. B **2001**, *19*, 2732-2735.

[62] Golzhauser, A.; Eck, W.; Geyer, W.; Stadler, V.; Weimann, T.; Hinze, P.; Grunze, M. *Chemical nanolithography with electron beams.* Adv. Mater. **2001**, *13*, 806-809.

[63] Chance, R. R.; Prock, A.; Silbey, R. *Molecular fluorescence and energy transfer near interfaces.* Adv. Chem. Phys. **1978**, *37*, 1-65.

[64] Biebricher, A.; Paul, A.; Tinnefeld, P.; Golzhauser, A.; Sauer, M. *Controlled three-dimensional immobilization of biomolecules on chemically patterned surfaces.* J. Biotechnol. **2004**, *112*, 97-107.

[65] Hirschfeld, T. *Quantum efficiency independence of the time integrated emission from a fluorescent molecule.* Appl. Opt. **1976**, *15*, 3135.

[66] Lomascolo, M.; Creti, A.; Leo, G.; Vasanelli, L.; Manna, L. *Exciton relaxation processes in colloidal core/shell ZnSe/ZnS nanocrystals.* Appl. Phys. Lett. **2003**, *82*, 418-420.

[67] Wang, X.; Qu, L.; Zhang, J.; Peng, X.; Xiao, M. *Surface-Related Emission in Highly Luminescent CdSe Quantum Dots.* Nano Lett. **2003**, *3*, 1103-1106.

[68] Dahan, M.; Levi, S.; Luccardini, C.; Rostaing, P.; Riveau, B.; Triller, A. *Diffusion Dynamics of Glycine Receptors Revealed by Single-Quantum Dot Tracking.* Science **2003**, *302*, 442-445.

[69] Efros, A. L.; Rosen, M. *Random telegraph signal in the photoluminescence intensity of a single quantum dot.* Phys. Rev. Lett. **1997**, *78*, 1110-1113.

[70] Kuno, M.; Fromm, D. P.; Hamann, H. F.; Gallagher, A.; Nesbitt, D. J. *Nonexponential "blinking" kinetics of single CdSe quantum dots: A universal power law behavior.* J. Chem. Phys. **2000**, *112*, 3117-3120.

[71] Shimizu, K. T.; Neuhauser, R. G.; Leatherdale, C. A.; Empedocles, S. A.; Woo, W. K.; Bawendi, M. G. *Blinking statistics in single semiconductor nanocrystal quantum dots.* Phys. Rev. B **2001**, *63*, 205316/205311-205316/205315.

[72] Hohng, S.; Ha, T. *Near-Complete Suppression of Quantum Dot Blinking in Ambient Conditions.* J. Am. Chem. Soc. **2004**, *126*, 1324-1325.

[73] Michalet, X.; Pinaud, F.; Lacoste, T. D.; Dahan, M.; Bruchez, M. P.; Alivisatos, A. P.; Weiss, S. *Properties of fluorescent semiconductor nanocrystals and their application to biological labeling.* Single Mol. **2001**, *2*, 261-276.

[74] Jovin, T. M. *Quantum dots finally come of age.* Nat. Biotechnol. **2003**, *21*, 32-33.

[75] Michalet, X.; Pinaud, F. F.; Bentolila, L. A.; Tsay, J. M.; Doose, S.; Li, J. J.; Sundaresan, G.; Wu, A. M.; Gambhir, S. S.; Weiss, S. *Quantum Dots for Live Cells, in Vivo Imaging, and Diagnostics.* Science **2005**, *307*, 538-544.

[76] Ambrose, W. P.; Moerner, W. E. *Fluorescence Spectroscopy and Spectral Diffusion of Single Impurity Molecules in a Crystal.* Nature **1991**, *349*, 225-227.

[77] Lu, H. P.; Xie, X. S. *Single-molecule spectral fluctuations at room temperature.* Nature **1997**, *385*, 143-146.

[78] Ha, T.; Enderle, T.; Chemla, D. S.; Selvin, P. R.; Weiss, S. *Quantum jumps of Single Mol. at room temperature.* Chem. Phys. Lett. **1997**, *271*, 1-5.

[79] Tinnefeld, P.; Buschmann, V.; Herten, D. P.; Han, K.-T.; Sauer, M. *Confocal Fluorescence Lifetime Imaging Microscopy (FLIM) at the Single Molecule Level.* Single Mol. **2000**, *1*, 215-223.

[80] Ha, T.; Enderle, T.; Ogletree, D. F.; Chemla, D. S.; Selvin, P. R.; Weiss, S. *Probing the interaction between two single molecules: Fluorescence resonance energy transfer between a single donor and a single acceptor.* Proc. Natl. Acad. Sci. USA **1996**, *93*, 6264-6268.

[81] Basche, T.; Kummer, S.; Brauchle, C. *Direct Spectroscopic Observation of Quantum Jumps of a Single- Molecule.* Nature **1995**, *373*, 132-134.

[82] Panzer, O.; Gohde, W.; Fischer, U. C.; Fuchs, H.; Mullen, K. *Influence of oxygen on single molecule blinking.* Adv. Mater. **1998**, *10*, 1469-1472.

[83] Veerman, J. A.; Garcia-Parajo, M. F.; Kuipers, L.; van Hulst, N. F. *Time-varying triplet state lifetimes of single molecules.* Phys. Rev. Lett. **1999**, *83*, 2155-2158.

[84] Widengren, J.; Schwille, P. *Characterization of photoinduced isomerization and back- isomerization of the cyanine dye Cy5 by fluorescence correlation spectroscopy.* J. Phys. Chem. A **2000**, *104*, 6416-6428.

[85] Bernard, J.; Fleury, L.; Talon, H.; Orrit, M. *Photon Bunching in the Fluorescence From Single Mol. - a Probe For Intersystem Crossing.* J. Chem. Phys. **1993**, *98*, 850-859.

[86] Weston, K. D.; Carson, P. J.; Metiu, H.; Buratto, S. K. *Room-temperature fluorescence characteristics of single dye molecules adsorbed on a glass surface.* J. Chem. Phys. **1998**, *109*, 7474-7485.

[87] Orrit, M.; Bernard, J. *Single pentacene molecules detected by fluorescence excitation in a p-terphenyl crystal.* Phys. Rev. Lett. **1990**, *65*, 2716-2719.

[88] Empedocles, S. A.; Norris, D. J.; Bawendi, M. G. *Photoluminescence spectroscopy of single CdSe nanocrystallite quantum dots.* Phys. Rev. Lett. **1996**, *77*, 3873-3876.

[89] Empedocles, S. A.; Bawendi, M. G. *Quantum-confined Stark effect in single CdSe nanocrystallite quantum dots.* Science **1997**, *278*, 2114-2117.

[90] Empedocles, S.; Bawendi, M. *Spectroscopy of Single CdSe Nanocrystallites.* Acc. Chem. Res. **1999**, *32*, 389-396.

[91] Schlegel, G.; Bohnenberger, J.; Potapova, I.; Mews, A. *Fluorescence Decay Time of Single Semiconductor Nanocrystals.* Phys. Rev. Lett. **2002**, *88*, 137401/137401-137401/137404.

[92] Fisher, B. R.; Eisler, H.-J.; Stott, N. E.; Bawendi, M. G. *Emission Intensity Dependence and Single-Exponential Behavior in Single Colloidal Quantum Dot Fluorescence Lifetimes.* J. Phys. Chem. B **2004**, *108*, 143-148.

[93] Kuno, M.; Fromm, D. P.; Hamann, H. F.; Gallagher, A.; Nesbitt, D. J. *"On"/"off" fluorescence intermittency of single semiconductor quantum dots.* J. Chem. Phys. **2001**, *115*, 1028-1040.

[94] Lounis, B.; Moerner, W. E. *Single photons on demand from a single molecule at room temperature.* Nature **2000**, *407*, 491-493.

[95] Lounis, B.; Bechtel, H. A.; Gerion, D.; Alivisatos, P.; Moerner, W. E. *Photon antibunching in single CdSe/ZnS quantum dot fluorescence.* Chem. Phys. Lett. **2000**, *329*, 399-404.

[96] Brokmann, X.; Giacobino, E.; Dahan, M.; Hermier, J. P. *Highly efficient triggered emission of single photons by colloidal CdSe/ZnS nanocrystals.* Appl. Phys. Lett. **2004**, *85*, 712-714.

[97] Brokmann, X.; Messin, G.; Desbiolles, P.; Giacobinol, E.; Dahan, M.; Hermier, J. P. *Colloidal CdSe/ZnS quantum dots as single-photon sources.* New J. Phys. **2004**, *6*, No pp. given.

[98] Dekel, E.; Gershoni, D.; Ehrenfreund, E.; Spektor, D.; Garcia, J. M.; Petroff, P. M. *Multiexciton Spectroscopy of a Single Self-Assembled Quantum Dot.* Phys. Rev. Lett. **1998**, *80*, 4991-4994.

[99] Kulakovskii, V. D.; Bacher, G.; Weigand, R.; Kummell, T.; Forchel, A.; Borovitskaya, E.; Leonardi, K.; Hommel, D. *Fine Structure of Biexciton Emission in Symmetric and Asymmetric CdSe/ZnSe Single Quantum Dots.* Phys. Rev. Lett. **1999**, *82*, 1780-1783.

[100] Moreau, E.; Robert, I.; Manin, L.; Thierry-Mieg, V.; Gerard, J. M.; Abram, I. *Quantum Cascade of Photons in Semiconductor Quantum Dots.* Phys. Rev. Lett. **2001**, *87*, 183601/183601-183601/183604.

[101] Zwiller, V.; Jonsson, P.; Blom, H.; Jeppesen, S.; Pistol, M.-E.; Samuelson, L.; Katznelson, A. A.; Kotelnikov, E. Y.; Evtikhiev, V.; Bjork, G. *Correlation spectroscopy of excitons and biexcitons on a single quantum dot.* Phys. Rev. A **2002**, *66*, 053814/053811-053814/053817.

[102] Tellinghuisen, J.; Wilkerson Jr., C. W. *Bias and precision in the estimation of exponential decay parameters from sparse data.* Anal. Chem. **1993**, *65*, 1240-1246.

[103] Enderlein, J.; Goodwin, P. M.; VanOrden, A.; Ambrose, W. P.; Erdmann, R.; Keller, R. A. *A maximum likelihood estimator to distinguish Single Mol. by their fluorescence decays.* Chem. Phys. Lett. **1997**, *270*, 464-470.

[104] Enderlein, J.; Sauer, M. *Optimal algorithm for single-molecule identification with time- correlated single-photon counting.* J. Phys. Chem. A **2001**, *105*, 48-53.

[105] Maus, M.; Cotlet, M.; Hofkens, J.; Gensch, T.; De Schryver, F. C.; Schaffer, J.; Seidel, C. A. M. *An experimental comparison of the maximum likelihood estimation and nonlinear least squares fluorescence lifetime analysis of single molecules.* Anal. Chem. **2001**, *73*, 2078-2086.

[106] Tinnefeld, P.; Muller, C.; Sauer, M. *Time-varying photon probability distribution of individual molecules at room temperature.* Chem. Phys. Lett. **2001**, *345*, 252-258.

[107] Michler, P.; Imamoglu, A.; Mason, M. D.; Carson, P. J.; Strouse, G. F.; Buratto, S. K. *Quantum correlation among photons from a single quantum dot at room temperature.* Nature **2000**, *406*, 968-970.

[108] Zrenner, A. *A close look on single quantum dots.* J. Chem. Phys. **2000**, *112*, 7790-7798.

[109] Neuweiler, H.; Sauer, M. *Using photoinduced charge transfer reactions to study conformational dynamics of biopolymers at the single-molecule level.* Curr. Pharm. Biotechno. **2004**, *5*, 285-298.

[110] Piestert, O.; Barsch, H.; Buschmann, V.; Heinlein, T.; Knemeyer, J.-P.; Weston, K. D.; Sauer, M. *A single-molecule sensitive DNA hairpin system based on intramolecular electron transfer.* Nano Lett. **2003**, *3*, 979-982.

[111] Stoehr, K.; Haefner, B.; Nolte, O.; Wolfrum, J.; Sauer, M.; Herten, D.-P. *Species-Specific Identification of Mycobacterial 16S rRNA PCR Amplicons Using Smart Probes.* Anal. Chem. **2005**, *77*, 7195-7203.

[112] Neuweiler, H.; Schulz, A.; Boehmer, M.; Enderlein, J.; Sauer, M. *Measurement of submicrosecond intramolecular contact formation in peptides at the single-molecule level.* J. Am. Chem. Soc. **2003**, *125*, 5324-5330.

[113] Scheffler, S.; Sauer, M.; Neuweiler, H. *Monitoring antibody binding events in homogeneous solution by single-molecule fluorescence spectroscopy.* Z. Phys. Chem.-München **2005**, *219*, 665-678.

[114] Neuweiler, H.; Doose, S.; Sauer, M. *A microscopic view of miniprotein folding: Enhanced folding efficiency through formation of an intermediate.* Proc. Natl. Acad. Sci. USA **2005**, *102*, 16650-16655.

[115] Förster, T. *Zwischenmolekulare Energiewanderung und Fluoreszenz.* Annalen der Physik **1948**, *2*, 55-75.

[116] Heilemann, M.; Tinnefeld, P.; Sanchez Mosteiro, G.; Garcia Parajo, M.; Van Hulst, N. F.; Sauer, M. *Multistep Energy Transfer in Single Molecular Photonic Wires.* J. Am. Chem. Soc. **2004**, *126*, 6514-6515.

[117] Garcia-Parajo, M. F.; Hernando, J.; Mosteiro, G. S.; Hoogenboom, J. P.; van Dijk, E. M. H. P.; van Hulst, N. F. *Energy transfer in single-molecule photonic wires.* ChemPhysChem **2005**, *6*, 819-827.

[118] Ulman, A. *Formation and Structure of Self-Assembled Monolayers.* Chemical Reviews **1996**, *96*, 1533-1554.

[119] Hainfeld, J. F.; Powell, R. D. *New frontiers in gold labeling.* J. Histochem. Cytochem. **2000**, *48*, 471-480.

[120] Mosesson, M. W.; Siebenlist, K. R.; Meh, D. A.; Wall, J. S.; Hainfeld, J. F. *The location of the carboxy-terminal region of g chains in fibrinogen and fibrin D domains.* Proc. Natl. Acad. Sci. USA **1998**, *95*, 10511-10516.

[121] Luo, R. Z. T.; Beniac, D. R.; Fernandes, A.; Yip, C. C.; Ottensmeyer, F. P. *Quaternary structure of the insulin-insulin receptor complex.* Science **1999**, *285*, 1077-1080.

[122] Elghanian, R.; Storhoff, J. J.; Mucic, R. C.; Letsinger, R. L.; Mirkin, C. A. *Selective colorimetric detection of polynucleotides based on the distance-dependent optical properties of gold nanoparticles.* Science **1997**, *277*, 1078-1080.

[123] Reynolds, R. A., III; Mirkin, C. A.; Letsinger, R. L. *Homogeneous, Nanoparticle-Based Quantitative Colorimetric Detection of Oligonucleotides.* J. Am. Chem. Soc. **2000**, *122*, 3795-3796.

[124] Reynolds, R. A., III; Mirkin, C. A.; Letsinger, R. L. *A gold nanoparticle/latex microsphere-based colorimetric oligonucleotide detection method.* Pure and Applied Chemistry **2000**, *72*, 229-235.

[125] Pena, S. R. N.; Raina, S.; Goodrich, G. P.; Fedoroff, N. V.; Keating, C. D. *Hybridization and Enzymatic Extension of Au Nanoparticle-Bound Oligonucleotides.* J. Am. Chem. Soc. **2002**, *124*, 7314-7323.

[126] Alivisatos, A. P.; Johnsson, K. P.; Peng, X.; Wilson, T. E.; Loweth, C. J.; Bruchez, M. P., Jr.; Schultz, P. G. *Organization of 'nanocrystal molecules' using DNA.* Nature **1996**, *382*, 609-611.

[127] Csaki, A.; Maubach, G.; Born, D.; Reichert, J.; Fritzsche, W. *DNA-based molecular nanotechnology.* Single Mol. **2002**, *3*, 275-280.

[128] Drexhage, K. H.; Kuhn, H.; Mobius, D.; Tillmann, P. *Aufbau von Systemen monomolekularer Schichten oberflächenaktiver Farbstoffe.* Ber. Bunsen Phys. Chem. **1966**, *70*, 1179.

[129] Drexhage, K. H.; Kuhn, H.; Schäfer, F. P. *Variation of fluorescence decay time of a molecule in front of a mirror.* Ber. Bunsen Phys. Chem. **1968**, *72*, 329.

[130] Drexhage, K. H. *Influence of a dielectric interface on fluorescence decay time.* Proc. Int. Conf. Lumin. **1970**, 693-701.

[131] Kuhn, H. *Classical aspects of energy transfer in molecular systesm.* J. Chem. Phys. **1970**, *53*, 101-108.

[132] Chance, R. R.; Prock, A.; Silbey, R. *Lifetime of an emitting molecule near a partially reflecting surface.* J. Chem. Phys. **1974**, *60*, 2744-2748.

[133] Chance, R. R.; Prock, A.; Silbey, R. *Lifetime of an excited molecule near a metal mirror. Energy transfer in the europium (3+)/silver system.* J. Chem. Phys. **1974**, *60*, 2184-2185.

[134] Chance, R. R.; Prock, A.; Silbey, R. *Classical theory of energy transfer.* J. Chem. Phys. **1975**, *62*, 2245-2253.

[135] Chance, R. R.; Prock, A.; Silbey, R. *Decay of an emitting dipole between two parallel mirrors.* J. Chem. Phys. **1975**, *62*, 771-772.

[136] Chance, R. R.; Miller, A. H.; Prock, A.; Silbey, R. *Fluorescence and energy transfer near interfaces. Complete and quantitative description of the europium(3+) ion/mirror (Eu3+/mirror) systems.* J. Chem. Phys. **1975**, *63*, 1589-1595.

[137] Chance, R. R.; Prock, A.; Silbey, R. *Frequency shifts of an electric-dipole transition near a partially reflecting surface.* Phys. Rev. A **1975**, *12*, 1448-1452.

[138] Chance, R. R.; Miller, A. H.; Prock, A.; Silbey, R. *Luminescent lifetimes near multiple interfaces. Quantitative comparison of theory and experiment.* Chem. Phys. Lett. **1975**, *33*, 590-592.

[139] Chance, R. R.; Prock, A.; Silbey, R. *Comments on the classical theory of energy transfer. II. Extension to higher multipoles and anisotropic media.* J. Chem. Phys. **1976**, *65*, 2527-2531.

[140] Gueroui, Z.; Libchaber, A. *Single-molecule measurements of gold-quenched quantum dots.* Phys. Rev. Lett. **2004**, *93*, 166108/166101-166108/166104.

[141] Dubertret, B.; Calame, M.; Libchaber, A. J. *Single-mismatch detection using gold-quenched fluorescent oligonucleotides.* Nat. Biotechnol. **2001**, *19*, 365-370.

[142] Maxwell Dustin, J.; Taylor Jason, R.; Nie, S. *Self-assembled nanoparticle probes for recognition and detection of biomolecules.* J. Am. Chem. Soc. **2002**, *124*, 9606-9612.

[143] Persson, B. N. J.; Avouris, P. *On the nature and decay of electronically excited states at metal surfaces.* J. Chem. Phys. **1983**, *79*, 5156-5162.

[144] Persson, B. N. J.; Andersson, S. *Dynamical processes at surfaces: Excitation of electron-hole pairs.* Phys. Rev. B **1984**, *29*, 4382-4394.

[145] Persson, B. N. J.; Lang, N. D. *Electron-hole-pair quenching of excited states near a metal.* Phys. Rev. B **1982**, *26*, 5409-5415.

[146] Makarova, O. V.; Ostafin, A. E.; Miyoshi, H.; Norris, J. R., Jr.; Meisel, D. *Adsorption and encapsulation of fluorescent probes in nanoparticles.* J. Phys. Chem. B **1999**, *103*, 9080-9084.

[147] Aguila, A.; Murray, R. W. *Monolayer-Protected Clusters with Fluorescent Dansyl Ligands.* Langmuir **2000**, *16*, 5949-5954.

[148] Levi, S. A.; Mourran, A.; Spatz, J. P.; Van Veggel, F. C. J. M.; Reinhoudt, D. N.; Moller, M. *Fluorescence of dyes adsorbed on highly organized, nanostructured gold surfaces.* Chem. Eur. J. **2002**, *8*, 3808-3814.

[149] Dulkeith, E.; Morteani, A. C.; Niedereichholz, T.; Klar, T. A.; Feldmann, J.; Levi, S. A.; van Veggel, F. C. J. M.; Reinhoudt, D. N.; Moller, M.; Gittins, D. I. *Fluorescence Quenching of Dye Molecules near Gold Nanoparticles: Radiative and Nonradiative Effects.* Phys. Rev. Lett. **2002**, *89*, 203002/203001-203002/203004.

[150] Huang, T.; Murray, R. W. *Quenching of [Ru(bpy)3]2+ Fluorescence by Binding to Au Nanoparticles.* Langmuir **2002**, *18*, 7077-7081.

[151] Rossetti, R.; Brus, L. E. *Time resolved energy transfer from electronically excited 3B3u pyrazine molecules to planar silver and gold surfaces.* J. Chem. Phys. **1982**, *76*, 1146-1149.

[152] Gebauer, W.; Langner, A.; Schneider, M.; Sokolowski, M.; Umbach, E. *Luminescence quenching of ordered p-conjugated molecules near a metal surface: Quaterthiophene and PTCDA on Ag(111).* Phys. Rev. B **2004**, *69*, 155431/155431-155431/155438.

[153] Kato, N.; Caruso, F. *Homogeneous, Competitive Fluorescence Quenching Immunoassay Based on Gold Nanoparticle/Polyelectrolyte Coated Latex Particles.* J. Phys. Chem. B **2005**, *109*, 19604-19612.

[154] Inacker, O.; Kuhn, H. *Energy transfer dye to specific singlet or triplet energy acceptors in monolayer assemblies.* Chem. Phys. Lett. **1974**, *27*, 317-321.

[155] Killesreiter, H. *Enhanced decay of excited dyes measured by competing charge transfer at the phase boundary of molecular crystals.* J. Lumin. **1976**, *12-13*, 857-863.

[156] Sokolov, K.; Chumanov, G.; Cotton, T. M. *Enhancement of Molecular Fluorescence near the Surface of Colloidal Metal Films.* Anal. Chem. **1998**, *70*, 3898-3905.

[157] Ditlbacher, H.; Felidj, N.; Krenn, J. R.; Lamprecht, B.; Leitner, A.; Aussenegg, F. R. *Electromagnetic interaction of fluorophores with designed two-dimensional silver nanoparticle arrays.* Appl. Phys. B **2001**, *73*, 373-377.

[158] Lakowicz, J. R.; Shen, B.; Gryczynski, Z.; D'Auria, S.; Gryczynski, I. *Intrinsic fluorescence from DNA can Be enhanced by metallic particles.* Biochem. Biophys. Res. Comm. **2001**, *286*, 875-879.

[159] Malicka, J.; Gryczynski, I.; Lakowicz, J. R. *Enhanced emission of highly labeled DNA oligomers near silver metallic surfaces.* Anal. Chem. **2003**, *75*, 4408-4414.

[160] Lakowicz, J. R. *Radiative decay engineering 5: metal-enhanced fluorescence and plasmon emission.* Anal. Biochem. **2005**, *337*, 171-194.

[161] Moskovits, M. *Surface-enhanced spectroscopy.* Rev. Mod. Phys. **1985**, *57*, 783-826.

[162] Grahn, H. T.; Editor *Semiconductor Physics: An Introduction*, **1998**.

[163] Gaponenko, S. v. *Optical Properties of Semiconductor Nanocrystals*, **1998**.

[164] Ekimov, A. I.; Onushchenko, A. A.; Tsekhomskii, V. A. *Exciton absorption by copper(I) chloride crystals in a glassy matrix.* Fizika i Khimiya Stekla **1980**, *6*, 511-512.

[165] Ekimov, A. I.; Onushchenko, A. A. *Quantum dimensional effect in three-dimensional microcrystals of semiconductors.* Pis'ma v Zhurnal Eksperimental'noi i Teoreticheskoi Fiziki **1981**, *34*, 363-366.

[166] Henglein, A. *Photodegradation and fluorescence of colloidal cadmium sulfide in aqueous solution.* Ber. Bunsen Ges. **1982**, *86*, 301-305.

[167] Ekimov, A. I.; Onushchenko, A. A. *Quantum size effect in optical spectra of semiconductor microcrystals.* Fizika i Tekhnika Poluprovodnikov **1982**, *16*, 1215-1219.

[168] Efros, A. L. *Interband light absorption in a semiconductor sphere.* Fizika i Tekhnika Poluprovodnikov **1982**, *16*, 1209-1214.

[169] Murray, C. B.; Norris, D. J.; Bawendi, M. G. *Synthesis and characterization of nearly monodisperse CdE (E = sulfur, selenium, tellurium) semiconductor nanocrystallites.* J. Am. Chem. Soc.**1993**, *115*, 8706-8715.

[170] Hines, M. A.; Guyot-Sionnest, P. *Synthesis and Characterization of Strongly Luminescing ZnS-Capped CdSe Nanocrystals.* J. Phys. Chem. **1996**, *100*, 468-471.

[171] Dabbousi, B. O.; Rodriguez-Viejo, J.; Mikulec, F. V.; Heine, J. R.; Mattoussi, H.; Ober, R.; Jensen, K. F.; Bawendi, M. G. *(CdSe)ZnS Core-Shell Quantum Dots: Synthesis and Optical and Structural Characterization of a Size Series of Highly Luminescent Materials.* J. Phys. Chem. B **1997**, *101*, 9463-9475.

[172] Chan, W. C. W.; Nile, S. *Quantum dot bioconjugates for ultrasensitive nonisotopic detection.* Science **1998**, *281*, 2016-2018.

[173] Aldana, J.; Wang, Y. A.; Peng, X. *Photochemical Instability of CdSe Nanocrystals Coated by Hydrophilic Thiols.* J. Am. Chem. Soc. **2001**, *123*, 8844-8850.

[174] Bruchez, M., Jr.; Moronne, M.; Gin, P.; Weiss, S.; Alivisatos, A. P. *Semiconductor nanocrystals as fluorescent biological labels.* Science **1998**, *281*, 2013-2016.

[175] Gerion, D.; Pinaud, F.; Williams, S. C.; Parak, W. J.; Zanchet, D.; Weiss, S.; Alivisatos, A. P. *Synthesis and Properties of Biocompatible Water-Soluble Silica-Coated CdSe/ZnS Semiconductor Quantum Dots.* J. Phys. Chem. B **2001**, *105*, 8861-8871.

[176] Akerman, M. E.; Chan, W. C. W.; Laakkonen, P.; Bhatia, S. N.; Ruoslahti, E. *Nanocrystal targeting in vivo.* Proc. Natl. Acad. Sci. USA **2002**, *99*, 12617-12621.

[177] Ishii, D.; Kinbara, K.; Ishida, Y.; Ishii, N.; Okochi, M.; Yohda, M.; Aida, T. *Chaperonin-mediated stabilization and ATP-triggered release of semiconductor nanoparticles.* Nature **2003**, *423*, 628-632.

[178] Tsay, J. M.; Doose, S.; Pinaud, F.; Weiss, S. *Enhancing the Photoluminescence of Peptide-Coated Nanocrystals with Shell Composition and UV Irradiation.* J. Phys. Chem. B **2005**, *109*, 1669-1674.

[179] Doose, S.; Tsay, J. M.; Pinaud, F.; Weiss, S. *Comparison of photophysical and colloidal properties of biocompatible semiconductor nanocrystals using fluorescence correlation spectroscopy.* Anal. Chem. **2005**, *77*, 2235-2242.

[180] Han, M.; Gao, X.; Su, J. Z.; Nie, S. *Quantum-dot-tagged microbeads for multiplexed optical coding of biomolecules.* Nat. Biotechnol. **2001**, *19*, 631-635.

[181] Larson, D. R.; Zipfel, W. R.; Williams, R. M.; Clark, S. W.; Bruchez, M. P.; Wise, F. W.; Webb, W. W. *Water-soluble quantum dots for multiphoton fluorescence imaging in vivo.* Science **2003**, *300*, 1434-1437.

[182] Gao, X.; Nie, S. *Quantum Dot-Encoded Mesoporous Beads with High Brightness and Uniformity: Rapid Readout Using Flow Cytometry.* Anal. Chem. **2004**, *76*, 2406-2410.

[183] Dubertret, B.; Skourides, P.; Norris, D. J.; Noireaux, V.; Brivanlou, A. H.; Libchaber, A. *In vivo imaging of quantum dots encapsulated in phospholipid micelles.* Science **2002**, *298*, 1759-1762.

[184] Jaiswal, J. K.; Mattoussi, H.; Mauro, J. M.; Simon, S. M. *Long-term multiple color imaging of live cells using quantum dot bioconjugates.* Nat. Biotechnol. **2003**, *21*, 47-51.

[185] Kim, S.; Lim, Y. T.; Soltesz, E. G.; De Grand, A. M.; Lee, J.; Nakayama, A.; Parker, J. A.; Mihaljevic, T.; Laurence, R. G.; Dor, D. M.; Cohn, L. H.; Bawendi, M. G.; Frangioni, J. V. *Near-infrared fluorescent type II quantum dots for sentinel lymph node mapping.* Nat. Biotechnol. **2004**, *22*, 93-97.

[186] Lidke, D. S.; Nagy, P.; Heintzmann, R.; Arndt-Jovin, D. J.; Post, J. N.; Grecco, H. E.; Jares-Erijman, E. A.; Jovin, T. M. *Quantum dot ligands provide new insights into erbB/HER receptor-mediated signal transduction.* Nat. Biotechnol. **2004**, *22*, 198-203.

[187] Xie, R.; Kolb, U.; Li, J.; Basche, T.; Mews, A. *Synthesis and Characterization of Highly Luminescent CdSe-Core CdS/Zn0.5Cd0.5S/ZnS Multishell Nanocrystals.* J. Am. Chem. Soc. **2005**, *127*, 7480-7488.

[188] Klimov, V. I. *Optical Nonlinearities and Ultrafast Carrier Dynamics in Semiconductor Nanocrystals.* J. Phys. Chem. B **2000**, *104*, 6112-6123.

[189] Efros, A. L.; Rosen, M. *The electronic structure of semiconductor nanocrystals.* Annual Review of Materials Science **2000**, *30*, 475-521.

[190] Mittleman, D. M.; Schoenlein, R. W.; Shiang, J. J.; Colvin, V. L.; Alivisatos, A. P.; Shank, C. V. *Quantum size dependence of femtosecond electronic dephasing and vibrational dynamics in CdSe nanocrystals.* Phys. Rev. B **1994**, *49*, 14435-14447.

[191] Benisty, H.; Sotomayor-Torres, C. M.; Weisbuch, C. *Intrinsic mechanism for the poor luminescence properties of quantum-box systems.* Phys. Rev. B **1991**, *44*, 10945-10948.

[192] Bockelmann, U.; Egeler, T. *Electron relaxation in quantum dots by means of Auger processes.* Phys. Rev. B **1992**, *46*, 15574-15577.

[193] Klimov, V. I.; McBranch, D. W. *Femtosecond 1P-to-1S electron relaxation in strongly confined semiconductor nanocrystals.* Phys. Rev. Lett. **1998**, *80*, 4028-4031.

[194] Guyot-Sionnest, P.; Shim, M.; Matranga, C.; Hines, M. *Intraband relaxation in CdSe quantum dots.* Phys. Rev. B **1999**, *60*, R2181-R2184.

[195] Klimov, V. I.; Schwarz, C. J.; McBranch, D. W.; Leatherdale, C. A.; Bawendi, M. G. *Ultrafast dynamics of inter- and intraband transitions in semiconductor nanocrystals: Implications for quantum-dot lasers.* Phys. Rev. B **1999**, *60*, R2177-R2180.

[196] Efros, A. L.; Kharchenko, V. A.; Rosen, M. *Breaking the phonon bottleneck in nanometer quantum dots: role of Auger-like processes.* Solid. State. Comm. **1995**, *93*, 281-284.

[197] Klimov, V. I.; McBranch, D. W.; Leatherdale, C. A.; Bawendi, M. G. *Electron and hole relaxation pathways in semiconductor quantum dots.* Phys. Rev. B **1999**, *60*, 13740-13749.

[198] Underwood, D. F.; Kippeny, T.; Rosenthal, S. J. *Ultrafast Carrier Dynamics in CdSe Nanocrystals Determined by Femtosecond Fluorescence Upconversion Spectroscopy.* J. Phys. Chem. B **2001**, *105*, 436-443.

[199] Nirmal, M.; Norris, D. J.; Kuno, M.; Bawendi, M. G.; Efros, A. L.; Rosen, M. *Observation of the "dark exciton" in CdSe quantum dots.* Phys. Rev. Lett. **1995**, *75*, 3728-3731.

[200] Bawendi, M. G.; Carroll, P. J.; Wilson, W. L.; Brus, L. E. *Luminescence properties of cadmium selenide quantum crystallites: resonance between interior and surface localized states.* J. Chem. Phys. **1992**, *96*, 946-954.

[201] Nirmal, M.; Murray, C. B.; Bawendi, M. G. *Fluorescence-line narrowing in CdSe quantum dots: surface localization of the photogenerated exciton.* Phys. Rev. B **1994**, *50*, 2293-2300.

[202] Crooker, S. A.; Barrick, T.; Hollingsworth, J. A.; Klimov, V. I. *Multiple temperature regimes of radiative decay in CdSe nanocrystal quantum dots: Intrinsic limits to the dark-exciton lifetime.* Appl. Phys. Lett. **2003**, *82*, 2793-2795.

[203] Efros, A. L.; Rosen, M.; Kuno, M.; Nirmal, M.; Norris, D. J.; Bawendi, M. *Band-edge exciton in quantum dots of semiconductors with a degenerate valence band: dark and bright exciton states.* Phys. Rev. B **1996**, *54*, 4843-4856.

[204] Labeau, O.; Tamarat, P.; Lounis, B. *Temperature Dependence of the Luminescence Lifetime of Single CdSe/ZnS Quantum Dots.* Phys. Rev. Lett. **2003**, *90*, 257404/257401-257404/257404.

[205] Nirmal, M.; Dabbousi, B. O.; Bawendi, M. G.; Macklin, J. J.; Trautman, J. K.; Harris, T. D.; Brus, L. E. *Fluorescence intermittency in single cadmium selenide nanocrystals.* Nature **1996**, *383*, 802-804.

[206] Banin, U.; Bruchez, M.; Alivisatos, A. P.; Ha, T.; Weiss, S.; Chemla, D. S. *Evidence for a thermal contribution to emission intermittency in single CdSe/CdS core/shell nanocrystals.* J. Chem. Phys. **1999**, *110*, 1195-1201.

[207] Nirmal, M.; Brus, L. *Luminescence Photophysics in Semiconductor Nanocrystals.* Acc. Chem. Res. **1999**, *32*, 407-414.

[208] Frantsuzov, P. A.; Marcus, R. A. *Explanation of quantum dot blinking without the long-lived trap hypothesis.* Phys. Rev. B **2005**, *72*, 155321/155321-155321/155310.

[209] Wang, L.-W.; Califano, M.; Zunger, A.; Franceschetti, A. *Pseudopotential Theory of Auger Processes in CdSe Quantum Dots.* Phys. Rev. Lett. **2003**, *91*, 056404/056401-056404/056404.

[210] Krauss, T. D.; Brus, L. E. *Charge, Polarizability, and Photoionization of Single Semiconductor Nanocrystals.* Phys. Rev. Lett. **1999**, *83*, 4840-4843.

[211] Krauss, T. D.; O'Brien, S.; Brus, L. E. *Charge and Photoionization Properties of Single Semiconductor Nanocrystals.* J. Phys. Chem. B **2001**, *105*, 1725-1733.

[212] Shimizu, K. T.; Woo, W. K.; Fisher, B. R.; Eisler, H. J.; Bawendi, M. G. *Surface-enhanced emission from single semiconductor nanocrystals.* Phys. Rev. Lett. **2002**, *89*, 117401.

[213] Lamoureux, G. V.; Whitesides, G. M. *Synthesis of dithiols as reducing agents for disulfides in neutral aqueous solution and comparison of reduction potentials.* J. Org. Chem. **1993**, *58*, 633-641.

[214] Verberk, R.; van Oijen, A. M.; Orrit, M. *Simple model for the power-law blinking of single semiconductor nanocrystals.* Phys. Rev. B **2002**, *66*, 233202/233201-233202/233204.

[215] Verberk, R.; Orrit, M. *Photon statistics in the fluorescence of Single Mol. and nanocrystals: Correlation functions versus distributions of on- and off-times.* J. Chem. Phys. **2003**, *119*, 2214-2222.

[216] Kuno, M.; Fromm, D. P.; Johnson, S. T.; Gallagher, A.; Nesbitt, D. J. *Modeling distributed kinetics in isolated semiconductor quantum dots.* Phys. Rev. B **2003**, *67*, 125304/125301-125304/125315.

[217] Ebenstein, Y.; Mokari, T.; Banin, U. *Fluorescence quantum yield of CdSe/ZnS nanocrystals investigated by correlated atomic-force and single-particle fluorescence microscopy.* Appl. Phys. Lett. **2002**, *80*, 4033-4035.

[218] Wuister, S. F.; Swart, I.; van Driel, F.; Hickey, S. G.; Donega, C. d. M. *Highly Luminescent Water-Soluble CdTe Quantum Dots.* Nano Lett. **2003**, *3*, 503-507.

[219] Yao, J.; Larson, D. R.; Vishwasrao, H. D.; Zipfel, W. R.; Webb, W. W. *Blinking and nonradiant dark fraction of water-soluble quantum dots in aqueous solution.* Proc. Natl. Acad. Sci. USA **2005**, *102*, 14284-14289.

[220] Bawendi, M. G.; Wilson, W. L.; Rothberg, L.; Carroll, P. J.; Jedju, T. M.; Steigerwald, M. L.; Brus, L. E. *Electronic structure and photoexcited-carrier dynamics in nanometer-size cadmium selenide clusters.* Phys. Rev. Lett. **1990**, *65*, 1623-1626.

[221] Norris, D. J.; Efros, A. L.; Rosen, M.; Bawendi, M. G. *Size dependence of exciton fine structure in CdSe quantum dots.* Phys. Rev. B **1996**, *53*, 16347-16354.

[222] Norris, D. J.; Bawendi, M. G. *Measurement and assignment of the size-dependent optical spectrum in CdSe quantum dots.* Phys. Rev. B **1996**, *53*, 16338-16346.

[223] Sacra, A.; Norris, D. J.; Murray, C. B.; Bawendi, M. G. *Stark spectroscopy of CdSe nanocrystallites: the significance of transition linewidths.* J. Chem. Phys. **1995**, *103*, 5236-5245.

[224] Micic, O. I.; Cheong, H. M.; Fu, H.; Zunger, A.; Sprague, J. R.; Mascarenhas, A.; Nozik, A. J. *Size-Dependent Spectroscopy of InP Quantum Dots.* J. Phys. Chem. B **1997**, *101*, 4904-4912.

[225] Brunner, K.; Abstreiter, G.; Baehm, G.; Traenkle, G.; Weimann, G. *Sharp-line photoluminescence and two-photon absorption of zero-dimensional biexcitons in a GaAs/AlGaAs structure.* Phys. Rev. Lett. **1994**, *73*, 1138-1141.

[226] Tittel, J.; Goehde, W.; Koberling, F.; Basche, T.; Kornowski, A.; Weller, H.; Eychmueller, A. *Fluorescence Spectroscopy on Single CdS Nanocrystals.* J. Phys. Chem. B **1997**, *101*, 3013-3016.

[227] Li, X.-Q.; Arakawa, Y. *Optical linewidths in an individual quantum dot.* Phys. Rev. B **1999**, *60*, 1915-1920.

[228] Empedocles, S. A.; Neuhauser, R.; Shimizu, K.; Bawendi, M. G. *Photoluminescence from single semiconductor nanostructures.* Adv. Mater. (Weinheim, Germany) **1999**, *11*, 1243-1256.

[229] Empedocles, S. A.; Bawendi, M. G. *Influence of Spectral Diffusion on the Line Shapes of Single CdSe Nanocrystallite Quantum Dots.* J. Phys. Chem. B **1999**, *103*, 1826-1830.

[230] Seufert, J.; Weigand, R.; Bacher, G.; Kummell, T.; Forchel, A.; Leonardi, K.; Hommel, D. *Spectral diffusion of the exciton transition in a single self-organized quantum dot.* Appl. Phys. Lett. **2000**, *76*, 1872-1874.

[231] Muller, J.; Lupton, J. M.; Rogach, A. L.; Feldmann, J.; Talapin, D. V.; Weller, H. *Monitoring surface charge movement in single elongated semiconductor nanocrystals.* Phys. Rev. Lett. **2004**, *93*, 167402/167401-167402/167404.

[232] Miller, D. A. B.; Chemla, D. S.; Damen, T. C.; Gossard, A. C.; Wiegmann, W.; Wood, T. H.; Burrus, C. A. *Band-edge electroabsorption in quantum well structures: the quantum-confined Stark effect.* Phys. Rev. Lett. **1984**, *53*, 2173-2176.

[233] Polland, H. J.; Schultheis, L.; Kuhl, J.; Goebel, E. O.; Tu, C. W. *Lifetime enhancement of two-dimensional excitons by the quantum-confined Stark effect.* Phys. Rev. Lett. **1985**, *55*, 2610-2613.

[234] Seufert, J.; Obert, M.; Weigand, R.; Kummell, T.; Bacher, G.; Forchel, A.; Leonardi, K.; Hommel, D. *Correlated temporal fluctuations and random intermittence of optical transitions in a single quantum dot.* Phys. Status Solidi B **2001**, *224*, 201-205.

[235] Neuhauser, R. G.; Shimizu, K. T.; Woo, W. K.; Empedocles, S. A.; Bawendi, M. G. *Correlation between Fluorescence Intermittency and Spectral Diffusion in Single Semiconductor Quantum Dots.* Phys. Rev. Lett. **2000**, *85*, 3301-3304.

[236] Efros, A. L. *Luminescence polarization of cadmium selenide microcrystals.* Phys. Rev. B **1992**, *46*, 7448-7458.

[237] Rabani, E.; Hetenyi, B.; Berne, B. J.; Brus, L. E. *Electronic properties of CdSe nanocrystals in the absence and presence of a dielectric medium.* J. Chem. Phys. **1999**, *110*, 5355-5369.

[238] Empedocles, S. A.; Neuhauser, R.; Bawendi, M. G. *Three-dimensional orientation measurements of symmetric single chromophores using polarization microscopy.* Nature **1999**, *399*, 126-130.

[239] Chung, I.; Shimizu, K. T.; Bawendi, M. G. *Room temperature measurements of the 3D orientation of single CdSe quantum dots using polarization microscopy.* Proc. Natl. Acad. Sci. USA **2003**, *100*, 405-408.

[240] Brokmann, X.; Ehrensperger, M.-V.; Hermier, J.-P.; Triller, A.; Dahan, M. *Orientational imaging and tracking of single CdSe nanocrystals by defocused microscopy.* Chem. Phys. Lett. **2005**, *406*, 210-214.

[241] Brokmann, X.; Coolen, L.; Dahan, M.; Hermier, J. P. *Measurement of the Radiative and Nonradiative Decay Rates of Single CdSe Nanocrystals through a Controlled Modification of their Spontaneous Emission.* Phys. Rev. Lett. **2004**, *93*, 107403/107401-107403/107404.

[242] Patra, D.; Gregor, I.; Enderlein, J.; Sauer, M. *Defocused imaging of quantum-dot angular distribution of radiation.* Appl. Phys. Lett. **2005**, *87*, 101103/101101-101103/101103.

[243] Huong, N. Q.; Birman, J. L. *Origin of polarization in polar nanocrystals.* J. Chem. Phys. **1998**, *108*, 1769-1772.

[244] Schmidt, M. e.; Blanton, S. A.; Hines, M. A.; Guyot-Sionnest, P. *Polar CdSe nanocrystals: implications for electronic structure.* J. Chem. Phys. **1997**, *106*, 5254-5259.

[245] Blanton, S. A.; Leheny, R. L.; Hines, M. A.; Guyot-Sionnest, P. *Dielectric dispersion measurements of CdSe nanocrystal colloids: observation of a permanent dipole moment.* Phys. Rev. Lett. **1997**, *79*, 865-868.

[246] Shim, M.; Guyot-Sionnest, P. *Permanent dipole moment and charges in colloidal semiconductor quantum dots.* J. Chem. Phys. **1999**, *111*, 6955-6964.

[247] Klimov, V. I.; McBranch, D. W. *Auger-process-induced charge separation in semiconductor nanocrystals.* Phys. Rev. B **1997**, *55*, 13173-13179.

[248] Klimov, V. I.; Mikhailovsky, A. A.; McBranch, D. W.; Leatherdale, C. A.; Bawendi, M. G. *Mechanisms for intraband energy relaxation in semiconductor quantum dots: The role of electron-hole interactions.* Phys. Rev. B **2000**, *61*, R13349-R13352.

[249] Burda, C.; Link, S.; Mohamed, M.; El-Sayed, M. *The Relaxation Pathways of CdSe Nanoparticles Monitored with Femtosecond Time-Resolution from the Visible to the IR: Assignment of the Transient Features by Carrier Quenching.* J. Phys. Chem. B **2001**, *105*, 12286-12292.

[250] Gao, M.; Kirstein, S.; Moehwald, H.; Rogach, A. L.; Kornowski, A.; Eychmueller, A.; Weller, H. *Strongly Photoluminescent CdTe Nanocrystals by Proper Surface Modification.* J. Phys. Chem. B **1998**, *102*, 8360-8363.

[251] Kapitonov, A. M.; Stupak, A. P.; Gaponenko, S. V.; Petrov, E. P.; Rogach, A. L.; Eychmueller, A. *Luminescence Properties of Thiol-Stabilized CdTe Nanocrystals.* J. Phys. Chem. B **1999**, *103*, 10109-10113.

[252] Javier, A.; Magana, D.; Jennings, T.; Strouse, G. F. *Nanosecond exciton recombination dynamics in colloidal CdSe quantum dots under ambient conditions.* Appl. Phys. Lett. **2003**, *83*, 1423-1425.

[253] Wuister, S. F.; van Driel, F.; Meijerink, A. *Luminescence and growth of CdTe quantum dots and clusters.* Physical Chemistry Chemical Physics **2003**, *5*, 1253-1258.

[254] Wuister, S. F.; De Donega, C.; Meijerink, A. *Influence of thiol capping on the exciton luminescence and decay kinetics of CdTe and CdSe quantum dots.* J. Phys. Chem. B **2004**, *108*, 17393-17397.

[255] Wang, L.-W. *Calculating the Influence of External Charges on the Photoluminescence of a CdSe Quantum Dot.* J. Phys. Chem. B **2001**, *105*, 2360-2364.

[256] Zhang, K.; Chang, H.; Fu, A.; Alivisatos, A. P.; Yang, H. *Continuous Distribution of Emission States from Single CdSe/ZnS Quantum Dots.* Nano Lett. **2006**, *6*, 843-847.

[257] Shumway, J.; Franceschetti, A.; Zunger, A. *Correlation versus mean-field contributions to excitons, multiexcitons, and charging energies in semiconductor quantum dots.* Phys. Rev. B **2001**, *63*, 155316/155311-155316/155313.

[258] Moreau, E.; Robert, I.; Gerard, J. M.; Abram, I.; Manin, L.; Thierry-Mieg, V. *Single-mode solid-state single photon source based on isolated quantum dots in pillar microcavities.* Appl. Phys. Lett. **2001**, *79*, 2865-2867.

[259] Sebald, K.; Michler, P.; Passow, T.; Hommel, D.; Bacher, G.; Forchel, A. *Single-photon emission of CdSe quantum dots at temperatures up to 200 K.* Appl. Phys. Lett. **2002**, *81*, 2920-2922.

[260] Stevenson, R. M.; Thompson, R. M.; Shields, A. J.; Farrer, I.; Kardynal, B. E.; Ritchie, D. A.; Pepper, M. *Quantum dots as a photon source for passive quantum key encoding.* Phys. Rev. B **2002**, *66*, 081302/081301-081302/081304.

[261] Mirin, R. P. *Photon antibunching at high temperature from a single InGaAs/GaAs quantum dot.* Appl. Phys. Lett. **2004**, *84*, 1260-1262.

[262] Santori, C.; Fattal, D.; Pelton, M.; Solomon, G. S.; Yamamoto, Y. *Polarization-correlated photon pairs from a single quantum dot.* Phys. Rev. B **2002**, *66*, 045308/045301-045308/045304.

[263] Stevenson, R. M.; Young, R. J.; Atkinson, P.; Cooper, K.; Ritchie, D. A.; Shields, A. J. *A semiconductor source of triggered entangled photon pairs.* Nature **2006**, *439*, 179-182.

[264] Klimov, V. I.; Mikhailovsky, A. A.; McBranch, D. W.; Leatherdale, C. A.; Bawendi, M. G. *Quantization of multiparticle Auger rates in semiconductor quantum dots.* Science **2000**, *287*, 1011-1013.

[265] Achermann, M.; Hollingsworth, J. A.; Klimov, V. I. *Multiexcitons confined within a subexcitonic volume: Spectroscopic and dynamical signatures of neutral and charged biexcitons in ultrasmall semiconductor nanocrystals.* Phys. Rev. B **2003**, *68*, 245302/245301-245302/245305.

[266] Caruge, J. M.; Chan, Y.; Sundar, V.; Eisler, H. J.; Bawendi, M. G. *Transient photoluminescence and simultaneous amplified spontaneous emission from multiexciton states in CdSe quantum dots.* Phys. Rev. B **2004**, *70*, 085316/085311-085316/085317.

[267] Fisher, B.; Caruge, J. M.; Zehnder, D.; Bawendi, M. *Room-Temperature Ordered Photon Emission from Multiexciton States in Single CdSe Core-Shell Nanocrystals.* Phys. Rev. Lett. **2005**, *94*, 087403/087401-087403/087404.

[268] Fisher, B.; Caruge, J.-M.; Chan, Y.-T.; Halpert, J.; Bawendi, M. G. *Multiexciton fluorescence from semiconductor nanocrystals.* Chem. Phys. **2005**, *318*, 71-81.

[269] Betzig, E. *Single Mol. Observed By Near-Field Scanning Optical Microscopy.* Science **1994**, *263*, 159-159.

[270] Xie, X. S.; Dunn, R. C. *Probing Single-Molecule Dynamics.* Science **1994**, *265*, 361-364.

[271] Dunn, R. C. *Near-Field Scanning Optical Microscopy.* Chem. Rev. **1999**, *99*, 2891-2927.

[272] Koopman, M.; Cambi, A.; De Bakker, B. I.; Joosten, B.; Figdor, C. G.; Van Hulst, N. F.; Garcia-Parajo, M. F. *Near-field scanning optical microscopy in liquid for high resolution single molecule detection on dendritic cells.* FEBS Lett. **2004**, *573*, 6-10.

[273] Dyba, M.; Hell, S. W. *Focal Spots of Size l/23 Open Up Far-Field Fluorescence Microscopy at 33 nm Axial Resolution.* Phys. Rev. Lett. **2002**, *88*, 163901/163901-163901/163904.

[274] Churchman, L. S.; Okten, Z.; Rock, R. S.; Dawson, J. F.; Spudich, J. A. *Single molecule high-resolution colocalization of Cy3 and Cy5 attached to macromolecules measures intramolecular distances through time.* Proc. Natl. Acad. Sci. USA **2005**, *102*, 1419-1423.

[275] Heilemann, M.; Margeat, E.; Kasper, R.; Sauer, M.; Tinnefeld, P. *Carbocyanine Dyes as Efficient Reversible Single-Molecule Optical Switch.* J. Am. Chem. Soc. **2005**, *127*, 3801-3806.

[276] Funatsu, T.; Harada, Y.; Tokunaga, M.; Saito, K.; Yanagida, T. *Imaging of Single Fluorescent Molecules and Individual Atp Turnovers By Single Myosin Molecules in Aqueous-Solution.* Nature **1995**, *374*, 555-559.

[277] Cherny, D. I.; Fourcade, A.; Svinarchuk, F.; Nielsen, P. E.; Malvy, C.; Delain, E. *Analysis of various sequence-specific triplexes by electron and atomic force microscopies.* Biophysical Journal **1998**, *74*, 1015-1023.

[278] Woolley, A. T.; Guillemette, C.; Cheung, C. L.; Housman, D. E.; Lieber, C. M. *Direct haplotyping of kilobase-size DNA using carbon nanotube probes.* Nat. Biotechnol. **2000**, *18*, 760-763.

[279] Zhou, D.; Bruckbauer, A.; Ying, L.; Abell, C.; Klenerman, D. *Building three-dimensional surface biological assemblies on the nanometer scale.* Nano Lett. **2003**, *3*, 1517-1520.

[280] Beier, M.; Hoheisel, J. D. *Versatile derivatization of solid support media for covalent bonding on DNA-microchips.* Nucleic Acids Research **1999**, *27*, 1970-1977.

[281] Koberling, F.; Mews, A.; Philipp, G.; Kolb, U.; Potapova, I.; Burghard, M.; Basche, T. *Fluorescence spectroscopy and transmission electron microscopy of the same isolated semiconductor nanocrystals.* Appl. Phys. Lett. **2002**, *81*, 1116-1118.

[282] Van Sark, W. G. J. H. M.; Frederix, P. L. T. M.; Bol, A. A.; Gerritsen, H. C.; Meijerink, A. *Blueing, bleaching, and blinking of single CdSe/ZnS quantum dots.* ChemPhysChem **2002**, *3*, 871-879.

[283] Sauer, M.; Arden-Jacob, J.; Drexhage, K. H.; Gobel, F.; Lieberwirth, U.; Muhlegger, K.; Muller, R.; Wolfrum, J.; Zander, C. *Time-resolved identification of individual mononucleotide molecules in aqueous solution with pulsed semiconductor lasers.* Bioimaging **1998**, *6*, 14-24.

[284] Tinnefeld, P., *Multiparameter-Einzelmolekülspektroskopie auf der Basis spektral aufgelöster Fluoreszenzlebensdauermikroskopie.* Ruprecht-Karls-Universität, Heidelberg, **2002**.

[285] Lukosz, W.; Kunz, R. E. *Light emission by magnetic and electric dipoles close to a plane interface. I. Total radiated power.* J. Opt. Soc. Am. A **1977**, *67*, 1607-1615.

[286] Macklin, J. J.; Trautman, J. K.; Harris, T. D.; Brus, L. E. *Imaging and time-resolved spectroscopy of Single Mol. at an interface.* Science **1996**, *272*, 255-258.

[287] Kraus, R. M.; Lagoudakis, P. G.; Mueller, J.; Rogach, A. L.; Lupton, J. M.; Feldmann, J.; Talapin, D. V.; Weller, H. *Interplay between Auger and Ionization Processes in Nanocrystal Quantum Dots.* J. Phys. Chem. B **2005**, *109*, 18214-18217.

[288] Chang, K.; Xia, J.-B. *The effects of electric field on the electronic structure of a semiconductor quantum dot.* Journal of Applied Physics **1998**, *84*, 1454-1459.

[289] Heller, W.; Bockelmann, U.; Abstreiter, G. *Electric-field effects on excitons in quantum dots.* Phys. Rev. B **1998**, *57*, 6270-6273.

[290] Wen, G. W.; Lin, J. Y.; Jiang, H. X.; Chen, Z. *Quantum-confined Stark effects in semiconductor quantum dots.* Phys. Rev. B **1995**, *52*, 5913-5922.

[291] Menendez-Proupin, E.; Trallero-Giner, C. *Electric-field and exciton structure in CdSe nanocrystals.* Phys. Rev. B **2004**, *69*, 125336/125331-125336/125339.

[292] Enderlein, J. *Theoretical study of detection of a dipole emitter through an objective with high numerical aperture.* Opt. Lett. **2000**, *25*, 634-636.

[293] Enderlein, J. *Fluorescence detection of Single Mol. near a solution/glass interface - an electrodynamic analysis.* Chem. Phys. Lett. **1999**, *308*, 263-266.

[294] Lounis, B.; Bechtel, H. A.; Gerion, D.; Alivisatos, P.; Moerner, W. E. *Photon antibunching in single CdSe/ZnS quantum dot fluorescence.* Chem. Phys. Lett. **2000**, *329*, 399-404.

[295] Messin, G.; Hermier, J. P.; Giacobino, E.; Desbiolles, P.; Dahan, M. *Bunching and antibunching in the fluorescence of semiconductor nanocrystals.* Opt. Lett. **2001**, *26*, 1891-1893.

[296] Tinnefeld, P.; Weston, K. D.; Vosch, T.; Cotlet, M.; Weil, T.; Hofkens, J.; Mullen, K.; De Schryver, F. C.; Sauer, M. *Antibunching in the emission of a single tetrachromophoric dendritic system.* J. Am. Chem. Soc. **2002**, *124*, 14310-14311.

[297] Lin, S. C.; Tseng, F. G.; Huang, H. M.; Huang, C. Y.; Chieng, C. C. *Microsized 2D protein arrays immobilized by micro-stamps and micro-wells for disease diagnosis and drug screening.* Fresen. J. Anal. Chem. **2001**, *371*, 202-208.

[298] Ying, L.; Bruckbauer, A.; Zhou, D.; Gorelik, J.; Shevchuk, A.; Lab, M.; Korchev, Y.; Klenerman, D. *The scanned nanopipette: a new tool for high resolution bioimaging and controlled deposition of biomolecules.* Phys. Chem. Chem. Phys **2005**, *7*, 2859-2866.

7 Publication List

[1] Biebricher, A.; Paul, A.; Tinnefeld, P.; Golzhauser, A.; Sauer, M. *Controlled three-dimensional immobilization of biomolecules on chemically patterned surfaces.* Journal of Biotechnology **2004**, *112*, 97-107.

[2] Tinnefeld, P.; Buschmann, V.; Weston, K. D.; Biebricher, A.; Herten, D.-P.; Piestert, O.; Heinlein, T.; Heilemann, M.; Sauer, M. *How single molecule photophysical studies complement ensemble methods for a better understanding of chromophores and chromophore interactions.* Rec. Res. Dev. Phys. Chem. **2004**, *7*, 95-125.

[3] Herten, D.-P.; Biebricher, A.; Heilemann, M.; Heinlein, T.; Mueller, C.; Schluetter, P.; Tinnefeld, P.; Weston, K. D.; Sauer, M.; Wolfrum, J. *Optical single molecule techniques for analytical and biological applications.* Rec. Res. Dev. Appl. Phys. **2004**, *7*, 345-368.

[4] Heinlein, T.; Biebricher, A.; Schlueter, P.; Roth, C. m.; Herten, D.-P.; Wolfrum, J.; Heilemann, M.; Mueller, C.; Tinnefeld, P.; Sauer, M. *High-resolution colocalization of single molecules within the resolution gap of far-field microscopy.* ChemPhysChem **2005**, *6*, 949-955.

[5] Biebricher, A.; Sauer, M.; Tinnefeld, P. *Radiative and Nonradiative Rate Fluctuations of Single Colloidal Semiconductor Nanocrystals.* J. Phys. Chem. B **2006**, *110*, 5174-5178.

8 Abbreviations

ADC	Analog-to-Digital Converter
APD	Avalanche Photodiode
APS	Aminopropylsilane
BX	Biexciton
CPS	Cellular Positioning System
DNA	Desoxyribonucleic acid
FIFO	First-in-First-out
FRET	Fluorescence Resonance Energy Transfer
FWHM	Full-Width-Half-Maximum
GPS	Global Positioning System
HOMO	Highest Occupied Molecular Orbital
IC	Internal Conversion
IRF	Instrumental Response Function
ISC	Intersystem Crossing
LA	Longitudinal Acoustic
LO	Longitudinal Optical
lSE	linear Stark Effect
LUMO	Lowest Unoccupied Molecular Orbital
MEA	Mercaptoethylamine
MLE	Maximum Likelihood Estimator
NC	Nanocrystal
NpCF	Nitrophenylchloroformiate
NSOM	Near-Field Scanning
PBN	Phonon Bottleneck
PBS	Phosphate Buffered Saline
PET	Photoinduced Electron Transfer
PL	Photoluminescence
PSF	Point Spread Function
QCSE	Quantum-Confined Stark Effect

qSE	quadratic Stark Effect
SAM	Self-Assembled Monolayer
SD	Spectral Diffusion
SEF	Surface-Enhanced Fluorescence
SERS	Surface-Enhanced Raman Spectroscopy
SFLIM	Spectrally-resolved Fluorescence Lifetime Microscopy
SFMS	Single Molecule Fluorescence Spectroscopy
SM	Single Molecule
SPS	Single-Photon Source
STED	Stimulated Emission Depletion
SYNC	Synchronization
TA	Transversal Acoustic
TAC	Time-to-Amplitude Converter
TCSPC	Time-Correlated Single Photon Counting
TEM	Transmission Electron Microscopy
TEPA	Tetraethylenepentaamine
TIR	Total Internal Reflection
TO	Tranversal Optical
TX	Triexciton
X	Exciton

9 Acknowledgements

First and foremost I want to thank Prof. Dr. Markus Sauer for the opportunity to work in his group and for his constant and reliable support.
I am greatly indebted to Dr. Philip Tinnefeld who was indispensable for crucial discussions and let me share his deep insights and knowledge of SM spectroscopy.

I want to thank Prof. Dr. Armin Gölzhäuser and Anne Paul for the preparation of the Gold patterns.
Likewise, I have to be thankful to Prof. Dr. Joachim Spatz and Roman Glass for preparation of golddot surfaces.

I am grateful to Dr. Thomas Heinlein who introduced me into SM microscopy and scientific work, Dr. Dirk-Peter Herten and Christian M. Roth who were responsible for much of the software. Furthermore, I thank Dr. Christian Müller for his calculations.

Finally, I am thankful to the whole group in D3 in Bielefeld for constant fun and motivation during the work, especially
-Mark Schüttpelz and Dr. Joachim Ross, for their kind support and the enjoyable working atmosphere in the office
-for the general support, Reinhild Pätzmann concerning administration and burocracy, Stefan Wörmer concerning computer and printing, Dr. Gerd Wiebusch concerning laser and optics, and Dr. Rudolf Böttner for his encouragement
-the old "Heidelbergers" Hannes Neuweiler, Hannes Barsch, and Mike Heilemann for a lot of fun during and apart from work; the same goes to Robert Kasper
-Achim Donnermeier and Ralf Wilke for the nice little talks

However, the greatest thanks are to my family, especially my parents without whose assistance and patience this work would have not been possible.